Doctoral Thesis

Université de Limoges
Ecole Doctorale Sciences et Ingénierie (SI) ED 653
IRCER - Institute of research for ceramics UMR CNRS 7315

Thesis to obtain the degree of
Docteur de l'Université de Limoges
IRCER, Axe 3 - organisation structurale multiéchelle des matériaux

Presented and supported by
Raghvender
Le 22 February 2023

AB-INITIO STUDY OF THE STRUCTURE OF TELLURIUM-OXIDE BASED GLASSES: A STEP FORWARD IN ESTABLISHING THE STRUCTURE-PROPERTIES RELATIONSHIPS

Thesis supervised by Assil BOUZID and Olivier MASSON

Jury :

Président de Jury :
Dr. Philippe THOMAS
Directeur de Recherche CNRS – IRCER, Université de Limoges, Limoges (France)

Rapporteurs :
Dr. Guillaume FERLAT
Maître de conférences (HDR) – Sorbonne Université (France)

Dr. Pierre BORDET
Directeur de Recherche CNRS – Université Grenoble Alpes (France)

Examinateurs :
Dr. Oliver ALDERMAN
ISIS Neutron and Muon Source – Rutherford Appleton Laboratory (England)

Dr. Assil BOUZID
Chargé de recherche CNRS – IRCER, Université de Limoges, Limoges (France)

Prof. Olivier MASSON
Professeur – Université de Limoges, Limoges (France)

Invités :
Dr. Evgenii M. ROGINSKII
Associate Professeur – Ioffe Institute, St. Petersburg (Russia)

To my parents and grandparents,
Your unwavering love and support have propelled me towards this significant milestone.
With profound gratitude and love, I dedicate this thesis to all of you.

Remember to look up at the stars and not down at your feet. Try to make sense of what you see and wonder about what makes the universe exist. Be curious. And however difficult life may seem, there is always something you can do and succeed at. It matters that you don't just give up.

Stephen Hawking

Acknowledgement

I am overwhelmed with gratitude and appreciation as I write this section of my thesis. Completing this thesis has been a journey filled with challenges, milestones, and achievements. It would not have been possible without the support and guidance of my supervisor, colleagues, and friends. They have played a significant role in shaping my academic and personal growth, and for that, I am immensely grateful.

First and foremost, I would like to express my sincere gratitude to my supervisor, Assil BOUZID and Olivier MASSON, for thier unwavering support, guidance, and mentorship throughout my academic journey. Their expertise, patience, and attention to detail have helped me to develop critical thinking skills and a deeper understanding of my research topic. They have challenged me to think beyond the surface level, to ask difficult questions and to push my limits, for which I am eternally grateful.

I am also grateful to my colleagues David HAMANI, Sylvian CADARS, Olivier NOGUERA, Philippe THOMAS, Abid BERGHOUT and Evgenii ROGINSKII. Their encouragement, feedback, and insights have been invaluable in shaping my research ideas and honing my writing skills. I am fortunate to have been part of a vibrant community of scholars who are passionate about their work, and who have provided a supportive environment for me to thrive. Additionally, I would like to extend my sincere appreciation to the computational department (Rodolph PINON and Nicolas CALVE) and administrative department (special thanks to Paméla BATHIAS and Nadine TCHEFRANOFF) for your invaluable support. Your technical expertise, timely assistance, and administrative guidance have been instrumental in ensuring the smooth progress of this project.

To my friends Munni KUMARI, Ravikant KUMAR, Firas SHUAIB, Roberta Morais FERRERIA, Kinga SZTYMELA, Dylan VALLETT who have been a source of joy and inspiration, I thank you for your unwavering support and encouragement. You have been a constant reminder that there is more to life than academic pursuits and have helped me to maintain a balance between my academic and personal life. Your presence in my life has been a blessing, and I am grateful for every moment that we have spent together.

Special thanks to my family, who have been my biggest supporters, both emotionally and financially. Without their unwavering support, I would not have been able to pursue my academic dreams. They have been a constant source of inspiration, motivation, and encouragement

throughout my journey, and for that, I am eternally grateful. To my parents, who have instilled in me a love for learning and who have sacrificed so much to provide for my education, I owe a debt of gratitude that I can never fully repay.

To my siblings Neha and Sweta, who have always been there for me, offering their support, encouragement, and a listening ear. Your unwavering love and support have been a source of strength and motivation, and I am grateful for every moment that we have shared. In addition, I would also like to thank my little nephews (Ankur and Ayush) and niece (Pari) for always bringing a smile to my face by thier innocent and sometimes silly antics. In times of stress, their playful spirits have helped me to take a step back and remember to enjoy life's simple pleasures.

Finally, I would like to express my gratitude to all those who have contributed to this research in various ways, but whose names cannot be mentioned here. Your feedback, insights, and contributions have been invaluable, and I am grateful for the time and effort that you have invested in my work.

In conclusion, completing this thesis has been an incredible journey, filled with ups and downs, and I am grateful to have had the support of my supervisor, colleagues, friends, and family. I have learned so much through this process and have developed skills that will serve me well in my future academics/non-academics pursuits. Once again, thank you all for your support, encouragement, and guidance.

Droits d'auteurs

Contents

0 General introduction **26**

1 Bibliographical review of TeO_2-based glasses **30**

1.1 What is glass? . . . 31

1.2 Criteria of glass formation . . . 33

1.2.1 Goldschmidt's criterion of glass formation . . . 34

1.2.2 Zachariasen's continuous random network . . . 34

1.2.3 Dietzel's field strength criteria . . . 36

1.3 Tellurite based glasses . . . 38

1.3.1 Structure of crystalline TeO_2 polymorphs . . . 38

1.3.2 Structure of tellurite glasses . . . 42

1.3.2.1 Structure of pure TeO_2 glass . . . 42

1.3.2.2 Structure of modified tellurite glasses . . . 48

1.3.3 Properties of tellurite glasses . . . 52

1.3.3.1 Optical properties . . . 52

1.3.3.2 Vibrational properties . . . 55

2 *Ab-initio* modelling methods **61**

2.1 A brief introduction to density functional theory . . . 63

2.1.1 Many body interaction . . . 63

2.1.2 Born-Oppenheimer approximation . . . 64

2.1.3 Density Functional Theory . . . 66

2.1.4 Hohenberg-Kohn theorems . . . 68

2.1.5 The Kohn-Sham method . . . 71

2.1.6 Exchange-Correlation Functionals . . . 73

2.1.7 Basis Set . . . 76

2.1.8 Pseudopotential approximation . . . 79

2.2 *Ab-initio* Molecular Dynamics . . . 80

2.2.1 Born-Oppenheimer molecular dynamics . . . 81

2.2.2 Car-Parrinello molecular dynamics . . . 81
2.2.3 Temperature control . . . 83
2.2.3.1 Temperature in the NVE ensemble . . . 83
2.2.3.2 Temperature in the NVT ensemble . . . 83
2.3 Wannier functions . . . 85
2.4 Charge Analysis . . . 87
2.5 CP2K code . . . 88
2.6 *Ab-initio* principles of calculating NLO properties and Raman spectra . . . 89
2.6.1 Optical properties . . . 89
2.6.2 Raman spectra . . . 91
2.6.2.1 Vibrational analysis . . . 92
2.6.2.2 Raman tensor . . . 93

3 The structure of glassy and molten TeO_2 95
3.1 Generation and validation of the TeO_2 glass and melt models . . . 96
3.1.1 Methodology . . . 96
3.1.2 Glass and melt models . . . 98
3.2 Structural analysis . . . 106
3.2.1 Partial pair distribution function . . . 106
3.2.2 Coordination number . . . 107
3.2.3 Local environment and short-range disorder . . . 113
3.2.4 Charge Analysis . . . 117
3.2.5 Electronic localization function . . . 118
3.2.6 Efficiency of hybrid functional on electronic localization . . . 120
3.3 Conclusions . . . 121

4 Structure of Tl_2O-TeO_2 binary glasses 124
4.1 Generation and validation of the glassy models . . . 125
4.2 Structural analysis . . . 129
4.2.1 Pair distribution functions . . . 130
4.2.2 Coordination numbers . . . 134
4.2.3 Atomic local environment . . . 143
4.2.4 Rings statistics . . . 147
4.2.5 Bulk Modulus . . . 148
4.3 Relating structural and electronic properties . . . 150
4.3.1 Charge analysis . . . 150
4.3.2 Electronic localization function . . . 152

4.4 Conclusions . . . 154

5 Structure of TiO_2-Tl_2O-TeO_2 ternary glasses 155
5.1 Generation and validation of the glassy models . . . 156
5.2 Structural analysis . . . 158
5.2.1 Partial distribution functions . . . 160
5.2.2 Coordination number . . . 164
5.2.3 Atomic local environment . . . 169
5.2.4 Rings statistics . . . 174
5.2.5 Bulk modulus . . . 176
5.3 Conclusions . . . 178

6 Vibrational and optical properties of TeO_2-based glasses 179
6.1 Methodology . . . 180
6.2 Raman spectra . . . 182
6.2.1 Pure TeO_2 glass . . . 182
6.2.2 Modified TeO_2 glasses . . . 189
6.3 Non-linear optical properties . . . 193
6.4 Conclusions . . . 201

7 General conclusions 202

A Annexes 208
A.1 Classical molecular dynamics simulation of glasses . . . 209
A.1.1 Tl_2O-TeO_2 system . . . 209
A.1.1.1 Introduction . . . 209
A.1.1.2 Methodology . . . 209
A.1.1.3 Results and discussion . . . 213
A.1.1.4 Conclusions . . . 219
A.1.2 TiO_2-Tl_2O-TeO_2 system. . . . 221
A.2 *Ab-initio* simulation of TiO_2-TeO_2 glassy system . . . 223
A.3 *Ab-initio* simulation of SiO_2 glassy system . . . 226
A.4 Workflow of computing NLO properties . . . 228
A.5 Workflow of computing Raman spectra . . . 237
A.6 CP2K input file . . . 238
A.7 Structural analysis code : *amorphy* . . . 242

B Bibliography 245

References 246
List of Works 260

Table of Figures

1.1 V-T graph for glass forming liquid. Faster cooling rate gives higher glass transition temperature (T_g) than slower cooling rate [12]. 32

1.2 A_2O_3 (A: cation, O: oxygen) tetrahedral linkages in (a) crystalline and (b) glassy arrangement according to Zachariasen [14] random network theory. 35

1.3 (a) α-TeO_2 unit cell in perspective view showing a single sinusoidal "Te-O-Te" chain and and (b) representation of TeO_4 disphenoid (or, TeO_4E trigonal bipyramid) structural unit in α-TeO_2 crystal where E represents lone pair ($5s^2$). 39

1.4 β-TeO_2 crystal cell projection along c-axis. 40

1.5 (a) Three dimensional lattice of γ-TeO_2 and (b) representation of the basic TeO_{3+1} structural unit. Bond length are in Å. 41

1.6 A fragment of the TeO_2 glass model as obtained with MD simulation and illustrating typical chains and rings present in the structure. Oxygen atoms are represented as small sphere (red for BO and yellow for NBO), tellurium atoms are the medium seized spheres (black for four-coordinated, indigo for three-coordinated and dark green for five-coordinated Te) and Te lone pairs are the big transparent blue spheres. The solid lines represent the short Te-O bonds (< 2.02 Å) and dashed lines represent intermediate and long bonds (2.02 Å < d < 2.36 Å). The black bonds emphasis the rings in the structure and n is the circles indicates the amount of nodes in each found ring. Picture source [31]. 45

1.7 X-ray interference function $Q(S(Q)-1)$, for melt and glass TeO_2. Inset shows the structure factor $S(Q)-1$ for $Q \leq 5$ Å^{-1}, highlighting the shift in first diffraction peak in melt. Picture source [38]. 46

1.8 X-ray total distribution function computed by the sine Fourier transform of the interference function of figure [1.7], with $Q_{max} = 21.39$ Å^{-1} [38]. 47

1.9 Running Te coordination number as a function of distance. Picture source [38] . 48

1.10 Basic structural units found in tellurite crystals. The units are labelled in both conventional and Q^n_m notations. In the latter, m is the coordination number of the central Te atom (number of nearest neighbor oxygen atoms) and n represents the number of bridging oxygen and hence, $n \leq m$. 50

1.11 Depolymerization of TeO_4 unit into TeO_3 unit via TeO_{3+1} (1 long and 3 short bonds). . . . 51
1.12 Variation of fraction of BO/Non-bridging oxygen (NBO) with the mole fraction of the modifier content. Picture source [42] . . . 51
1.13 Third order nonlinear indexes $\chi^{(3)}$ ($m^2/V^2 \times 10^{-23}$) evolution at 0.8 μm with respect of nature of modifying oxide introduced to a $15(MO_x) - 85(TeO_2)$ (mol%) (M:x = Ga:1.5, Ba:1, Pb:1, Nb:2.5, Ti:2, Tl:0.5) glass compositions. Picture source [46]. . . . 54
1.14 Raman spectra comparison of experimental and theoretical (scaled by a factor of 1.1) TeO_2 glass. Picture source [30]. . . . 58
1.15 Composition dependence of the Raman spectra of $(TlO_{0.5})_x - (TeO_2)_{1-x}$ glassy samples. All the spectra are presented with the same arbitrary intensity scale. Picture source [50]. . . . 59

2.1 Sketch of many-body interaction between nuclei and electrons. . . . 63
2.2 Flowchart representation of working mechanism of self-consistent Kohn-Sham equation. . . . 74
2.3 Adding p-orbital to the s-orbital to obtain polarization effects. . . . 78
2.4 Adding d-orbital to the p-orbital to obtain polarization effects. . . . 79
2.5 Schematic representation of all-electron potential (dashed lines) and pseudopotential (solid lines) along with their respected wavefunctions. The vertical line r_c depicts the radius value after which both potentials behave similarly. . . . 80
2.6 Sketch representation of Born-Oppenheimer MD and Car-Parrinello MD trajectory spanned along Born-Oppenheimer potential energy surface. . . . 82
2.7 Illustration of excitation and de-excitation in energy levels using Stokes and Anti-stokes scattering in Raman Spectroscopy. . . . 91

3.1 Total reduced X-ray pair distribution function, $G_{xray}(r)$, for model 1 ,2, 3, 4 and 5, and experimental data [38] in the case of melt (red) and glass (black) TeO_2 phases. For better interpretation and clarity, a vertical shift to each of the curves are applied. . . . 101
3.2 Comparison of total X-ray Pair Distribution Function (PDF) for amorphous (black lines) and melt (red lines) phases of TeO_2 systems obtained from Model 6 and 7 to experimental results [38]. The curves are shifted vertically for better clarity. . . . 104
3.3 Experimental and computed (model 7) comparison of X-ray total structure factor for TeO_2 glass and melt. . . . 105

3.4 The partial distribution functions of $g_{\mathrm{TeTe}}(r)$, $g_{\mathrm{TeO}}(r)$, and $g_{\mathrm{OO}}(r)$ for glass (black lines) and melt (red lines) TeO_2. In the inset, the Te-Te distance distribution is decomposed into contributions from Te atoms linked by bridging O (green hue) and contributions from nearby Te atoms not directly sharing any O (blue color). Various pair distributions are shifted vertically to depict a clear representation. 106
3.5 Running Te-O coordination number ($n_{\mathrm{TeO}}(r)$) of glassy (black color) and melt (red color) TeO_2 system. Results obtained by integration of the Te-O partial PDF (solid lines) and based on Wannier centers (dashed lines) are compared to experimental results (circles) from Ref. [38]. Vertical dashed lines indicate distance cut-offs, and the dashed horizontal line indicates the ideal Te^{4+} coordination number. 108
3.6 (a) A sample picture of the environment for bonds in glassy TeO_2. Wannier Centers (designated as W), Te (brown), and O (red) (cyan). . Three distinct Wannier centers are identified: The lone pair (LP) valence electrons not participating in bonding are represented by W_{Te}^{LP}, W_{O}^{LP} and W_B along Te-O bond. (b) A typical Te environment where the O neighbors are determined using a cutoff distance (left picture) and MLWF constraint (right image). 109
3.7 Distribution of the Wannier centers around Te (top panel) and O (bottom panel) in glass (black lines) and melt (red lines) TeO_2 system. 109
3.8 Bond angle distribution $\Theta_{W_{Te}^{LP}\text{-Te-O}}$ simulated on $\alpha-$ (red), $\beta-$ (green), $\gamma-$ (blue) and glassy TeO_2 (black) using Te-O distance cutoff of 2.4 Å. Various distribution is shifted vertically for clear representation. Additionally, vertical line shows the selected cutoff angle of 73°. 111
3.9 Running Te-O coordination number (n_{TeO}) of glassy (top panel) and melt (bottom panel) TeO_2. Results obtained based on Wannier centers with variable angular constraint thresholds. 112
3.10 Decomposition of l-fold fractions of Te (l = 2, 3, 4 and 5) and O (l = 1, 2 and 3) evaluated on glass (black) and melt (red) TeO_2. 113
3.11 Distribution of the average bond asymmetry function calculated on amorphous (a) and melt (c) TeO_2 system and its breakdown into contributions from TeO_n units (n=3,4 and 5). Distribution of Te-O distances calculated on glass (b) and melt (d) TeO_2 where O atoms are either bridging or non-bridging. 115
3.12 2-D Histogram of Te-O distance vs bridge asymmetry (Te-O-Te) is illustrated for glass (top) and melt (bottom) TeO_2 system. 116

3.13 Average NACs for various l-fold (a) Te (l=3,4 and 5) and (b) O (l=1,2 and 3). Bottom compact figures illustrate distribution of NACs for glass and melt in the case of Te (c) and O (d). 118
3.14 2-D Histogram distribution of 2-fold bridging oxygen (Te-O-Te) asymmetry vs the NACs f for glassy and melt phases of TeO_2 system. 119
3.15 ELF was calculated for symmetric and asymmetric bridges in representative TeO_2 network glass fragments on the Te-O-Te plane. The ELF map is overlaid with the atomic structure of each component. Above the Te-O-Te plane, only Te (brown) and O (red) are depicted. For the sake of clarity, H atoms were employed but not shown to passivate O atoms. 120
3.16 The distribution of the Wannier function spreads as a function of the distance between Te or O atoms and the Wannier centers computed at the PBE level of theory (top panel) and PBE0 level of theory (bottom panel). 121

4.1 Comparison of total X-ray scattering PDF G(r) between experiments (solid lines) [113] and *ab-initio* MD simulation (dashed lines) for $(TlO_{0.5})_x - (TeO_2)_{1-x}$ binary glassy system with various concentrations (x). Experimental and simulated data for x = 0% are taken from Alderman *et. al.* [38] and calculated from PBE0 hybrid XC functional (see chapter [3]) 127
4.2 Comparison of total X-ray structure factor computed (dashed lines) for various $(TlO_{0.5})_x - (TeO_2)_{1-x}$ binary glasses with experimental data (solid lines) [113]. Experimental and simulated data for x = 0% are taken from Alderman *et. al.* [38] and calculated from PBE0 hybrid XC functional (see chapter [3]) 129
4.3 The partial pair correlation functions $g_{O\text{-}O}(r)$, $g_{Te\text{-}O}(r)$, $g_{Tl\text{-}O}(r)$, $g_{Te\text{-}Te}(r)$, $g_{Te\text{-}Tl}(r)$ and $g_{Tl\text{-}Tl}(r)$ for various concentration of modifier in binary $(TlO_{0.5})_x - (TeO_2)_{1-x}$ glass. 130
4.4 Histogram of distribution of bond-distances in Te chemical groups with bridging oxygen (dashed lines) and non-bridging oxygen (solid lines). All the peaks are normalized with the number of Te atoms present in each concentration. 131
4.5 Histogram of distribution of bond-distances in Tl chemical groups with bridging oxygen (dashed lines) and non-bridging oxygen (solid lines). 132
4.6 Histogram of distribution of bond-distances between bridging-bridging oxygen (dashed), non-bridging oxygen - non-bridging oxygen (solid) and non-bridging - bridging oxygen (x symbol) linkages. 133
4.7 Histogram of distribution of the Wannier centers around Te (top panel) and O (bottom panel) in various $(TlO_{0.5})_x - (TeO_2)_{1-x}$ binary glass. 135

4.8 Histogram of difference of sum of Te-W and O-W center to TeO distance. . . . 135
4.9 Bond angle distribution of angles formed by Te with its lone pair (W) and oxygen atom (Θ (W-Te-O)). In glasses, TeO cut-off of 2.46 Å is used while in the case of crystals cut-off of 2.3 Å is used. 136
4.10 For all the $(\mathrm{TlO}_{0.5})_x - (\mathrm{TeO}_2)_{1-x}$ binary glasses taken into consideration, the running coordination number ($n_{\text{Te-O}}$) using MLWF formalism as a function of TeO pair distance. Vertical dashed lines indicate distance cut-offs, and the dashed horizontal line indicates the ideal Te^{4+} coordination number. 137
4.11 Structural depolymerization of Te-O-Te bridge by addition of Tl_2O modifier. Text in the red categorizes oxygen atom into bridging oxygen (BO) or non-bridging oxygen (NBO). 138
4.12 Various Tl and Te center environments in $Tl_2Te_3O_7$, $Tl_2Te_2O_5$, and Tl_2TeO_3 crystalline polymorphs. 139
4.13 Structural fragment illustrating possible Tl^+ cation linkages with bridging oxygen (red color) and non-bridging oxygen (green lines). 141
4.14 Running coordination of considered binary glasses. Top panel represents the coordination number $n_{\text{Tl-O}}$ as a function of distance obtained using integration of partial Tl-O PDF. Middle panel represents running $n_{\text{Tl-NBO}}$ with respect to non-bridging oxygen (NBO). Bottom panel shows running $n_{\text{Tl-BO}}$ with respect to bridging oxygen (BO). 142
4.15 Percentage of l-fold coordinated Te atoms in all the considered composition of $(\mathrm{TlO}_{0.5})_x - (\mathrm{TeO}_2)_{1-x}$ binary glasses. Values less than 2% are ignored. 144
4.16 Percentage of l-fold coordinated Tl atoms in all the considered composition of $(\mathrm{TlO}_{0.5})_x - (\mathrm{TeO}_2)_{1-x}$ binary glasses. Further, values less than 2% are ignored. 145
4.17 Top panel shows the decomposition of l-fold percentage for different neighbor contribution. Bottom panel displays the evolution of percentage of bridging and non-bridging oxygen for various concentrations. 146
4.18 Rings size distribution profile for various compositions in various $(\mathrm{TlO}_{0.5})_x - (\mathrm{TeO}_2)_{1-x}$ binary glasses. For clarity, a vertical shift of 0.2 along with horizontal dashed line representing the zeros of various concentration curves is provided. . 148
4.19 Representation of rings in x=30% and 40% in $(\mathrm{TlO}_{0.5})_x - (\mathrm{TeO}_2)_{1-x}$ binary glass. Color code of atoms, red : oxygen, green : tellurium, blue : thallium. . . 149
4.20 Evolution of the calculated bulk modulus for various compositions in $(\mathrm{TlO}_{0.5})_x - (\mathrm{TeO}_2)_{1-x}$ binary glasses. 150

4.21 Electron localization function representation described for Tl-O-Tl (right) bridge and Te-O-Tl (left) bridge. Red, green and blue sphere shows oxygen, tellurium, and thallium atoms, respectively. 153

5.1 Typical thermal cycle protocol used for quenching various considered $(TiO_2)_x - (TlO_{0.5})_y - (TeO_2)_{1-x-y}$ ternary glasses (shown for Ti10-Tl10 glassy composition). 158
5.2 Snapshots of x = 10%, y = 30% of $(TiO_2)_x - (TlO_{0.5})_y - (TeO_2)_{1-x-y}$ glassy system. 159
5.3 Description of total G(r) PDF for various compositions in $(TiO_2)_x - (TlO_{0.5})_y - (TeO_2)_{1-x-y}$ glassy system. Solid lines represent the computed G(r) while the dashed line shows experimental data [131]. For clarity, a vertical shift of 2 units is provided between various compositions. 160
5.4 Comparison of computed X-ray diffraction total PDF G(r) between similar thallium-oxide composition in binary $(TlO_{0.5})_x - (TeO_2)_{1-x}$ and ternary $(TiO_2)_x - (TlO_{0.5})_y - (TeO_2)_{1-x-y}$ glassy system. 161
5.5 Partial pair distribution function $g_{\alpha\text{-}\beta}(r)$, for various possible pairs between atomic elements in $(TiO_2)_x - (TlO_{0.5})_y - (TeO_2)_{1-x-y}$ ternary glassy system. . 162
5.6 Edge and corner sharing representation of TiO_x polyhedra. Color code (red : oxygen, magenta : titanium) 163
5.7 Histogram distribution of Te-W (top panel), Ti-W (middle panel) and O-W (bottom panel) pair distances $(TiO_2)_x - (TlO_{0.5})_y - (TeO_2)_{1-x-y}$. 164
5.8 For all the compositions in the $(TiO_2)_x - (TlO_{0.5})_y - (TeO_2)_{1-x-y}$ ternary glasses taken into consideration, the running coordination number ($n_{Te\text{-}O}$) using MLWF formalism as a function of TeO pair distance. 165
5.9 Running coordination ($n_{Ti\text{-}O}$) in $(TiO_2)_x - (TlO_{0.5})_y - (TeO_2)_{1-x-y}$ ternary glass. Vertical dashed line represents the considered radius of the first coordination shell around Ti. 167
5.10 Coordination number distributions around Te atom in $(TiO_2)_x - (TlO_{0.5})_y - (TeO_2)_{1-x-y}$ ternary glass. Circles and square represent the 5% and 10% of TiO_2 modifier concentration. 169
5.11 Structural unit representation of TeO_4 unit. Green sphere: Tellurium, Red sphere: Oxygen 171
5.12 Bond-angles distribution of O-Te-O angles in $(TiO_2)_x - (TlO_{0.5})_y - (TeO_2)_{1-x-y}$ ternary glasses. 171

5.13 Polyhedra generated by TiO_x units in $(TlO_{0.5})_x-(TeO_2)_{1-x}$ binary and $(TiO_2)_x-(TlO_{0.5})_y-(TeO_2)_{1-x-y}$ ternary glass. Red sphere: Oxygen, Magenta sphere: Titanium 172
5.14 Angles O-Ti-O in $(TiO_2)_x-(TlO_{0.5})_y-(TeO_2)_{1-x-y}$ 173
5.15 Description of l-folds around Tl^+ ion in various composition of $(TiO_2)_x-(TlO_{0.5})_y-(TeO_2)_{1-x-y}$ ternary glass. l-fold fractions less than 2% are not shown in the figure. Circular and square marks represent ternary glass at 5% and 10% TiO_2 modifier concentration respectively. 174
5.16 Description of l-folds around O for various compositions in $(TiO_2)_x-(TlO_{0.5})_y-(TeO_2)_{1-x-y}$ ternary glass. Top panel represents the percentage of categorization of various l-folds into different kinds of neighbor. Bottom panel displays the evolution of concentration of bridging oxygen (BO) and non-bridging oxygen (NBO) for various glass composition. Fractions less than 2% is not represented. 175
5.17 Connectivity profiles of various compositions in $(TiO_2)_x-(TlO_{0.5})_y-(TeO_2)_{1-x-y}$ ternary glass. Y-axis, represents, R(n), number of rings with size (n), and is normalized to total number of atoms in each model. Vertical bars represent the standard deviation in the obtained values. For clarity, a shift of 0.2 units between each composition along with dashed horizontal lines showing zeros for particular curve are provided. 176
5.18 Visualization of n-size rings in $(TiO_2)_x-(TlO_{0.5})_y-(TeO_2)_{1-x-y}$ ternary glass. Red sphere: Oxygen, Magenta sphere: Titanium, Green sphere: Tellurium, Blue sphere: Thallium 177

6.1 Computational workflow used for computing Raman spectra. 181
6.2 Calculated Raman spectra on glassy TeO_2 (a) and glassy SiO_2 (b) compared to experimental results from Refs. [143],[144] and [145], respectively. A 15% blue shift was applied to the Raman shift in the case of TeO_2. The Raman intensity is normalized to the maximum peak intensity. 182
6.3 Simulated Raman spectra of glassy TeO_2 (a) and glassy SiO_2 (b) at different temperatures. The spectra are normalized to the highest frequency band, where the effect of pre-factor is minimal. 184
6.4 Calculated (a) Raman spectra and (b) the structural motifs involved in the vibrational modes. 186
6.5 Frequency dependence of displacement weights of Te and O atoms in Raman active vibrational modes. 187
6.6 Calculated phonon density of states of amorphous TeO_2 and SiO_2. 188

6.7 Phonon dispersion and phonon density of states of (a) paratellurite α-TeO_2 and (b) crystobalite α-SiO_2 (bottom). 190
6.8 Computed Raman spectra of $(TlO_{0.5})_x - (TeO_2)_{1-x}$ binary glassy system. A vertical shift has been provided in the intensity of each composition for clarity. . 192
6.9 Computed Raman spectra of $(TiO_2)_x - (TlO_{0.5})_y - (TeO_2)_{1-x-y}$ ternary glassy system. A vertical shift has been provided in the intensity of each composition for clarity. 194
6.10 Ratio of non-linear susceptibility planar average $\langle\chi^{(3)}\rangle$ of pure TeO_2 and SiO_2 dependence on system size. Convergence of the fit is performed by log function $(a \times \ln(x-b)+c)$. 196
6.11 Description of evolution of various linear and non-linear properties in $(TlO_{0.5})_x - (TeO_2)_{1-x}$ and $(TiO_2)_x - (TeO_2)_{1\text{-}x}$ (y = 0) and ternary $(TiO_2)_x - (TlO_{0.5})_y - (TeO_2)_{1-x-y}$ glasses. Orange color horizontal dashed lines displays the value obtained experimentally for paratellurite [150]. Violet color dashed line shows the ratio of $\chi^{(3)}$ in TeO_2 to SiO_2 glass as observed by Kim et al. [18]. 200

A.1 Schematic representation of interactions between shells and/or cores in Te−Tl−O systems used in our work. 211
A.2 Three crystalline thallium tellurite crystal structures used in the fit of IAP. (a) α-$Tl_2Te_2O_5$: space group - $P2_1/n$, (b) $Tl_2Te_3O_7$: space group - P_1, (c) Tl_2TeO_3 : space group - Pban. Color code: oxygen (red), tellurium (green) and thallium (cyan). 212
A.3 Illustration of the fitting flowchart used to develop the Te−Tl−O IAP. Parameters fixed during the fit are shown in rectangular boxes, while the variable parameter is displayed along the arrows. 213
A.4 (a) Temperature and (b) Total Energy variation as function of Time for x=0.4 in $(TlO_{0.5})_x - (TeO_2)_{1-x}$; Black and Red lines represent NVT and NPT ensembles respectively. 216
A.5 (a) Lattice constant of the smallest cell vector 217
A.6 Comparison of G(r) between experiments and classical MD for $(TlO_{0.5})_x - (TeO_2)_{1-x}$ amorphous system with various concentrations (x). Solid lines: experimental; dashed lines: classical MD (analysed over the last 20ps of NPT run). A shift of 2 units is given to various concentrations for better analysis of the graph. 218

A.7 Comparison of S(q) X-ray diffraction between experiments and classical MD for $(TlO_{0.5})_x - (TeO_2)_{1-x}$ amorphous system with various concentrations (x). Solid lines: experimental; dashed lines: classical MD (analyzed over the last 20 ps of NPT run). A shift of 2 units is given to various concentrations for better analysis of the graph. 220
A.8 Description of total G(r) PDF for various compositions in $(TiO_2)_x - (TlO_{0.5})_y - (TeO_2)_{1-x-y}$ glassy system. Solid lines represent the computed G(r) from classical MD simulations while the dashed line shows experimental data [131]. For clarity, a vertical shift of 2 units is provided between various compositions. . . . 222
A.9 Thermal cycle for x = 5% in $(TiO_2)_x - (TeO_2)_{1-x}$ binary glass. 223
A.10 Comparison of total X-ray scattering PDF G(r) between experiments (solid lines) [113] and *ab-initio* MD simulation (dashed lines) for $(TiO_2)_x - (TeO_2)_{1-x}$ binary glassy system with various concentrations (x). A shift of 2 units in the y-axis is given to various concentrations for better clarity of the graph. 224
A.11 The partial pair correlation functions $g_{O\text{-}O}(r)$, $g_{Te\text{-}O}(r)$, $g_{Ti\text{-}O}(r)$, $g_{Te\text{-}Te}(r)$, $g_{Te\text{-}Ti}(r)$ and $g_{Ti\text{-}Ti}(r)$ for various concentration of modifier in binary $(TiO_2)_x - (TeO_2)_{1-x}$ glass. The curves are shifted vertically for clarity. 225
A.12 Thermal cycle for 432 atom size SiO_2 glass. 226
A.13 Comparison of total X-ray and partial O-O, Si-O, Si-Si g(r) PDFs for various simulation sizes. 227
A.14 O-Si-O bond-angle distribution for various simulation sizes. 227
A.15 Second order polynomial fit of α_{xx} with respect to E_x to obtain parameters $\frac{\partial \mu_x}{\partial E_x}$, β_{xxx} and γ_{xxxx}. 228
A.16 Computational workflow used for computing linear and non-linear optical properties. Bash and python scripts are mentioned below. 229
A.17 Codes utilized for structural analysis of amorphous system 242

List of Tables

1.1 Radius ratio for typical glass-former [13]. 34
1.2 Classification of cations based on their Dietzel's field strength [16]. 37
1.3 Bond lengths and bond angles of α-TeO_2 crystal [25]. 39
1.4 Bond lengths and bond angles of β-TeO_2 crystal [27]. 40
1.5 Bond lengths and bond angles of γ-TeO_2 crystal [27]. 41
1.6 Distribution (%) of Q_m^n structural units at various temperature in TeO_2 [30] system. 42
1.7 Centers of partial correlation function first peaks at various liquid phase temperatures [30]. 43
1.8 Average coordination number of Te and O in TeO_2 system at various temperature obtained with R_{cut} = 2.36 Å [30]. 43
1.9 Optical properties of SiO_2 and TeO_2 glasses [18]. 52
1.10 Isotropic bond and reduced polarizabilities (a.u.). O^* represents double-bonded oxygen [45]. 53
1.11 Isotropic bond and reduced second hyper-polarizabilities (a.u.). O^* represents double-bonded oxygen [45]. 54
1.12 Linear and non-linear properties of various modified tellurite glasses [9]. 55
1.13 Linear and Non-linear properties of various glasses at 1.5 μm [47]. 56
1.14 Vibrational frequencies, reduced masses, force constant and Raman scattering intensities for $Te(OH)_4$ [48]. 57
1.15 Vibrational frequencies, reduced masses, force constant and Raman scattering intensities for $(OH)_3$Te-O-Te$(OH)_3$ [48]. 57
1.16 Vibrational frequencies, reduced masses, force constant and Raman scattering intensities for (OH)OTe-O-Te$(OH)_3$ [48]. 58

3.1 Various Density Functional Theory (DFT) setups used to study the model best capable of describing experimental data. In addition, the thermal cycle used for heat and quench is also reported. 100
3.2 Q_m^n fractions of Te units in glass and melt TeO_2 114

4.1 Description of $(TlO_{0.5})_x - (TeO_2)_{1-x}$ amorphous systems with various concentrations (x) in a cubic simulation cell. 126
4.2 Coordination number ($n_{Te\text{-}O}$) for all the considered modifier concentration in $(TlO_{0.5})_x - (TeO_2)_{1-x}$ binary glass and crystalline polymorphs. 138
4.3 Estimation of coordination number ($n_{Tl\text{-}O}$ = $n_{Tl\text{-}BO}$ + $n_{Tl\text{-}NBO}$) evaluated at $r_{cut\text{-}off}$ = 3.26 Å for $(TlO_{0.5})_x - (TeO_2)_{1-x}$ binary glasses and crystalline polymorphs. . 141
4.4 Q_m^n values (in percentage) evaluated for Te environments with $r_{cut\text{-}off}$ = 2.46 Å. Values less than 2% are ignored due to statistical error. 144
4.5 Evolution of Te NAC (e) charges for various l-folds and its mean value in $(TlO_{0.5})_x - (TeO_2)_{1-x}$ binary glasses at various compositions x. 151
4.6 Evolution of Tl NAC (e) charges for various l-folds and its mean value in $(TlO_{0.5})_x - (TeO_2)_{1-x}$ binary glasses at various compositions x. 151
4.7 Distribution of O NAC (e) and its dissociation into various cationic local environment contribution in $(TlO_{0.5})_x - (TeO_2)_{1-x}$ binary glasses at various compositions x. Rows highlighted in red color shows NBO contributions. 152

5.1 Description of $(TiO_2)_x - (TlO_{0.5})_y - (TeO_2)_{1-x-y}$ amorphous system with various molar concentrations in x and y. ρ and ρ_0 represents volumetric mass and number (simulation cell) densities [9]. For simplicity, we have abbreviated each system concentrations with the symbols shown in brackets of first column. . . . 157
5.2 Location of first peak (in Å) for $g_{\alpha\text{-}\beta}(r)$ partial PDF in figure (5.5) for various concentrations in $(TiO_2)_x - (TlO_{0.5})_y - (TeO_2)_{1-x-y}$ glassy systems. 161
5.3 Coordination number ($n_{Te\text{-}O}$) for all the considered modifier concentration in $(TiO_2)_x - (TlO_{0.5})_y - (TeO_2)_{1-x-y}$ ternary glass system. 166
5.4 Coordination number ($n_{Ti\text{-}O}$) for all the considered modifier concentration in $(TiO_2)_x - (TlO_{0.5})_y - (TeO_2)_{1-x-y}$ ternary glass system. 167
5.5 Estimation of coordination number ($n_{Tl\text{-}O}$ = $n_{Tl\text{-}BO}$ + $n_{Tl\text{-}NBO}$) evaluated at $r_{cut\text{-}off}$ = 3.26 Å for $(TiO_2)_x - (TlO_{0.5})_y - (TeO_2)_{1-x-y}$ ternary glass system. 168
5.6 Q_m^n values (in percentage) evaluated for Te environments with $r_{cut\text{-}off}$ = 2.48 Å and Wannier formalism constraints. Values less than 2% are ignored due to statistical error. 170
5.7 Bulk modulus of various composition in $(TiO_2)_x - (TlO_{0.5})_y - (TeO_2)_{1-x-y}$ ternary glasses along with the comparison with similar composition of TeO_2 in binary $(TlO_{0.5})_x - (TeO_2)_{1-x}$ glass. 177

6.1 Linear susceptibility $\chi^{(1)}$ and third order non-linear susceptibility $\chi^{(3)}$ in 10^{-22} m^2/V^2 calculated for glassy TeO_2 and glassy SiO_2. Experimental reference values from Ref. [150]–[152] are given in parentheses for α-TeO_2 (paratellurite). 195
6.2 Diagonal $\chi_d^{(3)}$, non-diagonal $\chi_{nd}^{(3)}$, and average $\langle\chi^{(3)}\rangle$ ratios calculated for glassy TeO_2 with respect to glassy SiO_2. Experimental reference values for α-TeO_2 (paratellurite) from Ref. [150] 197
6.3 Refractive index, first and third order non-linear susceptibility calculated for pure TeO_2, binary $(TlO_{0.5})_x - (TeO_2)_{1-x}$ and SiO_2 glassy system. We also provide the diagonal χ_d^3 (10^{-22} m^2/V^2) and non-diagonal χ_{nd}^3 (10^{-22} m^2/V^2) averages of the χ^3 (10^{-22} m^2/V^2) matrix, in addition $\langle\chi^{(3)}\rangle$. Experimental results for paratellurite are given in small parenthesis. 198
6.4 Refractive index, first and third order non-linear susceptibility calculated for binary $(TiO_2)_x - -(TeO_2)_{1-x}$ and ternary $(TiO_2)_x - (TlO_{0.5})_y - (TeO_2)_{1-x-y}$ glassy system. We also provide the diagonal χ_d^3 (10^{-22} m^2/V^2) and non-diagonal χ_{nd}^3 (10^{-22} m^2/V^2) averages of the χ^3 (10^{-22} m^2/V^2) matrix, in addition to $\langle\chi^{(3)}\rangle$. Experimental results for paratellurite are given in small parenthesis. 199
6.5 Diagonal χ_d^3, non-diagonal χ_{nd}^3, and $\langle\chi^{(3)}\rangle$ ratios calculated for pure TeO_2, binary $(TlO_{0.5})_x - (TeO_2)_{1-x}$ and $(TiO_2)_x - (TeO_2)_{1\text{-}x}$ and ternary $(TiO_2)_x - (TlO_{0.5})_y - (TeO_2)_{1-x-y}$ glasses with respect to glassy SiO_2. Experimental reference values from Ref. [150] are given parenthesis. 200

A.1 Obtained Buckingham IAP parameters for thallium core-oxygen shell and thallium shell-thallium shell interaction along with the charges and spring constants. Data for Te_c^{4+}-O_{sh}^{2-} and O_{sh}^{2-}-O_{sh}^{2-} interactions have been taken from Torzuoli *et al.* [153] work. 214
A.2 Percentage change in reproducing lattice parameters (a, b, c) compared with experiments and the mean absolute error (MAE) of investigated crystalline Tl (I) based oxides has been shown. A cut-off bond length of 3 Å is used in describing different Tl (I) environments (for the case of $TlGaO_2$, cut-off of 3.3Å is used). . 215
A.3 Tl^+-O^{2-} bond distances for three different Tl−Te−O crystalline structures based on experimental data and calculations from our IAP. 215
A.4 Description of $(TlO_{0.5})_x - (TeO_2)_{1-x}$ amorphous system with various concentrations (x). Percentage change in density ($\Delta\rho$) between experimental (Expt.) density and after NPT run i.e. final calculated (Calc.) density. All configurations feature tetragonal simulation cell. 218

A.5 Buckingham IAP parameters for various core-shell interaction along with the charges and spring constants in $(TiO_2)_x - (TlO_{0.5})_y - (TeO_2)_{1-x-y}$ ternary glasses. 221
A.6 Description of $(TiO_2)_x - (TeO_2)_{1-x}$ amorphous systems with various concentrations (x) in a cubic simulation cell. 223

List of Abbreviations

AO – Atomic Orbital.

BAD – Bond-angle Distribution Function.
BLYP – Becke-Lee-Yang-Parr.
BO – Briding oxygen.
BOMD – Born-Oppenheimer Molecular Dynamics.

CGTO – Contracted Gaussian Type Orbital.
CPMD – Car-Parrinello Molecular Dynamics.

DFT – Density Functional Theory.
DOF – degree of freedom.
DZVP – Double Zeta Valence Polarization.

GGA – Generalized Gradient Approximation.
GPW – Gaussian Plane Wave.
GTH – Goedecker-Teter-Hutter.
GTO – Gaussian Type Orbital.

HEG – Homogeneous electron gas.
HF – Hartree-Fock.

LCAO – Linear Combination of Atomic Orbitals.
LDA – Local Density Approximation.

MD – Molecular Dynamics.
MLWF – Maximally-Localized Wannier Function.

NBO – Non-bridging oxygen.

PBE – Perdew-Burke-Ernzerhof.

PDF – Pair Distribution Function.

PES – Potential energy surface.

RDM – Reduced density matrix.

SE – Schrödinger equation.

STO – Slater Type Orbital.

TZVP – Triple Zeta Valence Polarization.

WFC – Wannier function center.

0

General introduction

For several decades, numerous heavy metal oxide glasses have been studied, and they continue to pique interest from a fundamental standpoint as well as for applications in optical limiters, optical-switches, modulators, displays, lasers, amplifiers etc. The great transmittance from visible to near-infrared, minimal phonon energies, large chemical stability, wide acceptance of rare-earth ions doping, and pronounced nonlinear optical response of a range of heavy metal oxide glasses warrant additional research. Because of these properties, heavy metal oxide glasses were able to be used successfully in a variety of devices. Tellurium oxide (TeO_2) glasses are among the heavy metal oxides that offer various benefits over other oxide glasses for its applications in non-linear optical (NLO) devices. In particular, TeO_2 glasses exhibit third order NLO properties 50 times higher than conventional silicate glasses, making them promising candidates for frequency conversion mechanisms, optical switches and other applications. The existence of a stereochemically active electron lone pair $5s_2$ of the Te atoms, when bonded to oxygen, and the nature of the Te-O-Te bridges in the glassy network of TeO_2 are thought to be at the origin of the high non-linear optical properties. TeO_2 glasses typically have a linear refractive index of around 2, a huge transmittance window in the visible and infrared region up to 7μm [1], [2], a low photon cut-off energy ($\approx$ 700 cm^{-1}), a good mechanical resistance, and a high chemical durability [3]. As a result, tellurite glasses are promising materials for a wide range of applications (laser hosts [4], optical switching devices [5], erasable optical recording media [6], Raman amplification [7], [8] etc.) and have been the focus of several research works.

Despite the fact that several previous studies have investigated the structure of TeO_2 glass, the short and medium range orders in this material remain a matter of debate. Particularly, the coordination number of the tellurium atom in pure TeO_2 glass is a topic of ongoing controversy in the literature. Furthermore, more studies are needed to better achieve an understanding of the melt and the glassy TeO_2 systems.

Additionally, TeO_2 is a poor glass former, which necessitates the addition of a modifier oxide (MO) to achieve a better stability of the glassy phase. The addition of MO to TeO_2 glass, usually leads to a decrease of its non-linear properties. Interestingly, the opposite trend has been observed for Tl_2O modifier, as its addition, contrary to other MO leads to maintain the high optical non-linearity of TeO_2 based glasses. However, most aspects of the Tl^+ local environments in the amorphous matrix remain unknown, such as how thallium atoms interact with bridging oxygens (BO) and non-bridging oxygens (NBO) in the glassy systems and how do they evolve as a function of the concentration of MO.

Although the addition of a thallium oxide modifier maintains the non-linear index of TeO_2 glasses,

it has a limited effect in improving its mechanical properties [9]. In an effort to get around this issue, researchers have examined the effects of adding a second modifier (titanium oxide) that leads to a potential stabilization of $(TlO_{0.5})_x - (TeO_2)_{1-x}$ binary glass. It was concluded that adding TiO_2 and Tl_2O MOs to TeO_2 preserves the exceptional optical characteristics of pure TeO_2 glass while improving its mechanical and thermal stability. However, to date the description of the atomic scale environments in the ternary glass remain unknown.

At this stage, *ab-initio* molecular dynamics, which is based on a quantum mechanical interpretation of the interaction between the particles, can be used to study the atomistic model description of TeO_2 based glasses. In practice, we conduct a methodological study that aims to establish a reliable simulation protocol capable of reproducing experimental data. Subsequently, we compute the various physio-chemical properties once the glassy model has been established. This thesis attempts to provide answers to the open questions cited above and is organized in six chapters as follows:

The first chapter recalls the essence of TeO_2-based glasses properties and the physics behind their outstanding behavior. We recall the criteria of glass formation and the most relevant theories of network organization in glasses. Subsequently, we briefly discuss the structure of crystalline TeO_2 followed by a literature review of works focusing on the structure of glassy matrix in TeO_2 system. Further, we also highlight the previous works on the influence of modifier oxide in TeO_2 glassy structure. Finally, we close this chapter by discussing the optical and vibrational properties of modified tellurite glasses.

In chapter 2, the principle of *ab-initio* methods used to model materials at the atomic scale are presented. The ability to simulate the dynamics of materials at the atomic scale via *ab-initio* molecular dynamics (MD) makes it a powerful tool in computing various properties of the material. In particular, we briefly describe the main formulation of density functional theory (DFT). Subsequently, we briefly discuss the methodology for computing non-linear optical properties and Raman spectra in the case of glassy systems.

In the next chapter, we have carried out *ab-initio* MD by resorting to a variety of DFT based schemes. Here we have shown the role of hybrid functional in better reproducing the experimental measurements. Using the obtained model, we compute the Te coordination number using maximally localized Wannier formalism (MLWF) for glassy and melt TeO_2. In addition, we also discuss the various local environments around Te. Further, we focus on the short-range disorder around Te and O atom and show that the asymmetry in Te-O-Te bridges is more pronounced in the

melt TeO_2 compared to the glass. Finally, we correlate the various Te and O local environments with electronic structure by performing charge and electron localization function (ELF) analysis.

Chapter 4 focuses on understanding how $TlO_{0.5}$ influence the network of TeO_2 glass. In particular, we comment on trends in the PDF when varying the composition x in $(TlO_{0.5})_x - (TeO_2)_{1-x}$ glasses. Further, we also analyze various local environments around Te, Tl and O atoms. We see that adding Tl leads to a depolymerization of the network and hence to a weakening of the mechanical strength of the glass. We close this chapter, by performing charge and ELF analyzes and discuss the nature of Tl-O and Te-O chemical bonding.

Next chapter 5 deals with, understanding the role of TiO_2 in $(TlO_{0.5})_x - (TeO_2)_{1-x}$ binary glasses. In particular, introducing TiO_2 have shown to improve the thermal and mechanical stability of the tellurite glass. However, it lowers the non-linear optical index of the material. We find that the incorporating TiO_2 does not lead to a depolymerization of the glassy network and in fact, promotes the binding of the structure.

In the last chapter, Raman spectra are computed using DFT and finite difference method. In particular, we focus on pure TeO_2 glass and attempt to study the origin of the strong Boson peak in comparison to SiO_2 glass Raman spectra. Further, we also study the evolution of Raman spectra as a function of the composition in binary $(TlO_{0.5})_x - (TeO_2)_{1-x}$ and ternary $(TiO_2)_x - (TlO_{0.5})_y - (TeO_2)_{1-x-y}$ glasses. Additionally, we correlate the TeO_2 glassy structure to the high non-linear susceptibility and compare the obtained optical properties to those calculated for conventional silicate glasses. To do this, we calculate the $\chi^{(1)}$ and various components of $\chi^{(3)}$ to understand the evolution of linear and nonlinear properties of tellurite based glasses at various compositions of modifier oxides.

As such this thesis work makes a step forward towards the understanding of TeO_2 based glasses in a close correlation to their macroscopic properties by relying on advanced modelling techniques.

1

Bibliographical review of TeO_2-based glasses

Summary

1.1 What is glass? **31**
1.2 Criteria of glass formation **33**
1.2.1 Goldschmidt's criterion of glass formation 34
1.2.2 Zachariasen's continuous random network 34
1.2.3 Dietzel's field strength criteria 36
1.3 Tellurite based glasses **38**
1.3.1 Structure of crystalline TeO_2 polymorphs 38
1.3.2 Structure of tellurite glasses 42
1.3.2.1 Structure of pure TeO_2 glass 42
1.3.2.2 Structure of modified tellurite glasses 48
1.3.3 Properties of tellurite glasses 52
1.3.3.1 Optical properties 52
1.3.3.2 Vibrational properties 55

1.1 What is glass?

GLASS is a complex disordered material with a structure that straddles between the crystalline and the liquid states. It is often described as a non-equilibrium super-cooled liquid. At high temperatures, this behaves like a liquid with atoms or molecules free to move about, however, when the liquid is cooled, the atoms reorganize themselves into a relatively more efficient packing resulting in a better defined short and especially medium-range orders. This reorganization process ceases after certain temperature, thus there is no long-range order present in the glassy state and the atomic arrangements resemble more to that of a liquid. In general, glasses have a solid-like appearance. It exhibits similar mechanical and thermal properties in correspondence with its crystalline form. However, contrastingly to most crystals, glasses do not have a well-defined melting point. Furthermore, glasses exhibit a range of remarkable properties such as mechanically strong, hard surface that is resistant to abrasion and corrosion, elastic (up to a breaking point), isotropic, extensive optical properties, heat-absorbent and good insulator/conductor etc.

In order to be employed in a given product, a material must possess certain physio-chemical properties that fits the target application. At this point, glasses offer great opportunities due to the fact that their properties can be modified in controlled and continuous manner to meet specific requirements. With a proper selection of raw materials and processing techniques it is feasible to tailor the desired properties, chemical composition, and ease of shape. Further, glasses can be constructed into transparent or colored materials. It can be spun like a spider's web or sculpted into a massive mirror weighing tons. It can be made more delicate than paper [10] or as strong as steel [11].

To understand glasses thermodynamically, let's consider a small volume of material at a high temperature well above the melting temperature in a liquid state. The state of this material can be represented at point "a" in the volume-temperature diagram (see figure [1.1]). As we cool the melt, the volume of the system decreases along the path "abc". In figure [1.1], point "b" represents the melting temperature T_m at which the Gibbs free energy of melt equals to that of the corresponding crystalline state. At this temperature, a small amount of crystal nuclie starts to appear within the liquid, however, to further crystallize, there is a need of either a presence of sufficiently large number of nuclei or the existence of a large crystal growth rate. The under-cooling that causes a specific group of atoms to go from a liquid to a crystalline state and the rate at which atoms from the liquid may be carried to the crystal liquid interface are two variables that contribute to the wide area at point "c". Under further cooling to any temperature below point "c" would normally result into the conversion of the material into the crystalline state, with long range order and periodic atomic arrangements. If this occurs, the

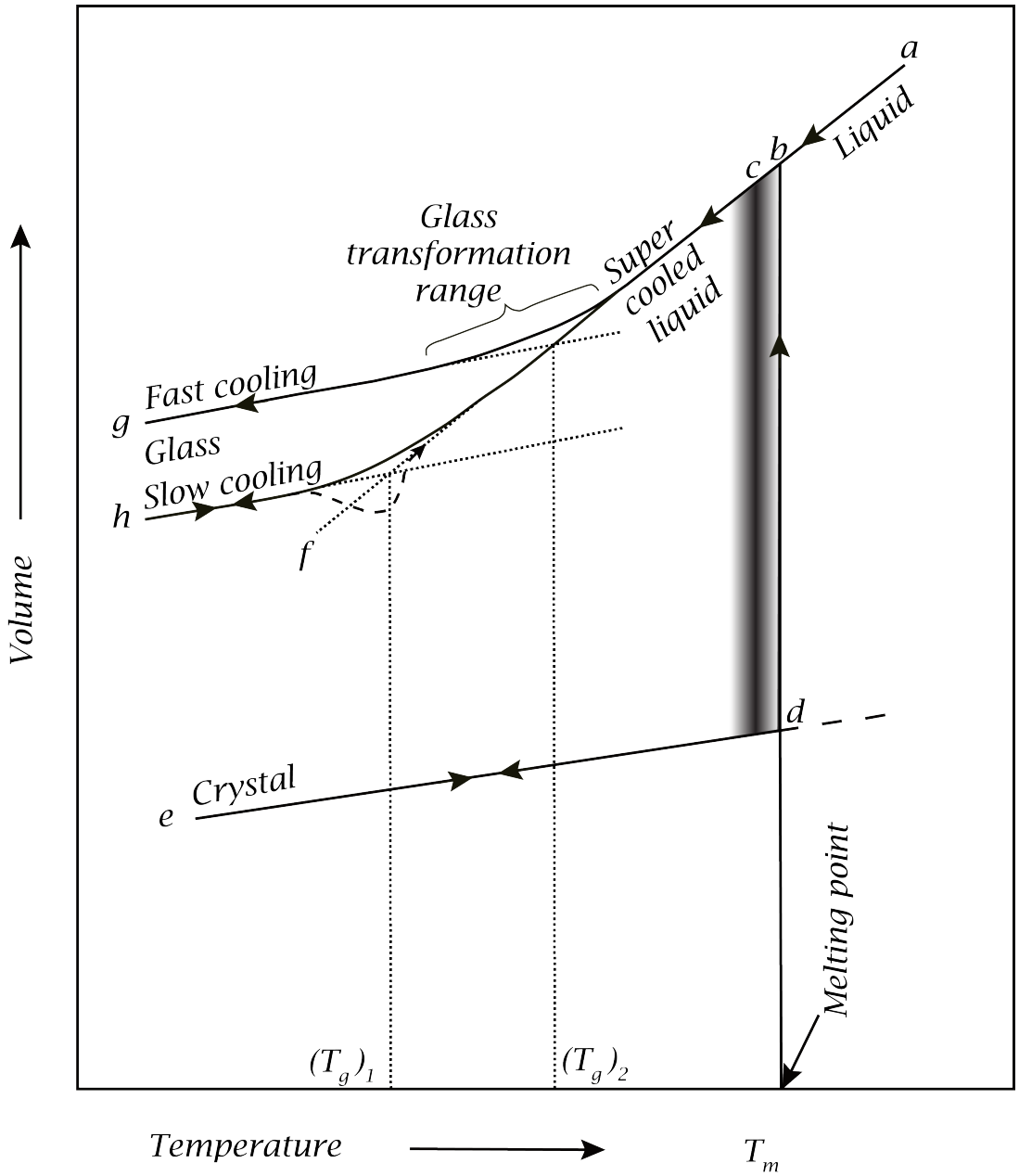

Figure 1.1: V-T graph for glass forming liquid. Faster cooling rate gives higher glass transition temperature (T_g) than slower cooling rate [12].

volume will decrease sharply to the corresponding volume of crystal at point "d" and from now the "de" path is followed upon further continued cooling.

If the crystallization of the liquid does not occur under cooling below the melting temperature (mostly due to high cooling rate), a super-cooled liquid following the line "bcf" is obtained with no discontinuities in the V-T graph. At this stage, the liquid continues to shrink by rearranging its structure as the temperature decreases. Upon further cooling, the atoms become less and less mobile, thus the viscosity increases. As the liquid is cooled further, the increase in viscosity becomes so large that the atoms can no longer completely rearrange to the equilibrium liquid structure characterized at that temperature. Therefore, the liquid starts to deviate from the path "bcf" towards the curve of decreasing slope "bcg" until the viscosity becomes so large that the structure of the liquid becomes frozen and depends weakly on temperature. In the low-temperature region, the frozen liquid is in a glassy state and has solid-like characteristics in terms of mechanical strength.

The intersection of the extrapolated glass line and the super-cooled liquid line is termed as glass transition temperature (T_g). The departure from the super-cooled liquid line is dependent on the cooling rate. Lower cooling rates allow the atoms to rearrange for longer time, and thus it stays on the "bcf" line for longer duration before reaching point "h". This longer rearrangement time yields smaller specific volume and a lower glass transition temperature in contrast to cooling at higher rates.

In conclusion, a glass is described as "an amorphous solid displaying a region of glass transition (from relatively viscous and fluid state to hard and brittle state) behavior and utterly lacking in long range order and periodic atomic arrangements." Any substance whether organic, inorganic or metallic, manufactured by any technique showing such properties can be termed as glass.

1.2 Criteria of glass formation

Before the 20th century, the majority of known glasses were silicate-based, however, few non-silicate-based glasses were later found. In order to understand why some materials easily produce glasses while others do not, several theories have been proposed. In the following subsections, the most relevant criteria of glass formation will be briefly outlined.

1.2.1 Goldschmidt's criterion of glass formation

Goldschmidt is widely regarded as the founder of modern crystal chemistry. He used an empirical approach to justify the formation of glass. During his era, attempts were made to interpret observable glass properties primarily qualitatively. He proposed that if the cation to anion radius ratio $(r_c : r_a)$ is between 0.2 and 0.4, the compound can form a glass [13]. He further supported up his claims with tests on several compounds as listed in the table [1.1]. According to Goldschmidt, this range of the radius ratio defines the tetrahedral arrangement

Compound	Radius Ratio (r_c: r_a)
SiO_2	$r_{Si} : r_O \approx 0.28$
B_2O_3	$r_B : r_O \approx 0.14$
P_2O_5	$r_P : r_O \approx 0.25$
GeO_2	$r_{Ge} : r_O \approx 0.31$
BeF_2	$r_{Be} : r_F \approx 0.25$

Table 1.1: Radius ratio for typical glass-former [13].

of oxygen atoms surrounding cation atoms, which are required for the formation of the glass. However, this theory makes no attempt to explain why tetrahedral coordination should be so favorable to the formation of the glass. Furthermore, the model does not appear to work the other way around, for example, BeO has a radius ratio that is approximately identical to SiO_2, but still, it is not possible to prepare the former compound in vitreous form. Owning to such shortcomings, soon a better theory was proposed.

1.2.2 Zachariasen's continuous random network

Some years later, Zachariasen [14] in his research extended the Goldschmidt's theory and made an effort to justify why particular coordination numbers may promote the production of glass. According to Zachariasen's random network theory, glasses and their corresponding crystals share the same order of atomic forces due to similar mechanical properties. In addition, Zachariasen rules of glass formation postulates that atomic arrangements in the glassy network are due to corner sharing of randomly oriented cation centered polyhedra. This randomness in three-dimensional network would result in a higher internal energy in contrast to the corresponding crystalline arrangement, however, the difference in the internal energy must be small otherwise the driving forces would substantially lead to crystallization.

The analogy of structural arrangements between crystalline and glassy systems for a hypothetical A_2O_3 compound in 2-dimension is depicted in the figure [1.2]. It is apparent from the figure, that both structures are composed of AO_3 triangles joined with each other via corner sharing linkages. However, the atomic arrangements in the glassy network has disorder due to the varied

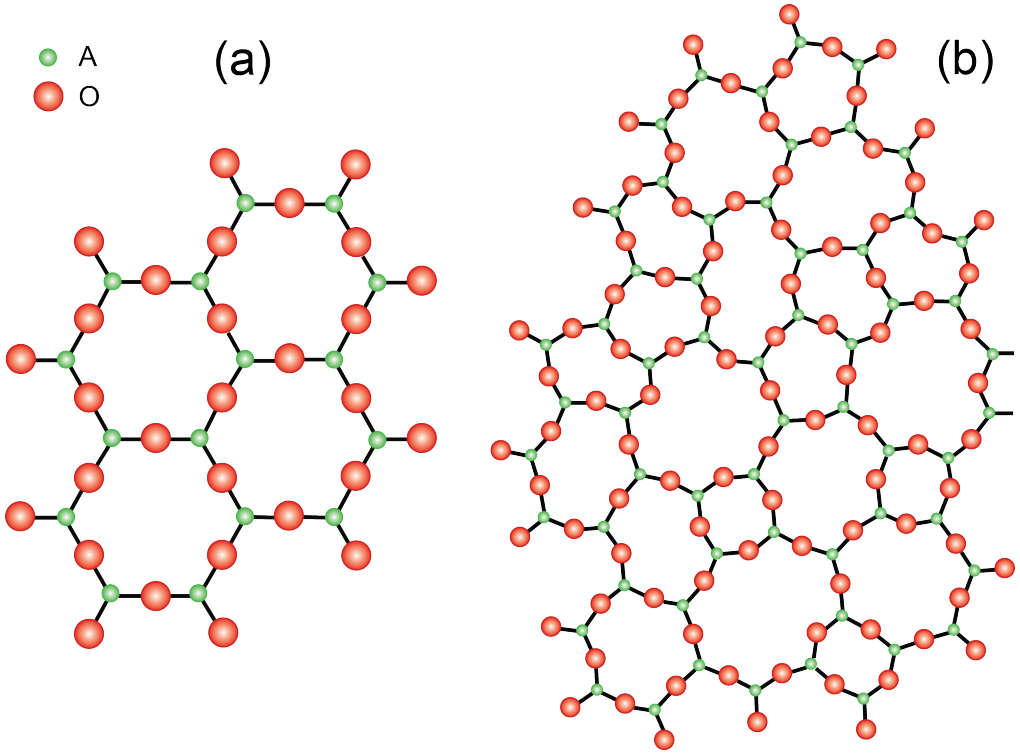

Figure 1.2: A_2O_3 (A: cation, O: oxygen) tetrahedral linkages in (a) crystalline and (b) glassy arrangement according to Zachariasen [14] random network theory.

A-O-A bond angles and A-O bond lengths. These disorder provides the strucural flexibity in the network connections allowing the glassy arrangement to be possible. Note worthily we see that O-A-O angles themselves need not be distorted significantly in the glassy network as compared with their crystalline counterpart.

Additionally, if we have compound AO and assume that the cation polydera were triangles then it is easy to realize that its glassy structure cannot exist as under this configuration each A around O is required to have a coordination number of 3. This implies that each oxygen is shared by three A's, thus ordering will be topologically restrained. Zachariasen, therefore, defines four glass formation rules for a compound A_mO_n:

1. oxygen (anion) atom must be linked with a maximum of two cations A,
2. cation should have oxygen coordination up to 4,
3. cation polyhedra should be linked by corners, not faces nor edges,
4. a minimum of three corners must be shared.

Zachariasen's random network is a widely supported model in structural theory of glass formation. However, the theory predicts the formation of P_2O_3, As_2O_3, Sb_2O_3, V_2O_5, Sb_2O_5, Nb_2O_5, Ta_2O_5 etc. glasses, but none of these oxides were known to form by ordinary means, even though

all of them do form glasses when stabilizing modifier oxide is added [15]. The discovery of glassy metals, semiconducting chalcogenides, and other heavy metal fluoride glasses that have no oxygen, have further challenged the random network theory.

1.2.3 Dietzel's field strength criteria

Dietzel's field strength criterion [16] extends Goldschmidt's rules of an atomic size (and polarizability) to the effect of cation charges. In this way, he took into account the impact of forces interacting between cations and anions as a melt solidifies. Field strength F for cation (assuming that anion is oxygen) is introduced as:

$$F = \frac{Z_c}{(r_c + r_o)^2} = \frac{Z_c}{a^2}, \tag{1.1}$$

where, $a = r_c + r_o$, r_c and r_o are the radii of the cation and the anion, respectively, and Z_c is the cation charge. Table [1.2], gathers the values of field strength of various cations [16] and their classification into network-formers, network-modifiers, and intermediates.

According to Dietzel, network forming cations have high field strength between $F \approx 1.4$ to 2, while the network modifying cations have low field strength ranging from $F \approx 0.1$ to 0.4. Additionally, intermediates have field strength in between network former and network modifiers as $F \approx 0.5$ to 1.0. Under cooling, the high field strength cations repel each other strongly and compete for the oxygen atom to achieve denser packing. Furthermore, the smaller ionic radius of high field strength cations requires low coordination number polyhedra with oxygen. These two factors promote disordered arrangements Generally, while the low field strength cation can relatively come close to each other which results in high coordination polyhedra. Using the idea of field strength, Dietzel was able to account for the behavior of cooling a melt which otherwise could not be explained solely on the basis of Zachariasen's rules.

These discussed criteria establish distinct methods for evaluating whether or not specific oxide molecules will form a glass and how likely that is to happen. Moreover, these various models, help in identifying the choice of modifier which can further be utilized to enhance the properties of a given glass. Though, the discussed theories are insightful in understanding the glassy matrix of ordinary glasses like SiO_2, they fall short in explaining glasses whose network structure becomes complex and largely influenced by the nature of bonding and the presence of lone pair electrons in its constituent molecules, such as TeO_2. Glassy TeO_2 and its modified oxides are the main focus of this PhD thesis. Therefore, in the upcoming sections, we provide a review of the structure of both glassy and crystalline TeO_2.

Element	Valence Z	Ionic radius (for CN =6 r (Å))	Most frequent coordination number CN	Ionic distance for oxides a (Å)	Field strength at distance of O^{2-} ions Z/a^2	Function in glass structure
K	1	1.33	8	2.77	0.13	
Tl	1		3	2.53	0.16	
Na	1	0.98	6	2.30	0.19	
Li	1	0.78	6	2.10	0.23	
Ba	2	1.43	8	2.86	0.24	Network
Pb	2	1.32	8	2.74	0.27	modifier
Sr	2	1.27	8	2.69	0.28	$Z/a^2 \approx 0.1...0.4$
Ca	2	1.06	8	2.48	0.33	
Mn	2	0.91	6	2.23	0.40	
Fe	2	0.83	6	2.15	0.43	
Mn	2	0.83	4	2.03	0.49	
Mg	2	0.78	6	2.10	0.45	
			4	1.96	0.53	
Zr	4	0.87	8	2.28	0.77	
Be	2	0.34	4	1.53	0.86	Intermediate
Fe	3	0.67	6	1.99	0.76	$Z/a^2 \approx 0.5...1.0$
			4	1.88	0.85	
Al	3	0.57	6	1.89	0.84	
			4	1.77	0.96	
Te	4		4	2.00	1.00	
Ti	4	0.64	6	1.96	1.04	
B	3	0.20	4	1.50	1.34	
Ge	4	0.44	4	1.66	1.45	Network
Si	4	0.39	4	1.60	1.57	former
P	5	0.34	4	1.55	2.10	$Z/a^2 \approx 1.5...2.0$
B	3	0.20	3		1.63	

Table 1.2: Classification of cations based on their Dietzel's field strength [16].

1.3 Tellurite based glasses

The most prevalent types of oxide glasses are silicates, which are fundamentally made up of four oxygen atoms linked to a central silicon atom in a tetrahedron-shaped unit. Under quenching, the tetrahedra linked via bonding oxygen are randomly oriented in three-dimensional network. Boron and phosphorous oxide are the other examples of good network former elements in glasses. However, unlike others, tellurium oxide is not a good glass former and require rapid quenching techniques to form a glass. Based on Dietzel's field strength criteria, the Te^{4+} cation has a field strength of 0.99 which lies under the category of intermediate and is closer to the network former rather than the network modifiers (see table [1.2]). As a result, pure TeO_2 is only a conditional glass former and is not very stable thermally with respect to devitrification [17]–[20]. Therefore, understanding the processes which prevents the glass formation under normal conditions requires an understanding of the TeO_2 structure.

1.3.1 Structure of crystalline TeO_2 polymorphs

This section introduces the crystalline structure of tellurium oxide (TeO_2). Crystalline phases are indeed good prototype of the short-range order in tellurite glasses as put forward by Zachariasen's rules. TeO_2 with a melting temperature T = 1006 K exhibits four known structural polymorphs as paratellurite α-TeO_2, tellurite β-TeO_2, γ-TeO_2 and δ-TeO_2.

Paratellurite is stable at room temperature and standard pressure while tellurite is metastable and is the natural form of the tellurium oxide mineral. These two polymorphs may be thought of as various arrangements of TeO_4 disphenoid units. Two more polymorphs of TeO_2, namely the γ [21], [22] and δ [21], [23] phases were identified at the IRCER laboratory via recrystallized TeO_2 rich glasses in TeO_2-WO_3 [21] and TeO_2-$NbO_{2.5}$ [24] systems.

α-TeO_2 polymorph

Paratellurite α-TeO_2 is the most studied polymorph of TeO_2. The work of P. A. Thomas *et al.* [25] reports the structure to be in $P4_12_12$ space group with cell parameters a = b = 4.8082 Å and c = 7.6212 Å. As shown in the figure [1.3], each tellurium atom is linked to 4 oxygen atoms with two equatorial (short) bonds and two axial (long) bonds. The structural unit of α-TeO_2 can be described as a TeO_4 disphenoid with the two equatorial distances (2 x 1.879 Å) shorter than the two axial distances (2 x 2.121 Å). This structural unit is also often described as TeO_4E trigonal bipyramid (tbp) where the other third equatorial directions is occupied by the $5s^2$ electronic lone pair (E) of the tellurium atom. The environment of Te atoms is sometimes viewed as sitting in a highly distorted octahedra when distant oxygen atoms (up to $\approx$ 2.9 Å) are considered other than equatorial and axial oxygens.

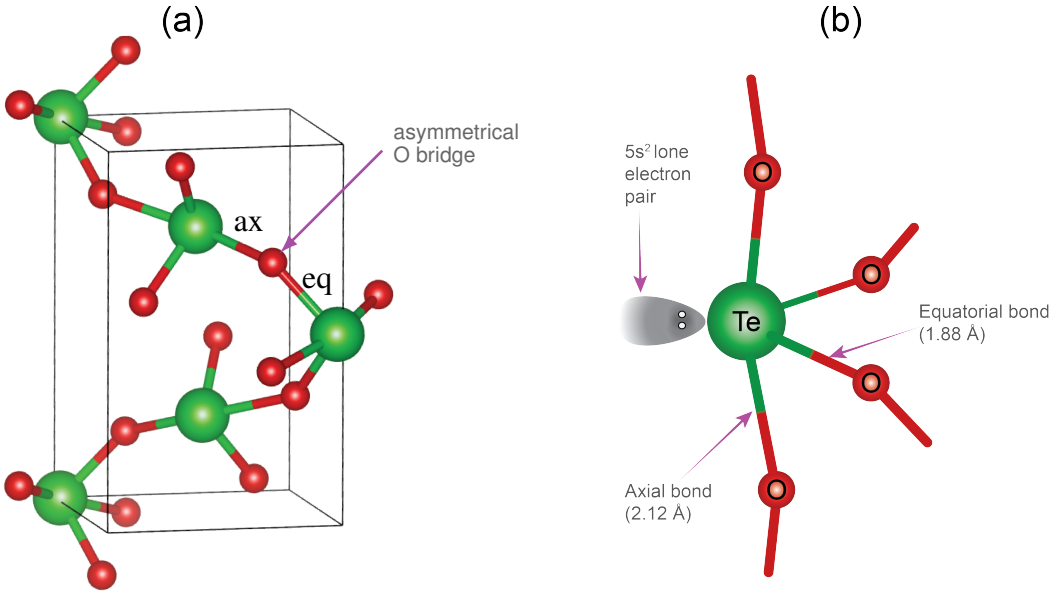

Figure 1.3: (a) α-TeO_2 unit cell in perspective view showing a single sinusoidal "Te-O-Te" chain and and (b) representation of TeO_4 disphenoid (or, TeO_4E trigonal bipyramid) structural unit in α-TeO_2 crystal where E represents lone pair ($5s^2$).

The crystal structure of α-TeO_2 can be regarded as a network of corner sharing TeO_4 disphenoids. In this configuration, each oxygen atom is bonded to two tellurium atoms by axial and equatorial bonds forming an asymmetrical bridge (see figure [1.3 (a)]). The bond-lengths and bond-angle parameters of the above crystal structure are given in table [1.3].

Bond length (Å)		**Bond Angle (deg.)**	
Te-O_{eq}	1.879	O_{eq}-Te-O_{eq}	103.37
Te-O_{eq}	1.879	O_{eq}-Te-O_{ax}	88.32
Te-O_{eq}	2.121	O_{eq}-Te-O_{ax}	84.22
Te-O_{eq}	2.121	O_{ax}-Te-O_{ax}	167.97
		Te-$_{eq}O_{ax}$-Te	138.61

Table 1.3: Bond lengths and bond angles of α-TeO_2 crystal [25].

β-TeO_2 polymorph

This is the natural form of tellurium oxide which transforms irreversibly to α polymorph at 600° C. The β polymorph shows Pbca (space group) orthorhombic structure with the unit cell parameters a = 12.035 Å, b = 5.464 Å and c = 5.607 Å [26]. The β-TeO_2 polymorph differs from the α-TeO_2 polymorph as the crystal lattice of the former has a layered structure (see figure [1.4]) with weakly bonded layers and the later forms a three-dimensional network. In

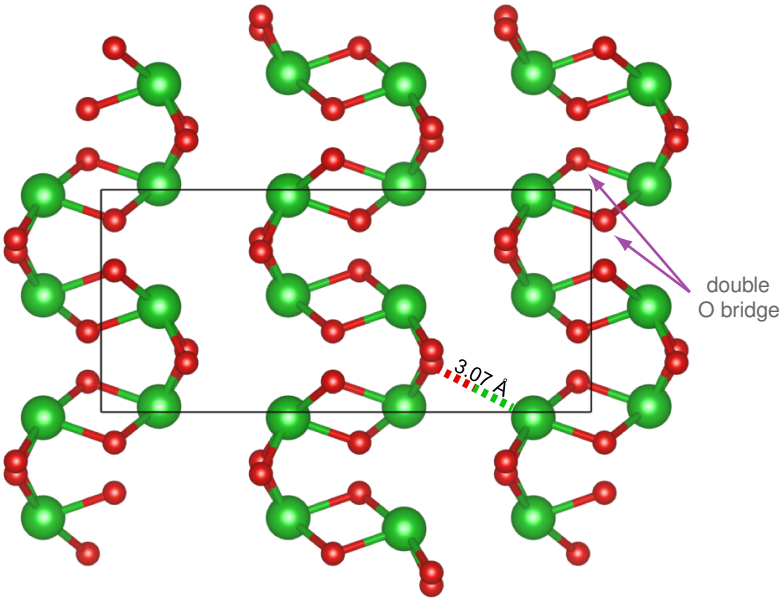

Figure 1.4: β-TeO_2 crystal cell projection along c-axis.

β-TeO_2 polymorph, TeO_4 disphenoids share edges i.e. tellurium atoms are linked with two oxygen atoms via double bridge. The bond-length and bond-angle parameters of the β-TeO_2 crystal structure are given in table [1.4].

Bond length (Å)		**Bond Angle (deg.)**	
Te-$O_{eq}(1)$	1.877	$O_{eq}(1)$-Te-$O_{eq}(2)$	101.15
Te-$O_{eq}(2)$	1.927	$O_{eq}(1)$-Te-$O_{ax}(1)$	78.13
Te-$O_{eq}(1)$	2.196	$O_{eq}(1)$-Te-$O_{ax}(2)$	90.06
Te-$O_{eq}(2)$	2.070	$O_{eq}(2)$-Te-$O_{ax}(1)$	90.03
		$O_{eq}(2)$-Te-$O_{ax}(2)$	89.67
		$O_{ax}(1)$-Te-$O_{ax}(2)$	167.89
		Te-$_{eq}O_{ax}(1)$-Te	101.88
		Te-$_{eq}O_{ax}(2)$-Te	137.46

Table 1.4: Bond lengths and bond angles of β-TeO_2 crystal [27].

γ-TeO_2 polymorph

This polymorph [28] as displayed in figure [1.5] was discovered much later than α and β polymorphs at IRCER lab via X-ray diffraction of recrystallized TeO_2-rich glasses in TeO_2-WO_3 [21] and TeO_2-$NbO_{2.5}$ [21] systems. The crystal was prepared by slowly heating pure TeO_2 glasses up to 390° C and then followed by annealing the sample for 24 hours.

The γ-TeO_2 crystal belongs to $P2_12_12_1$ space group and exhibit orthorhombic symmetry with the unit cell parameter as a = 4.8809 Å , b = 8.5668 Å and c = 4.3433 Å. This structure can also be described as corner-sharing TeO_4 disphenoids. The structural motif of γ-TeO_2 crystal shows highly distorted structure than motifs in α and β polymorphs. In the structural unit of this polymorph, one bond is much longer than the three other bonds thus it is often referred to as TeO_{3+1} unit (see figure [1.5b]). Below, table [1.5] reports the bond length and bond angle

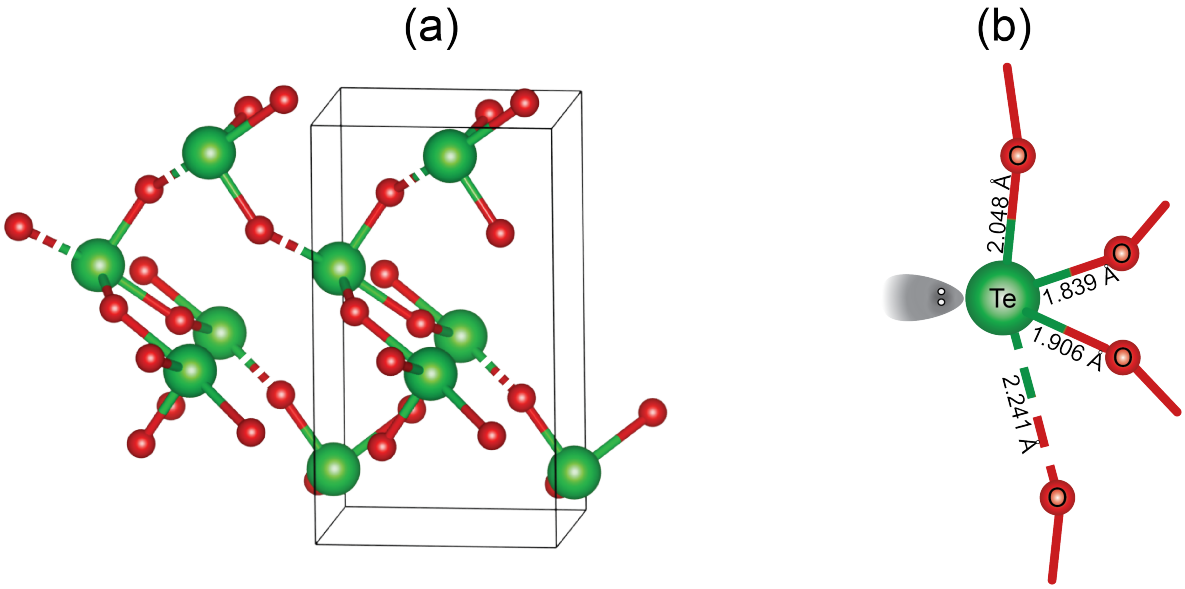

Figure 1.5: (a) Three dimensional lattice of γ-TeO_2 and (b) representation of the basic TeO_{3+1} structural unit. Bond length are in Å.

parameters of γ-TeO_2 polymorph.

Bond length (Å)		**Bond Angle (deg.)**	
Te-$O_{eq}(1)$	1.839	$O_{eq}(1)$-Te-$O_{eq}(2)$	100.36
Te-$O_{eq}(2)$	1.906	$O_{eq}(1)$-Te-$O_{ax}(1)$	91.69
Te-$O_{eq}(1)$	2.241	$O_{eq}(1)$-Te-$O_{ax}(2)$	93.14
Te-$O_{eq}(2)$	2.048	$O_{eq}(2)$-Te-$O_{ax}(1)$	75.60
		$O_{eq}(2)$-Te-$O_{ax}(2)$	78.68
		$O_{ax}(1)$-Te-$O_{ax}(2)$	154.28
		Te-$_{eq}O_{ax}(1)$-Te	131.6
		Te-$_{eq}O_{ax}(2)$-Te	125.18

Table 1.5: Bond lengths and bond angles of γ-TeO_2 crystal [27].

The δ-TeO_2 polymorph has a fluorite-type average structure with a very high positional disorder, especially for oxygen. It is best described as an intermediate state between the amorphous and crystalline states [29].

1.3.2 Structure of tellurite glasses

According to the Zachariasen random network theory, the fundamental building block of pure TeO_2 glass should be similar to that of TeO_2 crystal which are TeO_4 / TeO_{3+1} units (see figure [1.3b] and [1.5b]). Moreover, the theory also suggests that in the 3D glassy network of pure TeO_2 these fundamental disphenoids should be dispersed randomly and connected continuously via oxygen atoms, therefore preventing any presence of terminal oxygen (Te=O chemical groups).

However, several studies addressed in the forthcoming subsections, present no clear consensus about the presence of terminal oxygen in pure TeO_2 glassy matrix. In addition, these studies show ambiguous values of Te coordination number in the pure TeO_2 glass. Further, in the later subsection, we will also discuss the structural reorganization that occurs as a result of the addition of modifying oxides to the network of TeO_2 glass. Additionally, we also emphasize on the role of bridging oxygen (BO: oxygen atom connected via at least two non-network modifier) and non-bridging oxygen (NBO: either terminal oxygen or oxygen atom connected to only on non-network modifier) in structural depolymerization of the TeO_2 glassy network.

1.3.2.1 Structure of pure TeO_2 glass

In the 2008 study by Pietrucci *et al.* [30], authors provide insights into the structure of TeO_2 glass by quenching a randomly placed 32 units of TeO_2 in a cubic simulation cell at fixed experimental density of 5.84 g.cm^{-3} using *ab-initio* molecular dynamics within the framework of density functional theory.

At high temperature of T = 2400 K, the study reports the broad first minima in Te-O pair correlation function centered around 3.3 Å. Te-O can hardly form a bond at such large distances, thus the authors used an empirical cut-off distance of R_{cut} = 2.36 Å for analyzing the structure. Several Q^n_m (n: number of bridging oxygen; m: number of bonding oxygen in TeO_x) units have been reported at this temperature with major contribution i.e., more than 12% from Q^4_4, Q^3_4, Q^3_3 and Q^2_3 units. Meanwhile, low coordination unit Q^2_4, Q^1_3, Q^2_2 and Q^1_2 are also present contributing to less than 10% of total Te units along with a negligible amount of isolated TeO_2 i.e. Q^0_2. It is also noteworthy to mention the presence of highly connected Q^5_5 and Q^4_5 units with a non-negligible fraction ($\approx$ 5%). The average value of Q^n_m units are shown in table [1.6].

Temperature	Q^1_3	Q^2_3	Q^3_3	Q^2_4	Q^3_4	Q^4_4	Q^4_5	Q^5_5
T = 2400 K	5.2	19.1	18.6	3.7	14.1	17.5	3.2	6.5
T = 1000 K	2.6	17.7	21.7	1.2	14.4	31.7	1.8	7.9
T = 300 K	0.6	14.9	20.4	-	17.1	35.9	-	9.4

Table 1.6: Distribution (%) of Q^n_m structural units at various temperature in TeO_2 [30] system.

Further, the quenching process has been followed by equilibrating the liquid at T = 1000 K. The comparison of position of partial correlation function first peaks at T = 2400 K and T = 1000 K liquid are reported in the table [1.7]. To obtain a glassy state, the system has been consequently quenched to T = 300 K. Table [1.6], shows the comparison and the evolution of the distribution of Q_m^n units at different temperatures. The Q_2^n units at T = 1000 K and T = 300 K have vanished in comparison to their populations at T = 2400 K, but fully linked units have grown at the expense of less connected ones. Further, table [1.6] reveals that at room temperature,

Temperature	Te-O (Å)	O-O (Å)	Te-Te (Å)
T = 2400 K	2.0	2.8	3.7
T = 1000 K	1.93	2.78	3.7

Table 1.7: Centers of partial correlation function first peaks at various liquid phase temperatures [30].

amorphous TeO_2 is dominated by Q_4^4 units, along with the presence of more than 50% of other Q_m^n units, indicating that the glassy network of TeO_2 is not merely a random network of Q_4^4 units like in crystals. Furthermore, the authors reported the presence of 14% of terminal oxygen with 1% of three coordinated oxygen. The average coordination number of oxygen and tellurium at various temperatures are reported in table [1.8].

Temperature	Te	O
T = 2400 K	3.42	1.95
T = 1000 K	3.67	1.89
T = 300 K	3.69	1.85

Table 1.8: Average coordination number of Te and O in TeO_2 system at various temperature obtained with R_{cut} = 2.36 Å [30].

Moreover, the coordination numbers of O atoms with Te atoms, as reported at different temperatures, show inconsistency with our expected linear relationship. We suspect that the inconsistencies in the reported values may be attributed to typographical errors or other sources of inaccuracies. Despite the fact that the study was instructive, the small simulation size under periodic boundary conditions might have a misleading influence on the overall provided TeO_2 glass results. Further, extremely high cooling rates result in the freezing of an abundance of structural units found in the melt phase, as a result the properties of glass resembles to those of its corresponding liquid.

Later Barney *et al.* provided an experimental study of pure TeO_2 glass based on neutron diffraction atomic PDF and Raman spectroscopy. The authors indicated the presence of two-thirds TeO_4 disphenoids and one-third TeO_3 trigonal pyramids with a terminal oxygen atom [17]. These findings are in contrast TeO_2's crystalline polymorphs, which are made entirely

of four-coordinated (TeO_4 and TeO_{3+1}) units. The terminal oxygen in the case TeO_3 units, suggests the presence of doubly bonded (Te=O) oxygen. Furthermore, the short-range structure of glass, and crystalline α-TeO_2 were found to be significantly different where the former having a coordination number n_{TeO} = 3.68 (n_{OTe} = 1.84) and later depicting n_{TeO} = 3.95 (n_{OTe} = 1.98) at R_{cut} = 2.36 Å. Additionally, the authors also reported the presence of 16% of terminal oxygen which is in accordance with the study of Pietrucci *et al.* [30].

At almost the same time at IRCER, Gulenko *et al.* [31] for the first time derived an interatomic potential for Te-O and O-O interaction in TeO_2 glass and performed classical molecular dynamics simulation on a model containing 672 TeO_2 units, thus overcoming the limitation of the small model sizes and the huge quenching rate in the work of Pietrucci *et al.*. Additionally, the authors of this study have utilized a core-shell model [32] in which massless shell is coupled to a core with mass equal to the atomic mass by an an-harmonic spring. This work suggests that pure TeO_2 glass is made up of different TeO_x structural units (x = 3, 4, 5). This work also led to the conclusion that the structure of pure TeO_2 glass is similar to that of a γ-TeO_2 polymorph. Additionally, the study suggests that the Te coordination number in the modelled glass was 3.63, which is well in line with the study of Pietrucci *et al.* [30] and Barney *et al.* [17]. Further, this works also reported the presence of 21% of NBO in the glass structure. In addition, the investigation of rings statistics performed by the authors revealed that TeO_2 glass contains large rings (n > 10), terminated chains, and poor connectivity (see figure [1.6]). The large number of NBO atoms and the stereochemical impact of the Te electronic lone pair are to account for depolymerized network. Additionally, the authors propose that the existence of NBO atoms and large rings are the reason behind the instability of pure TeO_2 glass.

In the subsequent work by Garaga *et al.* [33], the authors have studied the possibility of having lower Te coordination number than 4 in TeO_2 glass using combined solid state-NMR, Raman spectroscopy, X-ray diffraction (to confirm amorphicity) and first-principles techniques. In this work, the authors declined any presence of terminal oxygen in pure TeO_2 glass. Structural explanation is supported based on the Gupta-Cooper constraint model [34], [35]. In this scheme, based on the average number of polyhedral vertices V and their connectivity C, the degrees of freedom f of a network of polyhedra is calculated as:

$$f = d - C\left[\delta - \frac{1}{2V}\delta(\delta+1)\right], \tag{1.2}$$

where, δ and d are parameters equal to 3 in the case of three-dimensional polyhedra. For instance, pure TeO_2 glass, entirely composed of TeO_4 unit has V = 5 and C = 9/5. Thus, f comes out to be -6/25, implying that the glass is over-constrained and difficult to form. However, if there is only a terminal oxygen i.e., TeO_3 unit in glassy network, then V = 4 and C = 3/2. The value of f for this structural unit comes out to be f = +3/4. Furthermore, in a mixture of 75% of TeO_4 units

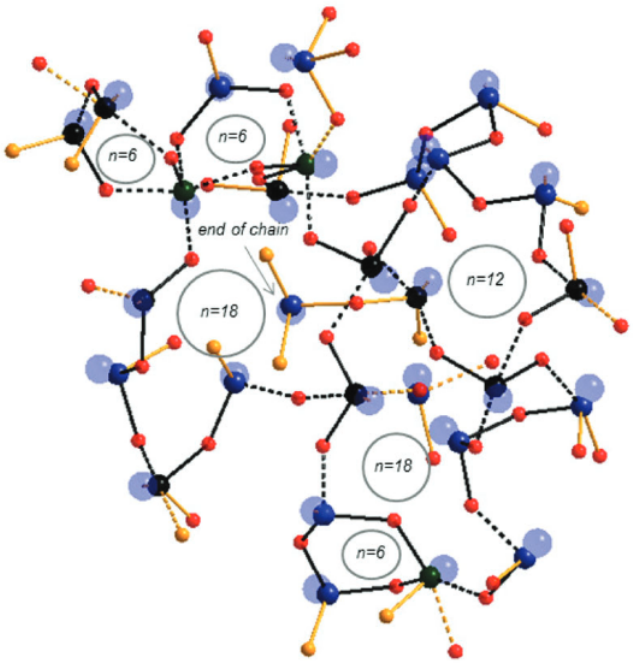

Figure 1.6: A fragment of the TeO_2 glass model as obtained with MD simulation and illustrating typical chains and rings present in the structure. Oxygen atoms are represented as small sphere (red for BO and yellow for NBO), tellurium atoms are the medium seized spheres (black for four-coordinated, indigo for three-coordinated and dark green for five-coordinated Te) and Te lone pairs are the big transparent blue spheres. The solid lines represent the short Te-O bonds (< 2.02 Å) and dashed lines represent intermediate and long bonds (2.02 Å < d < 2.36 Å). The black bonds emphasis the rings in the structure and n is the circles indicates the amount of nodes in each found ring. Picture source [31].

and 25% of TeO_3 units in pure TeO_2 glass, the effective f comes out to be zero leading to Te coordination number of 3.75, which is a bit higher than the previously reported values.

Any Te coordination number less than 4 implies the existence of terminal oxygen or TeO_3 units, according to the aforementioned arguments. Furthermore, any contribution of TeO_3 units to the glassy TeO_2 network would cause $f > 0$ [36], removing the issue of over-coordination and making TeO_2 a good glass former, in contrast to the experimental findings. Thus, this study [33] concludes that no terminal oxygens are present in the glassy network. Moreover, the authors describe the lower Te coordination by assuming the presence of TeO_{3+1} units instead of TeO_3 units in TeO_2 glass. TeO_{3+1} unit has 3 relatively short bonds ($\approx$ 1.85-2.1 Å) and 1 long bond ($\approx$ 2.2-2.4 Å). Any presence of terminal oxygen would have resulted in a related trend in ^{17}O NMR spectrum of TeO_2 glass, but no such trend was seen in their analysis. In addition, such presence would have made the TeO_2 glass too easy to form in reality.

Later, Marple *et al.* [37] in their communication described the complexity of the Te-O coordination environment in TeO_2 glass based on 2D ^{125}Te isotropic-anisotropic chemical shift correlation

NMR spectroscopy. NMR data indicates that 89% of TeO_4 disphenoids units are present. Furthermore, their findings revealed the presence of TeO_3 or TeO_{3+1} environment units in TeO_2 glass. Additionally, the authors claim that a tiny percentage (11%) of TeO_3 (TeO_{3+1}/ $Te(=O)_{2/2}$ terminal oxygen) units containing $\approx$ 5-6 % terminal type oxygen may have gone undetected in a prior investigation by Garaga using ^{17}O NMR. The Te coordination number reported is approximately 3.9, which is somewhat higher than Garaga's proposition based on equation [1.2].

Recently Alderman *et al.* [38] studied both the melt and the glass phases of TeO_2 using high-energy X-ray diffraction and by analyzing PDFs. Since, X-ray diffraction methods are less sensitive to O-O pairs than Te-O and Te-Te pairs as compared to neutron diffraction applied previously by Barney *et al.* [17] and Niida *et al.* [39], it helps to clearly emphasize the contributions of short and long Te-O bond pairs, as well as large Te-Te pairs. In this work, the

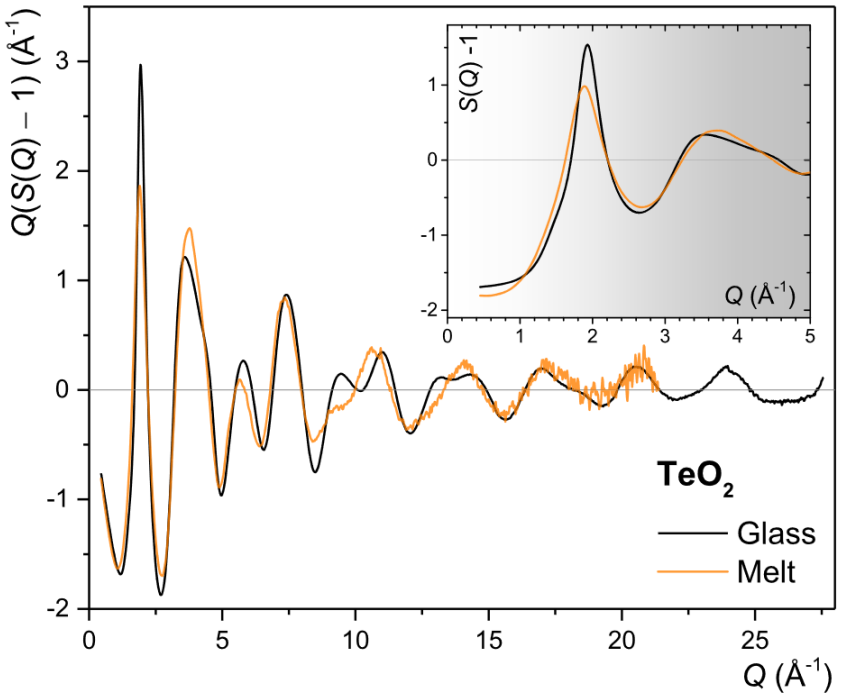

Figure 1.7: X-ray interference function $Q(S(Q)-1)$, for melt and glass TeO_2. Inset shows the structure factor $S(Q)-1$ for $Q \leq 5$ Å^{-1}, highlighting the shift in first diffraction peak in melt. Picture source [38].

authors assert that the density of TeO_2 glass is higher than that of the melt as anticipated from the shift of the first diffraction peak in the S(Q) to lower Q in the melt versus the glass (see inset of figure [1.7]). This shift towards lower Q implies larger real-space periodicity for Te-Te pair distribution. In addition, increased nearest-neighbor Te-Te distance in total pair distribution function T(r), indicates that the melt is less dense than its glassy counterpart (see figure [1.8]).

Despite, the lower density of the melt, the first peak position in the Te-O PDF corresponding to

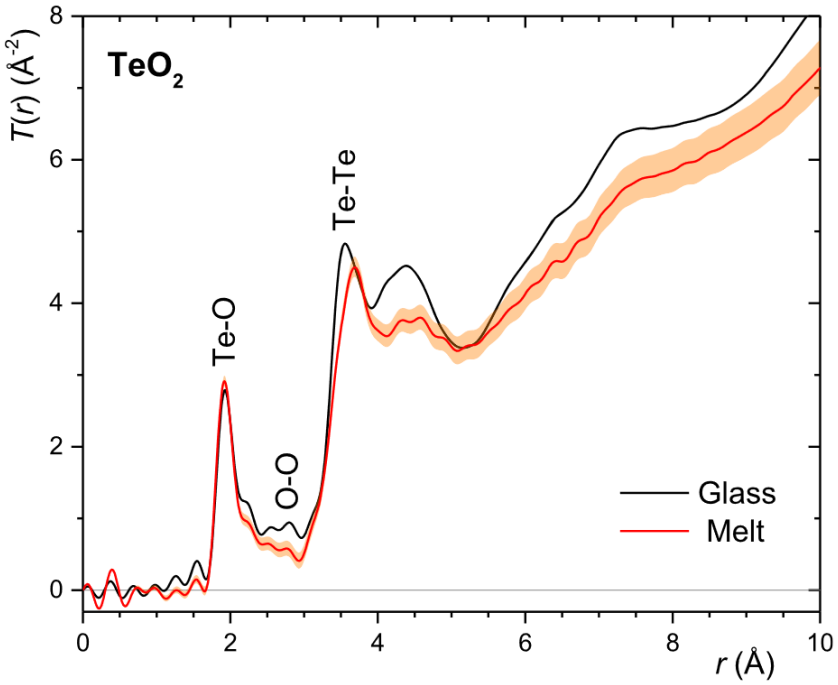

Figure 1.8: X-ray total distribution function computed by the sine Fourier transform of the interference function of figure [1.7], with $Q_{max} = 21.39$ Å^{-1} [38].

Te-O distance at 1.919(2) Å as found in the melt is shorter than that found in the glass 1.926(1) Å. This trend is the inverse of what would be predicted from isotropic thermal expansion in a fixed coordination environment which can be explained on the basis of asymmetry in the O-Te-O bridge. In fact, due to thermal fluctuations at higher temperature, the longer Te-O bonds suffer from greater anharmonicity which further leads to a contraction of shorter bonds to compensate. At some point, if the long bonds get even longer and weak enough, they will no longer be classified as a bonded interaction, and the overall consequence will be a decrease in the coordination number. Figure [1.9], shows Te coordination number as a function of Te-O distance. It can be seen that the Te coordination for the melt rises steeply compared to the glass before the cross-over around 2.2 Å. Te coordination number in the case of glass outnumbers the melt only after a sufficiently long Te-O distance, showing that longer Te-O bonds are more essential in characterizing the Te^{4+} environment in glassy than in melt TeO_2, where shorter bonds are more dominant. Apparently, there is no sign of a plateau in the Te coordination number evolution (see figure [1.9]), and hence no clear distinction between bonded and non-bonded coordination shells can be drawn. However, authors obtained a Te coordination of 4.22 in the glass and 4.09 in the melt based on a priorly established cut-off radius of 2.36 Å employed in earlier studies. Finally, the authors suggest that the occurrence of terminal oxygen (Te=O groups) is attributable to the substantial asymmetry in the Te-O-Te bridge, where an O atom can be considered detached from the distant Te atom in the Te-O-Te bridge.

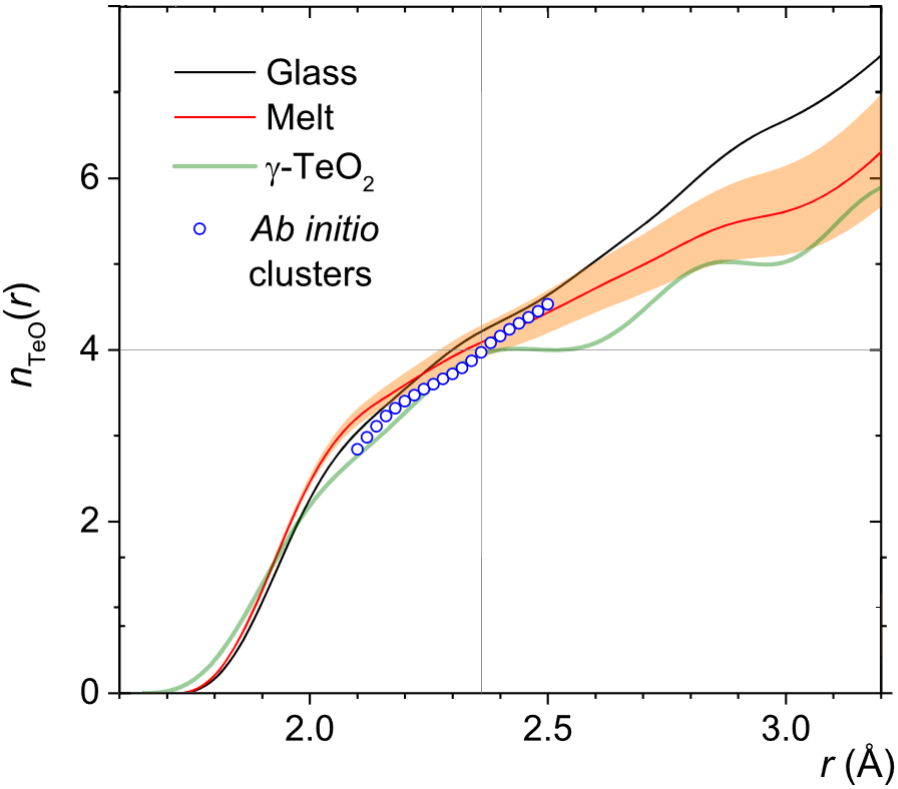

Figure 1.9: Running Te coordination number as a function of distance. Picture source [38]

1.3.2.2 Structure of modified tellurite glasses

Despite the technological importance of TeO_2 glass in non-linear optical systems, this glass does not form easily and has a poor metastability against devitrification. As a result, adding a modifier is required to increase the thermal stability and the mechanical resistance of TeO_2 glass.

Generally, modified glass forming oxides are made up of network modifiers and network formers with varying field strengths. Because the network former has a higher field strength than the network modifiers (see table [1.2]), it dominates the glassy structure and produces a more stable amorphous solid, which is unlikely to crystallize easily because its structure is governed by short range interactions to a greater extent, and crystallization would require significant breaking and forming of network connections. The network modifiers, in turn, weaken the structure by replacing the tightly coordinated network formers. In order for the network formers to preserve their polyhedral environments, modifiers (M) are always introduced in addition to the oxide (O) denoted as modifier oxide (MO_x). Generally, adding modifiers leads to lowering of the glass transition temperature. The building block in tellurite materials have two structural peculiarities, such as:

1. the local environment of Te^{4+} cation is asymmetric due to the steric effect of its lone electron pair,
2. the structural units may strongly vary according to the quantity and the kind of the added modifier oxide M_xO_y.

These peculiarities make the description of TeO_2 glass much more complex in comparison with other common glasses, such as silica. For example, consider the crystal structure of alkali-tellurites. The broad variety of tellurium structural environments seen in these crystals is thought to have a key role in alkali tellurite glass stabilization [40]. In practice, when alkali oxide modifiers (M) are introduced, different structural modifications occur due to the different electronegativity difference of Te-O and M-O bonds. For instance, α-TeO_2 is made up of $TeO_{4/2}$ disphenoids (all the oxygens in TeO_4 are connected with two tellurium atoms), whereas M_2TeO_3 (M = Li, Na, K, Cs) consists of $TeO_{3/0}$ trigonal pyramids (thus quasi-isolated TeO_3 units expressing $[TeO_3]^{2-}$ anions coordinated by alkali cations [41]). Figure [1.10] illustrates the different structural units present in modified tellurite glasses.

When ions such as alkali and/or alkali-earth ions are introduced into the glass, they depolymerize the network and create mainly ionic character bonds with oxygen. Non-bridging oxygen NBO is defined as oxygen that is mainly covalently bonded to one network former atom and is either terminal or ionically linked to another network modifier atom. As a result, breakage of the covalent bond (structural depolymerization) leads to mobile ionic species in the material and tellurite structural units form TeO_3/TeO_{3+1} units (see figure [1.11]). The characteristics of oxide glasses are determined by these modifying agents and their compositions. The existence of many distinct Q_m^n units, whose conversion into the Q_4^4 unit of TeO_2 crystals would require a significant reconfiguration of the network, has been suggested as a reason for the network modifier's meta-stability effect against recrystallization [40].

Since, the amount of Te-O-Te bridges is decreased due to the addition of modifier, these NBO reduce the ability to construct 3D covalent networks to a greater extent. Due to the enhanced mobility of NBO, this also results in a larger ability to relax the local network, resulting in a higher ratio of TeO_3 to TeO_4 arrangements. Various connection and structure around the tellurium atoms such as TeO_3 to TeO_4 polyhedral units and its concentration plays an important role in the stability of glass. The primary effect of glass relaxation is the coordinated movement of ions across large distances, as well as the breakdown and creation of covalent bonds (locally). Because of their weak and non-directional ionic connections, network modifiers are free to move in between NBO in the tellurite glass structure [27]. Moreover, the structural modification and properties of a glass depend on:

- the type of modifier ions used,

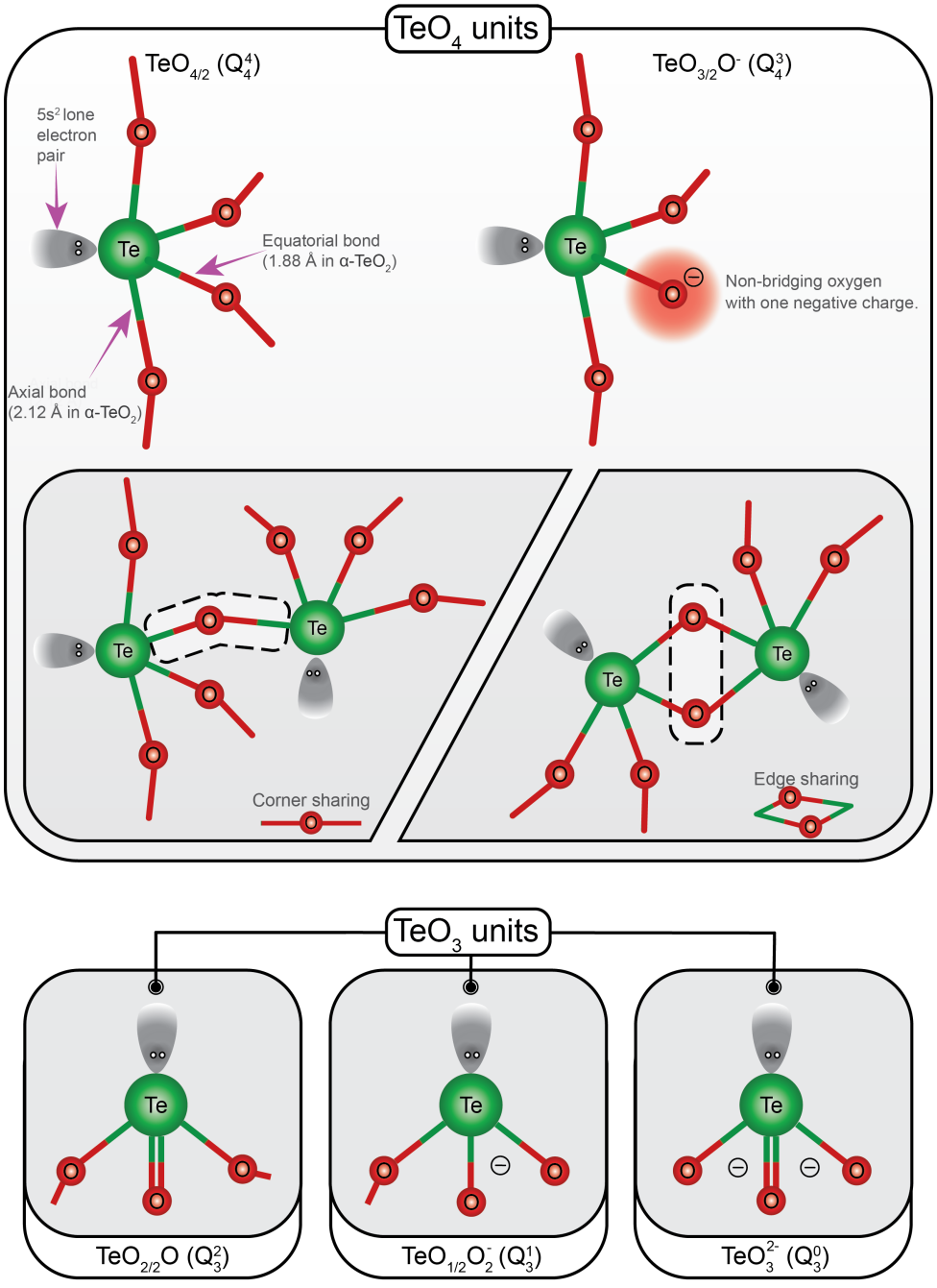

Figure 1.10: Basic structural units found in tellurite crystals. The units are labelled in both conventional and Q_m^n notations. In the latter, m is the coordination number of the central Te atom (number of nearest neighbor oxygen atoms) and n represents the number of bridging oxygen and hence, $n \leq m$.

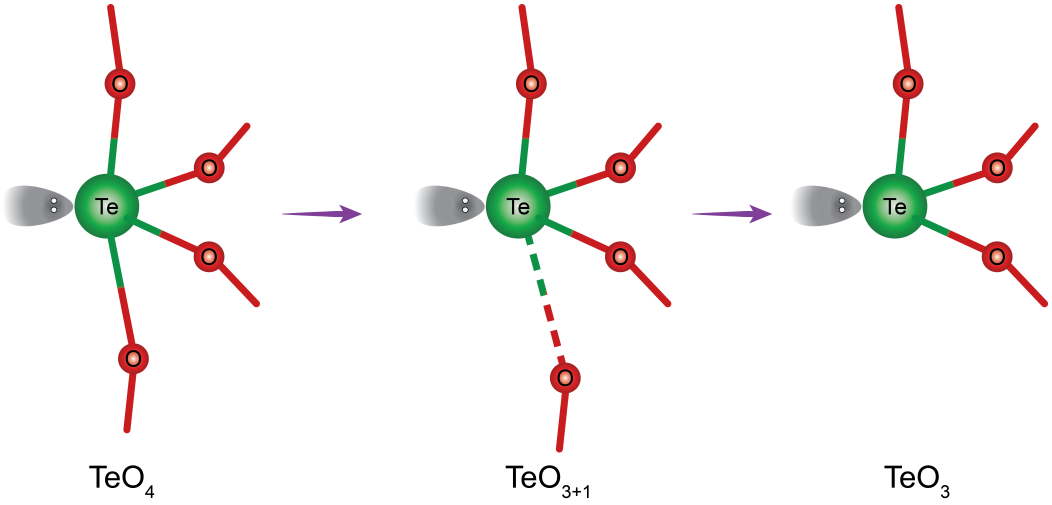

Figure 1.11: Depolymerization of TeO_4 unit into TeO_3 unit via TeO_{3+1} (1 long and 3 short bonds).

- the concentration of modifier ions, and
- the thermal history (cooling rate) of the glass sample.

Thus, a high concentration of modifier ions generally leads to a high fraction of NBO and to a low value of glass transition temperature T_g. A schematic variation of the fraction of bridging-oxygen (BO) and NBO with the mole fraction of the modifier content is shown in figure [1.12].

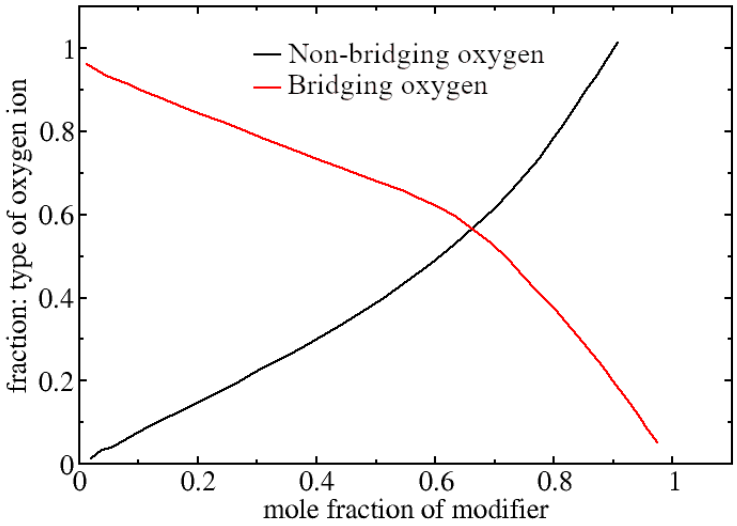

Figure 1.12: Variation of fraction of BO/NBO with the mole fraction of the modifier content. Picture source [42]

1.3.3 Properties of tellurite glasses

1.3.3.1 Optical properties

Kim *et al.* [18] measured the linear and nonlinear optical properties of pure TeO_2 glass for the first time. The characteristics of pure TeO_2 glass are compared to those of conventional silicate glasses in this study. TeO_2 glass has a higher linear refractive index than SiO_2 glass, and third-order non-linear susceptibility ($\chi^{(3)}$) calculated using the third-harmonic generation method for TeO_2 glass was found to be 50 times greater than SiO_2 glass. Table [1.9], summarizes the obtained optical properties on pure TeO_2 and SiO_2 glasses.

Glass	Linear Refractive index (at 1.9 μm)	$\chi^{(3)}$ (10^{-13} esu)	Optical energy band gap (eV)
SiO_2	1.439	0.28	9.0
TeO_2	2.121	14.10	3.37

Table 1.9: Optical properties of SiO_2 and TeO_2 glasses [18].

Further insights from Kim *et al.* work

In the Kim *et al.* study [18], $\chi^{(3)}$ of pure TeO_2 glass was obtained using a reference value of $\chi^{(3)}$ of pure SiO_2 = 0.28 $\times$ 10^{-13} esu ($\sim$ 3.916 $\times$ 10^{-22} m^2/V^2), which was taken from the work of Buchalter *et al.* [43] study published in 1982. From the Buchalter study, Kim *et al.* deduced the value of $\chi^{(3)}$ of pure TeO_2 to be 14.1 $\times$ 10^{-13} esu ($\sim$ 197.2 $\times$ 10^{-22} m^2/V^2). Later, the review study of Milam *et al.* [44] published in 1998, however, is presently regarded as the reference work for providing the updated non-linear optical values of pure SiO_2. From Milam *et al.* study, $\chi^{(3)}$ of pure SiO_2 can be calculated to be $\sim$ 2.095 $\times$ 10^{-22} m^2/V^2 which is almost the half of $\chi^{(3)}$ of pure SiO_2 used in Kim's work. Nevertheless, from Kim *et al.* work, if we still consider the $\chi^{(3)}$ of pure TeO_2 glass to be 50 times the $\chi^{(3)}$ of pure SiO_2 glass, then $\chi^{(3)}$ of pure TeO_2 with Milam's correction for SiO_2 comes out to be $\sim$ 105.498 $\times$ 10^{-22} m^2/V^2.

Afterwards the research of Noguera *et al.* [45] aimed at finding the origins of the non-linear optical properties in TeO_2 based materials from the perspective of electron pairs attributed to each chemical bond using *ab-initio* molecular orbital approach. Based on the arguments presented in the previous section, authors have used the $(TeO_2)_p$ polymer molecules to model fragment of the local structure present in TeO_2 glass. The chemical formula for the fragments used in this study are $Te(OH)_4$, TeO_2, $(OH)_3$Te-O-Te$(OH)_3$ and $(TeO_2)_3$

Table [1.10] reports the reduced polarizabilities, isotropic bond polarizabilities and the cluster

polarizabilities. Moreover, the presented values of polarizabilities in the case of O lp, O* lp and O-H bp are the mean value of all of their individual values. The sum of bond polarizabilities in the cluster is denoted by $\alpha_{cluster}$. Furthermore, α_{red} is the bond additive reduced polarizability, which is the sum of total bond polarizabilities of a fragment (Te environment) that contribute to the material's net polarizability. It is defined as:

$$\alpha_{red} = \alpha(\text{Te-O bp}) * 4 + \alpha(\text{Te lp}) * 1 + \alpha(\text{O lp}) * 4. \tag{1.3}$$

It has been noted that the reduced value in the case of isolated TeO_2 molecule is smaller in comparison to the bigger polymerization number. Based on the polymerization number, electron pairs do not display a consistent evolution of polarizabilities. This showed that the linear polarizability of an electron pair in a localized molecular orbital is unaffected by the arrangement of other electron pairs or ionic cores, and that these bond polarizabilities are transferable.

	$Te(OH)_4$	TeO_2	$(OH)_3$Te-O-Te$(OH)_3$	$(TeO_2)_3$
Te-O bp	4.13	-	4.54	5.41
Te=O* bp	-	5.82	-	6.34
Te lp	11.69	9.65	12.75	12.64
O lp	3.13	-	3.24	2.65
O* lp	-	2.30	-	3.32
O-H bp	1.64	-	1.71	-
$\alpha_{cluster}$	74.24	42.13	115.6	134.66
α_{red}	40.68	42.13	43.87	45.92

Table 1.10: Isotropic bond and reduced polarizabilities (a.u.). O* represents double-bonded oxygen [45].

Similarly, table [1.11], shows the reduced second hyperpolarizabilities for the studied clusters. The isolated TeO_2 molecule has lower second hyperpolarizabilities than the other clusters, indicating that the origin of high hyperpolarizabilities in TeO_2 based materials can be linked to structural units polymerization. Thus, based on this study, the origin of the high nonlinear optical properties in TeO_2 based materials was attributed to electronic lone pair present on tellurium ion along with the polymerization of the structural units.

As discussed earlier, pure TeO_2 does not easily form glass and requires the addition of a modifier oxide. However, it was established that introducing a modifier to the glassy network of TeO_2 reduces its high non-linear index. Yet, investigations demonstrate that using thallium as a modifier oxide preserves the large amplitude of the non-linear index in TeO_2 glassy material (see figure [1.13]). It is important to highlight that even though the absolute values of $\chi^{(3)}$ in figure [1.13] are less than half the values of pure TeO_2 (see further remarks on Kim *et al.*), it is not reasonable to compare these values as the experimental setups utilized for obtaining $\chi^{(3)}$ in the different studies could have led to strong variation in the reported values.

	$Te(OH)_4$	TeO_2	$(OH)_3Te\text{-}O\text{-}Te(OH)_3$	$(TeO_2)_3$
Te-O bp	1113	-	1104	1346
Te=O* bp	-	705	-	1507
Te lp	3746	1770	5147	4021
O lp	681	-	1001	515
O* lp	-	1000	-	1977
O-H bp	-3	-	-32	-
$\alpha_{cluster}$	13362	6951	31015	40720
α_{red}	10920	6951	13567	14197

Table 1.11: Isotropic bond and reduced second hyper-polarizabilities (a.u.). O* represents double-bonded oxygen [45].

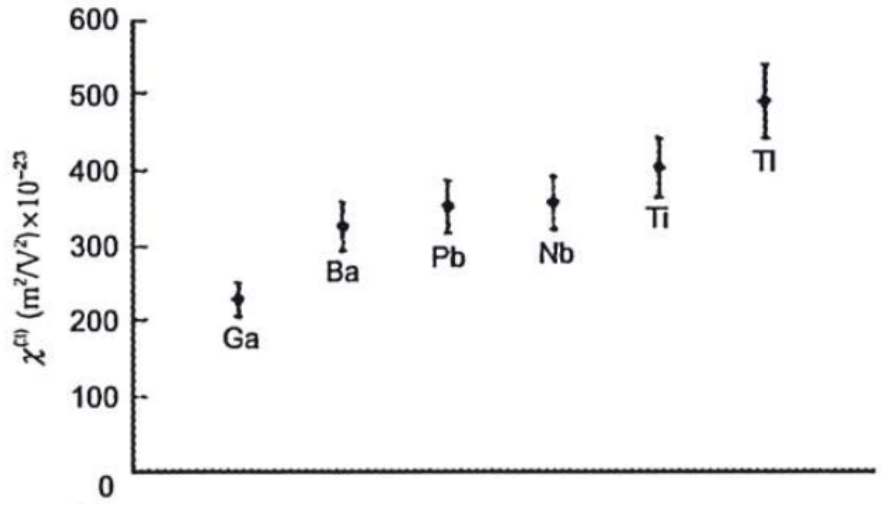

Figure 1.13: Third order nonlinear indexes $\chi^{(3)}$ ($m^2/V^2 \times 10^{-23}$) evolution at 0.8 μm with respect of nature of modifying oxide introduced to a $15(MO_x) - 85(TeO_2)$ (mol%) (M:x = Ga:1.5, Ba:1, Pb:1, Nb:2.5, Ti:2, Tl:0.5) glass compositions. Picture source [46].

Despite the high $\chi^{(3)}$ of $(TlO_{0.5})_x - (TeO_2)_{1-x}$ binary glass, it was observed that both the mechanical and thermal properties of binary glass are even inferior to those of pure TeO_2 glass due to the presence of long Tl-O bonds [9]. Therefore, introducing $TlO_{0.5}$ modifier serves no purpose in our prerequisite of improving the stability of TeO_2 glass. To resolve this issue, the authors of Ref. [9] added titanium oxide (TiO_2) in addition to thallium oxide (Tl_2O) to increase the thermal stability while maintaining high non-linear optical properties. The former improves the mechanical and thermal stability while the latter retains the high non-linear optical properties, see table [1.12]. Furthermore, adding just TiO_2 to the glassy TeO_2 results in good stability but poor optical characteristics since no solitary TeO_3 ions are produced and the glassy structure stays fully polymerized. This observation appears to be in contrast with the previous work by Noguera

et al. [45] which suggests that high value of $\chi^{(3)}$ is due to the polymerization of the network.

Glass composition (mol%)	Refractive Index n	Re $\chi^{(3)}$(x 10^{-13}/esu) [Re $\chi^{(3)} \times 10^{-22}$/ ($m^2/V^2$)]	
$10GaO_{1.5}$-$30TlO_{0.5}$-$60TeO_2$	1.95	26.3	[367.83]
10ZnO-$30TlO_{0.5}$-$60TeO_2$	1.95	24.8	[346.85]
5PbO-$28.5TlO_{0.5}$-$66.5TeO_2$	1.99	45.8	[640.56]
$5TiO_2$-$30TlO_{0.5}$-$65TeO_2$	2.12	52.5	[734.26]
$5BiO_{1.5}$-$38TlO_{0.5}$-$57TeO_2$	1.97	44.4	[620.98]

Table 1.12: Linear and non-linear properties of various modified tellurite glasses [9].

In another work, Jeansannetas *et al.* [47] examined the correlation between thallium tellurite glasses structure and their nonlinear optical characteristics. In general, modifier ions alter the structural unit of TeO_2 glasses by converting the TeO_4 unit into the TeO_3 unit via an intermediary TeO_{3+1} unit. TeO_2 glass's non-linear properties are decreased as a result of this modification. However, the amplitude of non-linear optical properties of tellurite glasses are maintained, according to the authors, if heavy modifier cations (Te^{4+}, Bi^{3+}, Pb^{2+}, Tl^{+}) with ns^2 lone pair, such as Tl^{+}, are present.

Next study focuses on investigating the effects of modifier's lone pair on the optical properties of tellurite glasses. Linear and nonlinear indices of various studied oxides have been reported in table [1.13]. It is noteworthy that from the values reported in table [1.13], the addition of thallium cations in tellurite glasses contribute to the increased linear and non-linear optical indexes.

1.3.3.2 Vibrational properties

In the work of Uchino *et al.* [48], the Raman scattering intensities and vibration frequencies of TeO_2 glass were calculated at the Hartree-Fock level of theory by investigating small clusters resembling to the atomic local structures of TeO_2 glass. The vibrational excitations in amorphous systems are spatially localized rather than indefinitely extended as in perfect crystals, distinguishing them from their crystalline counterparts. As a result, due to this difference, vibrations in glasses may be investigated entirely in terms of structural unit dynamics, regardless of the surrounding units. Thus, in the analysis of vibrational modes of TeO_2 glass, the authors adopted a molecular model where the nearby structural units are vibrationally decoupled and carried out *ab-initio* calculations on several tellurium oxy-hydroxide molecules.

In order to understand the effect of coupling between TeO_4 disphenoid present in the TeO_2 glass, the authors have studied three clusters:

Glasses (mol%)	n_0	n_2 (m^2/W) x 10^{-19}	$\chi^{(3)}$(V^2/m^2) x 10^{-22}
Herasil	1.467 ± 0.01	0.121 ± 0.09	0.46
Suprasil	1.422 ± 0.03	0.25 ± 0.2	0.89
86.5 $Ca(PO_3)_2$-13.5 Nb_2O_5	1.608 ± 0.05	0.18 ± 0.083	0.80
95$NaPO_3$-5$Na_2B_4O_7$-30 TiO_2	1.615 ± 0.03	1.33 ± 0.26	6.1
95$NaPO_3$-5$Na_2B_4O_7$-30 Nb_2O_2	1.772 ± 0.03	2.06 ± 0.25	14.1
SF59	1.880 ± 0.02	4.50 ± 0.50	28.2
SF6	1.788 ± 0.01	2.15 ± 0.23	12.0
90 TeO_2-10 Al_2O_3	2.003 ± 0.06	5.38 ± 1.19	38.1
90 TeO_2-10 Nb_2O_5	2.144 ± 0.03	6.93 ± 0.72	56.3
85 TeO_2-15 Nb_2O_5	2.145 ± 0.05	6.41 ± 0.93	52.1
80 TeO_2-20 Nb_2O_5	2.155 ± 0.05	5.94 ± 0.81	49.3
82 TeO_2-18 Tl_2O (0.69TeO_2-0.31$TlO_{0.5}$)	2.125 ± 0.02	8.60 ± 1.0	68.7
79 TeO_2-21 Tl_2O (0.65TeO_2-0.35$TlO_{0.5}$)	2.094 ± 0.02	8.90 ± 1.0	69.0
85 TeO_2-13.5 Tl_2O-1.5 Bi_2O_3	2.156 ± 0.07	9.10 ± 1.7	74.8

Table 1.13: Linear and Non-linear properties of various glasses at 1.5 μm [47].

1. $Te(OH)_4$ cluster resembling the isolated TeO_4 units.
2. $(OH)_3$Te-O-Te$(OH)_3$ cluster, to analyze the coupled interaction of Te-O-Te bond between two TeO_4 units.
3. (OH)OTe-O-Te$(OH)_3$ cluster, to investigate the interaction between TeO_4 tbp and TeO_3 trigonal pyramid units.

In this work, the authors reported the calculated vibrational frequencies to be 10-15% higher than experimental values. In the Raman spectrum of pure TeO_2 glass, multiple vibrational bands in the 400 to 800 cm^{-1} range have been seen. Further, these bands can be categorized into three distinct regions, as:

1. 400 cm^{-1} to 500 cm^{-1} region with broad band around 450 cm^{-1}
2. 600 cm^{-1} to 680 cm^{-1} region with strong band around 670 cm^{-1}
3. 720 cm^{-1} to 780 cm^{-1} region with shoulder around 780 cm^{-1}.

Frequencies corresponding to $Te(OH)_4$ molecule fall in the frequency range from $\approx$600 cm^{-1} to $\approx$690 cm^{-1} (see table [1.14]). These bands can be interpreted as corresponding to the experimentally observed band around $\approx$640 cm^{-1} of pure TeO_2 glass. The modes corresponding to the resultant frequencies are generally due to stretching vibrations of Te-O bonds within TeO_4 tbp. As a result, the obtained frequencies in this region show that neighboring TeO_4 are not strongly coupled with each other, hence the vibrational mode is localized in the TeO_4 trigonal bipyramid unit itself.

	Mode No.			
	1	2	3	4
Frequencies (cm^{-1})	596.3	640.1	688.8	689.3
Reduced masses (a.u.)	11.4	15.2	12.5	14.0
Force constants (mdyn/Å)	3.02	4.64	4.40	4.95
Raman scattering intensities ($Å^4$/amu)	7.76	2.10	20.46	6.69

Table 1.14: Vibrational frequencies, reduced masses, force constant and Raman scattering intensities for $Te(OH)_4$ [48].

Table [1.15], reports the calculated frequencies for $(OH)_3$Te-O-Te$(OH)_3$ cluster. In comparison to the $Te(OH)_4$ cluster, it has been found that the $(OH)_3$Te-O-Te$(OH)_3$ cluster has additional frequencies starting from 485.5 cm^{-1} and spanning till 800.5 cm^{-1}, despite having almost the same vibrational modes. The frequencies at 485.5 cm^{-1} and at 800.5 cm^{-1} can be associated to the bands observed experimentally in the region around 450 cm^{-1} and 780 cm^{-1}, respectively. Further, it has been anticipated that these two vibrational modes are due to bending of bridging oxygen (485.5 cm^{-1}) and stretching of Te-O bond (800.5 cm^{-1}). Computed (OH)OTe-O-Te$(OH)_3$

	Mode No.							
	1	2	3	4	5	6	7	8
Frequencies (cm^{-1})	485.5	558.5	618.2	628.1	655.1	684.7	701.6	800.5
Reduces masses (a.u.)	5.50	4.21	11.9	12.3	6.90	6.65	5.00	4.10
Force constants (mdyn/Å)	0.96	0.98	3.39	3.60	2.20	2.32	1.83	1.95
Raman scattering intensities ($Å^4$/amu)	5.59	7.03	6.02	3.28	8.34	14.56	20.18	7.18

Table 1.15: Vibrational frequencies, reduced masses, force constant and Raman scattering intensities for $(OH)_3$Te-O-Te$(OH)_3$ [48].

cluster frequencies are reported in table [1.16]. In higher frequencies (> 700 cm^{-1}) range, two frequencies at ≈780 cm^{-1} and ≈ 868 cm^{-1} have been computed. The former frequency can be attributed to the vibration of TeO_3 trigonal pyramid units, while the latter is due to stretching of doubly bonded oxygen in TeO_3 units. Since, the band around 868 cm^{-1} has not been observed in pure TeO_2 glass, authors claimed that TeO_3 units are absent in the glass.

Back to the study [30] of Pietrucci *et al.*, the authors computed the Raman spectra of pure TeO_2 glass on a small model of 32 TeO_2 units and compared it with experiments (see figure [1.14]). For TeO_2 glass, two peaks were reported experimentally, centered at 450 and 590 cm^{-1}, whereas the corresponding calculated Raman peaks were found to be 10% redshifted at 420 and 590 cm^{-1} respectively. Therefore, multiplying the frequencies by a factor of 1.1 offers

	Mode No.					
	1	2	3	4	5	6
Frequencies (cm^{-1})	512.1	641.3	666.2	696.1	776.1	867.7
Reduced masses (a.u.)	6.34	12.73	13.0	14.2	5.27	6.57
Force constants (mdyn/Å)	1.23	3.90	4.28	5.12	2.36	3.68
Raman scattering intensities ($Å^4$/amu)	1.20	3.62	12.26	11.54	4.49	13.23

Table 1.16: Vibrational frequencies, reduced masses, force constant and Raman scattering intensities for $(OH)OTe\text{-}O\text{-}Te(OH)_3$ [48].

a reasonable peak location estimates in comparison to experimental data. The inaccuracies in the description of bonding by DFT-GGA in crystalline TeO_2 can explain the origin of the redshift in frequencies [49].

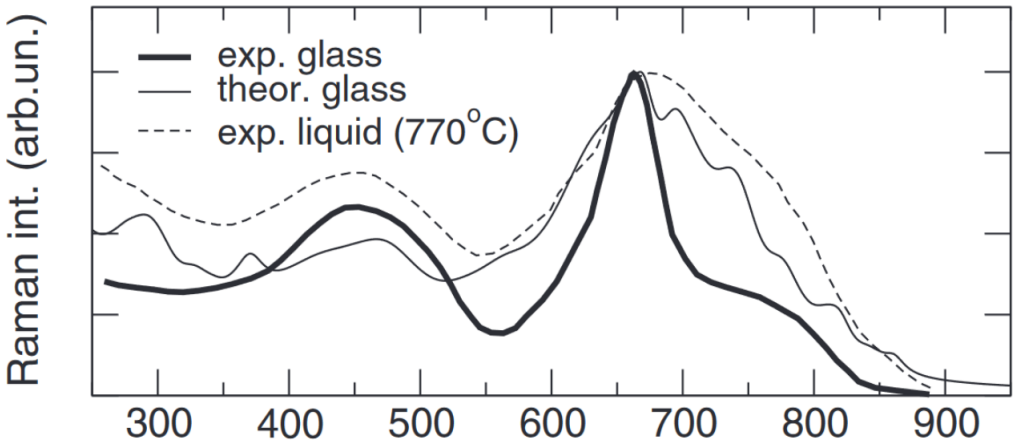

Figure 1.14: Raman spectra comparison of experimental and theoretical (scaled by a factor of 1.1) TeO_2 glass. Picture source [30].

Further, the authors assert that the calculated Raman peak at 420 cm^{-1} is due to Te-O-Te bending and that the peak at 590 cm^{-1} is due to Te-O-Te bridges stretching. Furthermore, the calculated Raman spectrum captures the wide experimental peak in the range of 720-820 cm^{-1}, but the former is considerably more pronounced. The simulated Raman spectra in this region appear to be more consistent with TeO_2 liquid experimental data [30]. In addition, the presence of non-bridging oxygen in the system is responsible for the high frequency range because non-bridging oxygen have a stronger and shorter bond. Nevertheless, the vibration spectra obtained in this work demonstrate that bridging oxygen dominates non-bridging oxygen at higher frequencies, which contrasts with the non-bridging oxygen peaks in the 720-820 cm^{-1} range. To explain this issue, the author hypothesizes that numerous Q_4^3 and Q_3^2 molecules in the liquid phase may have become frozen due to the extremely rapid cooling rate used to produce the glass.

The experimental studies [50], [47] of Raman spectra provides a deeper insight of evolution of structural changes in binary $(TlO_{0.5})_x - (TeO_2)_{1-x}$ glasses with various intermediate steps of increasing $TlO_{0.5}$ content from x = 0 to x = 0.5 as presented in figure [1.15]. The authors suggest that in TeO_2 glass, introducing Tl_2O modifier induces:

1. an intensity increase of the band at 720 cm^{-1} (associated with Te-NBO symmetric vibrations in TeO_3 units)
2. an intensity decrease of the band at 660 cm^{-1} (associated with Te-BO vibrations in TeO_4 units)
3. a disappearance of the band centered at 450 cm^{-1} (associated with bending vibrations of Te-O-Te bridges)
4. an increase of the intensity of the weak peak around 280 cm^{-1} (associated with Tl-O vibrations [47]).

This work supports the idea of structural depolymerization of the network in TeO_2 glass by transformation of TeO_4 units into solitary TeO_3 units and a decrease in the number of Te-O-Te linkages due to the addition of the modifier oxide as shown in figure [1.11].

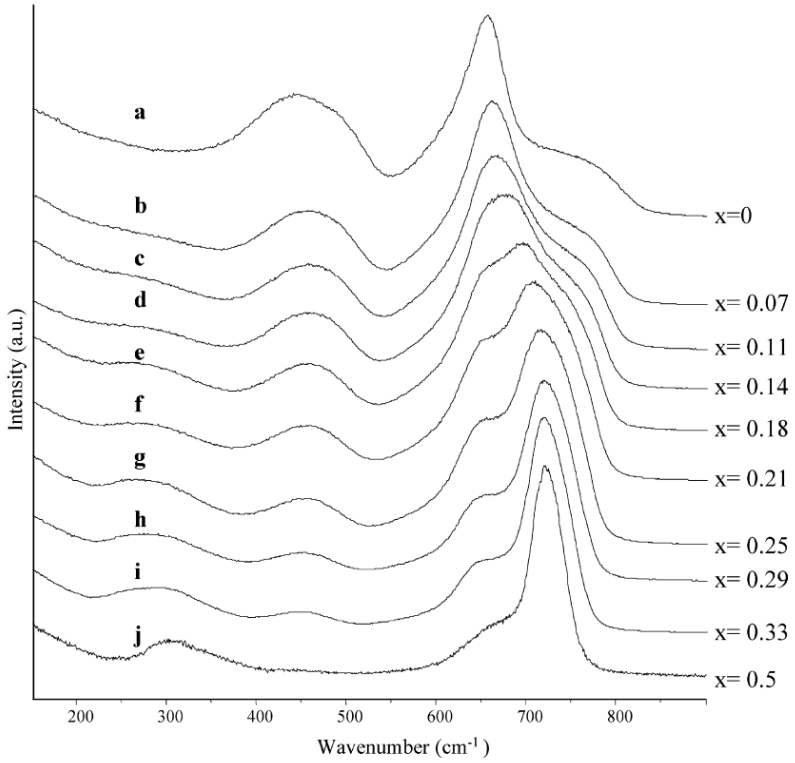

Figure 1.15: Composition dependence of the Raman spectra of $(TlO_{0.5})_x - (TeO_2)_{1-x}$ glassy samples. All the spectra are presented with the same arbitrary intensity scale. Picture source [50].

In conclusion of this chapter, it is clear that adding a modifier is necessary for the stability of TeO_2 glasses. Although, Tl maintains the non-linear optical properties, its addition does not result in an improvement in the TeO_2 glass mechanical or thermal properties. Furthermore, no research has been conducted regarding how the mechanical strength of TeO_2 glasses changes as a result of the addition of the Tl_2O modifier. Additionally, we observe that the literature-available studies do not provide a clear consensus on the existence of terminal oxygen and an unambiguous value for the Te coordination number in pure TeO_2 glass. We have also noted that past research did not provide a comprehensive analysis of the evolution of the structural and optical properties of TeO_2-based glasses as a function of modifier content. In particular, previous studies lacks to provide a coherent value of $\chi^{(3)}$ even for similar systems. Therefore, in the next chapters, we will apply *ab-initio* approach to comprehend how structure and non-linear optical characteristics are related in TeO_2-based glasses.

2

Ab-initio modelling methods

Summary

2.1 A brief introduction to density functional theory **63**
2.1.1 Many body interaction 63
2.1.2 Born-Oppenheimer approximation 64
2.1.3 Density Functional Theory 66
2.1.4 Hohenberg-Kohn theorems 68
2.1.5 The Kohn-Sham method 71
2.1.6 Exchange-Correlation Functionals 73
2.1.7 Basis Set 76
2.1.8 Pseudopotential approximation 79
2.2 *Ab-initio* Molecular Dynamics **80**
2.2.1 Born-Oppenheimer molecular dynamics 81
2.2.2 Car-Parrinello molecular dynamics 81
2.2.3 Temperature control 83
2.2.3.1 Temperature in the NVE ensemble 83
2.2.3.2 Temperature in the NVT ensemble 83
2.3 Wannier functions **85**
2.4 Charge Analysis **87**

2.5 CP2K code **88**
2.6 *Ab-initio* principles of calculating NLO properties and Raman spectra **89**
2.6.1 Optical properties 89
2.6.2 Raman spectra 91
2.6.2.1 Vibrational analysis 92
2.6.2.2 Raman tensor 93

The underlying physical laws necessary for the mathematical theory of a large part of physics and the whole of chemistry are thus completely known, and the difficulty lies only in the fact that the exact application of these laws leads to equations much too complicated to be soluble.

~P. A. M. Dirac

2.1 A brief introduction to density functional theory

2.1.1 Many body interaction

The description of a many-electron system (molecules, atoms, solids, clusters) under quantum mechanical regime requires the solution of the time independent Schrödinger equation (SE), given by:

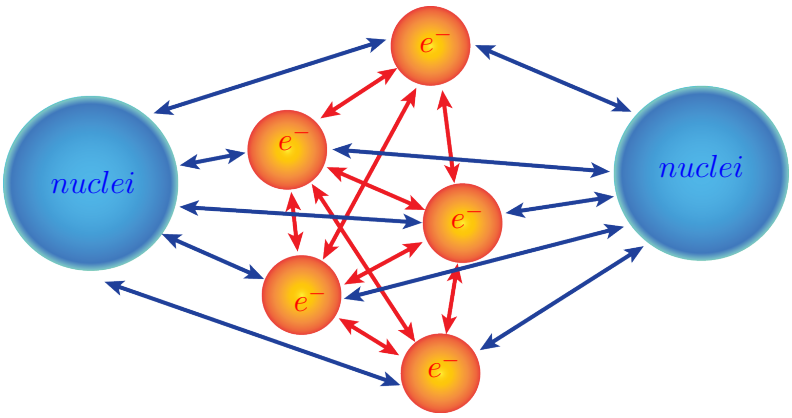

Figure 2.1: Sketch of many-body interaction between nuclei and electrons.

$$\hat{H}\Psi = E\Psi; \qquad \hat{H} = i\hbar\frac{\partial}{\partial t} \tag{2.1}$$

where $\hat{H}$ is the non-relativistic Hamiltonian operator with N nuclei and n electrons, and can be represented in position-space as (in atomic units):

$$\hat{H} = \underbrace{-\frac{1}{2}\sum_{I=1}^{N}\frac{1}{M_I}\nabla^2_{\mathbf{R}_I} + \frac{1}{2}\sum_{k<l}^{N}\frac{Z_k Z_l}{\mathbf{R}_{kl}}}_{\text{Nuclei contribution}} - \underbrace{\frac{1}{2}\sum_{j=1}^{n}\nabla^2_{\mathbf{r}_j} + \frac{1}{2}\sum_{i<j}^{n}\frac{1}{\mathbf{r}_{ij}}}_{\text{electron contribution}} - \underbrace{\sum_{k=1}^{N}\sum_{l=1}^{n}\frac{Z_k}{|\mathbf{R}_k - \mathbf{r}_l|}}_{\text{Nuclei-electron contribution}}, \quad (2.2)$$

where, M_I is the mass of the nuclei, $\mathbf{r}_i$ and $\mathbf{R}_i$ are position vectors of the electron and nuclei respectively, and Z_k being the atomic number. Solving the SE using equation [2.2] leads to the wave function $\Psi(\{\mathbf{R}_i\}, \{\mathbf{r}_k\}, t)$ which can be used to calculate the quantum mechanical expectation value of any operator $\hat{A}$ via the following equation $\langle A \rangle = \langle \Psi | \hat{A} | \Psi \rangle$.

As quoted by Dirac, despite the simplicity of the problem, exact analytical solutions exist for only a few systems, even in the case of single-particle approach, thus necessitating the use of approximation methods such as the variational principle or the perturbation theory to solve the SE. In theory, one can use a straightforward numerical solution, however the wavefunction $\Psi(\{\mathbf{R}_i\}, \{\mathbf{r}_k\}, t)$ solution becomes unrealistically computationally expensive owing to the enormous number of variables involved. The complexities, such as the large number of variables, the lack of easy interpretations, and the challenges in separation of degree of freedom (DOF) into a single-body problem, has led to development of newer approaches.

2.1.2 Born-Oppenheimer approximation

Due to the fact that nuclei are several orders of magnitude ($10^3 - 10^5$) more massive than electrons, they act differently under the same coulombic force. Thus, under typical time scale of nuclear motion, the electrons rapidly relax to the instantaneous ground-state configuration making it possible to disentangle the electronic DOF from the nuclear DOF. Born-Oppenheimer approximation asserts that while solving the SE for Hamiltonian operator in equation [2.2], one can assume that the nuclei remains stationary and just solve the SE using time-independent SE. Thereafter, we can solve the nuclear motion by taking the electronic energy eigenvalue contributing to the potential energy of the nuclei. The total wavefunction under the Born-Oppenheimer approximation can be expressed as:

$$\Psi(\{\mathbf{R}_i\}, \{\mathbf{r}_k\}, t) \approx \psi_e(\{\mathbf{R}_i\}, \{\mathbf{r}_k\})\psi_n(\{\mathbf{R}_i\}, t), \quad (2.3)$$

where $\psi_e(\{\mathbf{R}_i\}, \{\mathbf{r}_k\})$ is a wavefunction that depends on electronic coordinates and take nuclear coordinates as a parametric dependence. The Hamiltonian operator in equation [2.2]

can be written as:

$$\begin{aligned}
&\hat{H} = \hat{H}_e + \hat{H}_n, \text{ where} \\
&\hat{H}_e = -\frac{1}{2}\sum_{j=1}^{n}\nabla^2_{\mathbf{r}_j} + \frac{1}{2}\sum_{i<j}^{n}\frac{1}{|\mathbf{r}_{ij}|} - \underbrace{\sum_{K=1}^{N}\sum_{l=1}^{n}\frac{Z_k}{|\mathbf{R}_K - \mathbf{r}_l|}}_{\hat{V}_{ext}} + \underbrace{\sum_{K<L}^{N}\frac{Z_K Z_L}{|\mathbf{R}_{KL}|}}_{\hat{V}_{nn}}, \\
&\hat{H}_n = -\frac{1}{2}\sum_{K=1}^{N} M_K \nabla^2_{\mathbf{R}_K},
\end{aligned} \tag{2.4}$$

where $\hat{H}_e$ is the electronic contribution of equation [2.2] (with inclusion of constant $\hat{V}_{nn}$ term) and $\hat{H}_n$ is the nuclear contribution which under the Born-Oppenheimer approximation can be dropped due to the low kinetic energy of the nuclei. Therefore, under the Born-Oppenheimer approximation and considering equation [2.4] and equation [2.3] the time-independent SE becomes:

$$\begin{aligned}
\hat{H}\Psi(\{\mathbf{R}_i\},\{\mathbf{r}_k\},t) &\approx (\hat{H}_e)\psi_e(\{\mathbf{R}_i\},\{\mathbf{r}_k\})\psi_n(\{\mathbf{R}_i\},t) \\
&= \psi_n(\{\mathbf{R}_i\},t)(\hat{H}_e\psi_e(\{\mathbf{R}_i\},\{\mathbf{r}_k\})).
\end{aligned} \tag{2.5}$$

Thus, the time-independent SE due to electronic DOF can be expressed as:

$$\hat{H}_e\psi_e(\{\mathbf{R}_i\},\{\mathbf{r}_k\}) = E_e(\mathbf{R}_i)\psi_e(\{\mathbf{R}_i\},\{\mathbf{r}_k\}), \tag{2.6}$$

with eigenvalue E_e is known as the adiabatic contribution of the electronic energy and can later be used to compute the total Hamiltonian $\hat{H}$. Utilizing equation [2.3] and equation [2.6] to evaluate the time-dependent Hamiltonian equation [2.4] as:

$$\begin{aligned}
\hat{H}\psi_e(\{\mathbf{R}_i\},\{\mathbf{r}_k\})\psi_n(\{\mathbf{R}_i\},t) =& \hat{H}_n\psi_e(\{\mathbf{R}_i\},\{\mathbf{r}_k\})\psi_n(\{\mathbf{R}_i\},t) + \hat{H}_e\psi_e(\{\mathbf{R}_i\},\{\mathbf{r}_k\})\psi_n(\{\mathbf{R}_i\},t), \\
\hat{H}\psi_n(\{\mathbf{R}_i\},t) =& \left[\underbrace{-\frac{1}{2}\sum_{K=1}^{N} M_K\nabla^2_{\mathbf{R}_K}}_{\hat{H}_n} + E_e(\mathbf{R}_i)\right]\psi_n(\{\mathbf{R}_i\},t).
\end{aligned} \tag{2.7}$$

At last, one can solve the equation [2.7] under the limit of classical mechanics and considering the nuclei to be classical point particles.

In conclusion, within the Born-Oppenheimer approximation, the problem of solving equation [2.2] has been reduced to solving equation [2.6]. For the remaining chapter, it is now assumed that we are solving the electronic DOF with nuclear coordinates being fixed, thus the $\mathbf{R}_i$ dependence in $\psi_e(\{\mathbf{R}_i\},\{\mathbf{r}_k\})$ representation will be dropped.

2.1.3 Density Functional Theory

"The tabulation of one variable requires a page, of two variables a volume, and of three variables a library; but the full specification of a single wavefunction of neutral Fe is a function of seventy eight variables. It would be rather crude to restrict to ten the number of values at which to tabulate this function, but even so, full tabulation of it would require 10^{78} *entries, and if this number could be reduced somewhat from considerations of symmetry, there would still not be enough atoms in the whole solar system to provide the material for printing such a table".*

$\sim$ D. R. Hartree

Even with the Born-Oppenheimer approximation, the problem of separating electronic DOF into n single-body problems requires the evaluation of $3n$ variables in the numerical resolution of $\psi_e(\{\mathbf{r}_k\})$ which makes it computationally unrealistic. Thus, further approximate approaches such as dimensionality reduction have been adopted. Despite, the fact that the wavefunction $\psi_e(\{\mathbf{r}_k\})$ depends on $3n$ variables, it is still possible to find the expectation value $\langle A\rangle = \langle\psi_e|\hat{A}|\psi_e\rangle$ with the help of other derived quantities that depends on fewer variables.

According to the Born-Oppenheimer approximation, the electron-nuclei interaction term in $\hat{H}_e$ under Coulomb potential of the nuclei in equation [2.6] is interpreted as a static external potential $V_{ext}(\mathbf{r})$,

$$V_{ext}(\mathbf{r}) = \sum_{I=1}^{N} \frac{Z_I}{|\mathbf{R}_I - \mathbf{r}|}, \tag{2.8}$$

where I is the summation index over all the nuclear variables. Thus, the nuclei-electron interaction operator can be defined as:

$$\hat{V}_{ext} = \sum_{j=1}^{n} V_{ext}(\mathbf{r}_j) = \sum_{j=1}^{n}\sum_{I=1}^{N} \frac{Z_I}{|\mathbf{R}_I - \mathbf{r}_j|}. \tag{2.9}$$

And the expectation value of the nuclei-electron operator can be expressed as:

$$\begin{aligned} V_{ne} = \langle\psi_e|\hat{V}_{ext}|\psi_e\rangle &= \int \psi_e^*(\mathbf{r}_1, \mathbf{r}_2, ..., \mathbf{r}_n) \sum_{j=1}^{n} V_{ext}(\mathbf{r}_j)\psi_e(\mathbf{r}_1, \mathbf{r}_2, ..., \mathbf{r}_n) d\mathbf{r}_1 d\mathbf{r}_2 ... d\mathbf{r}_n \\ &= n \int d\mathbf{r}_1 V_{ext}(\mathbf{r}_1) \int \psi_e^*(\mathbf{r}_1, \mathbf{r}_2, ..., \mathbf{r}_n)\psi_e(\mathbf{r}_1, \mathbf{r}_2, ..., \mathbf{r}_n) d\mathbf{r}_2 d\mathbf{r}_3 ... d\mathbf{r}_n, \end{aligned} \tag{2.10}$$

and hence we obtain,

$$V_{ne} = \left\langle \psi_e | \sum_{j=1}^{n} V_{ext}(\mathbf{r}_j) | \psi_e \right\rangle = \int d\mathbf{r} V_{ext}(\mathbf{r}) \rho(\mathbf{r}), \tag{2.11}$$

which is valid for single-particle multiplicative operator, with the single-particle density defined as:

$$\begin{aligned} \rho(\mathbf{r}_1) &= n \int \psi_e^*(\mathbf{r}_1, \mathbf{r}_2, ..., \mathbf{r}_n) \psi_e(\mathbf{r}_1, \mathbf{r}_2, ..., \mathbf{r}_n) d\mathbf{r}_2 d\mathbf{r}_3 ... d\mathbf{r}_n \\ &= \left\langle \psi_e | \sum_{j=1}^{n} \delta(\mathbf{r} - \mathbf{r}_j) | \psi_e \right\rangle, \end{aligned} \tag{2.12}$$

Likewise, for two-particle multiplicative operator such as electron-electron interaction term, it is possible to get:

$$V_{ee} = \left\langle \psi_e | \frac{1}{2} \sum_{i<j}^{n} \frac{1}{\mathbf{r}_{ij}} | \psi_e \right\rangle = \frac{1}{2} \int d\mathbf{r}_1 d\mathbf{r}_2 \frac{\Gamma(\mathbf{r}_1, \mathbf{r}_2)}{|\mathbf{r}_{12}|}, \tag{2.13}$$

where we define the two-particle density as:

$$\begin{aligned} \Gamma(\mathbf{r}_1, \mathbf{r}_2) &= n(n-1) \int \psi_e^*(\mathbf{r}_1, \mathbf{r}_2, ..., \mathbf{r}_n) \psi_e(\mathbf{r}_1, \mathbf{r}_2, ..., \mathbf{r}_n) d\mathbf{r}_3 ... d\mathbf{r}_n \\ &= \left\langle \psi_e | \sum_{i \neq j}^{n} \delta(\mathbf{r} - \mathbf{r}_i) \delta(\mathbf{r} - \mathbf{r}_j) | \psi_e \right\rangle. \end{aligned} \tag{2.14}$$

Similarly, the kinetic energy involving differential operator can be written as:

$$\begin{aligned} T &= -\left\langle \psi_e | \frac{1}{2} \sum_{i=1}^{N} n \nabla_{\mathbf{r}_i}^2 | \psi_e \right\rangle \\ &= -\frac{1}{2} n \int \psi_e^*(\mathbf{r}_1, \mathbf{r}_2, ..., \mathbf{r}_n) \nabla_{\mathbf{r}_1}^2 \psi_e(\mathbf{r}_1, \mathbf{r}_2, ..., \mathbf{r}_n) d\mathbf{r}_1 d\mathbf{r}_2 ... d\mathbf{r}_n \\ &= -\frac{1}{2} n \int [\nabla_{\mathbf{r}_1}^2 \psi_e^*(\mathbf{r}_1', \mathbf{r}_2, ..., \mathbf{r}_n) \psi_e(\mathbf{r}_1, \mathbf{r}_2, ..., \mathbf{r}_n)]_{\mathbf{r}_1 = \mathbf{r}_1'} d\mathbf{r}_1 d\mathbf{r}_2 ... d\mathbf{r}_n \\ &= -\frac{1}{2} \int d\mathbf{r}_1 [\nabla_{\mathbf{r}_1}^2 \gamma(\mathbf{r}_1; \mathbf{r}_1')]_{\mathbf{r}_1 = \mathbf{r}_1'}, \end{aligned} \tag{2.15}$$

here we define the first-order density matrix as:

$$\gamma(\mathbf{r}_1; \mathbf{r}_1') = n \int \psi_e^*(\mathbf{r}_1', \mathbf{r}_2, ..., \mathbf{r}_n) \psi_e(\mathbf{r}_1, \mathbf{r}_2, ..., \mathbf{r}_n)] d\mathbf{r}_2 d\mathbf{r}_3 ... d\mathbf{r}_n. \tag{2.16}$$

Thus, it is possible to express the total energy functional of the system in newly transformed

Reduced density matrix (RDM) formalism as:

$$E_e[\rho, \gamma, \Gamma] = T[\gamma(\mathbf{r}_1; \mathbf{r}_1^{'})] + V_{ne}[\rho(\mathbf{r})] + V_{ee}[\Gamma(\mathbf{r}_1, \mathbf{r}_2)] + V_{nn}. \tag{2.17}$$

The transformation of the various parameters of the electronic Hamiltonian $\hat{H}_e$ into RDM allows for the description of the quantum mechanical picture of any system merely using these RDM. Furthermore, because V_{nn} is a constant, in the equation [2.17], we drop this term while evaluation of SE equation.

Several advantages of working with electron density as a fundamental variable are:

- it is easy to tabulate,
- it is an experimental observable, and
- it is easy to visualize

Having established the advantages of using the density formulation, the essential questions to put light on before using density as a fundamental variable rather than wavefunction would be:

- is it possible to obtain all the information that can be obtained by wavefunction formulation via density formulation?
- is it possible to evaluate the quantum mechanical properties with electronic density solely?
- is it possible to develop a method to get the electronic density directly?

2.1.4 Hohenberg-Kohn theorems

Despite numerous attempts in formulating DFT, Hohenberg and Kohn for the first time offered the formal proof that led to the birth of modern DFT in their 1964 contribution [51]. They presented two theorems to support the right foundation of this approach.

Theorem 1 *For a system with N interacting electrons in an external potential $V_{ext}(\boldsymbol{r})$, the total energy is a unique functional of ground state electron density $\rho(\boldsymbol{r})$ up to a constant.*
Proof: (By reductio ad absurdum) Let's assume that the ground state of two N-electron systems are defined by two different types of external potential $V_{ext}^{(1)}(\mathbf{r})$ and $V_{ext}^{(2)}(\mathbf{r})$, see equation [2.10], which differs by more than an additive constant but lead to the same density.

$$V_{ext}^{(1)}(\mathbf{r}) \Rightarrow \hat{H}_e^{(1)} \Rightarrow \psi_e^{(1)} \Rightarrow \rho(\mathbf{r}) \Leftarrow \psi_e^{(2)} \Leftarrow \hat{H}_e^{(2)} \Leftarrow V_{ext}^{(2)}(\mathbf{r}). \tag{2.18}$$

The corresponding electronic Hamiltonian $\hat{H}_e$ operator from equation [2.4] in conjunction with SE can be written as:

$$\begin{aligned}
\hat{H}_e^{(1)} &= -\frac{1}{2}\sum_{j=1}^{n}\nabla_{\mathbf{r}_j}^2 + \frac{1}{2}\sum_{i<j}^{n}\frac{1}{\mathbf{r}_{ij}} - \sum_{l=1}^{n}V_{ext}^{(1)}(\mathbf{r}_l) + V_{nn}, \\
\hat{H}_e^{(2)} &= -\frac{1}{2}\sum_{j=1}^{n}\nabla_{\mathbf{r}_j}^2 + \frac{1}{2}\sum_{i<j}^{n}\frac{1}{\mathbf{r}_{ij}} - \sum_{l=1}^{n}V_{ext}^{(2)}(\mathbf{r}_l) + V_{nn}, \\
\hat{H}_e^{(1)}\psi_e^{(1)} &= E_1\psi_e^{(1)}; \qquad \hat{H}_e^{(2)}\psi_e^{(2)} = E_2\psi_e^{(2)},
\end{aligned} \tag{2.19}$$

where $\psi_e^{(1)}$ and $\psi_e^{(2)}$ are trial wavefunctions which minimizes E_1 and E_2 respectively. The density yielded by $\psi_e^{(1)}$ and $\psi_e^{(2)}$ is:

$$\rho(\mathbf{r}_1) = n\int \psi_e^*(\mathbf{r}_1, \mathbf{r}_2, ..., \mathbf{r}_N)\psi_e(\mathbf{r}_1, \mathbf{r}_2, ..., \mathbf{r}_N)d\mathbf{r}_2 d\mathbf{r}_3 ... d\mathbf{r}_N. \tag{2.20}$$

Then, using the variational principle one can show that:

$$\begin{aligned}
E_1 = \langle\psi_e^{(1)}|\hat{H}_e^{(1)}|\psi_e^{(1)}\rangle < \langle\psi_e^{(2)}|\hat{H}_e^{(1)}|\psi_e^{(2)}\rangle &= \langle\psi_e^{(2)}|\hat{H}_e^{(2)}|\psi_e^{(2)}\rangle + \langle\psi_e^{(2)}|\hat{H}_e^{(1)} - \hat{H}_e^{(2)}|\psi_e^{(2)}\rangle \\
E_1 < E_2 + \int d\mathbf{r}\rho(\mathbf{r})(V_{ext}^{(1)}(\mathbf{r}) - V_{ext}^{(2)}(\mathbf{r})).&
\end{aligned} \tag{2.21}$$

Based on the similar arguments, one can also show that with the change of indices, equation [2.21] can be rewritten as:

$$E_2 < E_1 + \int d\mathbf{r}\rho(\mathbf{r})(V_{ext}^{(2)}(\mathbf{r}) - V_{ext}^{(1)}(\mathbf{r})). \tag{2.22}$$

And summation of equation [2.21] and [2.22] results in contradiction as:

$$E_1 + E_2 < E_2 + E_1. \tag{2.23}$$

Hence, the notion that two distinct external potentials leading to same density were incorrect. As a result, the $\rho(\mathbf{r})$ can only represent one $V_{ext}(\mathbf{r})$, making the Hamiltonian operator $\hat{H}_e$ and thus ψ_e unique. In addition, since the density can be obtained from the wavefunction, this makes the energy functional $E[\rho]$ uniquely determinable by the external potential $V_{ext}(\mathbf{r})$. Similarly, $\rho(\mathbf{r})$ determines all the other ground state properties, such as $T[\rho]$ and $V_{ee}[\rho]$.

Theorem 2 *An universal energy functional $E[\rho]$ can be expressed in terms of density where the exact ground state of this functional is only produced by the ground state density.*
Proof: Assuming the ground state energy eigenvalue E_0 of the operator $\hat{H}_e$ and with collecting terms from equations [2.11], [2.13] and [2.15], E_0 is given by:

$$\begin{aligned} E_0[\rho] &= \langle\psi_e|\hat{H}_e|\psi_e\rangle \\ &= \underbrace{-\left\langle\psi_e|\frac{1}{2}\sum_{i=1}^{n}\nabla^2_{\mathbf{r}_i}|\psi_e\right\rangle + \left\langle\psi_e|\frac{1}{2}\sum_{i<j}^{n}\frac{1}{\mathbf{r}_{ij}}|\psi_e\right\rangle}_{\text{Universal term}} + \underbrace{\int d\mathbf{r}V_{ext}(\mathbf{r})\rho(\mathbf{r})}_{\text{System dependent}} \\ &= F_{HK}[\rho] + \int d\mathbf{r}V_{ext}(\mathbf{r})\rho(\mathbf{r}), \end{aligned} \tag{2.24}$$

where $F_{HK}[\rho]$ is the universal Hohenberg-Kohn functional that depends only on $\rho(\mathbf{r})$ and is constrained by, $n = \int d\mathbf{r}\rho(\mathbf{r})$. The explicit functional form of $F_{HK}[\rho]$ is unknown and thus, one has to resort to approximate methods.

Let us now consider a trial density $\tilde{\rho}(\mathbf{r})$ other than the true density $\rho(\mathbf{r})$ which also satisfies the constraints $\tilde{\rho}(\mathbf{r}) > 0$, $n = \int \tilde{\rho}(\mathbf{r})d\mathbf{r}$, and that defines its own external potential $\tilde{V}_{ext}(\mathbf{r})$, Hamiltonian operator $\hat{H}_e$, and therefore wavefunction $\tilde{\psi}_e$. Now the obtained wavefunction can be used as trial wavefunction for the true Hamiltonian operator $\hat{H}_e$ generated from the true external potential $V_{ext}(\mathbf{r})$. Thus, using the variational principle, equation [2.24] can be shown to follow:

$$\langle\tilde{\psi}_e|\hat{H}_e|\tilde{\psi}_e\rangle = F_{HK}[\tilde{\rho}] + \int d\mathbf{r}\tilde{V}_{ext}(\mathbf{r})\tilde{\rho}(\mathbf{r}) = E[\tilde{\rho}] \geq E_0[\rho] = \langle\psi_e|\hat{H}_e|\psi_e\rangle. \tag{2.25}$$

Therefore, the $E[\rho]$ functional acquire its minimum value $E_0[\rho]$ out of all the trial densities only if the input density is the true ground state density i.e. $\tilde{\rho}(\mathbf{r}) \equiv \rho(\mathbf{r})$.

The F_{HK} can be expanded as:

$$\begin{aligned} F_{HK} &= -\left\langle\psi_e|\frac{1}{2}\sum_{i=1}^{N}\nabla^2_{\mathbf{r}_i}|\psi_e\right\rangle + \underbrace{\frac{1}{2}\int d\mathbf{r}_1 d\mathbf{r}_2\frac{\Gamma(\mathbf{r}_1,\mathbf{r}_2)}{\mathbf{r}_{12}}}_{V_{ee}} \\ &= T[\rho] + \frac{1}{2}\int d\mathbf{r}_1 d\mathbf{r}_2\frac{\Gamma(\mathbf{r}_1,\mathbf{r}_2)}{\mathbf{r}_{12}}, \end{aligned} \tag{2.26}$$

where $T[\rho]$ represents the functional dependence of the kinetic energy on $\rho(\mathbf{r})$ due to the first Hohenberg-Kohn theorem. Furthermore, the two-particle density $\Gamma(\mathbf{r}_1,\mathbf{r}_2)$ can also be

decomposed as:

$$\Gamma(\mathbf{r}_1, \mathbf{r}_2) = \rho(\mathbf{r}_1)\rho(\mathbf{r}_2)[1 - f(\mathbf{r}_1, \mathbf{r}_2)], \tag{2.27}$$

where, $f(\mathbf{r}_1, \mathbf{r}_2)$ is the correlation function. With this decomposition, F_{HK} becomes:

$$F_{HK} = \underbrace{T[\rho]}_{\text{Kinetic energy}} + \underbrace{\frac{1}{2}\int d\mathbf{r}_1 d\mathbf{r}_2 \frac{\rho(\mathbf{r}_1)\rho(\mathbf{r}_2)}{\mathbf{r}_{12}}}_{E_H[\rho]\text{ (Classic coloumb interaction)}} + \underbrace{\frac{f(\mathbf{r}_1, \mathbf{r}_2)\rho(\mathbf{r}_1)\rho(\mathbf{r}_2)}{\mathbf{r}_{12}}}_{\text{Self-Interaction correction term}}. \tag{2.28}$$

Out of all the three terms mentioned above, only $E_H[\rho]$ can be calculated while the functional forms of the other two terms are unknown.

2.1.5 The Kohn-Sham method

Due to the unknown functional forms of two terms other than $E_H[\rho]$ (known as Hartree energy) in Hohenberg-Kohn functional F_{HK} discussed in equation [2.28], it is not possible to solve the SE for the true electronic Hamiltonian operator directly and thus one needs to resort to alternative approaches. In DFT, Kohn-Sham method is a formulation which attempts to solve the Hohenberg-Kohn functional F_{HK} by introducing a fictitious non-interacting system that resembles the real many-electron system in order to obtain one-electron Kohn-Sham orbitals. Under the Kohn-Sham scheme, equation [2.24] with the F_{HK} from equation [2.28] can be written as:

$$E[\rho] = T_s[\rho] + \int d\mathbf{r} V_{ext}(\mathbf{r})\rho(\mathbf{r}) + E_H[\rho] + E_{xc}[\rho], \tag{2.29}$$

where $T_s[\rho]$ is the kinetic energy of a non-interacting system. $E_{xc}[\rho]$ is the exchange-correlation functional is defined as

$$E_{xc}[\rho] = (T[\rho] - T_s[\rho]) + (V_{ee}[\rho] - E_H[\rho]). \tag{2.30}$$

Non-interacting $T_s[\rho]$ can be obtained for a certain $\rho(\mathbf{r})$ by solving the one-particle Kohn-Sham SE as:

$$\left(-\frac{1}{2}\nabla^2_{\mathbf{r}_i} + v_{eff}(\mathbf{r})\right)\psi_i = \epsilon_i \psi_i, \tag{2.31}$$

with ϵ_i denoting the Kohn-sham orbital energy, and $v_{eff}(\mathbf{r})$ known as Kohn-Sham effective potential chosen in such a way that the resulting Kohn-Sham orbital ψ_i generates the true ground

state density of the interacting system,

$$\rho(\mathbf{r}) = \sum_i |\psi_i|^2, \tag{2.32}$$

and leads to the functional form $T_s[\rho]$ as:

$$T_s[\rho] = \sum_i \epsilon_i - \int d\mathbf{r}\rho(\mathbf{r})v_{eff}(\mathbf{r}). \tag{2.33}$$

The energy functional from equation [2.29] can be written explicitly as:

$$E[\rho] = \sum_i \epsilon_i - \int d\mathbf{r}\rho(\mathbf{r})v_{eff}(\mathbf{r}) + \int d\mathbf{r}V_{ext}(\mathbf{r})\rho(\mathbf{r}) + E_H[\rho] + E_{xc}[\rho]. \tag{2.34}$$

According to Hohenberg-Kohn theorems, we minimize $E[\rho]$ in order to obtain the ground state density, as:

$$\delta E[\rho] = 0 = \sum_i \delta\epsilon_i - \int d\mathbf{r}\rho(\mathbf{r})\delta v_{eff}(\mathbf{r}) + \int d\mathbf{r}\delta\rho(\mathbf{r}) \left[-v_{eff}(\mathbf{r}) + V_{ext}(\mathbf{r}) + \frac{\delta E_H[\rho]}{\delta\rho(\mathbf{r})} + \frac{\delta E_{xc}[\rho]}{\delta\rho(\mathbf{r})} \right]. \tag{2.35}$$

The value of ϵ_i from equation [2.31] can be obtained as:

$$\epsilon_i = -\left\langle \psi_i | \frac{1}{2}\nabla^2_{\mathbf{r}_i} | \psi_i \right\rangle + \langle \psi_i | v_{eff}(\mathbf{r}) | \psi_i \rangle, \tag{2.36}$$

and thus,

$$\begin{aligned}
\delta\epsilon_i = & -\left\langle \delta\psi_i | \frac{1}{2}\nabla^2_{\mathbf{r}_i} | \psi_i \right\rangle + \langle \delta\psi_i | v_{eff}(\mathbf{r}) | \psi_i \rangle - \left\langle \psi_i | \frac{1}{2}\nabla^2_{\mathbf{r}_i} | \delta\psi_i \right\rangle + \langle \psi_i | v_{eff}(\mathbf{r}) | \delta\psi_i \rangle + \langle \psi_i | \delta v_{eff}(\mathbf{r}) | \psi_i \rangle \\
= & \left(\left\langle \delta\psi_i | - \frac{1}{2}\nabla^2_{\mathbf{r}_i} + v_{eff}(\mathbf{r}) | \psi_i \right\rangle \right) + \left(\left\langle \psi_i | - \frac{1}{2}\nabla^2_{\mathbf{r}_i} + v_{eff}(\mathbf{r}) | \delta\psi_i \right\rangle \right) + \langle \psi_i | \delta v_{eff}(\mathbf{r}) | \psi_i \rangle \\
= & \langle \delta\psi_i | \epsilon_i | \psi_i \rangle + \langle \psi_i | \epsilon_i | \delta\psi_i \rangle + \langle \psi_i | \delta v_{eff}(\mathbf{r}) | \psi_i \rangle \\
= & \cancel{\epsilon_i \delta\langle \psi_i | \psi_i \rangle} + \langle \psi_i | \delta v_{eff}(\mathbf{r}) | \psi_i \rangle
\end{aligned} \tag{2.37}$$

and hence,

$$\sum_i \delta\epsilon_i = \int d\mathbf{r}\rho(\mathbf{r})\delta v_{eff}(\mathbf{r}), \tag{2.38}$$

and incorporating this into equation [2.35] gives:

$$\delta E[\rho] = 0 = \int d\mathbf{r}\delta\rho(\mathbf{r}) \left[-v_{eff}(\mathbf{r}) + V_{ext}(\mathbf{r}) + \frac{\delta E_H[\rho]}{\delta\rho(\mathbf{r})} + \frac{\delta E_{xc}[\rho]}{\delta\rho(\mathbf{r})} \right]. \tag{2.39}$$

Now, since $\delta\rho(\mathbf{r})$ is arbitrary, thus the term in bracket must be zero, which leads to:

$$v_{eff}(\mathbf{r}) = V_{ext}(\mathbf{r}) + \underbrace{\frac{\delta E_H[\rho]}{\delta\rho(\mathbf{r})}}_{V_H} + \underbrace{\frac{\delta E_{xc}[\rho]}{\delta\rho(\mathbf{r})}}_{V_{xc}}. \tag{2.40}$$

The term V_H and V_{xc} in the above equation are known as Hartree and exchange-correlation potential, respectively. Substituting $v_{eff}(\mathbf{r})$ back in equation [2.34], gives the energy functional

$$E[\rho] = \sum_i \epsilon_i - \underbrace{\frac{1}{2}\int d\mathbf{r}_1 d\mathbf{r}_2 \frac{\rho(\mathbf{r}_1)\rho(\mathbf{r}_2)}{\mathbf{r}_{12}}}_{E_H} + E_{xc}[\rho] - \int d\mathbf{r}\rho(\mathbf{r})\frac{\delta E_{xc}[\rho]}{\delta\rho(\mathbf{r})}, \tag{2.41}$$

where the first term $\sum_i \epsilon_i$ is the sum over the eigenvalues of Kohn-Shan equation and is known as the "band structure energy". The Kohn-Sham equations are solved using a self-consistent iterative numerical technique. The flowchart in figure [2.2] depicts the workflow of the Kohn-Sham method.

Finally, we could utilize the output energy to compute the forces on atomic nuclei using the Feynman-Hellman theorem and use these forces to propagate the nuclei on space and time (for performing geometry optimization, MD etc.) using specific algorithms.

2.1.6 Exchange-Correlation Functionals

As sketched above, due to the unknown analytic functional form of $E_{xc}[\rho]$, various approximations are introduced in order to make the Kohn-Sham equation solvable. Furthermore, these functionals can be divided into mainly two categories: *empirical* (derived by fitting the parameters on known results on atoms and molecules), and *non-empirical* (these functionals are based on some physical rules). In the following sections, we introduce some of the most common $E_{xc}[\rho]$ functionals.

Local Density Approximation

This is the simplest approximation to the E_{xc} functional which is given by the expression:

$$E_{xc}^{LDA}[\rho] = \int \rho(\mathbf{r})\varepsilon_{xc}^{\text{hom}}[\rho]d\mathbf{r}, \tag{2.42}$$

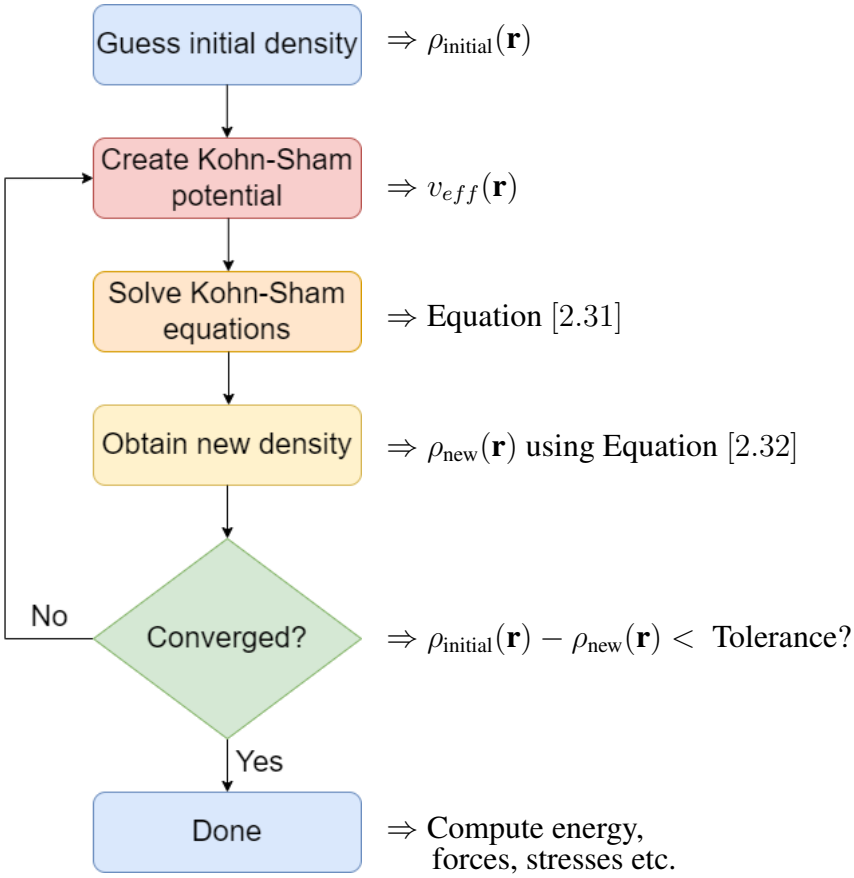

Figure 2.2: Flowchart representation of working mechanism of self-consistent Kohn-Sham equation.

where, the term $\varepsilon_{xc}^{\text{hom}}[\rho]$ is known as exchange-correlation energy per electron of homogeneous electron gas (HEG). A HEG is defined as a system composed of uniformly distributed electrons moving over a positive charge background, resulting in an electrically neutral system. The ground state electron density $\rho(\mathbf{r})$ of this Homogeneous electron gas (HEG) system remains constant over all values of $\mathbf{r}$. The term "local" in the name is due to the fact that the functional $E_{xc}[\rho]$ in equation [2.42] does not depends on the derivative of the electron density and thus can be approximated only for the cases with slowly varying densities with respect to atomic positions. If one treats the exchange and correlation part of the exchange-correlation energy $E_{xc}[\rho]$ separately, then it is possible to solve the former exchange part analytically in the case of Local Density Approximation (LDA), however for the latter correlation part one still has to resort to fitting methods based on other simulations such as Monte-Carlo methods [52].

Despite the lousy approximation in LDA formalism, the approach has been proved worthy in approximating several properties such as molecular topologies [53], single-particle and vibrational properties [54] and surface diffusion barriers in simple adsorption systems. However, LDA fails completely to describe the systems with multiple kinds of bonding nature such as ionic and covalent bonds. In addition, LDA is known for underestimating the exchange energy by 15% and

overestimating the correlation energy up to 200% [55], [56]. Furthermore, LDA overestimates the atomic bond-lengths and results in small lattice parameters and large bulk moduli [57], [58].

Generalized Gradient Approximation

The idea of a uniform density over real space in the case of LDA is non-physical as it is trivial to have higher electron density near the nuclei compared to the farther region. Thus, the Generalized Gradient Approximation (GGA) takes the first step in improving the approximation of the functional $E_{xc}[\rho]$ by incorporating gradient effects of electron density. The expression for GGA exchange-correlation functional can be described as:

$$E_{xc}^{GGA}[\rho, \nabla\rho] = \int \rho(\mathbf{r})\varepsilon_{xc}^{\text{hom}}[\rho]F_{xc}[\rho, \nabla\rho]d\mathbf{r}, \tag{2.43}$$

where, $F_{xc}[\rho, \nabla\rho]$ is known as an enhancement factor. Depending on the target properties of interest (structural properties, band structures, electronic properties, etc.) there exist various choices of $F_{xc}[\rho, \nabla\rho]$ in literature, making several flavors of GGA possible [59]–[63]. The enhancement factor $F_{xc}[\rho, \nabla\rho]$ can again be possibly split into exchange and correlation parts, as:

$$F_{xc}[\rho, \nabla\rho] = F_c[\rho, \nabla\rho] + F_x[\rho, \nabla\rho]. \tag{2.44}$$

It is worth to mentioning two popular exchange enhancement factors, namely Perdew-Burke-Ernzerhof (PBE) [62] and B88 [63] functionals. They can be represented analytically by the following equations:

$$\begin{aligned} s &\equiv \frac{|\nabla\rho(\mathbf{r})|}{2(3\pi^2)^{1/3}\rho(\mathbf{r})^{4/3}}, \\ F_x^{PBE}(s) &= 1 + k - \frac{k}{1 + \mu s^2/k}, \\ F_x^{B88}(s) &= 1 + \frac{\beta x(s)^2}{C[1 + 6\beta x(s)\sinh^{-1} x(s)]}, \end{aligned} \tag{2.45}$$

where $x(s) = 2(3\pi^2)^{1/3}s$ and $C = \frac{3}{2}\left(\frac{3}{4\pi}\right)^{1/3}$. The parameters μ and k in the case of PBE are non-empirical because they are generated based on some physical constraint on the system while in the case of B88, the parameter β is obtained via empirical fitting. The correlation component of $E_{xc}^{GGA}[\rho, \nabla\rho]$ may also be estimated using methods like Lee, Yang, and Parr's LYP functional [64]. The GGA method improves binding and atomic energies, but it can overestimate lattice constants, which in some cases can be better modelled using LDA due to accidental error cancellation.

Hybrid functional

For some materials, LDA and GGA approaches for electronic structure calculations may underestimate band gaps by more than 50% [65]. These errors frequently occur in the position of both the conduction and valence bands, resulting in transition energy errors of the order of the band-gap error [65]. Several hybrid functionals that bring the electronic structure closer to experimental values have been developed. Some functionals, for example, may yield accurate electronic band structures for good conductors (such as metals), but not for broad band-gap semiconductors. The scope of this thesis does not allow for a comprehensive examination of all of these methods, nevertheless, the hybrid functional pertinent to the study with this thesis is described in the following paragraph.

Usually, hybrid exchange-correlation functional is constructed as a linear combination of the Hartree-Fock (HF) exact exchange potential energy given by:

$$E_x^{HF} = -\frac{1}{2}\sum_{i,j}\int \psi_i^*(\mathbf{r}_1)\psi_j^*(\mathbf{r}_2)\frac{1}{\mathbf{r}_{12}}\psi_i(\mathbf{r}_2)\psi_j(\mathbf{r}_1), \tag{2.46}$$

and any number of exchange and correlation density functionals. PBE0 functional mixes 75% of PBE exchange energy functional with 25% of Hartree-Fock exchange energy, along with the full PBE correlation energy as follows:

$$E_{xc}^{PBE0} = 0.75E_x^{PBE} + 0.25E_x^{HF} + E_c^{PBE}. \tag{2.47}$$

2.1.7 Basis Set

After discussing the exchange and correlation functionals, the next step in solving the Kohn-Sham equation [2.31] is to select a basis set to expand the electronic wave functions. Mathematically, a basis set is a set of vectors that span a space, such as the i,j,k cartesian unit vectors, which spans the 3D cartesian space. The basis set in quantum chemistry, refers to the set of one particle functions used to construct molecular orbitals via methods such as the Linear Combination of Atomic Orbitals (LCAO). This basis set does not have to be orthogonal and are centered on an atom that defines the single electron atomic orbital. We have freedom in choosing the type of these single electron atomic orbital. Slater Type Orbital (STO) and Gaussian Type Orbital (GTO) are the two most popular functions we deal with in general.

Slater type orbital

In quantum molecular computations, STO are the natural basis functions. Nonetheless, their application has been limited, owing to challenges in their mathematical integration. They are

simple exponentials that accurately represent the eigenfunctions of the hydrogen atom. At $r \to \infty$, STO exhibit the anticipated exponential decay in the tail regions and the correct cusp behavior in $r \to 0$. STO's can be expressed as:

$$\phi_{abc}^{STO}(x, y, z) = N x^a y^b z^c e^{-\zeta r}, \tag{2.48}$$

where, N is a normalization constant and x, y, z are the cartesian coordinates, ζ is the strength of single electron function localization and a, b, c control the angular momentum L with a constraint as $L = a + b + c$. These STO's provide accurate short- and long-range order (at least for hydrogen atom), but owing to their inability to define nodes it becomes extremely hard to replicate $2s$ or $2p$ orbitals using these functions.

Gaussian type orbital

GTO's, on the other hand, are defined in much the same way as STO's, with the exception that the exponential is quadratic in radial distance.

$$\phi_{abc}^{GTO}(x, y, z) = N x^a y^b z^c e^{-\zeta r^2} \tag{2.49}$$

The advantage of constructing basis functions in this manner is that one can now perform quick gaussian integrals, and tricks such as product of two gaussian is also a gaussian aid in performing efficient computations. In contrast, the issue we have with these kinds of functions is that they are unable to accurately reproduce short and long range orders.

Contracted Gaussian type orbital

To solve this problem while still making use of the gaussian tactics, one may use a linear combination of these GTO's to construct a function that mimics the STO's, known as Contracted Gaussian Type Orbital (CGTO), expressed as:

$$\phi_{abc}^{CGTO}(x, y, z) = N \sum_{i}^{n} c_i x^a y^b z^c e^{-\zeta_i r^2}, \tag{2.50}$$

where n denotes the number of GTO's in linear combination. This type of basis function is commonly expressed in the literature as STO-nG, which is a combination of n Gaussian sets that imitates a STO.

Types of basis set

We can linearly contract these orbitals discussed above to further improve the accuracy of approximating the wavefunction. In several ways, it is possible to contract these orbitals as:

- Minimal basis set: One basis function (STO/GTO/CGTO) for each Atomic Orbital (AO) on each constituent atom. This basis set is not flexible enough to allow for proper representation of each AO necessitating the use of multiple functions.
- Double-Zeta (DZ) basis set : Two basis function for each k^{th} AO:

$$\phi_k = a_1\phi_k^{STO/GTO/CGTO}(r,\zeta_1) + a_2\phi_k^{STO/GTO/CGTO}(r,\zeta_2) \tag{2.51}$$

- Triple-Zeta (TZ) basis set : Three basis function for each k^{th} AO:

$$\phi_i = a_1\phi_k^{STO/GTO/CGTO}(r,\zeta_1) + a_2\phi_k^{STO/GTO/CGTO}(r,\zeta_2) + a_3\phi_k^{STO/GTO/CGTO}(r,\zeta_3) \tag{2.52}$$

- and so on.

According to the procedure described above, the evaluation of a typical Oxygen atom in a triple-zeta basis set requires 15 functions (3 x [1s function + 2s function + 3 * 2p function]). Now, because the inner (core) orbitals stay unaltered during any chemical interaction, we may apply the split-valence approach to reduce the computational cost even further. In the split-valence approach, the inner orbitals are pre-optimized, and just one function per AO is used, while for valence orbital AO are split (ns, np, nd, nf). With the triple-zeta basis set, Oxygen now only requires 13 functions to evaluate (1s function + 3 x [2s function + 3 x 2p function]) and the difference becomes even more substantial with increasing the atomic number.

Moreover, higher angular momentum is usually necessary to effectively account for polarization effects. The OH bond, for example, is largely characterized by the s-orbital of hydrogen and the 2s and 2p orbitals of oxygen. The electron distribution parallel to the bond will obviously differ from that perpendicular to the bond. Now, if we only consider the hydrogen atom, it is difficult to demonstrate this imbalance in the electron distribution using only s-type orbitals. However, adding a p-type orbital to the hydrogen atom may enhance the description of the OH bond (see figure [2.3]). Similarly, d-orbitals may be used to polarize p-orbitals, whereas f-orbitals can

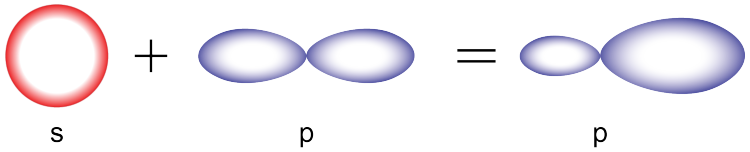

Figure 2.3: Adding p-orbital to the s-orbital to obtain polarization effects.

polarize d-orbitals, and so on, see figure [2.4].

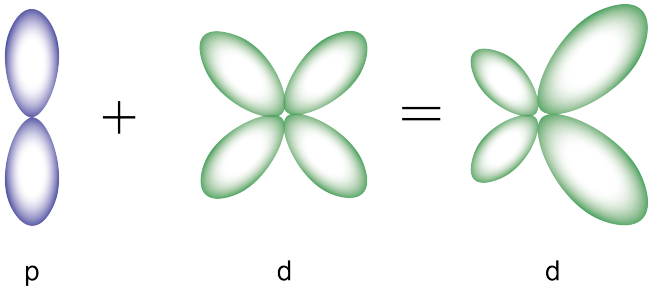

Figure 2.4: Adding d-orbital to the p-orbital to obtain polarization effects.

The addition of a polarization function to the DZ basis set using the split-valence approach yields a Double Zeta Valence Polarization (DZVP) basis set. Similarly, applying the same technique to the TZ basis set results in the Triple Zeta Valence Polarization (TZVP) basis set.

2.1.8 Pseudopotential approximation

When all electrons are used to solve the Kohn-Sham equation and when V_{ext} is built from the full coulomb potential, it makes the computation very expensive. Rapid oscillation of the wavefunction with high potential in the core region and the orthogonality across states necessitate the use of large basis set. To overcome this issue, one may declare that only the valence electrons participate in bonding while the inner electrons remain inert, allowing one to create a pseudopotential V_{pseudo} that accounts for the fixed core electrons and nucleus in an effective way (see figure [2.5]). Because the pseudo-wavefunction ψ_{pseudo} generated by this pseudopotential does not fluctuate rapidly in the core region, fewer basis sets are required, making the calculation more viable.

Furthermore, pseudopotentials are constructed in a way that they perfectly match the true coulomb potential in the valence region (see figure [2.5]). As a result, the charge density produced in the valence region is identical to the true charge density of the real system. Pseudopotentials are often built via *ab-initio* techniques. First, a real wavefunction with full coulomb potential is generated considering all electrons, and then the valence part of the wavefunction is calibrated to reduce oscillation in the core region. Finally, using this altered wavefunction (pseudowavefunction), the inverted SE equation is solved to yield the required pseudopotential.

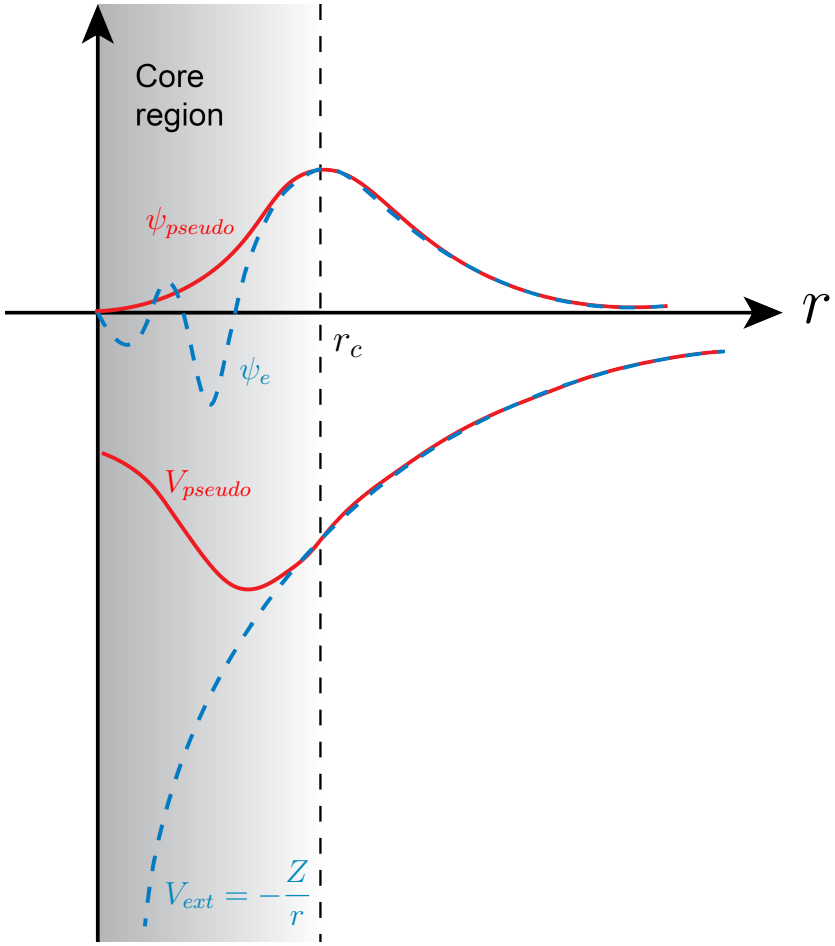

Figure 2.5: Schematic representation of all-electron potential (dashed lines) and pseudopotential (solid lines) along with their respected wavefunctions. The vertical line r_c depicts the radius value after which both potentials behave similarly.

2.2 *Ab-initio* Molecular Dynamics

Molecular Dynamics (MD) is a computer simulation scheme that allows to study the behavior of atoms and molecules at given thermodynamical conditions. In MD simulation techniques the motion of atoms/molecules is obtained by integrating their equations of motions. For a system with N particles in a simulation cell of volume V, there exist $3N$ collection of coordinates $\mathbf{r}(t)$ and $3N$ collection of momenta $\mathbf{p}(t)$ variables at a given time t in a $6N$ dimensional phase space. The goal of MD simulation is to obtain the trajectory of all particles by numerically solving Newton's equations of motion, with forces between particles and potential energies determined at each time step from DFT in the case of *ab-initio* MD.

2.2.1 Born-Oppenheimer molecular dynamics

Based on the description of Born-Oppenheimer approximation discussed in section [2.1.2] it is possible to separate nuclear and electronic DOF by assuming the adiabatic coupling operator to be zero. Thus, the equations of motion, for Born-Oppenheimer Molecular Dynamics (BOMD) at the electronic ground state are given as:

$$\begin{aligned} M_K \ddot{\mathbf{R}}_K(t) &= -\nabla_{\mathbf{R}_K} \min_{\psi_e} \{\langle \psi_e | \hat{H}_e | \psi_e \rangle\}, \\ \hat{H}_e \psi_e &= E_0 \psi_e, \end{aligned} \tag{2.53}$$

where, $\ddot{\mathbf{R}}_K(t)$ is the acceleration of particle K, M_K refers to the mass of nuclei which is assumed to be classical point particles. Thus, it is required to solve time independent SE for all the nuclear coordinates $(\mathbf{R}_1, \mathbf{R}_2, .., \mathbf{R}_M)$ from which one can calculate forces acting on each atom in order to propagate nuclei based on classical mechanics. The expression for forces acting on the atoms can be computed using the Hellmann-Feynman theorem as:

$$\mathbf{F}_k = -\nabla_{\mathbf{R}_k} \langle \psi_e | \hat{H}_e | \psi_e \rangle \tag{2.54}$$

Often, BOMD calculations are computationally expensive to perform because at each time step the Hamiltonian operator $\hat{H}_e$ is minimized by self-consistent convergence of electronic density (see flowchart in figure [2.2]). As a result, one can only afford short simulation times.

2.2.2 Car-Parrinello molecular dynamics

Car-Parrinello Molecular Dynamics (CPMD) is a method that allows reducing the computational expenses of performing molecular dynamics that includes electronic orbitals as an active DOF. The method was originally proposed by Roberto Car and Michele Parrinello [66]. In this approach, the electronic states ψ_e are treated as fictitious classical dynamical variables. The Lagrangian $\mathcal{L}_{CP}$ associated with this formalism is given by:

$$\mathcal{L}_{CP} = \underbrace{\sum_I^M \frac{m_I}{2} \dot{\mathbf{R}}_I^2 + \sum_i \mu \langle \dot{\phi}_i | \dot{\phi}_i \rangle}_{\text{kinetic energy}} - \underbrace{\langle \psi_e | \hat{H}_e | \psi_e \rangle}_{\text{potential energy}} + \underbrace{\sum_{ij} \lambda_{ij} (\mu \langle \phi_i | \phi_j \rangle - \delta_{ij})}_{\text{orthogonality constraint}}, \tag{2.55}$$

where, the second term represents kinetic energy of the fictitious electronic variables with fictitious mass μ and λ_{ij} in the last term are the lagrange multipliers that allows to ensure the orthonormality constraint of the Kohn-Sham orbitals. Further, one can use the Euler-Lagrange

equations to obtain the Newton's equations of motion:

$$\begin{aligned} \frac{d}{dt}\frac{\partial \mathcal{L}}{\partial \dot{\mathbf{R}}_I} &= \frac{\partial \mathcal{L}}{\partial \mathbf{R}_I}, \\ \frac{d}{dt}\frac{\partial \mathcal{L}}{\partial \dot{\phi}_i^*} &= \frac{\partial \mathcal{L}}{\partial \phi_i^*}, \end{aligned} \tag{2.56}$$

which gives:

$$\begin{aligned} m_I \ddot{\mathbf{R}}_I(t) &= -\frac{\partial}{\partial \mathbf{R}_I}\langle \psi_e | \hat{H}_e | \psi_e \rangle, \\ \mu \ddot{\phi}_i(t) &= -\frac{\delta}{\delta \phi_i^*}\langle \psi_e | \hat{H}_e | \psi_e \rangle + \frac{\delta}{\delta \phi_i^*}\{constraints\}. \end{aligned} \tag{2.57}$$

The first part in equation [2.57] describes the dynamics of ions at temperature $T_i \propto \sum_I m_I \dot{\mathbf{R}}_I^2$ while the second part governs the fictitious electronic motion and its evolution at fictitious temperature $T_e \propto \sum_i \mu \langle \dot{\phi} | \dot{\phi} \rangle$. In this framework, if the fictitious electronic temperature is small enough and the initial configuration wave functions are optimized to their ground state, the electronic subsystem will remain close to its instantaneous minimum energy (minimum of the Born-Oppenheimer energy surface) during the ions dynamical evolution as sketched in figure [2.6].

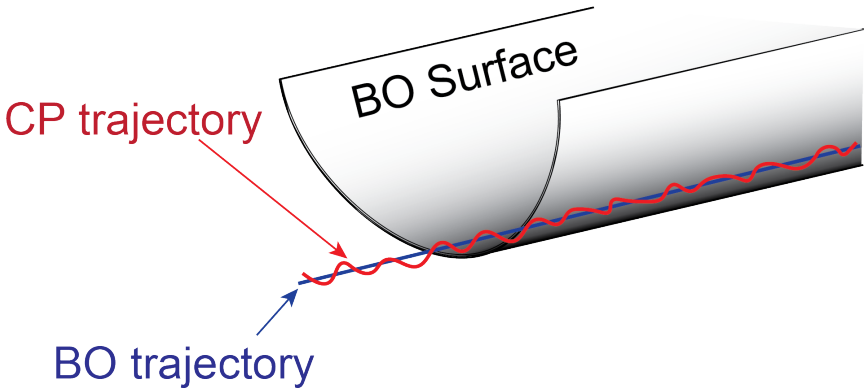

Figure 2.6: Sketch representation of Born-Oppenheimer MD and Car-Parrinello MD trajectory spanned along Born-Oppenheimer potential energy surface.

2.2.3 Temperature control

2.2.3.1 Temperature in the NVE ensemble

The temperature is a macroscopic thermodynamical property, and its instantaneous value depends on the kinetic energy via the particles momenta as follows:

$$\sum_{i=1}^{N} \frac{|\mathbf{p}_i|^2}{2m_i} = \frac{k_B T}{2}(3N - k) \tag{2.58}$$

where k_B and k is the Boltzmann constant and number of constraints respectively, and $3N - k = N_{df}$ refers to the DOF of the system. The average temperature <T> is identical to the macroscopic temperature.

2.2.3.2 Temperature in the NVT ensemble

In real world applications, the microcanonical ensemble does not correspond to the conditions under which most experiments are performed. In order to study the properties of the system at a specific temperature, MD simulation within the NVT ensemble, and using a thermostat is most suited.

Velocity rescaling

An obvious method to change the temperature of the system is to rescale the velocities of the particles in the system by multiplying them by a factor λ. The associated change in temperature ΔT can be evaluated as:

$$\begin{aligned} \Delta T &= \frac{1}{2}\sum_{i=1}^{N} 2\frac{m_i(\lambda v_i)^2}{N_{df}k_B} - \frac{1}{2}\sum_{i=1}^{N} 2\frac{m_i v_i^2}{N_{df}k_B} \\ &= (\lambda^2 - 1)T(t), \\ \lambda &= \sqrt{\frac{T_0}{T(t)}}. \end{aligned} \tag{2.59}$$

where, the temperature $T(t)$ is defined at time t and T_0 is the desired temperature. Now the factor λ can be used to multiply the velocities at each time-step to control the temperature. Despite its simplicity, the method does not allow fluctuations in the temperature consistent with the Boltzmann distribution.

Berendsen thermostat

To keep the temperature stable, the system is coupled to an external heat bath with a constant temperature T_0. At each time-step, velocities are rescaled so that the rate of temperature change

is proportional to the temperature difference, as:

$$\frac{dT(t)}{dt} = \frac{1}{\tau}(T_0 - T(t)), \tag{2.60}$$

where τ is an empirical parameter that governs the strength of coupling of the heat bath to the system. This equation depicts the exponential decay of the system towards the desired temperature. The temperature change ΔT from equation [2.60] can be represented as:

$$\Delta T = \frac{\delta t}{\tau}(T_0 - T(t)). \tag{2.61}$$

Thus, the above equation leads to the scaling factor:

$$\lambda^2 = 1 + \frac{\delta t}{\tau}\left(\frac{T_0}{T} - 1\right), \tag{2.62}$$

here, τ has the units of frequency, and its value should be carefully chosen, since $\tau \to 0$ results in unrealistically low temperature fluctuations, whilst $\tau \to \infty$ leaves the thermostat inactive, and the simulation is relegated to sampling the microcanonical ensemble. In the latter situation, temperature fluctuations will rise until it approaches the appropriate value of the microcanonical ensemble, but it will not reach the required canonical ensemble value. Furthermore, if τ is set to δt, then the Berendsen thermostat behaves identically to a velocity re-scaling system, see section [2.2.3.2].

Nosé-Hoover thermostat

In order, to make the system evolve at the target temperature, Berendsen thermostat has proved to be extremely efficient, however it does not produce the canonical ensemble, thus it is more relevant to have a formalism with a correct canonical sampling. In order to resolve these shortcomings, Nosé and Hoover [67]–[69] developed the idea of extended systems with additional artificial coordinates and velocities where the heat bath was considered as an integral part of the system. Let's assume that the system consists of N particles with coordinates $\mathbf{r}_i$, momenta $\mathbf{p}_i$, masses m_i and potential energy $E(\mathbf{r})$ (DFT energy, see equation [2.41]). In addition, additional degrees of freedom with artificial variable s, velocity $\dot{s}$ with associated effective mass $Q > 0$ are introduced where the magnitude of Q controls the coupling between the heat bath and the real system in order to regulate the temperature. Here, we also introduce the virtual variables (coordinates $\mathbf{r}_i^{'}$, momenta $\mathbf{p}_i^{'}$ and time $t^{'}$), which relates to the real system ($\mathbf{r}_i$, $\mathbf{p}_i$, t) as:

$$dt^{'} = sdt; \qquad \mathbf{r}_i^{'} = \mathbf{r}_i; \qquad s^{'} = s; \qquad \mathbf{p}_i^{'} = s\mathbf{p}_i, \tag{2.63}$$

because the atomic coordinates remain unchanged in extended coordinates, here we can think of the artificial coordinate s playing the role of a time-scaling parameter as it stretches the timescale in extended system by the factor of s (see Ref. [70]). The velocities transformation is expressed as:

$$\dot{\mathbf{r}}_i \equiv \frac{d\mathbf{r}_i}{dt} = s\frac{d\mathbf{r}_i}{dt'} = s\frac{d\mathbf{r}_i^{'}}{dt'} \equiv s\dot{\mathbf{r}}_i^{'}, \tag{2.64}$$

The Lagrangian $\mathcal{L}$ of the extended system with respect to equations [2.63] and [2.64] is chosen to be:

$$\mathcal{L} = \sum_i^N \frac{m_i}{2} s^2 \dot{\mathbf{r}}_i^{'2} - E(\mathbf{r}^{'}) + \frac{Q}{2}\dot{s}^2 - N_{df} k_B T \ln(s). \tag{2.65}$$

The first two terms in the above equation represent the kinetic and potential energy of the real system. The latter two terms denote the kinetic energy of s and the potential energy which is chosen in such a way that the formalism produces the canonical ensemble. This leads to the following equations of motion:

$$\ddot{\mathbf{r}}_i^{'} = \frac{\mathbf{F}_i^{'}}{m_i s^2} - \frac{2\dot{s}\dot{\mathbf{r}}_i^{'}}{s}, \tag{2.66}$$

$$\ddot{s} = \frac{1}{Qs}\left(\sum_i^N m_i s^2 \dot{\mathbf{r}}_i^{'2} - g k_B T_0\right), \tag{2.67}$$

where T_0 is the target temperature. These equations represent the microcanonical ensemble of the extended system. However, the energy of the real system is not constant as there is constant exchange of heat between the heat bath and the real system in order to maintain the real system temperature.

Now as with the case of Berendsen thermostat (see section [2.2.3.2]), Q in Nosé-Hoover formalism is chosen carefully, as with $Q \to \infty$ it will take long time to achieve canonical sampling due to the very long energy transfer time while with $Q \to 0$, unrealistic high frequency temperature fluctuations may occur.

2.3 Wannier functions

Wannier functions are a complete set of orthogonal functions built in a way that they allow one to obtain an in-depth understanding of the nature of the bonding present in the material. The

translation invariance of the Kohn-Sham orbital can be extended to periodic boundary conditions with the help of Bloch theorem. The Kohn-Sham orbital using Bloch theorem can be expressed as:

$$\psi_{n,\mathbf{k}}(\mathbf{r}+\mathbf{R}) = e^{i\mathbf{kR}}\psi_{n,\mathbf{k}}(\mathbf{r}), \tag{2.68}$$

where $\mathbf{R}$ is the lattice vector, k is a wavevector and n is a band index. The above equation is equivalent to:

$$\psi_{n,\mathbf{k}}(\mathbf{r}) = e^{i\mathbf{kr}}u_{n,\mathbf{k}}(\mathbf{r}), \tag{2.69}$$

where $u_{n,\mathbf{k}}(\mathbf{r})$ is lattice periodic function which satisfies $u_{n,\mathbf{k}}(\mathbf{r}) = u_{n,\mathbf{k}}(\mathbf{r}+\mathbf{R})$. Under the transformation $\mathbf{k}^{'} \rightarrow \mathbf{k}+\mathbf{G}$ with $\mathbf{G}$ as a reciprocal lattice vector in $u_{n,\mathbf{k}}(\mathbf{r})$, equations [2.68] and [2.69] can be shown to follow the relation:

$$u_{n,\mathbf{k}'} = u_{n,\mathbf{k}}e^{-i\mathbf{Gr}}, \tag{2.70}$$

thus, due to the presence of phase dependent term in the equation [2.70], there exist a gauge freedom in its choice.

The Kohn-Sham orbital is not well localized, however using a unitary and inverse Fourier transformation one can expand these orbitals into localized orbitals called Wannier functions $w_n(\mathbf{r}-\mathbf{R})$ as follows:

$$w_n(\mathbf{r}-\mathbf{R}) \equiv |\mathbf{R}n\rangle = \frac{V}{(2\pi)^3}\int_{\Gamma\text{-point}} \psi_{n,\mathbf{k}}(\mathbf{r})e^{-i\mathbf{kR}}d\mathbf{k}, \tag{2.71}$$

where, V is the volume of the primitive cell in real space. The above integration is only performed at Γ-point of the Brillouin zone in the case of amorphous and large systems.

Maximally Localized Wannier Function

One property that makes the use of wannier function really important is the possibility to compute Maximally-Localized Wannier Function (MLWF). The average value of the position operator ($\hat{\mathbf{r}} = -i\hbar\nabla_{\mathbf{k}}$) using equation [2.69] in the new wannier function basis set is given by:

$$\langle\mathbf{r}\rangle = \langle\mathbf{R}n|\hat{\mathbf{r}}|\mathbf{0}m\rangle = i\frac{V}{(2\pi)^3}\int d\mathbf{k}e^{i\mathbf{kR}}\langle u_{n,k}|\nabla_{\mathbf{k}}|u_{m,k}\rangle, \tag{2.72}$$

where $|\mathbf{0}m\rangle$ is the Wannier function at "home" unit cell. Similarly, the second order position operator $\hat{\mathbf{r}}^2$ can be written as:

$$\langle r^2\rangle = \langle \mathbf{R}n|\hat{r}^2|\mathbf{0}m\rangle = -\frac{V}{(2\pi)^3}\int d\mathbf{k}e^{i\mathbf{kR}}\langle u_{n,k}|\nabla^2_{\mathbf{k}}|u_{m,k}\rangle, \tag{2.73}$$

Now, based on equations [2.72] and [2.73] we define new notations as $\langle \mathbf{r}\rangle_n = \langle \mathbf{0}n|\hat{\mathbf{r}}|\mathbf{0}n\rangle$ and $\langle r^2\rangle_n = \langle \mathbf{0}n|\hat{r}^2|\mathbf{0}n\rangle$ and using them to construct a functional Ω, called spread, given by:

$$\Omega = \sum_n [\langle r^2\rangle_n - \langle \mathbf{r}\rangle_n^2]. \tag{2.74}$$

Thus, in order to achieve the MLWF we minimize the equation [2.74] with respect to the unitary transformation. Further, we compute Wannier function center (WFC) which allows to characterize the chemical bond between two atoms. The exact procedure is described in Ref. [71].

2.4 Charge Analysis

For performing charge analysis, the density-derived electrostatic and chemical partitioning approach (DDEC6) [72]–[75] as employed in CHARGEMOL package [76] has been utilized. The total electron density $\rho^{\text{tot}}(r)$ in the charge partitioning approach is divided into atomic contributions $\rho_A(r)$ at each spatial point using spherically symmetric weighting functions $w_A(r)$ constructed from reference ions:

$$\rho_A(r) = \rho^{tot}(r)\frac{w_A(r)}{\sum_i w_i(r)}, \tag{2.75}$$

Consequently, by integrating the atomic contribution throughout the whole space, the net atomic charges (NACs) (q_A) on atom A are determined as follows:

$$q_A = Z_A - \int \rho_A(r)dr, \tag{2.76}$$

where Z_A is the atomic number of atom A (nuclear charge). Further performing electronic structure minimization to get the total electron density at the PBE0 level of theory is recommended to achieve better accuracy in approximating partial charges on atom. Generally, in *ab-initio* simulation, pseudopotentials are employed instead of core electrons, therefore, DDEC scheme substitutes the core electrons with effective core potentials in the computation of $\rho_A(r)$ before DDEC6 partitioning.

Fundamentally, DDEC6 charge partitioning utilizes the distributed multipole expansion essentially to reproduce electrostatic potentials outside the electron distribution by partitioning the total

electron density at each place in space across atoms in such a fashion that precisely one electron distribution is allocated to each atom. We point out that the DDEC6 approach only depends on the overall electron distribution, making it a basis set independent strategy. Therefore, this technique, gives us an independent technique to evaluate the short-range order in terms of electronic structure, free of empirical parameters. It has been demonstrated that using this technique, transferable net atomic charges (NAC) may be produced while maintaining chemical consistency with the prescribed atomic spin moments and Pauling scale electronegativity tendencies.

2.5 CP2K code

All the DFT and MD simulations performed in this thesis have been carried out using the CP2K package, unless stated otherwise. One of the major issues with DFT is the high computational cost of orthogonalizing the wavefunction and computing the Hartree energy (E_H) that does not scale linearly with system size (see equation [2.31]), hence CP2K was chosen because of its efficient and scalable DFT implementation that enables simulation of larger systems. QUICKSTEP [77] is one of widely regarded methods of CP2K suite of programs, also known as Gaussian and plane waves (GPW) method in which for solving the Kohn-Sham equations, the wavefunctions (Kohn-Sham orbitals) are expanded using atom centered Gaussian basis together with an auxiliary basis of plane wave for the expansion of the electronic density. Due to their localized nature, compactness (finite extend) and possible analytical solutions available, Gaussian functions are efficient and fairly straightforward to compute. Further, the use of plane waves on regular grids allows for efficient computation of Hartree energy (E_H) as one may make use of the effectiveness of Fast Fourier Transform (FFT) methods (especially in the case of periodic boundary conditions). As a result, the Kohn-Sham matrix (and total energy) can be computed in quasi-linear scaling [the FFT is $\mathcal{O}(n \times \log(n))$] and so can easily scale to thousands of atoms/electrons. Furthermore, the use of Goedecker-Teter-Hutter (GTH) pseudopotentials have shown high accuracy when employed in conjugation with GPW method [77]–[79]. An alternative to the conventional diagonalization method during self-consistent field (SCF), CP2K additionally employs the orbital transformation (OT) [80] method to orthogonalize the wavefunction in QUICKSTEP method. Implementing OT and QUICKSTEP method enables CP2K to have outstanding efficiency and ability to simulate massive systems within the DFT framework. Additionally, CP2K has been effectively optimized for the supercomputer by being parallelized using MPI and OpenMP [81]. The typical input file for performing quantum mechanical calculations using CP2K package will be provided in the appendix [A.6].

2.6 *Ab-initio* principles of calculating NLO properties and Raman spectra

The study of Raman spectra allows one to understand the fingerprints of various structural fragments within a material. In addition, studying the material's non-linear optical properties is essential for its application in frequency conversion mechanisms, Raman amplifications etc. Today, DFT is regarded as the de facto approach in materials science for studying the electronic and structural properties of materials. Principally, utilizing perturbation theory in conjugation with DFT enables the computation of derivatives of energy and its associated thermodynamical potentials up to any order. In the forthcoming subsections we present the general framework of the computation of simulated Raman spectra and non-linear optical properties using density functional perturbation theory and finite difference method.

2.6.1 Optical properties

When an atom or a molecule is subjected to an electric field **E**, the positively charged ion/nucleus is shifted in the direction of the field, while the negatively charged ion/electron is shifted in the opposite direction. As a result, their centers of charge no longer coincide, and a new electric field $\mathbf{E}_{ind}$ is induced, which resists the separation and helps in achieving equilibrium. The measure of this resistance is given by the dipole moment $\boldsymbol{\mu}$ and for small value of **E**, it is defined as:

$$\boldsymbol{\mu} = \alpha \mathbf{E}, \tag{2.77}$$

here, α is called polarizability and it is a second rank tensor.

However, we never deal with isolated atoms or molecules in the macroscopic world, therefore the quantity we are interested in is the dipole moment per unit volume, which is known as polarization **P** as:

$$\mathbf{P} = \boldsymbol{\mu}/V. \tag{2.78}$$

In the case of linear optics, we assume that the applied electric field is not too strong, thus polarized atoms have the ability to restore to their original positions once the electric field is turned off. Under this premise similar to equation [2.77], we can express polarization **P** as:

$$\mathbf{P} = \epsilon_0 \chi_e \mathbf{E}, \tag{2.79}$$

the proportionality constant, χ_e, is known as the electric susceptibility tensor of the medium and ϵ_0 being the permittivity of vacuum.

Non-linear Polarization

Further, in non-linear optics, equation [2.77] for dipole moment can be further generalized to strong applied electric field **E** using power series expansion as:

$$\mu_i = \alpha_{ij}E_j + \frac{1}{2!}\beta_{ijk}E_jE_k + \frac{1}{3!}\gamma_{ijkl}E_jE_kE_l, \tag{2.80}$$

where α, β, and γ are polarizability, second order third rank and third order fourth rank hyperpolarizabilities tensors respectively and E is the applied electric field along a given direction of the space. Differentiating Eq. [2.80] with respect to the electric field yields:

$$\alpha_{ij} = \frac{\partial \mu_i}{\partial E_j} - \beta_{ijk}E_k - \frac{1}{2}\gamma_{ijkl}E_kE_l. \tag{2.81}$$

where, the $\frac{\partial \mu_i}{\partial E_j}$ term is the polarizability at zero electric field. Similarly, we can express the Polarization **P** as a power series expansion of the field strength **E** as:

$$\mathbf{P} = \epsilon_0 \left[\chi_e^{(1)}\mathbf{E} + \chi_e^{(2)}\mathbf{E}^2 + \chi_e^{(3)}\mathbf{E}^3 + ...\right], \tag{2.82}$$

where $\chi_e^{(1)}$ denotes linear susceptibility, $\chi_e^{(2)}$ and $\chi_e^{(3)}$ are the second order third rank and third order fourth rank non-linear optical susceptibility tensors, respectively. For simplicity, we drop the subscript "e" notation from susceptibility symbol. The first-order second rank linear susceptibility can be deduced via the following equation:

$$\chi^{(1)} = \frac{4\pi}{V}\bar{\alpha}, \tag{2.83}$$

where $\bar{\alpha}$ is the isotropic average of the polarizability tensor at zero electric field and V is the volume of the simulation cell. Further, one can use $\chi^{(1)}$ to compute the linear refractive index of the system (n) as:

$$n = \sqrt{1 + \chi^{(1)}} \tag{2.84}$$

The β_{ijk} is related to the second-order nonlinear susceptibility $\chi^{(2)}$ and is zero for centrosymmetric systems. Finally, γ_{ijkl} is linked to the third order-order nonlinear susceptibility $\chi^{(3)}$ as follows:

$$\chi_{ijkl}^{(3)} = \frac{2\pi}{3V}\gamma_{ijkl}. \tag{2.85}$$

Based on these definitions one can compute the non-linear optical properties of a given material based on a DFT and finite different approach. Workflows for computing non-linear properties are provided in Appendix [A.4].

2.6.2 Raman spectra

Raman spectroscopy is a class of vibrational spectroscopy in which light is used to produce (excite) molecular vibration. Inelastic scattering of light causes the incident photon (frequency ω_i) to either lose energy $\hbar\omega_s = \hbar\omega_i - \hbar\omega_p$ (Stokes scattering) or gain energy $\hbar\omega_s = \hbar\omega_i + \hbar\omega_p$ (Anti-Stokes scattering) after the scattering, where ω_s and ω_p is the frequency of scattered light and phonon respectively. These phonons are fundamental vibration motions induced by the collective excitation of atoms or molecules in a periodic and elastic arrangement. It corresponds to a lattice of atoms or molecules vibrating evenly at a single frequency. This frequency is classically known as the normal mode frequency, and it is crucial because the lattice vibrations can be expressed as a superposition of these basic vibrations. Microscopically, Raman scattering is caused by photon-phonon interaction, and its intensity is defined by the change in polarizability with respect to atomic displacement corresponding to a certain vibration mode.

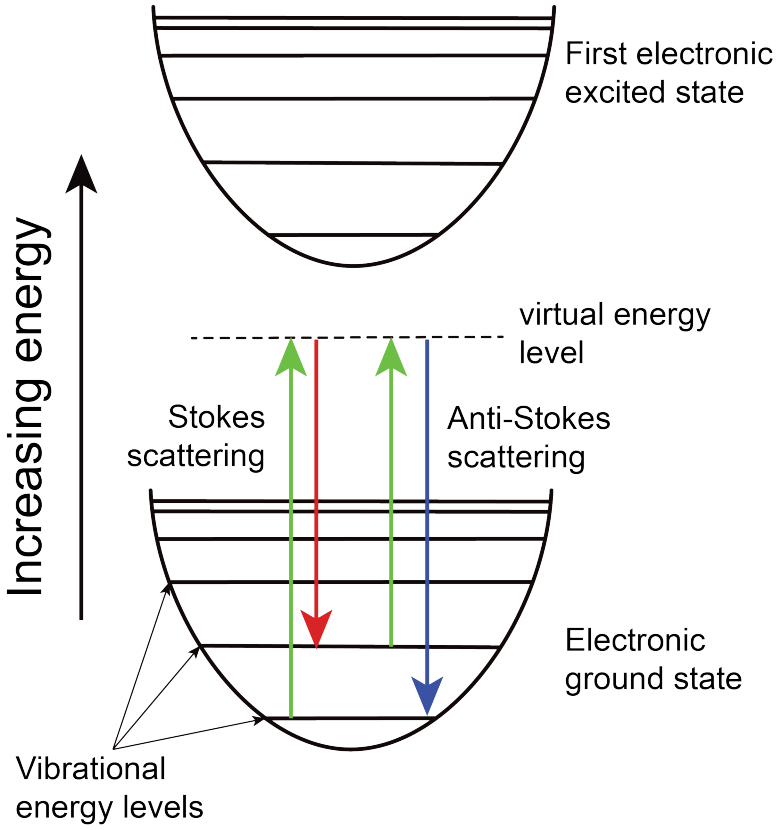

Figure 2.7: Illustration of excitation and de-excitation in energy levels using Stokes and Anti-stokes scattering in Raman Spectroscopy.

2.6.2.1 Vibrational analysis

Typically, the harmonic oscillation model under the Born-Oppenheimer approximation is used to compute normal modes and thus Raman spectra. If the molecule is in equilibrium, it will be at the lowest position (at least locally) on the Potential energy surface (PES). The cross-section of the PES profile around this position may therefore be considered to be approximately parabolic, such that the second derivative of energy with respect to a nuclear coordinate can be regarded as a force constant for the harmonic oscillation of an atom along this coordinate. As molecular vibrations are polyatomic i.e. include many atoms moving at the same time, this harmonic oscillator model may be extrapolated to multiple nuclear coordinates. In addition, the N nuclear coordinate harmonic oscillator can further be considered as 3N-independent harmonic oscillators, whose frequency are those of 3N classical normal modes.

This system may be described in two ways: in terms of phonon modes or in terms of normal modes. In phonon mode description, acoustic and optical phonons are the two types of phonons. The acoustic phonon has zero frequency vibration in the Brillouin zone's Γ-point and may be regarded as an ensemble movement of all the atoms in one direction, but the optical phonon has a high frequency and can interact with light at the Γ-point.

For describing normal modes, let's assume that each atom with Latin indices I is displaced from its position at R_I along the displacement pattern U_I^α, here Greek indices refer to cartesian components. The normal mode frequencies are calculated using:

$$\sum_{J,\beta}(C_{I,J}^{\alpha,\beta} - M_I\omega_p^2\delta_{\alpha\beta}\delta_{IJ})U_J^\beta = 0, \tag{2.86}$$

where, M_I is the mass of atom I and $C_{I,J}^{\alpha,\beta}$ is the force constant (Hessian) matrix represented by:

$$C_{I,J}^{\alpha,\beta}(R^\alpha - R^\beta) = \frac{\partial^2\mathcal{E}(\{R\})}{\partial R_I^\alpha \partial R_J^\beta}. \tag{2.87}$$

The description of Hessian matrix in reciprocal space is known as the dynamical matrix:

$$\tilde{C}_{IJ}^{\alpha\beta}(q) \equiv \sum_R e^{-iq.R}C_{IJ}^{\alpha\beta}(R) = \frac{1}{N_R}\frac{\partial^2\mathcal{E}}{\partial U_I^\alpha(q)U_J^\beta(q)}. \tag{2.88}$$

Thus, equation of motion [2.86] can be rewritten using [2.88] as:

$$\sum_{J,\beta} U_J^\beta(q)\tilde{C}_{IJ}^{\alpha\beta}(q) = M_I\omega_p^2(q)U_I^\beta(q). \tag{2.89}$$

Further, $\tilde{C}_{IJ}^{\alpha\beta}(q)$ can be diagonalized to obtain eigenvalues $\omega_p(q)$ and eigenvectors U_I^{α}.

2.6.2.2 Raman tensor

At the Γ-point in Brillouin zone, vibrational mode frequency determines the peak positions in Raman spectrum. Peak intensities in non resonant scattering process is calculated using Placzek approximation [82]. The intensity of the mth vibration mode in the Stokes process is given by:

$$I_m = \frac{(\omega_i - \omega_m)^4}{\omega_m} |e_i.A^m.e_s|^2 (n(\omega_m) + 1), \tag{2.90}$$

here e_s and e_i are the unit polarization vectors of the scattered and incident radiation, respectively. ω_m is the frequency of the phonon mode, $n(\omega_m)$ is the Bose-Einstein distribution given by

$$n(\omega_m) = \frac{1}{e^{\hbar\omega_m/k_BT} - 1}, \tag{2.91}$$

and

$$A_{ij}^m = \sqrt{V} \sum_{\alpha\beta} \frac{\partial \chi_{ij}^{(1)}}{\partial r_{\alpha\beta}} U_{\alpha\beta}^m, \tag{2.92}$$

is known as the Raman tensor with V being the cell volume [83]. The polarizability tensor term $\chi_{ij}^{(1)}$ can be calculated using linear response theory by determining the change of electric polarization **P** with respect to electric field **E** as:

$$\chi_{ij}^{(1)} = \frac{\partial P_i}{\partial E_j} = \frac{\partial^2 \mathcal{E}_{tot}}{\partial E_i \partial E_j}, \tag{2.93}$$

where, $\mathcal{E}_{tot}$ is the total energy of the system. We use finite difference approach to compute equation [2.93]. We note that in case of amorphous sample, the following rotational invariants [84] can be used:

$$\zeta_i = \frac{1}{3} \left(\alpha_{xx}^i + \alpha_{yy}^i + \alpha_{zz}^i \right), \tag{2.94}$$

$$\begin{aligned} \gamma_i^2 = \tfrac{1}{2} \left[(\alpha_{xx}^i - \alpha_{yy}^i)^2 + (\alpha_{yy}^i - \alpha_{zz}^i)^2 + (\alpha_{xx}^i - \alpha_{zz}^i)^2 \right] + \\ + \tfrac{3}{4} \left[(\alpha_{xy}^i + \alpha_{yx}^i)^2 + (\alpha_{xz}^i + \alpha_{zx}^i)^2 + (\alpha_{yz}^i + \alpha_{zy}^i)^2 \right], \end{aligned} \tag{2.95}$$

to express the intensity of the Raman bands for parallel and crossed polarization as:

$$\begin{aligned} I_i^{\perp} &= \frac{(\omega_L - \omega_i)^4}{\omega_i} [n(\omega_i) + 1] \frac{\gamma_i^2}{15}, \\ I_i^{\parallel} &= \frac{(\omega_L - \omega_i)^4}{\omega_i} [n(\omega_i) + 1] \frac{45\zeta_i^2 + 4\gamma_i^2}{45}. \end{aligned} \tag{2.96}$$

The total unpolarized Raman activity is a sum of both invariants $I_i^{tot} = I_i^{\parallel} + I_i^{\perp}$. Finally, the Raman intensity is calculated according to equation [2.96] where each peak of the simulated spectra is obtained as a sum of Lorentzians peaks constructed using the Raman activity of each vibrational mode with fixed half-width. In order to compute the Raman spectra for amorphous glasses at the DFT level of theory, we interface the CP2K code [77] with finite difference method. Codes and workflows used to achieve these calculations are available in Appendix [A.7]

3

The structure of glassy and molten TeO_2

Summary

3.1 Generation and validation of the TeO_2 glass and melt models **96**
3.1.1 Methodology 96
3.1.2 Glass and melt models 98
3.2 Structural analysis **106**
3.2.1 Partial pair distribution function 106
3.2.2 Coordination number 107
3.2.3 Local environment and short-range disorder 113
3.2.4 Charge Analysis 117
3.2.5 Electronic localization function 118
3.2.6 Efficiency of hybrid functional on electronic localization 120
3.3 Conclusions **121**

THE structure of TeO_2 crystals is dominated by almost regular TeO_4 disphenoids with tellurium coordination number equal to 4, however, the structural unit becomes much more convoluted in the amorphous state. Several pieces of research on the presence of terminal oxygens in TeO_2 glassy network has been accomplished in the last two decades. Apart from TeO_4 units, several other coordination states of tellurium atoms with significant concentration have been reported in the literature (see chapter [1]). There is currently no consensus about the existence of NBO atoms (terminal Te=O groups) in the pure TeO_2 glass. Even the precise value of the average tellurium coordination number, which can indicate the presence of terminal oxygen atoms (if smaller than four), is still up for contention in the community. Understanding the structural network and the coordination numbers in the pure TeO_2 glass is critical since it relates to the origin of the material's high non-linear index [85]. The electronic lone pair $(5s^2)$ of the tellurium atom when linked to oxygen has long been thought to be the source of these properties [86]. Recent research indicate that these features are, in large part, caused by the structure of the glass itself, particularly the type of the Te-O-Te bridge [87]. Therefore, in this chapter, we study various *ab-initio* setups to achieve the best possible structural model based on which we analyze the atomic-scale structure.

3.1 Generation and validation of the TeO_2 glass and melt models

3.1.1 Methodology

In order to characterize glassy and melt phases of TeO_2 models we resort to several *ab-initio* approaches employing different modelling methodologies. The following sections provide a detailed explanation of each approach.

Born-Oppenheimer molecular dynamics

Under this scheme, the electronic structure is minimized under the framework of DFT using the Quickstep module of CP2K software package [77]. Atom-centered TZVP type basis set [88] is used to describe the wavefunction while the expansion of electronic density is in terms of plane-wave basis set as implement in CP2K. The Gaussian Plane Wave (GPW) approach has shown to be effective for simulating large, dense systems like liquids and solids. In this study, the GTH pseudopotential [79] are used together with GGA (PBE [89], Becke-Lee-Yang-Parr (BLYP) [90], [91]) or PBE0 hybrid functional [92], [93].

The plane-wave cutoff for the representation of the electronic density is set to 500 Ry and the relative cutoff to 50 Ry in our study. The velocity Verlet technique is used to time propagate the atomic coordinates with a timestep of 1 fs. Additionally, the temperature of the system is controlled with a Nosé-Hover thermostat [67]–[69].

Car-Parrinello molecular dynamics

DFT under the GGA approximation was used in the description of the electronic structure. Particularly, two GGA functionals namely PBE [89] and BLYP [90], [91] were utilized. In the simulation cell, valence electrons are addressed explicitly and represented by an expansion of a plane-wave basis set with an energy cutoff of 80 Ry. The norm-conserving pseudopotential of Troullier-Martins type [94] are used to characterize the interactions between the valence and core electrons. The CPMD computer code's [95] implementation of molecular dynamics within the scheme of Car-Parrinello [96] was used. The integration of the equations of motion is performed with a fictitious electron mass of 500 a.u. and a time step of 0.12 fs, ensuring a good control of conserved quantities. A Nosé-Hoover thermostat [67]–[69] was used to control the temperature of both ionic and electronic degrees of freedom.

Second generation Car-Parrinello molecular dynamics

In order to reach long simulation timescale at a reasonable computational cost, we resort to the Second Generation Car-Parrinello molecular dynamics (SGCPMD) as implemented in the CP2K suite of programs [97]. Similar to CPMD, wavefunction optimization are avoided during the dynamics while allowing for the use of large integration time steps, which are of the order of BOMD. Moreover, we used a similar DFT setup to that of BOMD. The following equation governs the slightly dissipative Langevin-type dynamics produced by this scheme:

$$M_I \ddot{R}_I = F_{BO} - (\gamma_D + \gamma_L)\dot{R}_I + \Xi_I, \tag{3.1}$$

where R_I, M_I and F_{BO} are the ionic coordinates, particle mass and the Born-Oppenheimer forces, respectively. γ_L, γ_D and Ξ_I are the Langevin friction, intrinsic coefficients and a random noise term, respectively. Even though the Langevin dynamics is dissipative, reliable canonical sampling may be accomplished by properly selecting the friction coefficients in a way that forces the noise to obey to the fluctuation dissipation theorem [97]: $\langle \Xi(0)\Xi(t) \rangle = 6(\gamma_D + \gamma_L) M_I k_B T \delta(t)$. Additionally, the values of γ_L and γ_D were set to 0.1 fs^{-1} and 0.0005 fs^{-1}, respectively, for temperatures between 1000 K and 500 K and to 0.0007 fs^{-1} and 0.1 fs^{-1}, respectively, for temperatures below 500 K.

Pair distribution function

The quality of all the generated models is assessed by comparing the PDF computed from the models to those obtained experimentally using X-ray diffraction techniques. The PDF method is indeed the main and powerful method for accessing the short and medium range orders in amorphous materials. It provides the probability of finding two particles at a given distance in the system, and therefore the system's structural information. $g(r)$ is defined as:

$$g(r) = \frac{1}{4\pi\rho_0 r^2 N} \sum_i \sum_{i \neq j} \delta(r - r_{ij}), \tag{3.2}$$

where, ρ_0 is the average number density and N is the total number of atoms in the simulation cell. The distance between two atoms i and j is r_{ij}, and $\delta(r - r_{ij})$ is the Dirac delta function. In this work, we use the total reduced PDF $G(r)$, defined as:

$$G(r) = 4\pi r \rho_0 [g(r) - 1], \tag{3.3}$$

It can be directly obtained from the measured experimental structure factor/function $S(Q)$ via its Fourier transform as:

$$G(r) = \frac{2}{\pi} \int_0^{Q_{max}} Q[S(Q) - 1] sin(Qr) dQ, \tag{3.4}$$

where Q_{max} is the upper limit of momentum transfer that can be experimentally probed in a measurement.

3.1.2 Glass and melt models

The glassy phase of TeO_2 was produced by quenching the melt state. Several DFT setups with varied model sizes, thermal histories and quenching protocols have been tested in order to acquire an accurate description of the glass. In particular, seven models with varying DFT setups (see table [3.1]) were produced as follows: **Model 1** (CPMD-PBE-270), is made out of 270 atoms (90 Te and 180 O) in a periodic cubic box of 16.23 Å side length corresponding to the experimental density of 5.57 g.cm^{-3} [31]. Starting from a random initial configuration, the system followed a melt-quench thermal cycle using the CPMD method as follows: 5 ps at T = 300 K, 5 ps at T = 600 K, 45 ps at T = 1000 K, 30 ps at T = 600 K and 30 ps at T = 300 K. Both Te and O showed a significant diffusion coefficient (D_{Te} = 3.45×10^{-6} cm^2/s and D_O = 9.12×10^{-6} cm^2/s) at the melting temperature of 1000 K thereby ensuring a complete decorrelation from the initial random configuration. **Model 2** (CPMD-BLYP-270), was produced adopting a similar setup as in the case of Model 1 except the use of the BLYP XC functional. **Model 3** (CPMD-BLYP-480), is a 480 atoms model (160 Te and 320 O) at the experimental density. The glass phase was

produced using CPMD and BLYP XC functional after a thermal cycle as follows: 9 ps at T = 300 K, 8 ps at T = 600 K, 30 ps at T = 1000 K, 25 ps at T = 600 K and 20 ps at T = 300 K. The starting point of **Model 4** (CP2K-BLYP-480), is the last configuration of Model 3 at 1000 K that was annealed for a further 15 ps at the same temperature using CP2K and BLYP XC functional. The system was then quenched to produce the glass in two steps: 14 ps at T = 600 K, and 10 ps at T = 300 K. **Model 5** (SGCPMD-PBE-270), was produced through the second generation Car-Parrinello molecular dynamics and PBE XC functional on a 270 atoms system at the experimental density. A long quenching protocol was adopted for this model and features 370 ps detailed as follows: 45 ps for T = 1000 K, 45 ps for T = 900 K, 45 ps for T = 800 K, 45 ps for T = 700 K, 45 ps for T = 600 K, 45 ps for T = 500 K, 50 ps for T = 400 K, and 50 ps for T = 300 K (see table [3.1]). **Model 6** (CP2K-PBE0-270), was produced by resorting to Born-Oppenheimer MD using the CP2K code and the hybrid PBE0 XC functional. Starting from the last obtained configuration of Model 1 at T = 300 K, a thermal annealing cycle was applied to the system as follows: 1 ps at T = 300 K, 3 ps at T = 900 K, 4 ps at 1200 K, 3 ps at T = 900 K, 3 ps at T = 600 K, and 5 ps at T = 300 K. We note that, given the very high cost of hybrid functional molecular dynamics, we anneal the system at T = 1200 K, a temperature slightly higher than the melting point (T = 1006 K) in order to induce significant rearrangement of the structure. Finally, **Model 7** (CP2K-PBE0-variable-density-270), was produced by melt quenching using CP2K and PBE0 XC functional and allowing the density of the system to increase linearly from 5.09 g.cm^{-3} at the melt state [38] to 5.57 g.cm^{-3} at ambient temperature [31]. Precisely, the system was subject to the following variable density thermal cycle: 5 ps at T = 1200 K and ρ = 5.09 g.cm^{-3}, 5 ps at T = 1000 K and ρ = 5.09 g.cm^{-3}, 5 ps at T = 750 K and ρ = 5.25 g.cm^{-3}, 5 ps at T = 500 K and ρ = 5.40 g.cm^{-3}, and 6 ps at T = 300 K and ρ = 5.57 g.cm^{-3}. For all the models, statistical averages are performed on at least a 5 ps trajectory. We were able to examine the modelling technique for achieving a better atomic scale description of TeO_2 glass using the various DFT models. To that purpose, the model's quality is assessed by comparing the reduced total X-ray scattering PDF to experimental data of TeO_2 in the melt and glassy phases using a statistical average over the last 5 ps of the MD trajectory. The calculated $G(r)$ on all our models are illustrated in figures [3.1] and [3.2].

GGA functional effects

The choice of the exchange-correlation functional (XC) has a significant impact on the accuracy of the determined electronic and structural properties [98]. PBE and BLYP belonging to the GGA class of functional are the most commonly used due to their simplicity and computational cost efficiency. Both XC functionals have been used to produce TeO_2 models (Model 1 and Model 2), as shown in the table [3.1], and the models have been inspected by plotting the obtained PDFs presented in fig [3.1]. We notice that the first peak in PBE based Model 1 and BLYP based Model 2 shifts by $\sim$ 0.06 Å towards larger distances in comparison to the experimental first peak (see

Model	*ab-initio* code	Pseudo-potential	Number of atoms	Heat-Quench cycle (Temperature)	Description
Model 1	CPMD	PBE	270	5ps (300K) → 5ps (600K) → 45ps (1000K) → 30ps (600K) → 30ps (300K)	At experimental constant density of 5.57 g.cm^{-3}. Started from random initial configuration.
Model 2	CPMD	BLYP	270	5ps (300K) → 5ps (600K) → 45ps (1000K) → 30ps (600K) → 30ps (300K)	At experimental constant density of 5.57 g.cm^{-3}. Started from random initial configuration.
Model 3	CPMD	BLYP	480	9ps (600K) → 8ps (600K) → 30ps (1000K) → 25ps (600K) → 20ps (300K)	At experimental constant density of 5.57 g.cm^{-3}. Started from random initial configuration.
Model 4	CP2K	BLYP	480	— — 15ps (1000K) → 14ps (600K) → 10ps (300K)	At experimental constant density of 5.57 g.cm^{-3}. Started from last configuration of Model 3 at 1000K.
Model 5	SGPCMD	PBE	270	45ps (1000K) → 45ps (900K) → 45ps (800K) → 45ps (700K) → 45ps (600K) → 45ps (500K) → 50ps (400K) → 50ps (300K)	At experimental constant density of 5.57 g.cm^{-3}. Started from last configuration of Model 4 at T = 300 K.
Model 6	CP2K	PBE0	270	1ps (300K) → 3ps (900K) → 4ps (1200K) → 3ps (900K) → 3ps (600K) → 5ps (300K)	At experimental constant density of 5.57 g.cm^{-3}. Started from last configuration of Model 1 at 300K.
Model 7 (Variable density)	CP2K	PBE0	270	5ps (1200K) @ 5.09 g.cm^{-3} → 5ps (1000K) @ 5.09 g.cm^{-3} → 5ps (750K) @ 5.25 g.cm^{-3} → 5ps (500K) @ 5.40 g.cm^{-3} → 6ps (300K) @ 5.57 g.cm^{-3}	With variable density. Started from last configuration from Model 6 at T=1200 K.

Table 3.1: Various DFT setups used to study the model best capable of describing experimental data. In addition, the thermal cycle used for heat and quench is also reported.

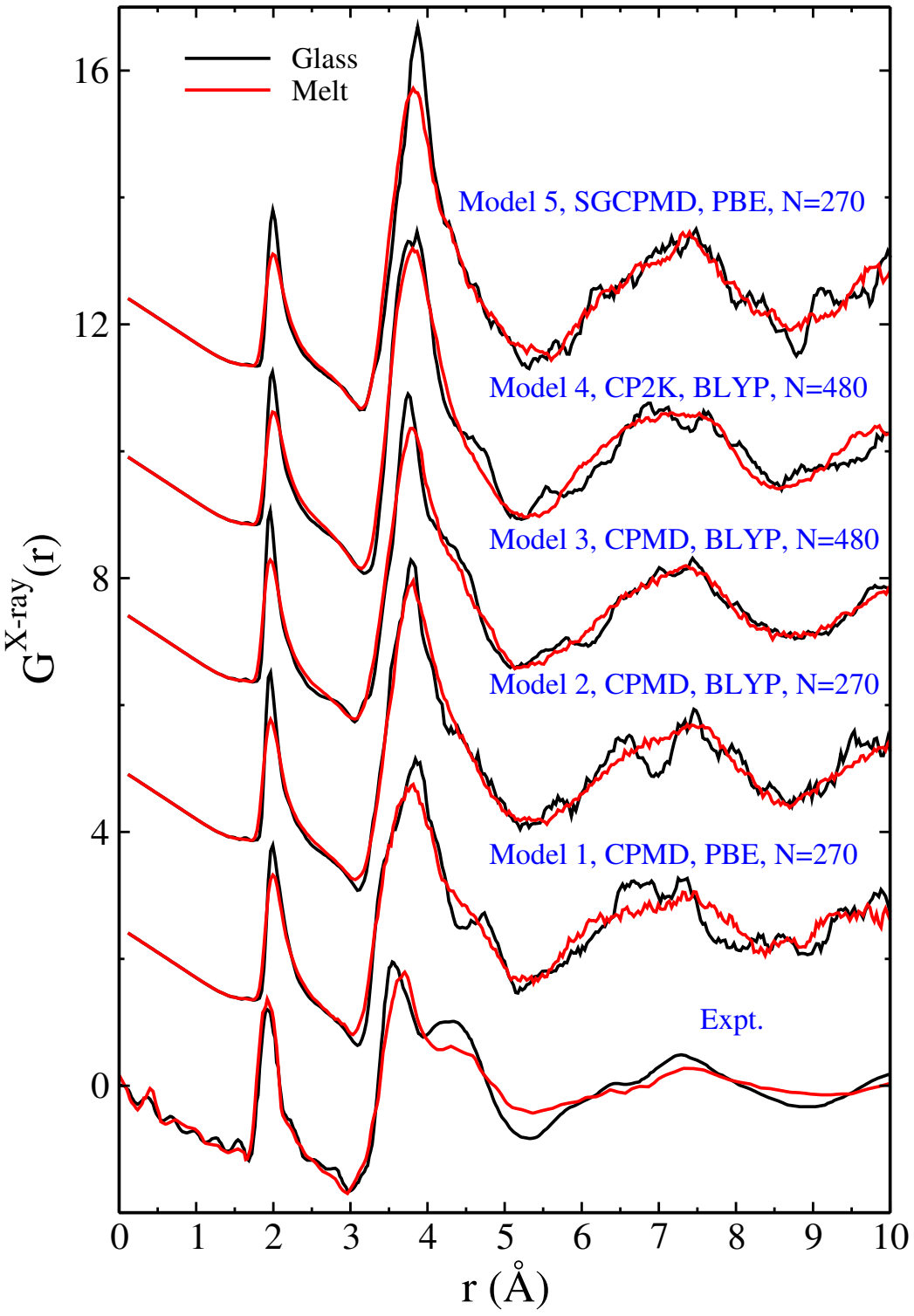

Figure 3.1: Total reduced X-ray pair distribution function, $G_{xray}(r)$, for model 1 ,2, 3, 4 and 5, and experimental data [38] in the case of melt (red) and glass (black) TeO_2 phases. For better interpretation and clarity, a vertical shift to each of the curves are applied.

fig [3.1]). Additionally, the second, and the third peaks in both models located in between 3 and 5.5 Å shows similar results within typical statistical fluctuation. These findings are in line with earlier research on TeO_2 crystalline phases, where PBE and BLYP functionals produced results for local structure that were very comparable [99]. The actual complexity, however, becomes apparent when analyzing the second peak since neither the melt nor the glassy phase (with both functionals) models can adequately account for the experimental results. Both models failure may be seen at two levels (see figure [3.1]):

1. In the case of experimental of TeO_2 system, the second peak located at 3.7 Å in the case of melt shifts towards lower distance to 3.55 Å in the glassy phase, however, no such a shift was seen in the case of BLYP and PBE XC functionals, as both shows the similar peak position upon cooling.
2. The intensity of the third peak centered around 4.3 Å in the melt of experimental PDF, rises as it goes to the glassy phase. Model 1 and 2, were not able to reproduce those peaks.

As a result, DFT setup utilized in Model 1 and Model 2 are not sufficient to provide a quantitative description of the structure of TeO_2 systems and demonstrate comparable performances of PBE and BLYP XC functionals.

Simulation cell size effects

In *ab-initio* molecular dynamics simulations, periodic boundary conditions are commonly used to simulate bulk materials and eliminate surface effects. The finite size effects owning to periodic boundary conditions can affect the simulated models. In particular, when the system features extended structural motifs like rings, chains, or voids, employing small periodic models may result in a poor description of the glassy network.

To address the issue with finite size effect, Models 3 and 4 with larger systems (480 atoms) were simulated utilizing BOMD and CPMD techniques, respectively. The resulting PDFs for both models are displayed in figure [3.1]. Both models are simulated independently starting from different initial configurations, in otherwise similar protocols. We find that there is no discernible variation in the overall form of the PDF when compared to models with 270 atoms for $r < 5$ Å. In addition, for $r > 5$ Å, small variation of the order of statistical fluctuations in glass was observed, this result suggests that a model size beyond 270 atoms has limited impact on the description of TeO_2 short and medium range structure.

Thermal cycle effects

The rate at which a material is quenched to achieve a glassy phase can have a significant impact on its structure. Even though *ab-initio* molecular dynamics approaches cannot achieve realistic quenching rates with current computing power, we compare the total X-ray PDFs obtained from two models (see figure [3.1]):

1. Model 1 : with a two steps quenching, following 30 ps at T = 600 K and T = 300 K each.
2. Model 5 : with quenching performed iteratively by reducing the temperature with a step of 100 K. At each temperature plateau starting from T = 1000 K to T = 300 K the system is equilibrated for 45 ps (see table [3.1]).

Both quench cycles lead to TeO_2 system where the calculated PDFs are remarkably similar, indicating that the quenching rate too has a limited effect on the TeO_2 glass final structure. Furthermore, in the case of model 5, the PDF does not reflect the difference between the molten and glassy phases that has been seen experimentally. It's also worth mentioning that a far slower quenching rate, orders of magnitude slower than the one used in this study, might lead to a further glass structural relaxation.

Further, we also made an attempt to simulate the pure TeO_2 glass using van der Waals (vdW) correction and NPT (constant number, pressure, and temperature) independently, but unfortunately, neither of these methods were able to reproduce the experimental trends.

Hybrid functionals effect

Based on the evaluation of all the previously stated models, it is determined that none of them can reproduce the experimental total X-ray PDF in the case of melt and glassy TeO_2 to a reasonable accuracy, implying that model attributes have a limited impact on the structure. Furthermore, the varied heat cycles have a small impact on the final PDF. Since all the calculations were done with GGA functionals, it may be possible that this level of theory is insufficient to get accurate results. In fact, from conceptual point of view, the geometry of the TeO_x structural units in TeO_2 systems are significantly reliant on the orientation of the Te electronic lone pair, which itself dependent on the electronic localization level. As a result, the functional used to characterize the electronic density localization is likely to have a considerable influence on the model's validity.

Despite the fact that GGA functionals provide sufficient accuracy for several applications, they are reported to induce electronic density delocalization, making them unsuitable for a proper description of the TeO_2 system. However, higher level of accuracy is necessary, and can be achieved with hybrid XC functionals. Hence, model 6 was produced by resorting to PBE0

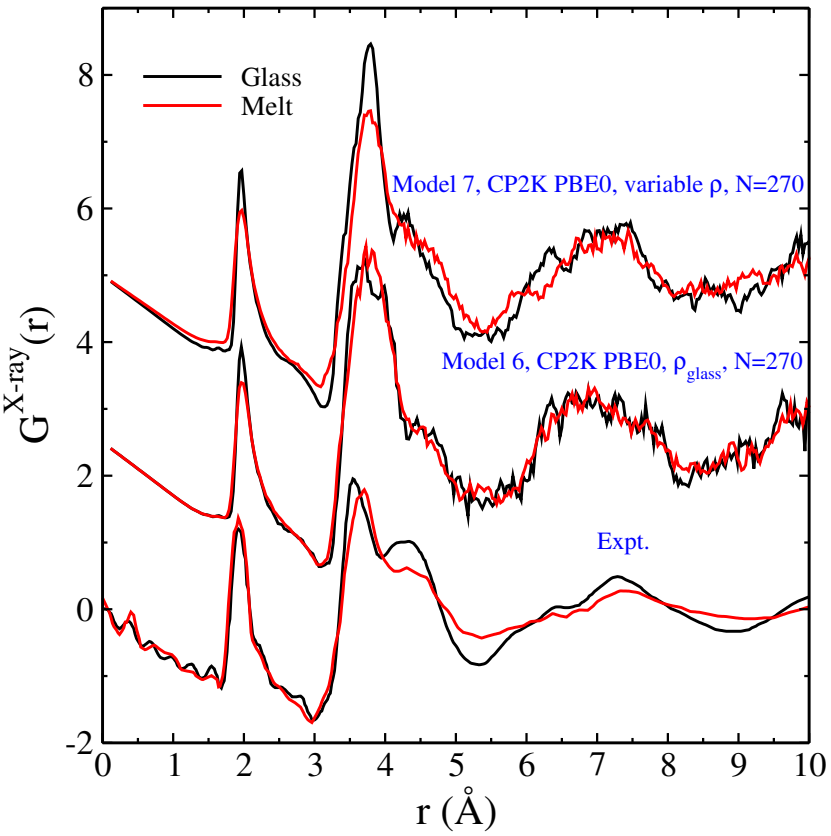

Figure 3.2: Comparison of total X-ray PDF for amorphous (black lines) and melt (red lines) phases of TeO_2 systems obtained from Model 6 and 7 to experimental results [38]. The curves are shifted vertically for better clarity.

hybrid functional. However, the high computational cost of running large molecular dynamics trajectories is the price to pay for achieving a higher precision. We focus on model 6 produced at the PBE0 level of theory and at constant experimental density. We anneal this model at T = 1200 K a temperature slightly larger than its melting point in order to get a liquid-like diffusion coefficient of Te and O ions. Model 6's melt and glass phases PDFs are shown in figure [3.2]. We find that the second peak in the case of glass and melt displays similar tendencies to experimental PDFs. Moreover, a shoulder develops around 4.5 Å in the case of TeO_2 glass, which is close to the experimental PDF's third peak around 4.3 Å, even though there is no discernible increase in the intensity of this shoulder from melt to glass. While this study indicates that, in comparison to GGA functionals, a better description of the electron localization has an immediate effect on the structural organization of the disordered system, a better reproduction of the third peak intensity would require additional efforts.

It is important to note that, the constant volume of the cell during the melt-quench cycle may have an impact on the third peak that is attributed to nearby Te-Te atoms. Therefore, the constant volume of the cell during the melt and quench cycle might alter the peak ascribed to Te atoms

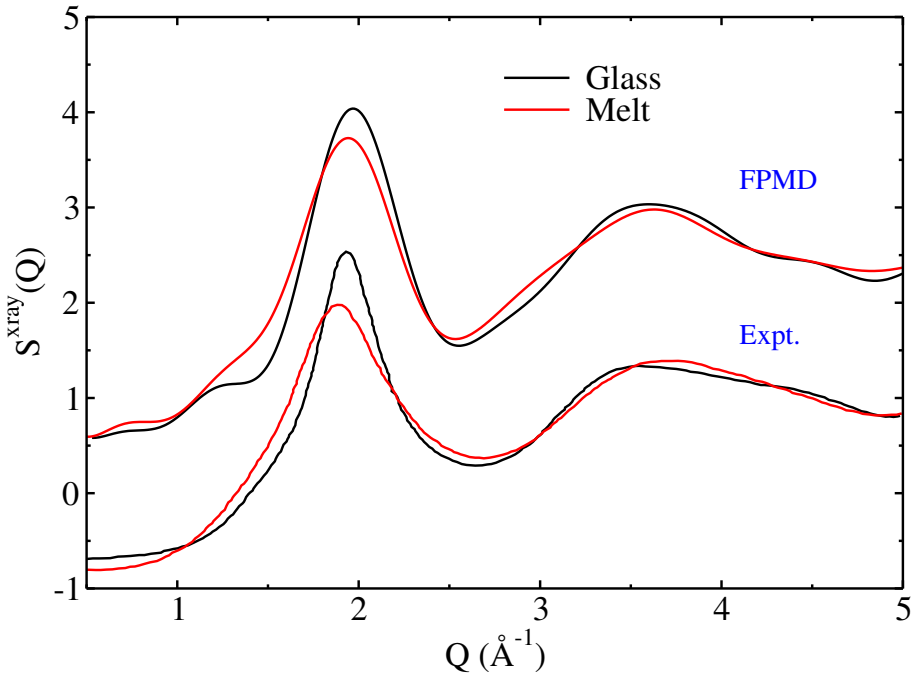

Figure 3.3: Experimental and computed (model 7) comparison of X-ray total structure factor for TeO_2 glass and melt.

(third experimental peak in PDF). A new model 7 has been produced to address this issue, as shown in table [3.1]. The sole difference between Model 7 and Model 6 is that the quench cycle in Model 7 offers a linear decrease in the system density from melt density to glass density. This approach is similar to performing molecular dynamics in an isobaric isothermal ensemble (NPT). While the simulated NPT ensemble necessitates extended molecular dynamics trajectories to converge the cell volume, in this technique, the melt density has been considered based on experimental reference and linearly decreased to that of the glass density. Figure [3.2] shows the calculated PDF for both PBE0 hybrid models at constant (model 6) and variable (model 7) densities. In the case of model 7, the peak at about 4.3 Å in TeO_2 glass is immediately distinguishable. Furthermore, as compared to the melt, the PDF of the glass has a greater second peak and a deeper second minima at 5.3 Å, which is qualitatively consistent with the experimental data. Despite having a larger peak intensity compared to the experimental PDF, Model 7 is able to capture the experimentally observed trends, resulting in a more accurate representation of the network organization after cooling. For completeness, we produced a variable density model at the PBE level of theory to better grasp the role of PBE0 in the variable density approach. However, it was found that the obtained model performs similar to Model 1.

We compared the X-ray total structure factor S(Q) (see figure [3.3]) to the experimental structure factor, in order to further validate the reliability of model 7. Overall, the S(Q) of Model 7 shows good agreement with experimental data. In addition, when the temperature is decreased,

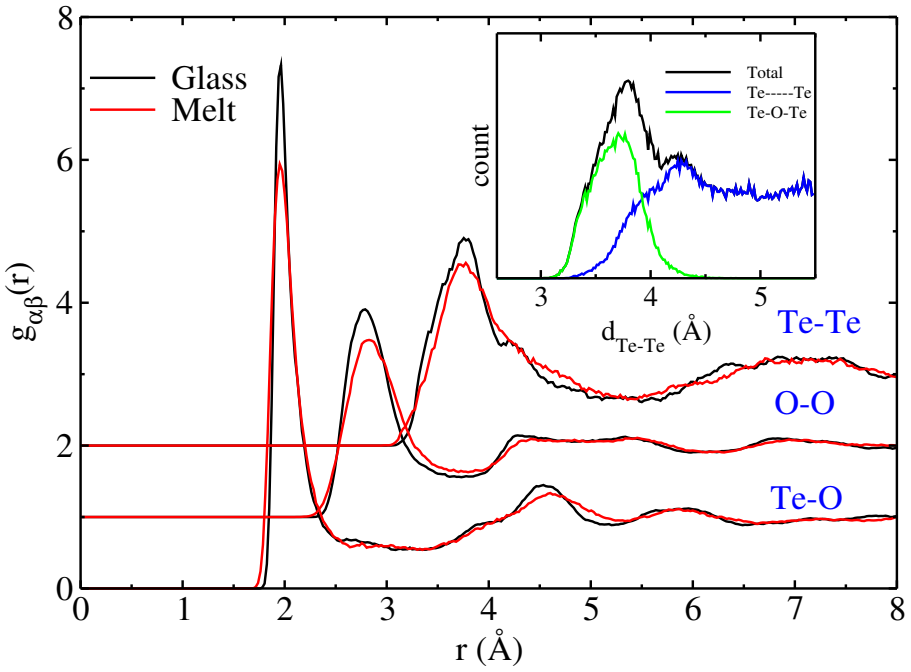

Figure 3.4: The partial distribution functions of $g_{\mathrm{TeTe}}(r)$, $g_{\mathrm{TeO}}(r)$, and $g_{\mathrm{OO}}(r)$ for glass (black lines) and melt (red lines) TeO_2. In the inset, the Te-Te distance distribution is decomposed into contributions from Te atoms linked by bridging O (green hue) and contributions from nearby Te atoms not directly sharing any O (blue color). Various pair distributions are shifted vertically to depict a clear representation.

the model can also show a shift and an intensity rise in the first peak of S(Q) as observed experimentally. Therefore, one can rely on model 7 to examine the atomic scale structure of glassy and molten TeO_2 with an unprecedented level of accuracy in light of all the concordant elements stated above. Hence, we will concentrate on a detailed structural study of model 7 obtained by PBE0 along with the variable density approach in the following sections.

3.2 Structural analysis

3.2.1 Partial pair distribution function

Insights into the atomic structure can be obtained from the partial pair distribution function (see figure [3.4]). For TeO_2 system we see three peaks representing various distribution of bonds.

1. Te-O partial PDF: First peak in Te-O distribution, represents most probable Te-O pair distance distribution. Under a careful examination, it is concluded that the peak centered around 1.964 Å in the case of glass shifts towards smaller distance (1.952 Å) at the melt temperature. This shift obtained from our model is in accordance with the experimental data where the same peak shifts from 1.926 to 1.919 Å when moving from the glass to the

melt. This slight overestimation of bond-length by 0.03-0.04 Å can be attributed to the DFT setup [30], [49].

2. O-O partial PDF: The O-O correlation raise after 2.3 Å, and its contribution to the total PDF is negligible due to the small scattering factor of oxygen atoms [$f_O(k_0 = 0) \approx Z_O = 8$] as compared to Te atom [$f_{Te}(k_0 = 0) \approx Z_{Te} = 52$]. With increasing the temperature, the position of this peak shifts from 2.79 Å to 2.83 Å.
3. Te-Te partial PDF: In this partial PDF, two features are observed under cooling from melt to glass,
   - a very small shift of Te-Te peak towards smaller distances is noticed.
   - Appearance of a shoulder around 4.2 Å in the glassy phase.

   The origin of these features can be explained on the basis of Te-Te connection where the shift in the Te-Te peak could be explained by the rise of Te-O-Te linkages under cooling and the appearance of the shoulder could be due to the formation of direct Te-Te spatial proximity as shown in the inset of the figure [3.4].

The shifts in the PDF of Te-O and O-O imply that under cooling a significant reorientation of local environments around Te atoms take place. Furthermore, the absence of Te-Te shoulder around 4.2 Å in the melt suggests that medium-range orders are also affected at high temperatures.

3.2.2 Coordination number

A deeper insight into the local environment of the generated TeO_2 model can be achieved by evaluating the coordination number of Te (n_{TeO}, with respect to oxygen) which is obtained by integrating the partial Te-O PDF until its first minimum as:

$$n_{TeO} = \int_0^{r_{cut}} \rho_O g_{TeO}(r) 4\pi r^2 dr. \tag{3.5}$$

where, ρ_O is the oxygen number density obtained via multiplying the atomic fraction of oxygen with the total number density. Figure [3.5], shows the evolution of n_{TeO} with respect to distance in the case of melt and glass. We notice that the calculated coordination number, n_{TeO}, is shifted to higher value of r than the experimental counterpart. This shift of 0.05 Å is due to the difference in the location of the first peak of Te-O experimental and calculated PDF (see figure [3.4]). It is important to note that, apart from the shift observed, the calculated coordination curve shows good accordance with their experimental counterpart. In particular, the curve shows a continuous increase over all the r range which reflects the absence of a clear first minimum in the Te-O partial PDF. It is noteworthy that our model reproduces the smaller n_{TeO} for the melt as compared to the glass in line with experimental findings. This reduction can be attributed to the increase of the short-range disorders around Te atoms at higher temperature [38]. Here, short range-disorder is defined as the deviation from the typical local structural arrangements

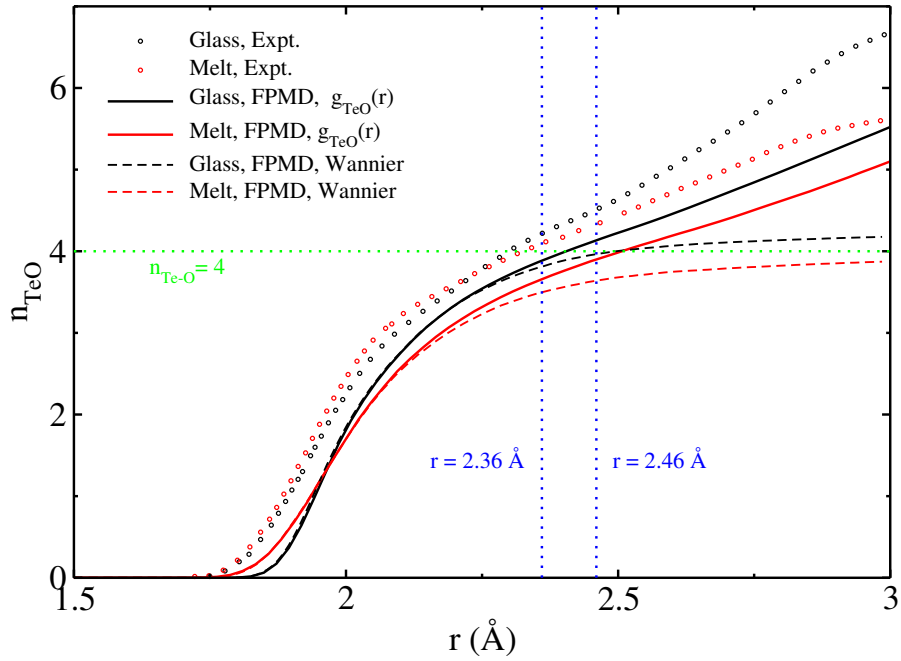

Figure 3.5: Running Te-O coordination number ($n_{\mathrm{TeO}}(r)$) of glassy (black color) and melt (red color) TeO_2 system. Results obtained by integration of the Te-O partial PDF (solid lines) and based on Wannier centers (dashed lines) are compared to experimental results (circles) from Ref. [38]. Vertical dashed lines indicate distance cut-offs, and the dashed horizontal line indicates the ideal Te^{4+} coordination number.

that are often observed in crystalline structures of TeO_2. In general, we hypothesize that at the melting temperature, Te suffers loss of longer and weaker bonds with O atoms leading to a reduction of the coordination number.

From the figure [3.5], we can conclude that an accurate estimation of the coordination number is not straightforward as one cannot unambiguously define the plateau region based on a Te-O distance cutoff. In previous works [30], [31], [38], researchers have used several Te-O distance cutoff varying from 2.36 to 2.46 Å to estimate the coordination number. In this study, the use of MLWF to obtain Wannier function center has been implemented to obtain deeper insight in the determination of the network connectivity present in TeO_2 glass. Under this approach, the Wannier functions are obtained by an on-the-fly unitary transformation of the Kohn-Sham orbitals under the constraint of minimizing the spatial expansion of the spread Ω (see chapter [2]). Therefore, the MLWF provides an accurate real-space representation of the electronic structure, which can be used to define the chemical bonds and lone pair electrons. These analyses are performed on top of 100 snapshots selected uniformly spaced over the last 10 ps of the trajectory at T = 300 K using hybrid functional. Figure [3.6a] shows a representative fragment of TeO_2 glass, where we distinguish three types of Wannier centers. W^{B} refers to centers occurring at a Te-O bond, W^{Te}_{LP} and W^{O}_{LP} refer to centers representative of lone-pair electrons at the vicinity of Te and O atoms, respectively.

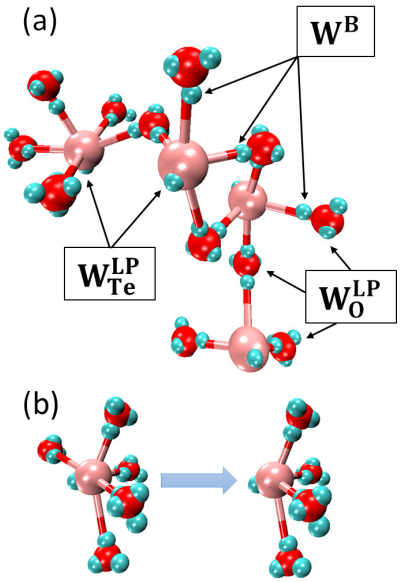

Figure 3.6: (a) A sample picture of the environment for bonds in glassy TeO_2. Wannier Centers (designated as W), Te (brown), and O (red) (cyan). . Three distinct Wannier centers are identified: The lone pair (LP) valence electrons not participating in bonding are represented by W^{LP}_{Te}, W^{LP}_{O} and W_B along Te-O bond. (b) A typical Te environment where the O neighbors are determined using a cutoff distance (left picture) and MLWF constraint (right image).

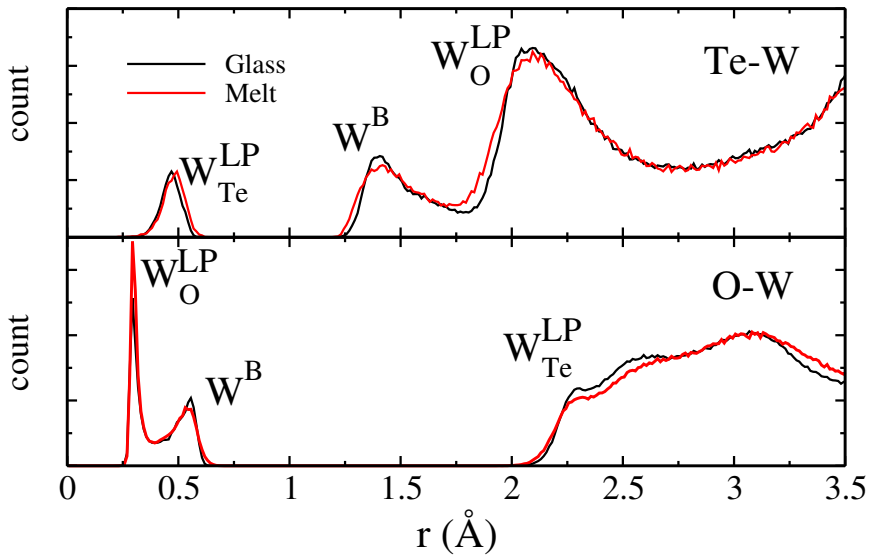

Figure 3.7: Distribution of the Wannier centers around Te (top panel) and O (bottom panel) in glass (black lines) and melt (red lines) TeO_2 system.

Figure [3.7], shows the distribution of various types of Wannier center distributions around Te and O in molten and glassy phases of TeO_2. All the important peaks relevant under this description of Te-O bonds have been labelled in the figure. Interestingly, in contrast to $g_{TeO}(r)$, it is possible to define Te-O cutoff distance based on the first minimum of Te-W and the second minimum of O-W distributions. In particular, these distances correspond to the farthest position of shared Wannier centers occurring along the Te-O bonds and when summed up provide a reasonable estimation of the Te-O cutoff. Based on this assumption we find that Te-O cutoff distances are 2.46 Å in the glass and 2.47 Å in the melt of TeO_2 system. We remark that this cutoff is 0.1 Å larger than the cutoffs reported in the previous studies (see chapter 1). The origin of this small difference can be attributed to two facts:

1. the small over estimation by 0.05 Å of Te-O bonds in partial PDF in reference to experimental data, and
2. the small uncertainty in the location of Wannier centers due to the statistical and disordered nature of the glassy system, making W^B shift slightly off the line joining Te and O atoms.

By integrating the Te-O partial PDF up to the obtained cutoff value, we find n_{TeO} to be 4.12 for the glass and 3.91 for the melt TeO_2. These results are in agreement with those obtained from experiments [38] based on a cutoff value of 2.36 Å which gives coordination to be 4.22 and 4.09 for glass and melt of TeO_2 respectively. Moreover, this examination reveals that the coordination number of Te is quite close to 4 rather than in the range of 3.6-3.7 as suggested by previous modelling results [30], [31] (see chapter [1]).

Despite that the method discussed above seems instructive, it still depends upon the choice of the cutoff distances. This issue can be uplifted using the MLFW formalism to define a chemical bond and therefore obtain the direct count of Te-O bonds in the whole system. To take into account the shift of Wannier centers, here, a chemical bond is considered if the difference of summed bond lengths of Te-W^B and O-W^B with Te-O bond length is less or equal to a tolerance value of 0.05 Å.

$$|d(\text{Te,W}) + d(\text{O,W}) - d(\text{Te,O})| \leq 0.05 \text{ Å}. \tag{3.6}$$

Moreover, there is a need to implement a further angle constraint as well for the evaluation of proper count of Te-O bonds as suggested in Ref. [31], since the angle formed in some cases by Te with its lone pair and the corresponding oxygen atom with less than some tolerance value cannot be classified as a Te-O chemical bond (see figure [3.6]b).

To obtain the value of the angle cutoff we have equilibrated three polymorphs of TeO_2 using PBE for 20 ps at T = 300 K. We subsequently plotted the Bond-angle Distribution Function (BAD) to

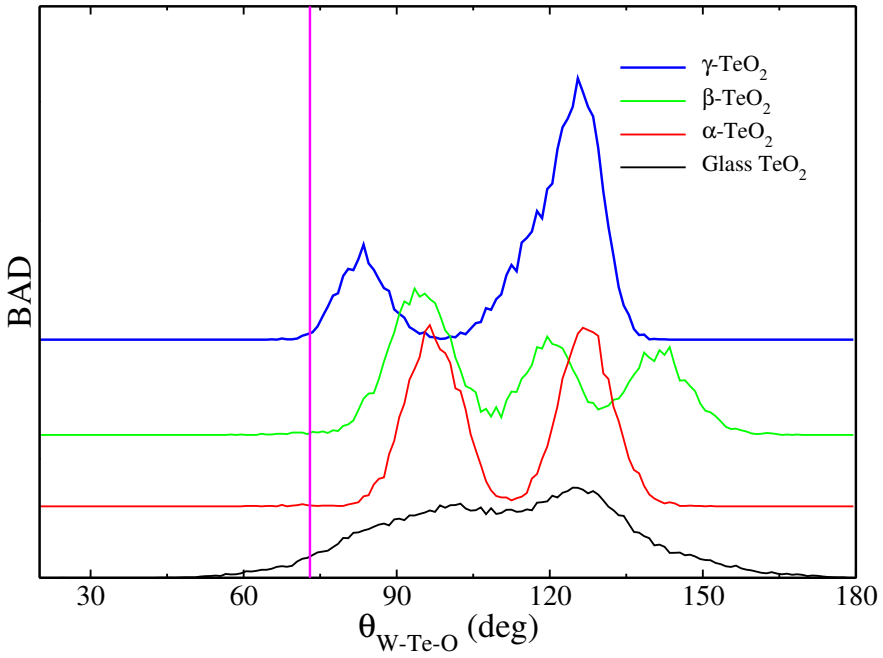

Figure 3.8: Bond angle distribution $\Theta_{W^{LP}_{Te}\text{-Te-O}}$ simulated on $\alpha-$ (red), $\beta-$ (green), $\gamma-$ (blue) and glassy TeO_2 (black) using Te-O distance cutoff of 2.4 Å. Various distribution is shifted vertically for clear representation. Additionally, vertical line shows the selected cutoff angle of 73°.

obtain the minimum angle $\theta_{\text{W-Te-O}}$ on top of 100 snapshots where Wannier centers were evaluated using PBE0 hybrid functional (see figure [3.8]). We note that the BAD features two main regions:

1. The first region is around 75-100° and corresponds to the angle between Te lone pair and Te-O axial bonds,
2. The second region corresponds to 110-160° originating from contribution from Te lone pair and equatorial oxygen atoms.

From the BAD figure [3.8], it is seen that only after a critical angle around 73°, BAD for crystal starts to rise, however in the case of glass a broad peak with an elongated tail less than the critical angle is seen. Therefore, we have plotted the convergence of n_{TeO} vs Te-O cutoff distance with the implementation of first constraint at various angle-cutoffs (see figure [3.9]). From our inspection we found that the angle cutoff of 73° is a reasonable cutoff and in the description of chemical bond we simply ignore all those bonds corresponding to $\Theta_{W^{LP}_{Te}\text{-Te-O}}$ angle less than 73°.

$$\Theta(W^{LP}_{Te} - \text{Te-O}) \geq 73^{\circ} \tag{3.7}$$

We note that by applying the distance and the angle constraints, we recompute Te-O coordination number (n_{TeO}) and present the results in figure [3.5]. We find that n_{TeO} in both glassy and molten TeO_2 reach a slightly evolving plateau region around a value of 4 and this remains true for TeO

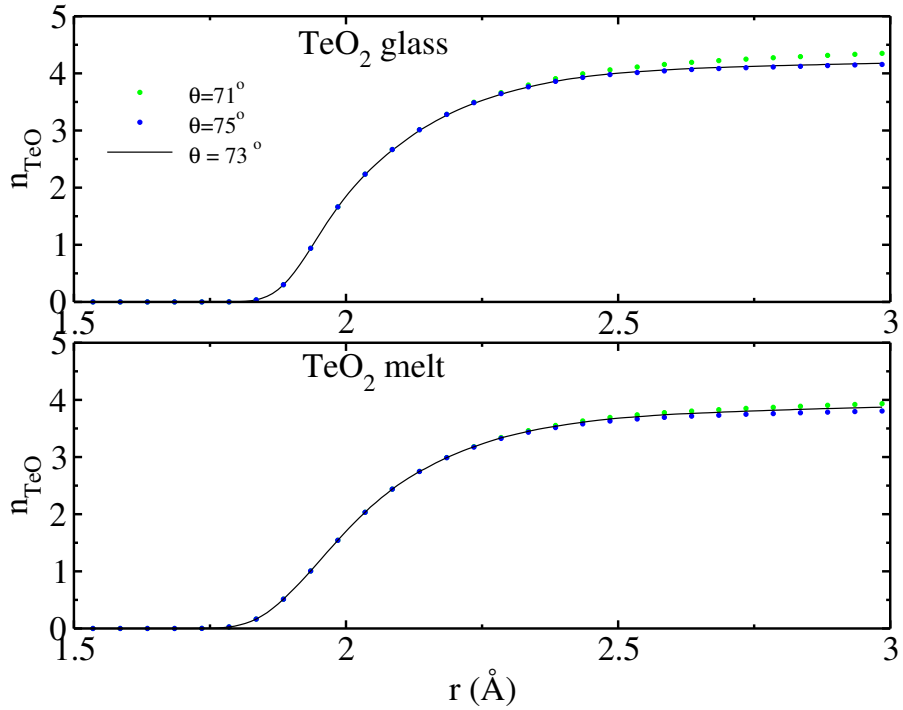

Figure 3.9: Running Te-O coordination number (n_{TeO}) of glassy (top panel) and melt (bottom panel) TeO_2. Results obtained based on Wannier centers with variable angular constraint thresholds.

bond lengths up to 3 Å. Under this new description the calculated coordination number for r cutoff values already established (2.46 Å in glass and 2.47 Å in the melt) are 3.96 and 3.65 in glassy and molten TeO_2. Even though the calculated coordination number is smaller than the one obtained via integrating partial PDFs due to the elimination of Te-O bonds that occur at physical distances but does not qualify as chemical bond, our results are in good agreement with the experimental obtained values [38] where n_{TeO} value was found to be around 4 with a hint that it is smaller in the melt than in the glass.

It is noteworthy that, for the region with $r < 2.3$ Å in figure [3.5], the experimentally measured n_{TeO} is larger in the melt than in the glass. The similar trend was also observed in our model, however in our model this crossover value of r is found to be around 1.97 Å. This difference in the location of the cross-over can be explained on the basis of differences in the first peak position observed in g_{TeO} PDFs. Actually, the experimental first peak corresponding to Te-O interactions is found to be more intense in the melt than in the glass, while the opposite trends were observed in our model. Normally, the intensity of n_{TeO} is subject to two competing effects

1. With quenching the first peak maximum in g_{TeO} is expected to increase in intensity due to the rise of the number of short Te-O bonds in glass.

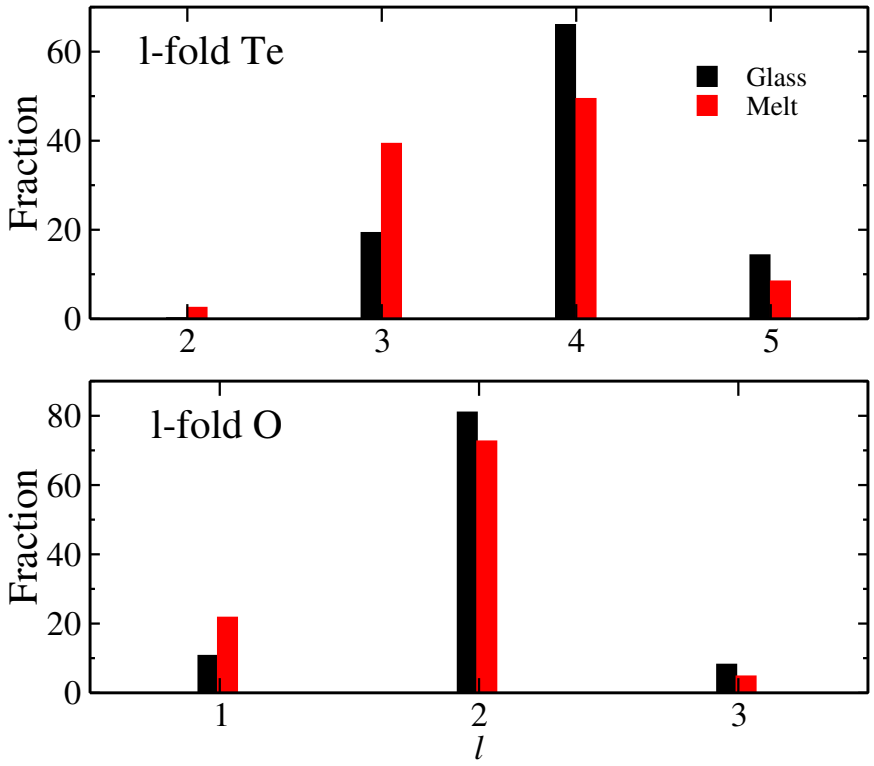

Figure 3.10: Decomposition of l-fold fractions of Te (l = 2, 3, 4 and 5) and O (l = 1, 2 and 3) evaluated on glass (black) and melt (red) TeO_2.

2. With increasing the system density, the first peak maximum is expected to decrease in intensity.

Therefore, the slight disparities between modelling and experiments may be caused by the adopted quenching process as well as the high error bar on the experimental melt density [38].

3.2.3 Local environment and short-range disorder

The following section of our investigation focuses on the distinct Te and O local environments. To do this, we decompose the first coordination shell surrounding a particular atom into several l-folds, where l is the number of closest neighbors. These l-fold environments are calculated in the same way (same cut-offs and Wannier constraints) that coordination numbers are evaluated, and the obtained results are presented in figure [3.10]. We found a dominating proportion (66.0%) of TeO_4 units, as well as a non-negligible fraction of under-coordinated TeO_3 units (19.3%) and over-coordinated TeO_5 units (14.3%). In addition, we disregard the proportion of 2-fold Te with a fraction of 2% of the order of statistical errors. This distribution is consistent with the Te average coordination of 4, since the under- and over-coordinated Te fractions balance out to achieve an overall averaged 4-fold coordination sphere. In the case of melt, however,

Q_m^n	Glass (%)	Liquid (%)
Q_3^1	-	2.5
Q_3^2	5.2	17.6
Q_3^3	14.1	19.2
Q_4^3	13.8	16.5
Q_4^4	52.0	32.1
Q_5^4	2.1	1.4
Q_5^5	12.2	6.9

Table 3.2: Q_m^n fractions of Te units in glass and melt TeO_2

this distribution changes significantly, with the percentage of TeO_4 and TeO_5 units decreasing to 49.4% and 8.4%, respectively. This development is accompanied by an increase in TeO_3 unit population up to 39.3%. Taken as a whole, the evolution of the Te local environment is consistent with the elongation of some Te-O bonds beyond a threshold distance, resulting in a drop in the average Te coordination number in the melt.

To further support our findings, an examination of Q_m^n units surrounding the Te atom is performed, where m is the total coordination number and n the number of oxygen atoms forming Te-O-Te bridges (see table [3.2]). Notably, as a function of temperature, we see a considerable increase in the proportion of Te units (Q_3^1, Q_3^2 and Q_4^3) having at least one non-bridging O atom. Even though indirectly, it is possible to claim that the reduction in the coordination number of Te atoms is caused by breakage of longer and weaker Te-O bonds in Te-O-Te bridges due to thermal fluctuations at higher temperatures. Additionally, we find that Te atoms that are linked to non-bridging oxygens show smaller bond distances than Te-O distances in Te-O-Te bridge (see figure 3.11 b-d). It is possible to quantify the rise in the short-range disorder surrounding Te by examining the asymmetry of Te-O bonds. To do this, we define the following bond asymmetry function for Te atom i as:

$$f_i = \frac{2}{m(m-1)} \sum_{j=1}^{m-1} \sum_{k=j+1}^{m} |d_{ij} - d_{ik}| \tag{3.8}$$

where d is the distance between the Te atom and one of its nearest O neighbors, and m is the number of nearest O neighbors of the Te atom. The average bond asymmetry f is positive for asymmetric environments and zero for Te atoms with equal length Te-O bonds. Furthermore, O-bridges asymmetry can be defined using the same equation. Figure [3.11 a-c] depicts various distributions of f for different local environments of the Te atom in glassy and molten TeO_2. The distribution is normalized to the total Te atoms.

The overall f distribution in the melt is wider than in the glass, with a move towards higher f

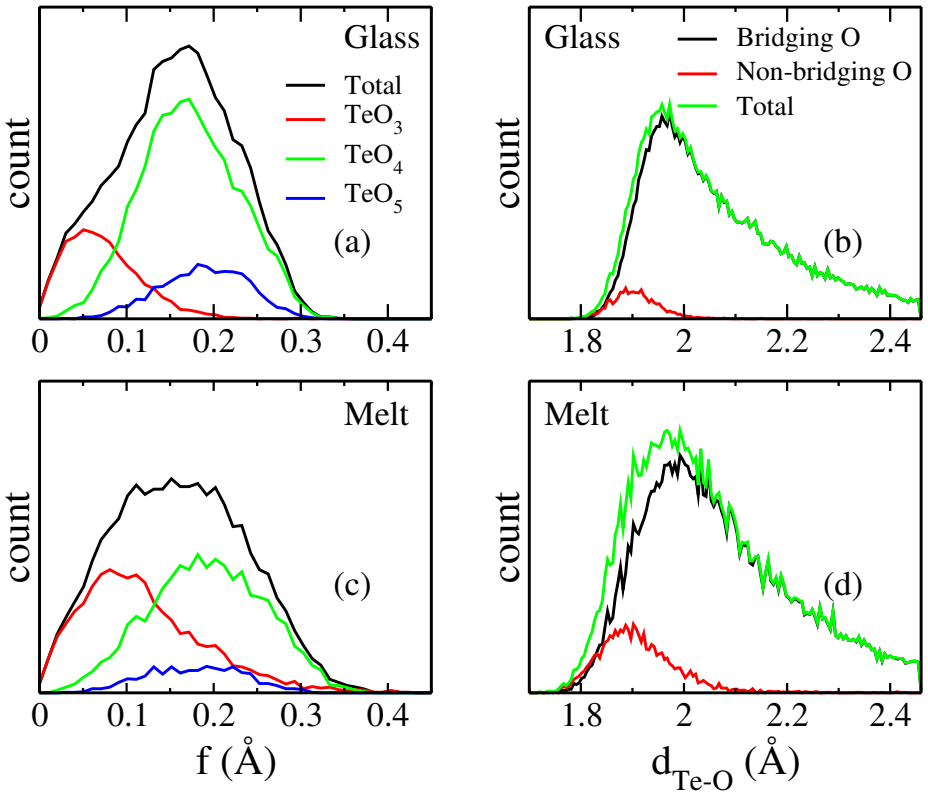

Figure 3.11: Distribution of the average bond asymmetry function calculated on amorphous (a) and melt (c) TeO_2 system and its breakdown into contributions from TeO_n units (n=3,4 and 5). Distribution of Te-O distances calculated on glass (b) and melt (d) TeO_2 where O atoms are either bridging or non-bridging.

values indicating an increase in the bond asymmetry as temperature rises. This trend may be explained by looking at the decomposition of f as a function of the Te local environments, which shows that the TeO_3 f distribution is moved to higher values in the melt. A similar, although less significant shift is also found in the TeO_4 f distribution, which coincides with a significant broadening. These elements imply that when the temperature rises, the disorder in TeO_4 units increases, causing long and weak Te-O bonds to break and the unit to change into significantly asymmetric TeO_3 units. These findings support the hypothesis that the short-range disorder increases with temperature, resulting in a decrease in the Te coordination number.

When it comes to the O atom, we find that it mostly has a two-fold coordinated structure with non-negligible amounts of one- and three-fold configurations. These findings are consistent with an O atom coordination number that is close to two. It's interesting to note that the melt has a higher percentage of 1-fold O atoms (21.8%) than the glass (10.7%). The fraction of 1-fold O increases as a function of temperature and is accompanied by a decrease in the fraction of 2-fold (from 81.0% in the glass to 72.6% in the melt) and 3-fold (from 8.2% in the glass to 4.8% in the melt) O units. We see that the occurrence of terminal Te=O groups can be possibly related with the increase of 1-fold O atoms. This pattern is consistent with the rise in the proportion of

under-coordinated Te atoms (TeO_3) and the rise in the asymmetry of the Te environments with temperature. Since the proportions of TeO_3 and TeO_5 motifs can be balanced and result in an overall n_{TeO} near to 4, our results demonstrate that an average coordination number n_{TeO} less than 4 cannot just simply be attributed to the presence of NBO in glassy TeO_2 as previously claimed. These outcomes are consistent with the judgments made in lights of NMR spectroscopy [37].

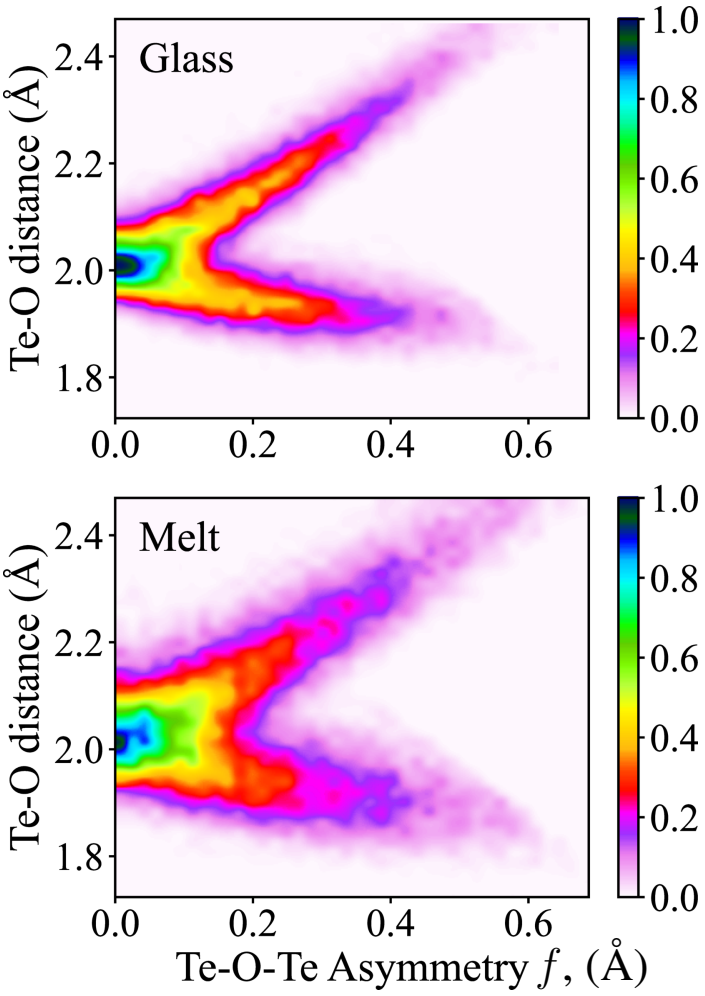

Figure 3.12: 2-D Histogram of Te-O distance vs bridge asymmetry (Te-O-Te) is illustrated for glass (top) and melt (bottom) TeO_2 system.

In both glassy and molten TeO_2, figure [3.12] depicts the evolution of the distribution of Te-O bonds in Te-O-Te bridges as a function of the bridge asymmetry (f). Te-O distances exhibit a broad spread around the average Te-O bond length for f values less than 0.2 Å. For f values larger than 0.2 Å, however, two populations of Te-O bonds emerge, one corresponding to short bonds less than 2 Å and the other corresponding to long bonds greater than 2 Å. The small bond shows a steady contraction as f rises, whereas the long bond experiences a quick elongation. We note that one can gain insight into structural correlations by employing f as a descriptor for the

local environment asymmetry that are otherwise invisible. By just examining the distribution of Te-O distances in Te-O-Te bridges, for instance, it is impossible to draw any meaningful conclusions about the local environment since this leads to two large, overlapping distributions. Regarding the melt, despite the widening of distribution seen owing to thermal fluctuations, similar distance variations as a function of f remain true as in the case of the glass, but with a somewhat larger population of bridges with significant asymmetry. These results are clearly compatible with the bond-valence sum rule's distortion theorem, which stipulates that when one of an atom's bond distance lowers, another bond must extend farther in order to fulfil the atom's valence (leading to an increase of the average bond length). According to the above inspection, it is likely that terminal Te=O groups can arise as a result of the Te-O-Te bridges growing asymmetry and particularly as a result of one Te-O bond's elongation.

3.2.4 Charge Analysis

We now attempt to make a link between the electronic structure to the Te and O local environments and coordination numbers. To achieve this, we used the density-derived electrostatic and chemical partitioning approach (DDEC6) [72]–[75] as utilized in CHARGEMOL package [76] (see chapter [2]). The evolution of Te and O NAC in TeO_2 glass and melt are depicted in figure [3.13] as a function of the coordination number and their local environment distributions.

In agreement with the predicted formal oxidation states ratio of Te and O in TeO_2, we find that these two elements have an average net atomic charge of +1.62 e and -0.81 e, respectively, in the glassy phase. Further, in the melt, O and Te exhibits average NAC equals to -0.80 e and +1.60 e, respectively. Te gets increasingly positively charged when additional O atoms are introduced to its first coordination shell, as seen by the evolution of Te NAC as a function of n_{TeO}, which exhibits a somewhat rising trend in both glassy and molten TeO_2. This is crucial for over-coordinated Te (5-fold Te), whose charge increases by +0.04 e and +0.03 e in the glass and the melt respectively when compared to 4-fold Te. With a decrease of -0.04 e and -0.05 e in the glass and melt, respectively, 1-fold O exhibits a higher negative NAC than 2-fold O when we look at the O NAC evolution in the figure [3.13 (b)]. The distributions of net atomic charges calculated for Te and O atoms demonstrate a strong link, on average, to the kind of local structural environment (figure [3.13 (c-d)]) despite their widening and asymmetry. The presence of Te=O chemical groups may be the cause of the significant shift in the NAC of the single folded O atom in this specific instance.

We report in figure [3.14], the evolution of the Te-O-Te bond asymmetry as a function of the 2-fold O NAC in attempt to elucidate the short-range disorder in Te-O-Te bridges in connection with electronic structure. Intriguingly, in glassy and molten TeO_2, we see a general trend for the 2-fold O NAC to be less important with rise in its associated bond asymmetry. Given that

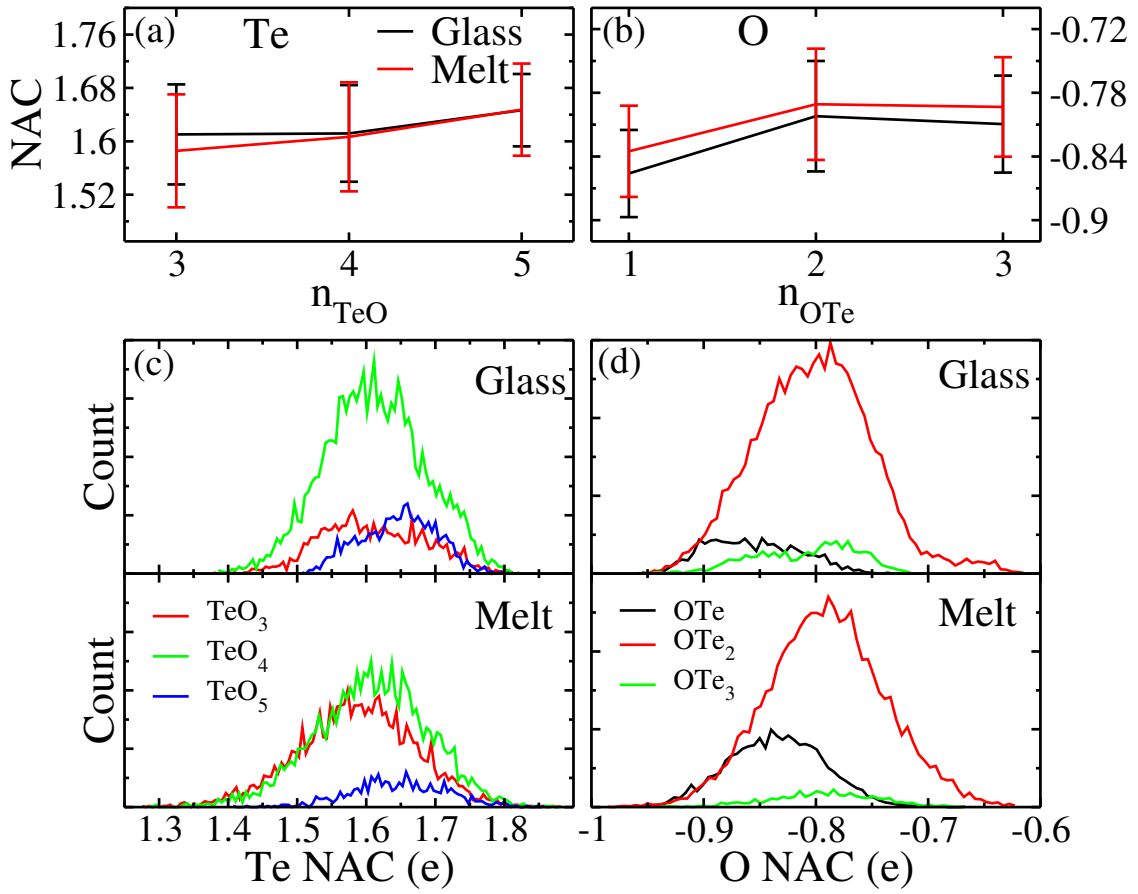

Figure 3.13: Average NACs for various *l*-fold (a) Te (*l*=3,4 and 5) and (b) O (*l*=1,2 and 3). Bottom compact figures illustrate distribution of NACs for glass and melt in the case of Te (c) and O (d).

the prolongation of one Te-O bond is the primary cause of the rise in bridge asymmetry (see fig. [3.12]) and that singly fold O atoms have a greater negative NAC than 2-fold O (see fig. [3.13]), one can extrapolate the following: if a Te atom is sufficiently pushed away from the O atom, the associated long Te-O bond can be thought of as broken, resulting in the O atom to transform into a Te=O group and featuring a significantly larger NAC. This happens in a Te-O-Te bridge, where the elongation of one Te-O bond causes a rise in the bridge asymmetry and a high negative O NAC. Even though there is no direct evidence for this process, our study reveals congruent elements that support its plausibility.

3.2.5 Electronic localization function

The electron localization function (ELF), which links the free electron states (paired and unpaired electrons) to the nature of chemical bonds, is yet another interesting indicator of the connection between bond asymmetry and electronic structure. In particular, ELF is a mathematical function that is used to analyze the distribution of electrons in a molecule or solid. It is defined as the probability density of finding a pair of electrons in a given region of space, divided by

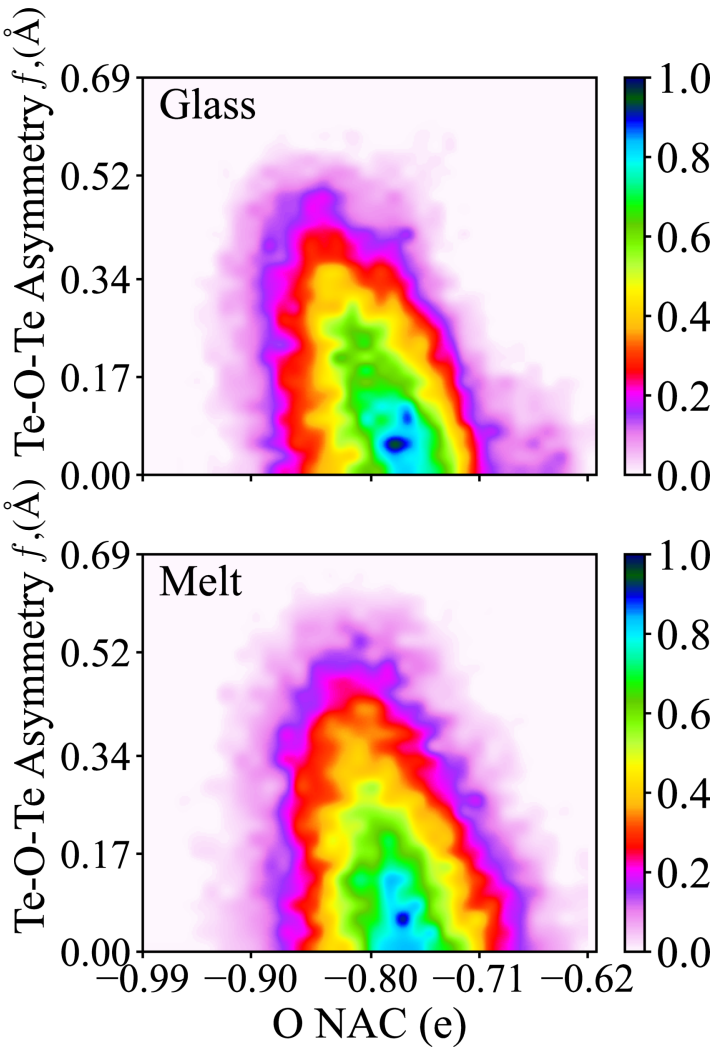

Figure 3.14: 2-D Histogram distribution of 2-fold bridging oxygen (Te-O-Te) asymmetry vs the NACs f for glassy and melt phases of TeO_2 system.

the probability density of finding the same pair of electrons in an ideal gas therefore yielding the value between 0 and 1. It provides a measure of the degree of electron localization or delocalization in a material, and can help to identify the presence of chemical bonds and lone pairs of electrons of the electronic structure. Lower ELF values indicate weak ionic, metallic, or van der Waals bonds, whereas ELF values close to 1 indicate the presence of strong covalent interactions along a given bond or lone pair electrons near a certain atom. Here, we calculate ELF using structural TeO_2 amorphous phase fragments. In particular, we choose two structural motifs, one with a nearly symmetric Te-O-Te bridge (Te-O distances of 1.96 Å and 2.04 Å), and another having an asymmetric Te-O-Te bridge (Te-O bonds with 1.97 Å and 2.21 Å). To maintain an overall charge neutrality for both motifs, we passivate O with H atoms and take into account the whole coordination shells of Te atoms. After relaxing H atoms at fixed Te and O locations, the ELF is calculated at the PBE0 level of theory. The computed ELF values for the plane containing the Te-O-Te bridge are shown in figure [3.15]. We observe a significant electron localization

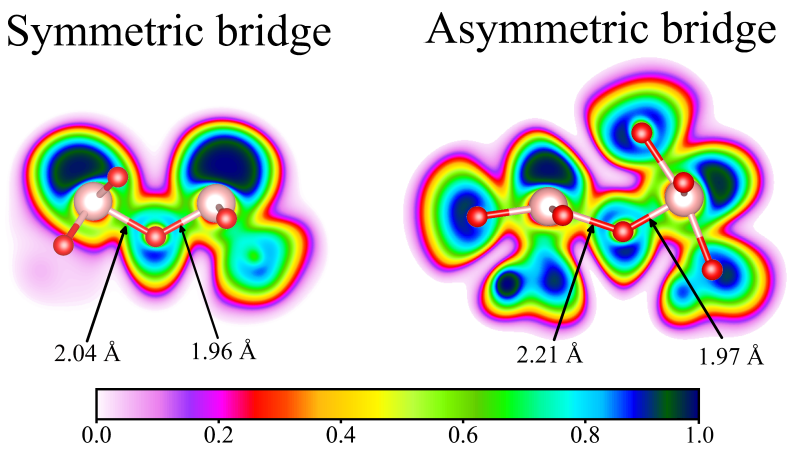

Figure 3.15: ELF was calculated for symmetric and asymmetric bridges in representative TeO_2 network glass fragments on the Te-O-Te plane. The ELF map is overlaid with the atomic structure of each component. Above the Te-O-Te plane, only Te (brown) and O (red) are depicted. For the sake of clarity, H atoms were employed but not shown to passivate O atoms.

with ELF values larger than 0.7 around Te and O atoms for both symmetric and asymmetric bridges, which could be linked with the electron lone pairs of the corresponding atoms.

Furthermore, we observe a strong electron localization along both sides of the center O atom in the symmetric Te-O-Te bridge, with ELF values greater than 0.6 suggesting that the electrons are nearly evenly distributed between the two Te atoms and the central O atom. Additionally, the ELF distribution value decreases as one gets closer to the Te atom, indicating the fact that the Te-O bonds in this fragment are iono-covalent. One observes that the electron localization distribution shows sizable variations for the asymmetric Te-O-Te bridge. While the ELF distribution along the short Te-O bond is identical to that seen around the symmetric bridge, the ELF along the long Te-O bond significantly decreases to values below 0.5 (see fig. [3.15]), indicating the presence of a weaker and more ionic nature of Te-O bond. O atoms becomes more negative as a result of capturing a greater percentage of shared electrons. These findings support the DDEC6 charge study, which established a connection between the bridge asymmetry and the O NAC.

3.2.6 Efficiency of hybrid functional on electronic localization

Finally, we focus on what makes PBE0 better in describing the structure of TeO_2. Fig. [3.16] shows the distribution of the Wannier functions spread as a function of their distance from Te atom calculated at PBE0 (model 7) and PBE (model 1) levels of theory. Regardless of the type of the Wannier center (W^{LP} or W^{B}), we remark that the absolute value of their spread is smaller in the case of PBE0 than PBE. This implies a better electronic localization from hybrid functional as expected.

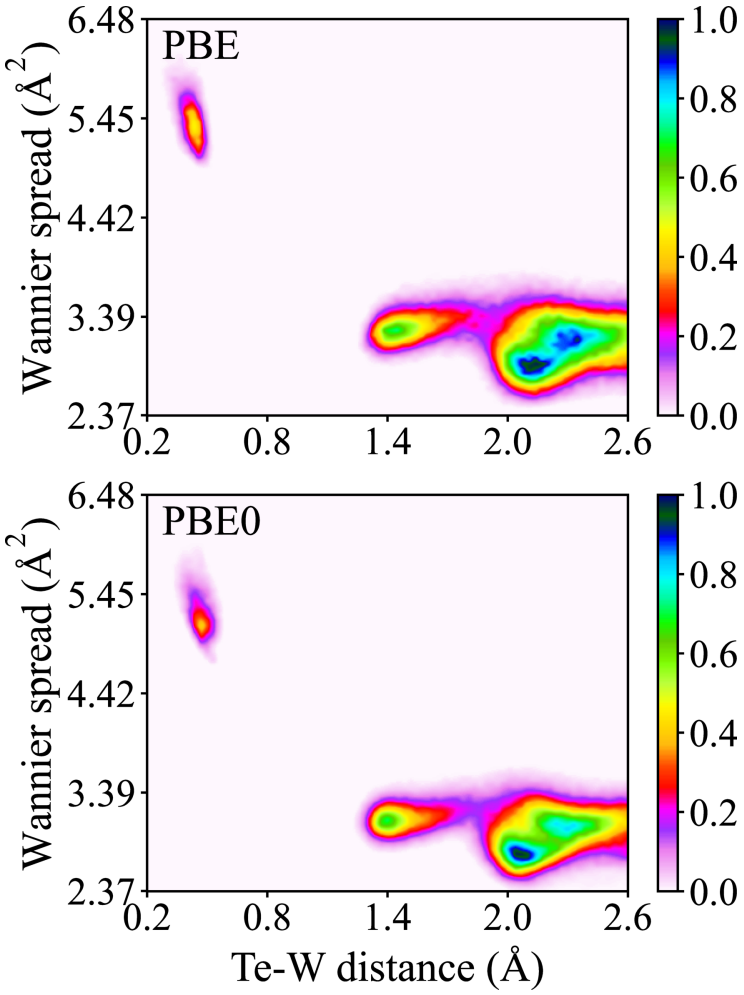

Figure 3.16: The distribution of the Wannier function spreads as a function of the distance between Te or O atoms and the Wannier centers computed at the PBE level of theory (top panel) and PBE0 level of theory (bottom panel).

3.3 Conclusions

In conclusion, using a number of DFT-based techniques, including BOMD, CPMD, and SGCPMD, we have performed first-principles molecular dynamics to generate atomistic models of TeO_2. The created models allowed us to evaluate the impacts of the DFT XC functional selection, model size effects, quenching rate effects, and variable density effects on the TeO_2 glass structure. We show that the only way to achieve an atomistic model of TeO_2 that fairly represents the structural characteristics seen experimentally is through molecular dynamics performed at the PBE0 level of theory in conjunction with a varying density melt-quench technique.

Our best model, in particular, is capable of simulating trends regarding the evolution of the PDF and S(Q) when TeO_2 transitions from melt to glass. As a result, this model was used as the foundation for an in-depth atomic-scale description of TeO_2 melt and glass. We first

concentrated on the investigation of partial pair correlation functions at melt and glassy phases, and we found by analyzing the first peak position that Te-O bond lengths are somewhat shorter in the melt than in the glass .

We demonstrated that, although allowing us to replicate the experimental observations, the integration of the partial PDFs does not give a straightforward value for n_{TeO} since a precise Te-O distance cutoff cannot be determined. By using the Wannier function formalism and providing a $r_{cut\text{-}off}$ independent description of the chemical bonds based on the locations of the Wannier centers and the geometry of the Te local environments, we were able to overcome this limitation. With the use of this method, we showed that Te has a coordination number of 3.96 in the glass and 3.65 in the melt, which is in accordance with recent experimental findings [38].

Subsequently, we examined the local surroundings of the atoms and demonstrate that Te is mostly found in 4-fold units with non-negligible proportions of 3- and 5-fold units. O atoms are commonly found in 2-fold units, however we also find a sizable number of non-bridging and 3-fold O atoms even in the glass. We found that the percentage of non-bridging O rises with temperature, which accounts for the decrease in the Te coordination number that has been reported. The bond asymmetry function, which characterizes the degree of asymmetry of a particular local environment depending on its different Te-O distances, is then introduced with an emphasis on the short-range disorder surrounding Te and O atoms. We demonstrated that the distribution of asymmetry around Te and O is wider throughout the melt.

We also deduced that an increase in temperature causes the asymmetry of TeO_4 units to grow, and consequently transforms into a highly asymmetric TeO_3 units. In fact, we find that two-fold O has a short (less than 2 Å) and a long bond (larger than 2 Å). Te-O-Te bridges are thought to change into terminal Te=O groups when the short-range disorder around the Te atom rises, as shown by the observation that the short bond slowly contracts while the long bond rapidly elongates as the asymmetry of two-fold O increases.

Finally, by examining the electronic structure of the atomic fragments, we solidified the structural analysis. According to the analysis of the net atomic charge, Te has a little lower charge in the melt than glass, whereas O has a slightly higher charge (less negative). It's interesting to note that, in comparison to other Te and O structural units, 5-fold Te and 1-fold O demonstrate more significant change in NAC. Furthermore, our findings demonstrate the relationship between the Te-O-Te bridge asymmetry and the 2-fold O NAC, where the O NAC tends to have greater negative values as f rises. Studying the electron localization function of a symmetric and an asymmetric Te-O-Te bridge reveals that in the former, Te-O bonds are iono-covalent with significant charge localization along the bond and higher ELF values near O, while in the latter, the short bond

exhibits a charge localization similar to that seen in symmetric bridges while the long bond exhibits a low charge localization along the Te-O connection, indicating an ionic interaction.

The results of hybrid functional molecular dynamics when used on oxide materials are benchmarked by our work. The image resulting from our work shows TeO_2 as a network composed of several TeO_x units with a significant short-range disorder. Bond asymmetry is a part of this disorder and increases as the temperature rises. Te coordination number decreases as a result, going from 3.96 in the glass to 3.65 in the melt. Additionally, the growing disorder surrounding two fold-O atoms causes one Te-O bond to lengthen, which in turn causes the O negative charge to rise and trend toward that seen for non-bridging O atoms. As a result, investigations of both structural and electronic properties offer consistent evidence that Te=O groups exist in TeO_2 glass.

4

Structure of Tl_2O-TeO_2 binary glasses

Summary

4.1 Generation and validation of the glassy models **125**
4.2 Structural analysis **129**
4.2.1 Pair distribution functions 130
4.2.2 Coordination numbers 134
4.2.3 Atomic local environment 143
4.2.4 Rings statistics 147
4.2.5 Bulk Modulus 148
4.3 Relating structural and electronic properties **150**
4.3.1 Charge analysis 150
4.3.2 Electronic localization function 152
4.4 Conclusions **154**

PURE TeO_2 is a conditional glass former [100] and requires rapid quenching rates to obtain stable amorphous samples [101]–[106]. To overcome this constraint, TeO_2 might be combined with other modifier oxides (MO) [107], [108]. Particularly, thallium oxide (Tl_2O) has drawn a great interest as a MO because, in contrast to other MOs, its inclusion causes the high non-linear optical properties of TeO_2-based materials [46], [109] to be maintained despite promoting structural depolymerization as shown by Raman spectroscopy [9], [110], [111]. The boron group's rarest element, thallium, is found in two oxide forms: thallous oxide (Tl_2O) and thallic oxide (Tl_2O_3). We are not aware of any study that indicates the effectiveness of Tl_2O_3 as a MO, while Tl_2O has been frequently studied as a MO in TeO_2-based glass [46], [108], [109], [111]. The TeO_4 disphenoids [106], [110], which makes up the atomic-scale structure of TeO_2 glass, has an electronic lone pair (LP) in the proximity of Te atom and are connected to each other via Te-O-Te linkages. The incorporation of modifier oxide into TeO_2 amorphous phase causes the original TeO_4 disphenoids to transform into TeO_3 trigonal pyramidal units, which reduces the coordination number of Te^{4+} cation and leads to structural depolymerization [107]. While this decrease in the coordination number often results in decline in the nonlinear optical properties of the material, the incorporation of Tl_2O modifier exhibits the opposite tendency.

The Tl^+ local environments in the amorphous matrix are mostly unknown. For instance, it is not well understood how thallium atom bonds with the bridging oxygens (BO) and non-bridging oxygens (NBO) in the structure of Tl_2O modified TeO_2 glasses. The experimental results on $(Tl_2O)_x$-$(TeO_2)_{1-x}$ glasses, aside from investigations based on Raman spectroscopy, were more concerned with the macroscopic characteristics rather than its atomic-scale description. To the best of our knowledge, there is no research on the computational study of the Tl_2O-TeO_2 amorphous system. At this level, *ab-initio* modelling can assist in identifying the contribution of thallium oxide to the structural and optical properties of Tl_2O-TeO_2 binary glasses.

4.1 Generation and validation of the glassy models

Using PACKMOL code [112], randomly oriented TeO_2 and Tl_2O molecules in a cubic simulation cell have been distributed in order to generate several random initial systems of $(TlO_{0.5})_x - (TeO_2)_{1-x}$ with different compositions (x). Particularly, we produced 5 models with various $TlO_{0.5}$ molar concentrations (parameters listed in table [4.1]) to comprehend the influence of Tl incorporation into TeO_2 glassy system.

Concentration (x)	No. of Tl/Te/O (Total)	ρ (g.cm^{-3}) [113]	Simulation cell lengths (Å)
x = 10%	16/144/296 (456)	5.85	19.57
x = 20%	32/128/272 (432)	6.12	19.47
x = 30%	48/112/248 (408)	6.40	19.38
x = 40%	72/108/252 (432)	6.68	20.07
x = 50%	90/90/225 (405)	6.95	20.00

Table 4.1: Description of $(TlO_{0.5})_x - (TeO_2)_{1-x}$ amorphous systems with various concentrations (x) in a cubic simulation cell.

We carried out *ab-initio* MD simulation using the quickstep module of the CP2K [77] with atom-centered Gaussian and plane waves (GPW) approach to solve the Kohn-Sham equation under the BOMD scheme. For all the atoms, molecularly optimized triple-zeta valence polarization Gaussian type basis set [88] was utilized to expand Kohn-Sham orbitals, in addition to the norm conserving pseudopotential of type GTH [78], [79]. Furthermore, the energy cut-off of 450 Ry and the relative cut-off of 50 Ry were utilized to establish the plane wave basis set. In addition, we employed GGA exchange-correlation energy using PBE functional [89]. For the models under consideration, all simulations were conducted with periodic boundary conditions. The dynamical equations were integrated with time step of 1 fs. Furthermore, the canonical ensemble (NVT ensemble) was used, in which the number of particles, volume of simulation cell, and system temperature are kept constant throughout the *ab-initio* MD simulation. Additionally, for controlling the temperature we have used Nosé-Hoover thermostat [67]–[69] with a time constant of 20 fs.

We have produced glassy systems through melt-quench protocol. The process starts with a quick simulation of the randomly initialized models for 5 ps at T = 300 K and 5 ps at T = 600 K, followed by equilibration run at the melting temperature of T = 1000 K. To ensure that liquids are well equilibrated, the system was maintained at this temperature for 45 ps until the diffusion coefficients of all atomic species demonstrated behavior consistent with that of a liquid. Subsequently, the glassy state was achieved by quenching/cooling the system down to room temperature from T = 1000 K by executing 30 ps of equilibration at intermediate temperatures of T = 600 K. Finally, the system was equilibrated for another 30 ps at T = 300 K in order to obtain the production trajectory. The results discussed in this work for the glass at T = 300 K was obtained by analyzing the last 10 ps of the production trajectory. Further, in this study, the output pressure for all the considered systems is found to be of the order of 2 GPa. To ensure that the results of structural analysis are not affected by any initial biases, each system is consistently relaxed by increasing the length of the simulation cell isotropically and recomputing the output pressure until a value less than 0.1 GPa is reached. Upon comparing the PDF of the relaxed

system with the unrelaxed system, it is observed that there is very limited difference, which is why the unrelaxed system is chosen for further analysis.

Further, structural comparison between the simulated glasses and experimental data at T = 300 K is performed by calculating the X-ray total pair distribution function G(r) (see figure [4.1]). The minor oscillations in experimental PDF at lower r in the range of 0 to 1.64 Å can be attributed to imperfections in the raw data corrections and the relatively small value of Q_{max} = 17 $Å^{-1}$ used in the Fourier transformation of the structure factor. Overall, our models reproduce the experimental

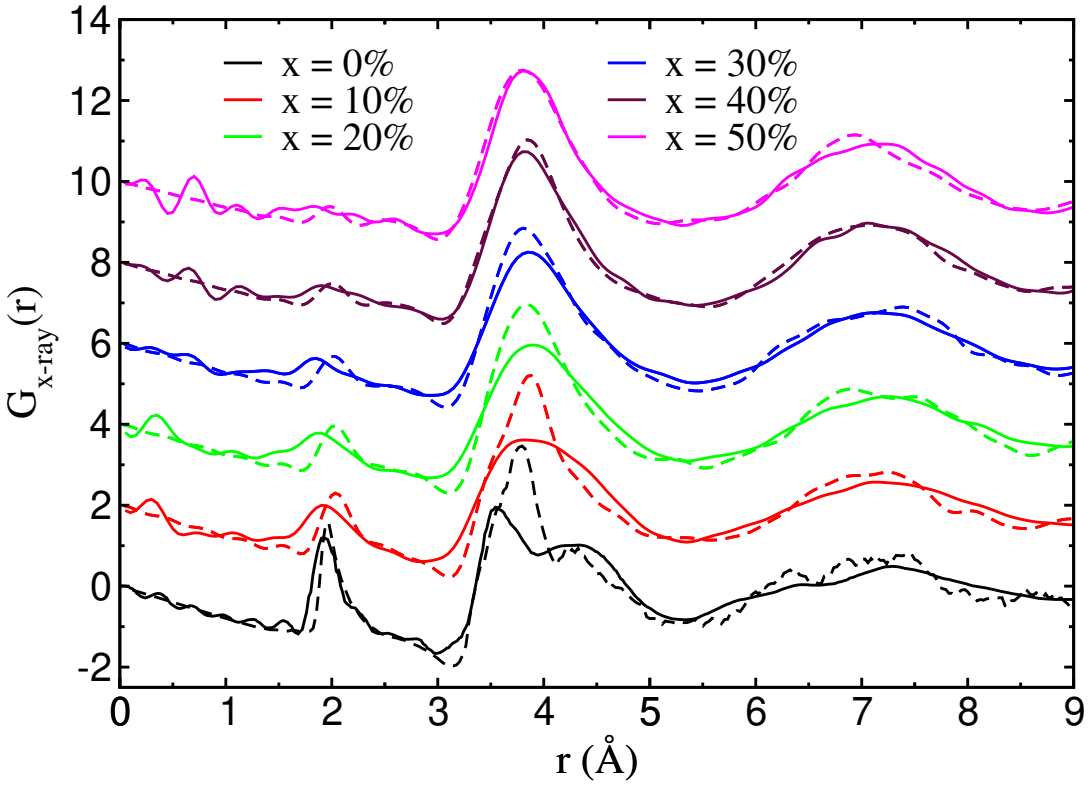

Figure 4.1: Comparison of total X-ray scattering PDF G(r) between experiments (solid lines) [113] and *ab-initio* MD simulation (dashed lines) for $(TlO_{0.5})_x - (TeO_2)_{1-x}$ binary glassy system with various concentrations (x). Experimental and simulated data for x = 0% are taken from Alderman *et. al.* [38] and calculated from PBE0 hybrid XC functional (see chapter [3])
. A shift of 2 units in the y-axis is given to various concentrations for better clarity of the graph.

trends with reasonably good accuracy. Our earlier research with pure TeO_2 (see chapter [3]) has shown that the PBE0 Hybrid functional should be used to solve the exchange-correlation part of the Kohn-Sham equation in order to more accurately replicate the observed peak around 4 Å. The hybrid functional performs electron localization more accurately to approximate the lone pair on the tellurium atom, therefore ensures better estimation of Te-Te distances (∼4 Å) than PBE functional. However, given the huge computational expenses of working with hybrid functional we decided to remain with PBE-GGA functional in the case of $(TlO_{0.5})_x - (TeO_2)_{1-x}$ binary

glassy system. It is significant to note that as tellurium atoms are replaced by thallium atoms in the system, the accuracy of the PDF G(r) increases, indicating that the role of hybrid functional becomes less important and that the PBE functional performs reasonably well with lesser tellurium content. The underlying reason behind this trend will be explored later in this chapter.

To begin with, we see that the calculated first peak which can be attributed to Te-O distances around 2.0 Å in the total PDF is shifted towards higher distances by ∼0.1 Å as compared to experimental counterpart. This shift in the position of the first peak can be assigned to the nature of the GGA functional which is known to promote over estimation of bond lengths. Additionally, similar to the experiments we see that the area enclosed by first peak decreases with the addition of thallium oxide molar concentration. We remark that our models show an overall good agreement with the experiments for distances larger than $r > 5$ Å. In addition, we do point out that the computed PDF capture all the experimental trends found in $(\mathrm{TlO}_{0.5})_x - (\mathrm{TeO}_2)_{1-x}$ binary glasses which indicates that our models are able to capture the structural reorganization in the glass at various compositions (x).

We have evaluated the performance of our models in real space, and now we proceed to its assessment in reciprocal space. To do so, we plot the total X-ray structure factor $S_{\text{X-ray}}(q)$ for all the compositions in $(\mathrm{TlO}_{0.5})_x - (\mathrm{TeO}_2)_{1-x}$ binary glasses simulated at T = 300 K and compared them with their experimental counterpart (see figure [4.2]). The total X-ray structure factor $S_{\text{X-ray}}(q)$ can be computed using following relation:

$$S_{\text{X-ray}}(q) - 1 = \sum_{\alpha=1}^{n} \sum_{\beta=1}^{n} \frac{c_\alpha c_\beta f_\alpha f_\beta}{|\langle f \rangle^2|} [S_{\alpha\beta}^{FZ}(q) - 1], \tag{4.1}$$

where, c_α and f_α are the atomic fraction and the corresponding scattering factors, respectively and $S_{\alpha\beta}^{FZ}(q)$ is the partial Faber-Ziman structure factor constructed from partial PDFs between atomic species α and β is defined as:

$$S_{\alpha\beta}^{FZ}(q) - 1 = \frac{4\pi\rho_0}{q} \int_0^\infty r[g_{\alpha\beta}(r) - 1] sin(qr) dr. \tag{4.2}$$

Here, ρ_0 is the atomic number density. We find an overall good level of agreement between the calculated and experimental $S_{\text{X-ray}}(q)$ across the whole experimental q range. Thus, based on the good performance of our models in both real and reciprocal space, we now proceed to the next section where we study in depth the partial contribution of each atomic pairs that lead to the observed evolution of the total PDF G(r).

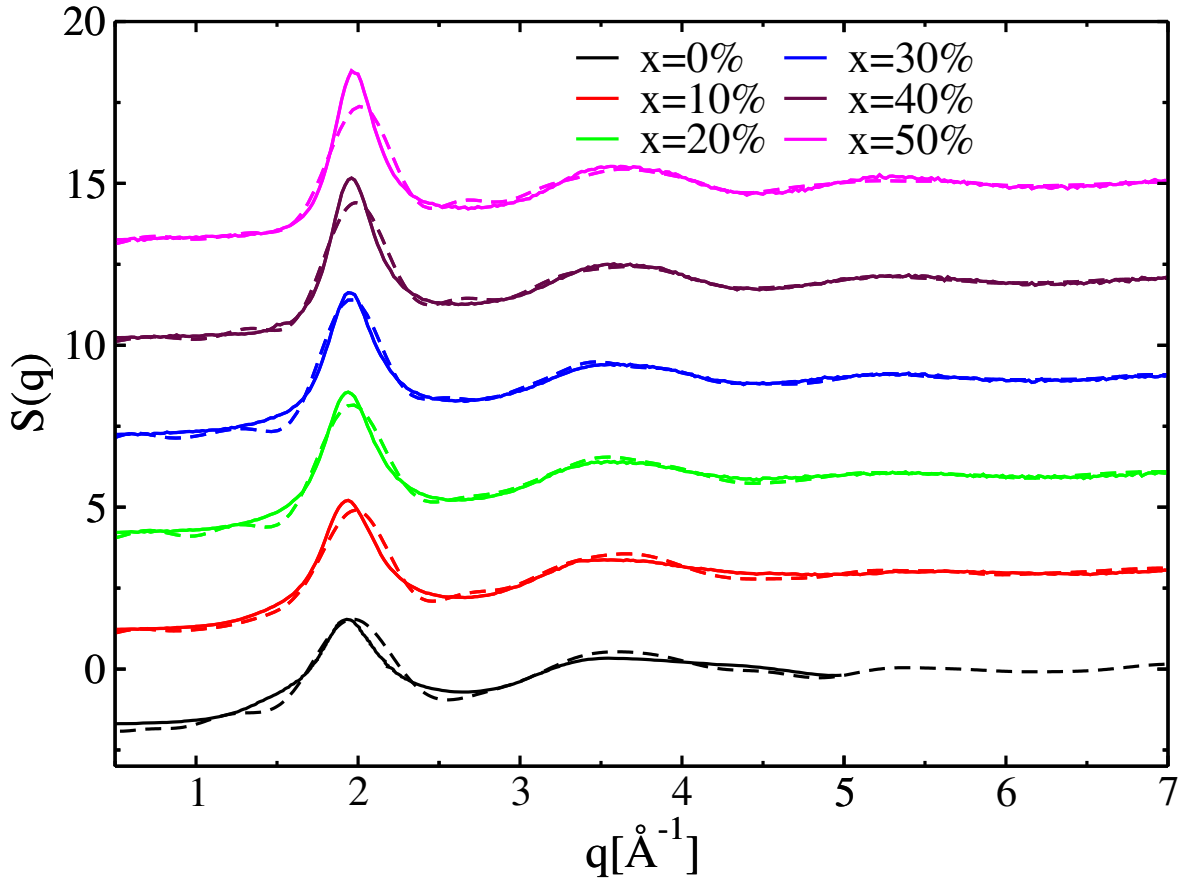

Figure 4.2: Comparison of total X-ray structure factor computed (dashed lines) for various $(TlO_{0.5})_x - (TeO_2)_{1-x}$ binary glasses with experimental data (solid lines) [113]. Experimental and simulated data for x = 0% are taken from Alderman *et. al.* [38] and calculated from PBE0 hybrid XC functional (see chapter [3])

. The curves are shifted vertically for clarity.

4.2 Structural analysis

In this section, we discuss the structural analysis of the $(TlO_{0.5})_x - (TeO_2)_{1-x}$ binary glasses. Commonly considered quantities like partial PDF, coordination numbers, atomic local environments will be discussed in this section. In addition, we also emphasize the role of bridging and non-bridging oxygen as its description is necessary to analyze the structural matrix with particular attention to the depolymerization of -Te-O-Te- network. We further investigate the rings statistics of the network generated by various compositions of glass. We also study the mechanical stability of the modified glassy systems by computing their bulk modulus. Finally, we close this section by computing the electron localization function (ELF) to understand the strength of bonding between various cations and oxygen in the system.

4.2.1 Pair distribution functions

Short-range correlation of $(TlO_{0.5})_x - (TeO_2)_{1-x}$ binary glasses were analyzed by calculating the partial PDFs $g_{\alpha\beta}(r)$. Various partial O-O, Te-O, Tl-O, Te-Te, Te-Tl and Tl-Tl PDFs are illustrated in figure [4.3]. In the forthcoming paragraphs, we focus on understanding how the partial PDFs evolve as a result of the inclusion of the thallium-oxide modifier. Furthermore, throughout this subsection, bridging-oxygens (BO) are defined as oxygen atoms bonded to at least two tellurium atoms, otherwise categorized as non-bridging oxygens (NBO).

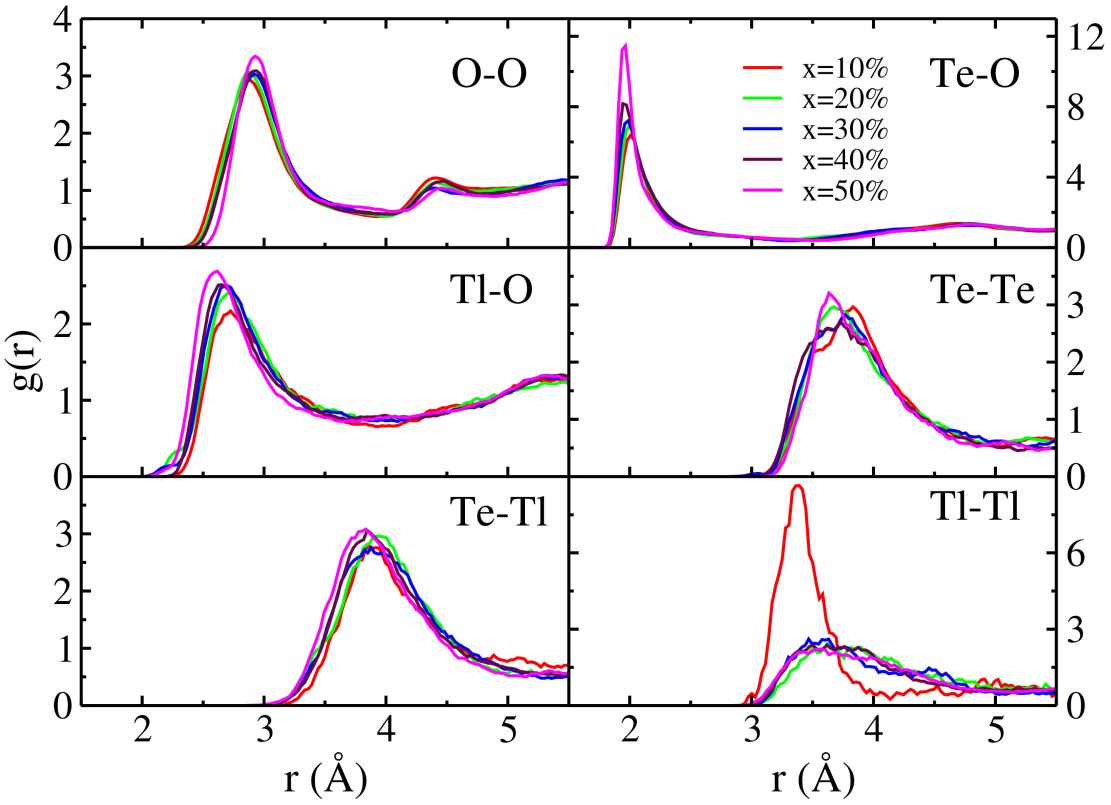

Figure 4.3: The partial pair correlation functions $g_{O\text{-}O}(r)$, $g_{Te\text{-}O}(r)$, $g_{Tl\text{-}O}(r)$, $g_{Te\text{-}Te}(r)$, $g_{Te\text{-}Tl}(r)$ and $g_{Tl\text{-}Tl}(r)$ for various concentration of modifier in binary $(TlO_{0.5})_x - (TeO_2)_{1-x}$ glass.

To begin with, in the case of the first peak of the Te-O partial PDF, two significant patterns may be seen. First, we see that increasing the modifier concentration leads to an increase in the intensity of the first peak (see figure [4.3]). To understand this trend, we split the Te-O bonds into the contribution from the Te-BO and that of Te-NBO bonds and plot the distribution of their distances (see figure [4.4]). From figure [4.4], as the concentration of the modifier increases, the intensity of the Te-BO bond distribution decreases and that of the Te-NBO bond distribution increases. Another way to look at it is that when Te-BO distribution declines, the area it covers is transferred to Te-NBO distribution, which has a more symmetric and narrower distribution. As a result, we see a rapid increase in intensity that corresponds to Te-NBO distribution. Therefore,

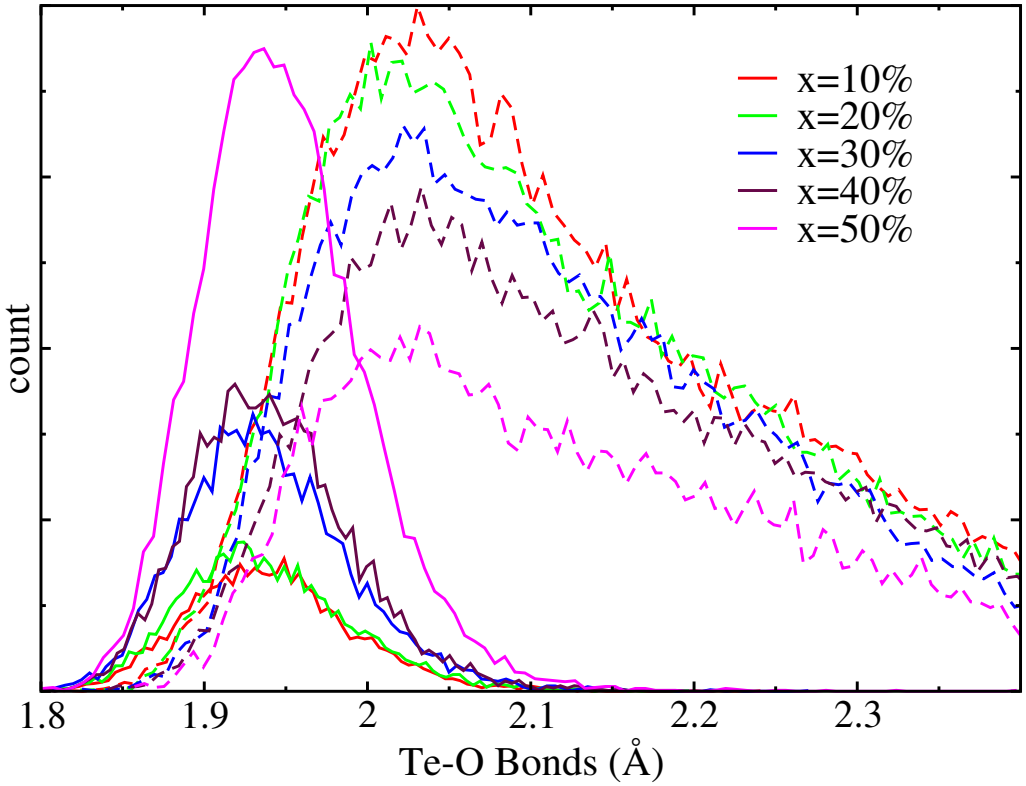

Figure 4.4: Histogram of distribution of bond-distances in Te chemical groups with bridging oxygen (dashed lines) and non-bridging oxygen (solid lines). All the peaks are normalized with the number of Te atoms present in each concentration.

we conclude that this explains the rising intensity in the first peak of the partial $g_{Te\text{-}O}(r)$ PDF (see figure [4.3]). Second, it appears that the first peak of $g_{Te\text{-}O}(r)$ has been slightly shifted toward a smaller value of r and this shift increases when more modifier units are added. This shift can be described on the basis of the breakdown of the Te-O-Te bridges which result in an increase in the population of NBOs. In general, TeO_3 contains terminal oxygen atoms, or Te-NBO pairs, which in order to balance the bond valence of Te cation, results in smaller average Te-NBO bond distances than Te-BO pairs. This prolepsis is supported by our observations of the Te-BO and Te-NBO distance distributions (see figure [4.4]), which shows that the contribution of Te-NBO bonds rises with increasing thallium-oxide concentration and have average distances that are 0.1 Å shorter than those of Te-BO bonds. Furthermore, we see that neither the Te-BO nor Te-NBO peak, at any concentration, exhibits a significant change in its peak location. Therefore, we draw the conclusion that the general shift of the Te-O peak in the partial PDF (see figure 4.3) to shorter distances with adding modifier content is caused by the rising population of Te-NBO pairs. These

findings are in line with the shift of first peak in experimental G(r) data shown in figure [4.1].

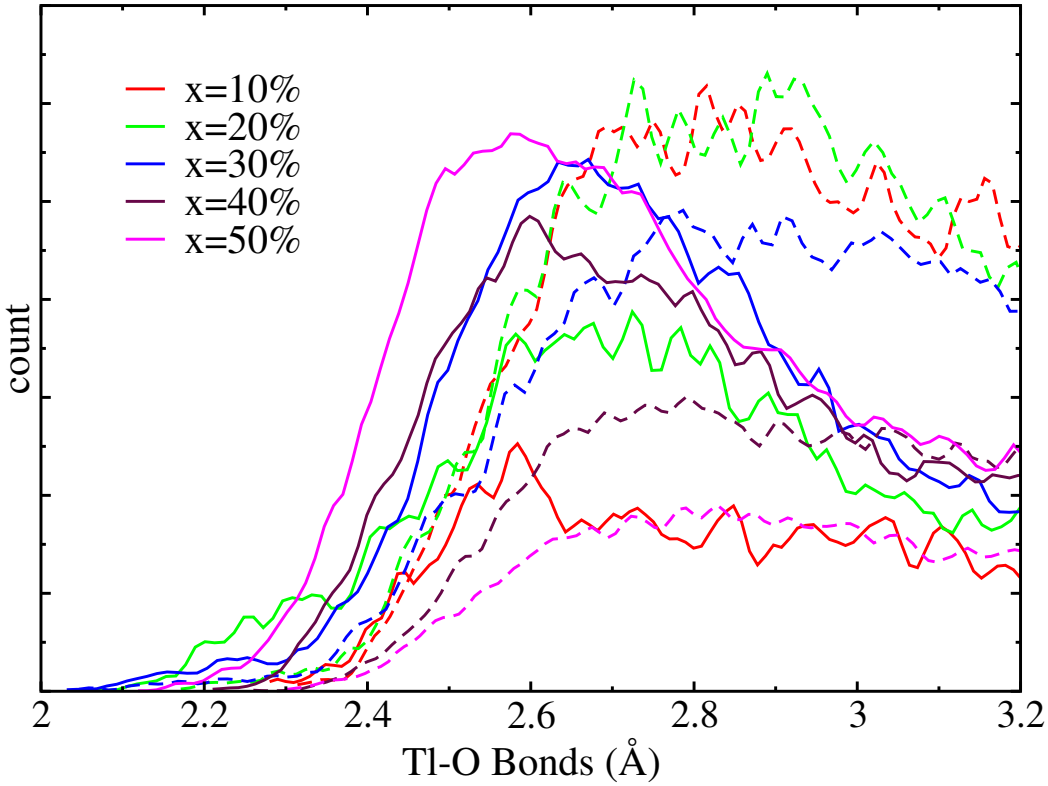

Figure 4.5: Histogram of distribution of bond-distances in Tl chemical groups with bridging oxygen (dashed lines) and non-bridging oxygen (solid lines).

As for Tl-O partial PDF, we observe a noticeable shift towards shorter distances, from the peak position at 2.74 Å for x = 10% to 2.61 Å for x = 50% (see figure [4.3]). To understand this behavior, we plot the histogram representation of Tl-BO and Tl-NBO distances (see figure [4.5]), which demonstrates that at x = 50% modifier concentrations, Tl-NBO distribution, displays maxima at smaller distances and dominates the glassy structure as opposed to the broad peak of Tl-BO distances. Further, we see that the intensity of the Tl-BO peak generally declines while the intensity of the Tl-NBO peak grows, which suggests that the addition of a modifier encourages a rise in Tl-NBO counts due to increasing NBO content and a fall in Tl-BO counts owing to a decrease in BO content. In addition, we also notice that the peak of Tl-NBO distances features a shift towards shorter distances with the addition of thallium oxide whereas the location of Tl-BO peak remains almost unchanged. Both the observation of the rising Tl-NBO population and the shift towards smaller distances explains the origin of movement of Tl-O peak in partial $g_{Tl\text{-}O}(r)$

PDF (see figure [4.3]) to lower r value. Additionally, we see that the first peak intensity in partial $g_{Tl\text{-}O}(r)$ PDF increases as the molar concentration of thallium oxide increases. This is simply due to the narrow distribution of Tl-NBO linkages compared to Tl-BO distance distribution (see figure [4.5]), which makes the $g_{Tl\text{-}O}(r)$ first peak relatively symmetric and hence, promotes the intensity of the first peak.

Further, we notice that adding thallium-oxide in TeO_2 glassy network leads to a slight shift of the $g_{O\text{-}O}(r)$ first peak from around 2.88 Å for x = 10% to 2.93 Å for x = 50% (see figure [4.3]). To explain this shift, we categorize oxygen atoms into BOs and NBOs, and subsequently plot the distribution of distances between BO-BO, NBO-NBO, and NBO-BO pairs (see figure [4.6]). First and foremost, we see that when thallium-oxide modifier is added, the contribution of

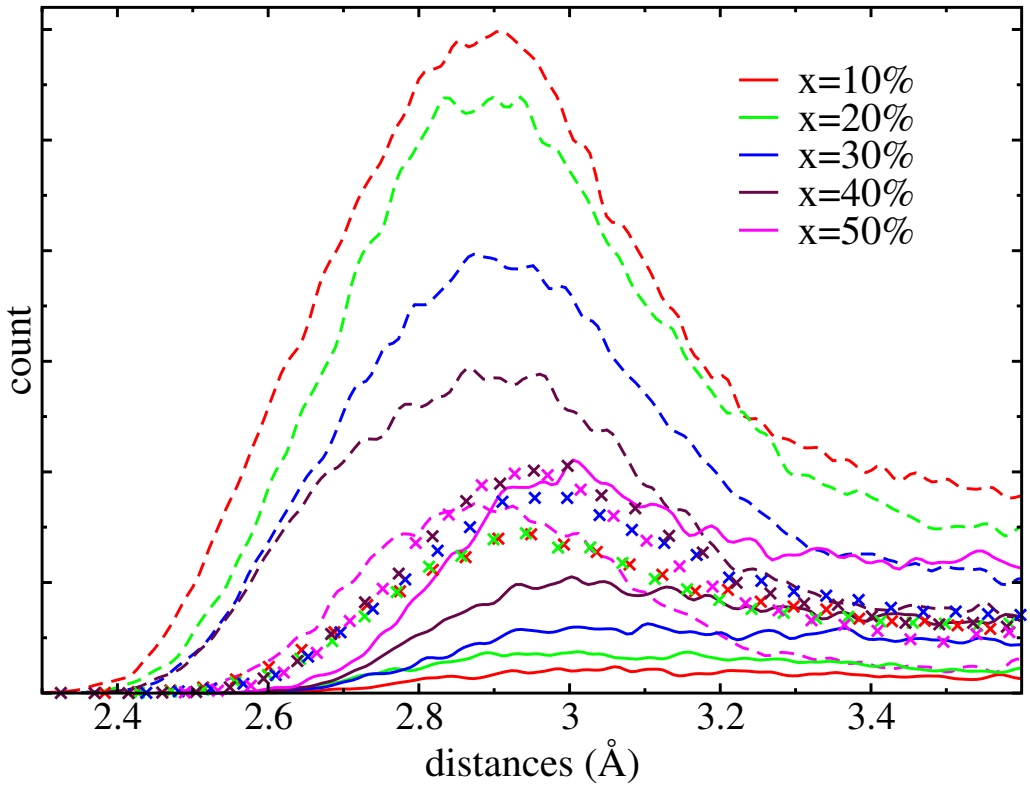

Figure 4.6: Histogram of distribution of bond-distances between bridging-bridging oxygen (dashed), non-bridging oxygen - non-bridging oxygen (solid) and non-bridging - bridging oxygen (x symbol) linkages.

the BO-BO pair starts to decline while the NBO-NBO and NBO-BO pairs show a rising trend. Secondly, we notice that NBO-NBO pairs generally feature their peak at higher distances than BO-BO pairs. We refer to chapter [3], where it was shown that NBOs have higher negative charges than BOs, which causes them to exhibit more self-repulsion to one another, resulting in larger NBO-NBO distances. Therefore, the rise in the distribution of NBO-NBO population and featuring its maxima at shorter distances than BO-BO distribution with addition of thallium oxide

modifier explains the observed shift in the partial PDF of O-O pair (see figure [4.3]), especially at x = 50% where NBO-NBO population exceeds BO-BO population (see figure [4.5]).

Furthermore, figure [4.3] shows that the addition of thallium oxide has a limited effect on the peak position for the partial PDFs of Te-Te and Te-Tl pairs. Particularly, the first peak of the Te-Te partial PDF for all the compositions shows a maxima at roughly 3.7 Å, almost exactly matching those obtained for pure TeO_2 glass. As for Tl-Tl correlation, a similar pattern was seen for various compositions, with the exception of x = 10%, where the small number of Tl atoms in our model are subject to large statistical fluctuations (clustering).

4.2.2 Coordination numbers

We assess the coordination number of distinct atoms to dig deeper into the investigation of local environments. In particular, we discuss the coordination environments around Te and Tl atoms.

Te-O coordination number

We begin by discussing the coordination number $n_{Te\text{-}O}$ of Te, which as discussed in chapter [3], due to the ill description of the first minima in the partial PDF of TeO pairs (see figure [4.3]), no unambiguous value of coordination number can be achieved. Therefore, in order to understand the complex bonding environments, we turn to the MLWF analysis and utilize hybrid PBE0 XC functional to evaluate the Wannier function centers (W) and plot the histogram of Te-W and O-W distances (see figure [4.7]). The W center assigned to the respective lone pairs of atoms are represented by the first peak, which is centered about 0.5 Å in the case of Te-W and 0.32 Å in the case of O-W pair distance distribution. Similar to this, bonding W are responsible for the second peak in both distributions. By adding the distances of second minima, which indicate the bonding W, in both distributions, one can estimate the $r_{cut\text{-}off}$ value characterizing the Te-O bond. We determine the $r_{cut\text{-}off}$ value in binary glasses to be 2.46 Å for all compositions. It is worth noting that identical results were also achieved with pure TeO_2 (see chapter [3]), indicating that the addition of thallium have a slight impact on the TeO bond length, and distance cut-offs ($r_{cut\text{-}off}$) remain constant.

Having established the distance cut-off ($r_{cut\text{-}off}$) value, we now move to computing the coordination number. To do so, we sit on each Te atom and look for O atom with the radius ($r_{cut\text{-}off}$). Now in order to characterize the selected Te-O pair as chemical bond, we impose two constraints. First, we introduce distance tolerance constraint in order to account for W^B centers shifted off the line joining TeO due to statistical or numerical inaccuracies. To account for this, we show (see figure [4.8]) the histogram distribution formed by the difference between the total of the Te-W and O-W distances to TeO distances within a sphere of 2.46 Å centered at Te. We can see

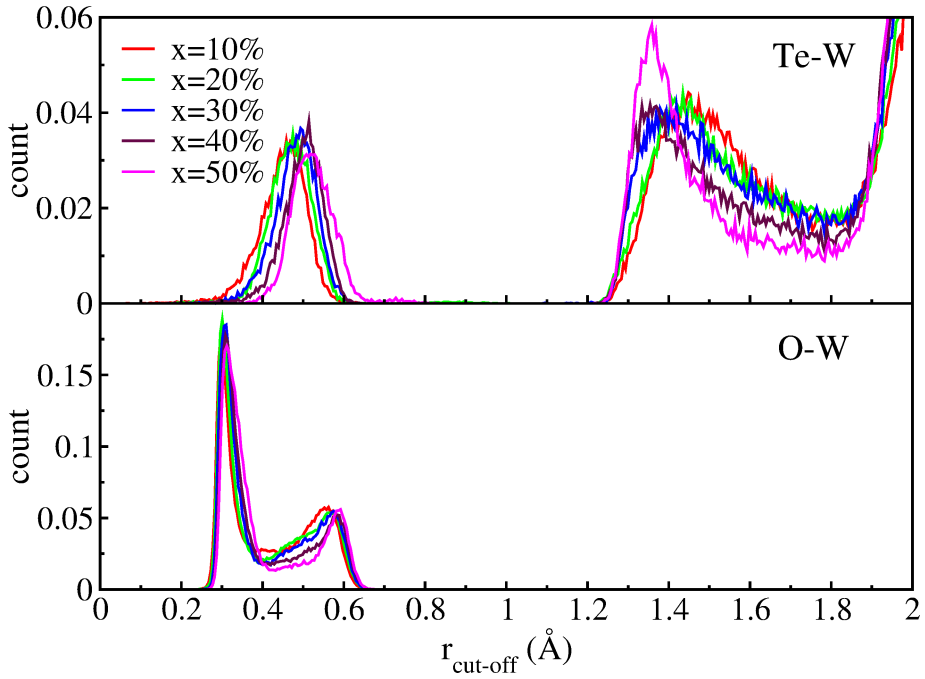

Figure 4.7: Histogram of distribution of the Wannier centers around Te (top panel) and O (bottom panel) in various $(TlO_{0.5})_x - (TeO_2)_{1-x}$ binary glass.

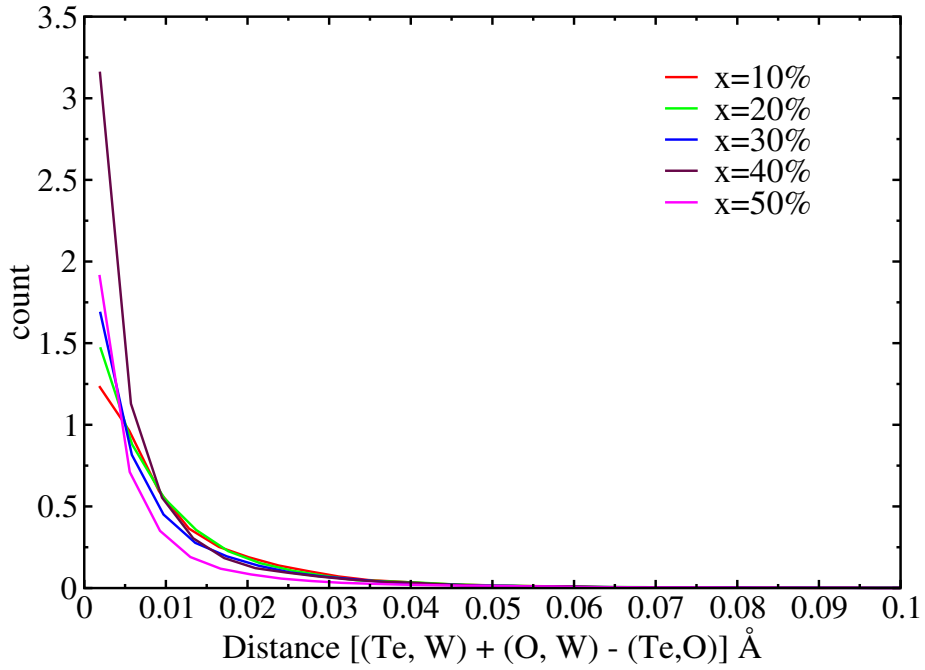

Figure 4.8: Histogram of difference of sum of Te-W and O-W center to TeO distance.

from the figure that 0.05 Å is a reasonable value to include the W^B centers that are displaced from TeO bonds, thus we implement the distance constraint as follows:

$$|d(\text{Te},\text{W}^\text{B}) + d(\text{O},\text{W}^\text{B}) - d(\text{Te},\text{O})| \leq 0.05 \text{ Å}. \tag{4.3}$$

Second, as discussed in our earlier work, some bonding W^B are oriented towards lone pair W^{LP}_{Te}, which does not qualify Te-O pairs to be identifiable as chemical bonds (see figure [3.6b]). Therefore, in order to obtain tolerance value of $\Theta(W^{LP}_{Te} - \text{Te-O})$ as discussed in chapter [3], we equilibrate three Te-Tl based polymorphs, namely $Tl_2Te_2O_3$, $Tl_2Te_2O_5$ and $Tl_2Te_3O_7$ using PBE XC functional at T = 300 K for 20 ps. Subsequently, we perform Wannier analysis using PBE0 hybrid XC functional on 100 evenly spaced snapshots taken from last 10 ps of the trajectory and plot the obtained BAD of angles formed by Te with its lone pair and O atom (see figure [4.9]). From the figure, we establish that the value of BAD only starts to rise after a value of 73°

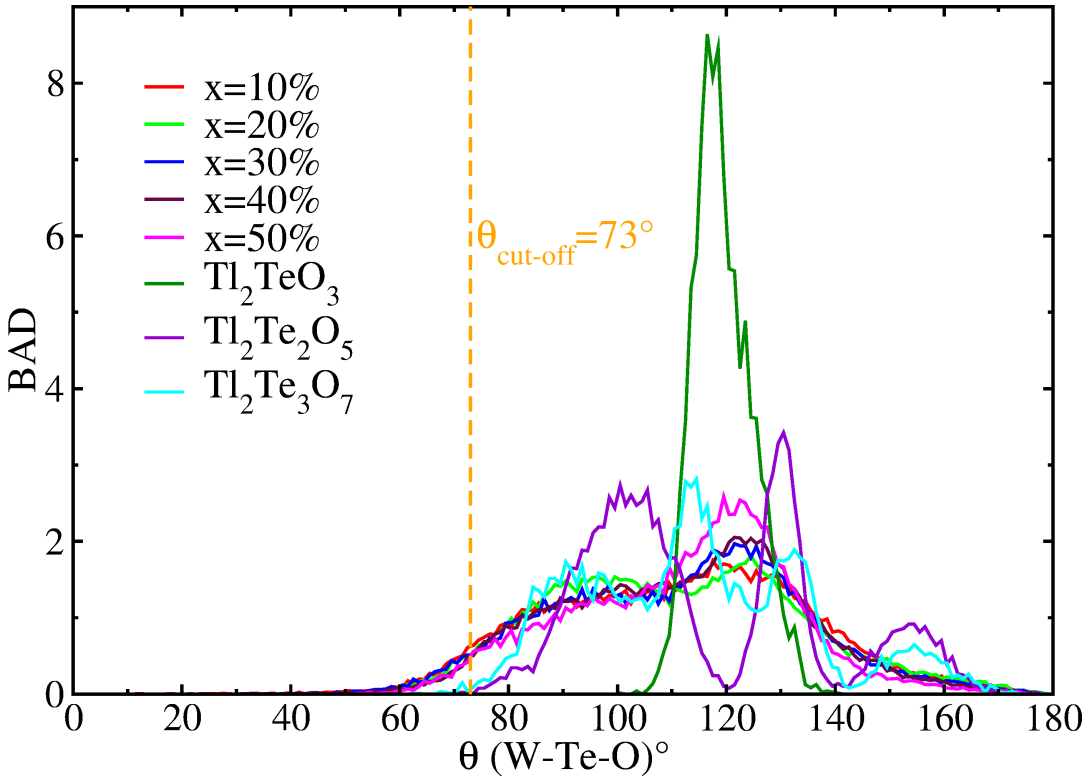

Figure 4.9: Bond angle distribution of angles formed by Te with its lone pair (W) and oxygen atom (Θ (W-Te-O)). In glasses, TeO cut-off of 2.46 Å is used while in the case of crystals cut-off of 2.3 Å is used.

for crystalline systems. Thus, based on this value we have ignored all Te-O bonds in structural motifs that form angle $\Theta(W^{LP}_{Te} - \text{Te-O})$ less than 73° in all compositions of the binary glass. As a result, for identifying Te-O bond to be a chemical bond, we implement the constraint

$$\Theta(W^{LP}_{Te} - \text{Te-O}) \geq 73°. \tag{4.4}$$

Using this approach, we can demonstrate that Te ions are bonded to two distinct types of oxygen as:

1. BO forming Te-BO-Te bridges, and
2. NBO formally due to terminal oxygen (Te=NBO) or Te-NBO-Tl linkages.

Using both constraints we also plot the running coordination number as a function of TeO distance (see figure [4.10]). It has been noted that in the modified glass, the coordination

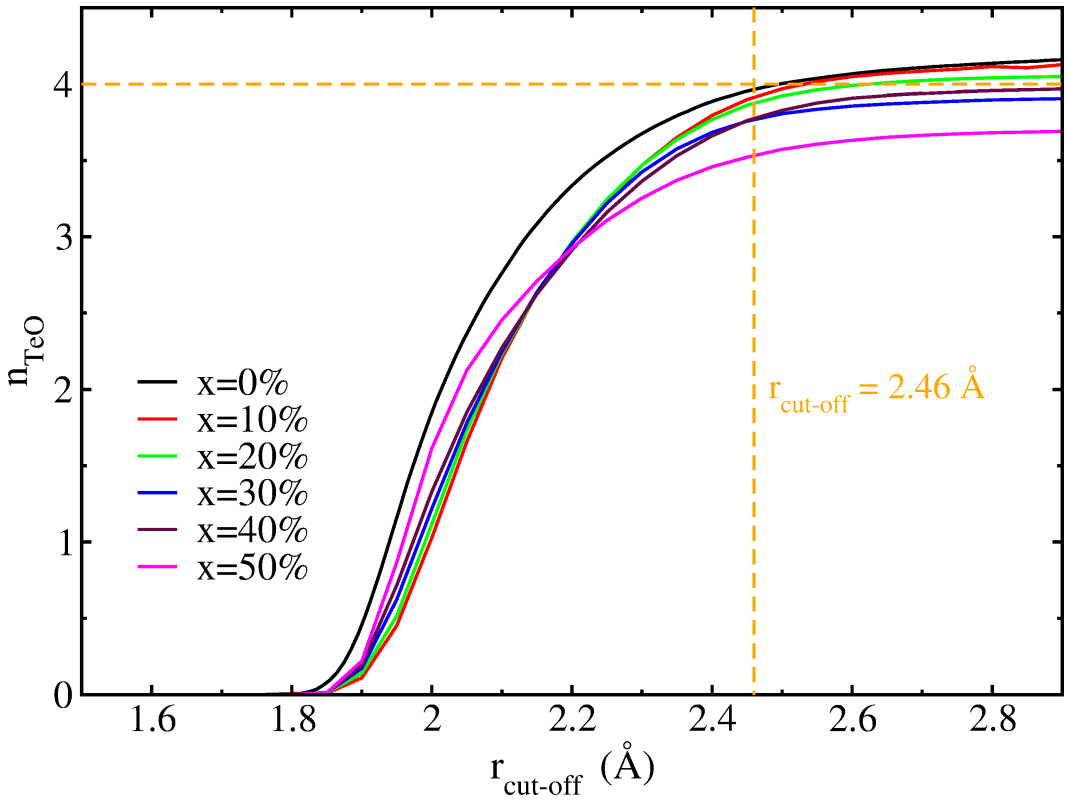

Figure 4.10: For all the $(TlO_{0.5})_x - (TeO_2)_{1-x}$ binary glasses taken into consideration, the running coordination number ($n_{Te\text{-}O}$) using MLWF formalism as a function of TeO pair distance. Vertical dashed lines indicate distance cut-offs, and the dashed horizontal line indicates the ideal Te^{4+} coordination number.

curve shows a crossover at $r \sim 2.2$ Å. For $r < 2.2$ Å, the coordination value $n_{Te\text{-}O}$ is greater in the glass with the highest modifier content and thereafter showing gradual decrease with decreasing modifier content. This observation is explained by the fact that with increasing Tl_2O modifier unit in the TeO_2 glass, the network generated by Te-BO-Te bridges breaks and is replaced by Tl-NBO-Te bridges which leads to structural depolymerization as shown in figure [4.11], therefore promoting NBO population. Furthermore, in figure [4.4] we can see that the distribution of Te-NBO distances increases with addition of modifier and the position of their maxima are shorter than Te-BO bonds lengths, resulting in high coordination numbers $n_{Te\text{-}O}$

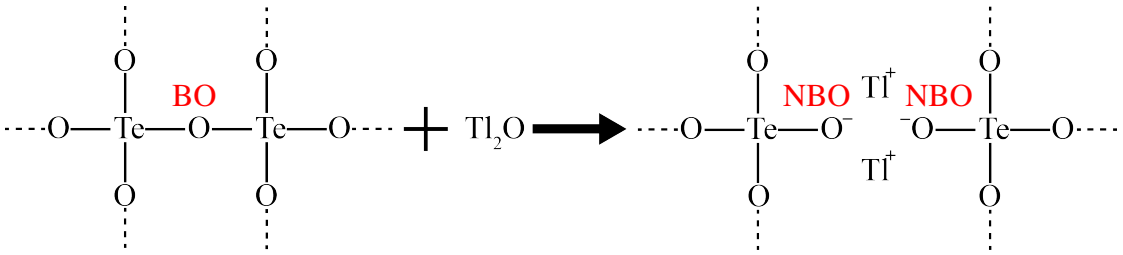

Figure 4.11: Structural depolymerization of Te-O-Te bridge by addition of Tl_2O modifier. Text in the red categorizes oxygen atom into bridging oxygen (BO) or non-bridging oxygen (NBO).

(as more NBO are accommodated in the Te coordination sphere) for higher modifier content at $r < 2.2$ Å. However, for $r > 2.2$ Å in $(TlO_{0.5})_x - (TeO_2)_{1-x}$ binary glass generally shows declining coordination value $n_{Te\text{-}O}$ with addition of modifier. This tendency may be stated due to an increase in the under-coordinated Te environments on the verge of a decrease in the over-coordinated Te environments with the addition of modifier, and its possible explanation will be addressed in the next section while discussing atomic l-folds of Te. Following these arguments, we see an opposite trend for x = 30% and x = 40%, this small shift can be attributed to statistical errors in producing MD trajectories. With the cut-offs established earlier ($r_{cut\text{-}off}$ = 2.46 Å) we report coordination value $n_{Te\text{-}O}$ in various compositions of glasses in table [4.2]. In general, we see that the incorporation of thallium oxide as a modifier in TeO_2 glassy network leads to a reduction of $n_{Te\text{-}O}$. The same examination and calculation of $n_{Te\text{-}O}$ for crystals would

Concentration (x)	$n_{Te\text{-}O}$ (at $r_{cut\text{-}off}$ = 2.46 Å)
x = 10%	3.91 ± 0.04
x = 20%	3.88 ± 0.04
x = 30%	3.77 ± 0.04
x = 40%	3.77 ± 0.04
x = 50%	3.53 ± 0.04
Crystals	
$Tl_2Te_3O_7$ (40%)	3.72 ± 0.06
α-$Tl_2Te_2O_5$ (50%)	3.76 ± 0.11 ($r_{cut\text{-}off}$ = 2.33 Å)
Tl_2TeO_3 (66%)	3.01 ± 0.02

Table 4.2: Coordination number ($n_{Te\text{-}O}$) for all the considered modifier concentration in $(TlO_{0.5})_x - (TeO_2)_{1-x}$ binary glass and crystalline polymorphs.

be another interesting marker to support the trends shown in the glasses. To do so, we consider three crystalline $Tl_2Te_3O_7$, $Tl_2Te_2O_5$, and Tl_2TeO_3 polymorphs, which correspond to 40%, 50%, and 66% of the $TlO_{0.5}$ modifier concentration, respectively and report the computed value of $n_{Te\text{-}O}$ in the table [4.2]. Interestingly, we see the same trend of an overall decreasing coordination number with rising the modifier concentration for crystals.

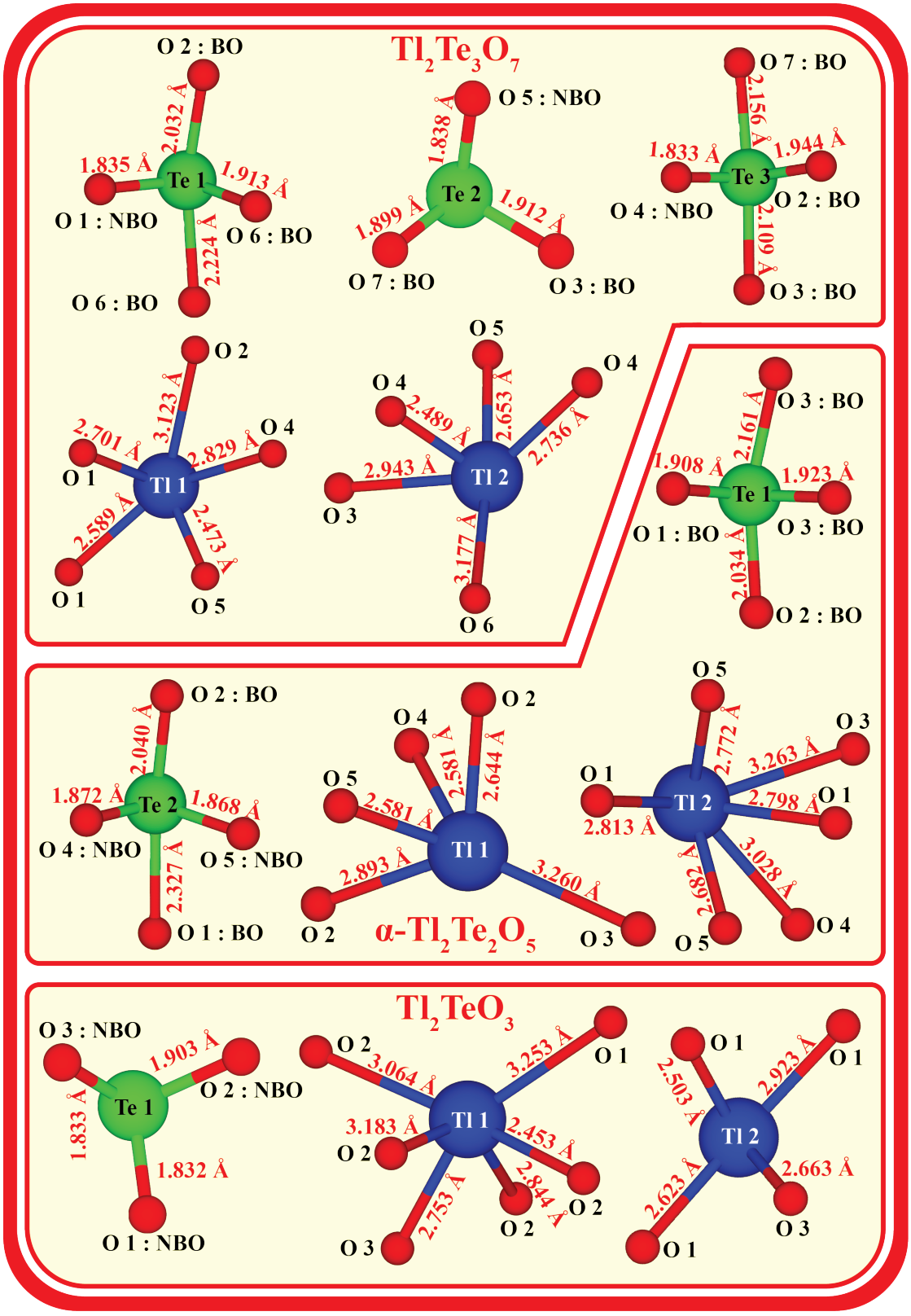

Figure 4.12: Various Tl and Te center environments in $Tl_2Te_3O_7$, $Tl_2Te_2O_5$, and Tl_2TeO_3 crystalline polymorphs.

Furthermore, we illustrate the various Te local motifs present in all the considered crystalline polymorphs (see figure [4.12]) in order to acquire an initial understanding of the analytical accessibility of $n_{Te\text{-}O}$ based on crystal chemistry consideration. We find that there are three different types of Te environments in the $Tl_2Te_3O_7$ crystalline system, where two Te units exhibiting four folds and one Te showing three folds. This results in an average $n_{Te\text{-}O}$ value of 3.67, which is quite close to the value of 3.72 mentioned in the table [4.2]. Similarly, in the case of $Tl_2Te_2O_5$ crystalline system, we find that there are two different types of Te motifs, each of which showcases four folds. Therefore, the average $n_{Te\text{-}O}$ value expected should be close to 4, and the value we obtain in the table [4.2] is 3.76, illustrating once again the effectiveness of our method. Last but not least is the Tl_2TeO_3 crystalline system, which has only one threefold Te structural motif leading to a value of $n_{Te\text{-}O}$ = 3, which agrees with the value of 3.01 in table [4.2]. Therefore, we conclude that the values obtained for glasses show similar trend as observed for crystalline systems and hence confirming the validity of $n_{Te\text{-}O}$ reported for glassy system. Hence, we find concordant results from a crystal chemistry consideration and Wannier based analysis, therefore reinforcing the validity of our methodology to be used in the case of glasses.

Tl-O coordination number

We now proceed to discuss the local environments of thallium. Coordination number ($n_{Tl\text{-}O}$) obtained via integrating the partial PDF $g_{Tl\text{-}O}(r)$ using equation [3.5] is illustrated in the top panel of figure [4.14]. In our analysis, we have seen that bonding Wannier centers due to Tl and O linkages are localized on oxygen atoms, therefore making it difficult to distinguish them from other Wannier centers due to lone pairs of oxygen atoms. As a result, the current formulation of our method based on Wannier analysis cannot be utilized to examine the chemical bonds between Tl and O.

In similar silicates based glasses [114]–[120], in addition to the two types of linkages Si-BO-Si and Si-NBO-M (M : Modifier), there is a third kind of oxygen bonding, identified as M-BO linkages, that is oxygen linked to two Si ions and an M ion, thus making BO triply connected. However, to the best of our knowledge, no verification of Tl-BO linkages in $(TlO_{0.5})_x - (TeO_2)_{1-x}$ binary glass has been reported in the literature. Figure [4.13], shows similar Tl-BO link possibilities at physical distances in the considered binary glasses. Therefore, in spirit of studying different types of Tl connection we utilize the analysis of the previous section with Te atoms to categorize oxygen atoms as BO and NBO, and consequently split the coordination $n_{Tl\text{-}O}$ into the $n_{Tl\text{-}BO}$ (see bottom panel in figure [4.14]) and $n_{Tl\text{-}NBO}$ (see middle panel in figure [4.14]) contributions. We see that $n_{Tl\text{-}NBO}$ increases with increasing modifier content. This behavior is in line with our expectation as adding more Tl ions introduces more Tl-NBO linkages due to rise in Tl-NBO population (see figure [4.5]) thus increasing the average coordination number $n_{Tl\text{-}NBO}$. Moreover, opposite trend has been noticed in the case of Tl-BO population which

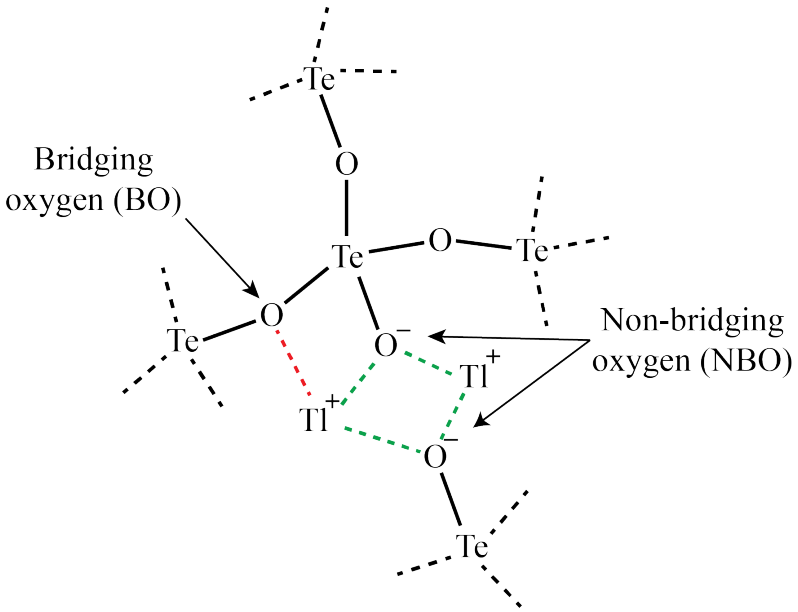

Figure 4.13: Structural fragment illustrating possible Tl^+ cation linkages with bridging oxygen (red color) and non-bridging oxygen (green lines).

decreases (see figure [4.5]) with adding modifier, therefore $n_{Tl\text{-}BO}$ also decreases. Furthermore, no plateau feature is seen in either $n_{Tl\text{-}NBO}$ or $n_{Tl\text{-}BO}$ coordination curve, thereby making it difficult to establish the first coordination shell cutoff radius. As a result, we assess the coordination number using the longest possible bond in the Tl-Te-O based crystals. The highest value, 3.26 Å, was found in $Tl_2Te_2O_5$ polymorph, and the coordination values obtained based on this cutoff are shown in the table [4.3].

Concentration (x)	$n_{Tl\text{-}O}$	$n_{Tl\text{-}BO}$	$n_{Tl\text{-}NBO}$
x = 10%	5.43 ± 0.20	4.04 ± 0.23	1.40 ± 0.17
x = 20%	5.59 ± 0.16	3.59 ± 0.16	2.00 ± 0.14
x = 30%	5.18 ± 0.13	2.70 ± 0.14	2.48 ± 0.10
x = 40%	4.67 ± 0.08	1.95 ± 0.09	2.72 ± 0.08
x = 50%	4.40 ± 0.07	1.27 ± 0.07	3.13 ± 0.07
Crystals			
$Tl_2Te_3O_7$ (40%)	5.03 ± 0.11	1.46 ± 0.11	3.58 ± 0.08
α-$Tl_2Te_2O_5$ (50%)	5.36 ± 0.11	2.25 ± 0.22	3.10 ± 0.24
Tl_2TeO_3 (66%)	4.67 ± 0.08	0.04 ± 0.01	4.64 ± 0.09

Table 4.3: Estimation of coordination number ($n_{Tl\text{-}O}$ = $n_{Tl\text{-}BO}$ + $n_{Tl\text{-}NBO}$) evaluated at $r_{cut\text{-}off}$ = 3.26 Å for $(TlO_{0.5})_x - (TeO_2)_{1-x}$ binary glasses and crystalline polymorphs.

As per our prior investigation, we also compare the $n_{Tl\text{-}O}$ value achieved in glasses as well of those Tl-Te based crystals. As a result, we calculated the $n_{Tl\text{-}O}$ value for $Tl_2Te_3O_7$, $Tl_2Te_2O_5$, and Tl_2TeO_3 polymorphs and include it in the table [4.3]. We also make an effort to connect the

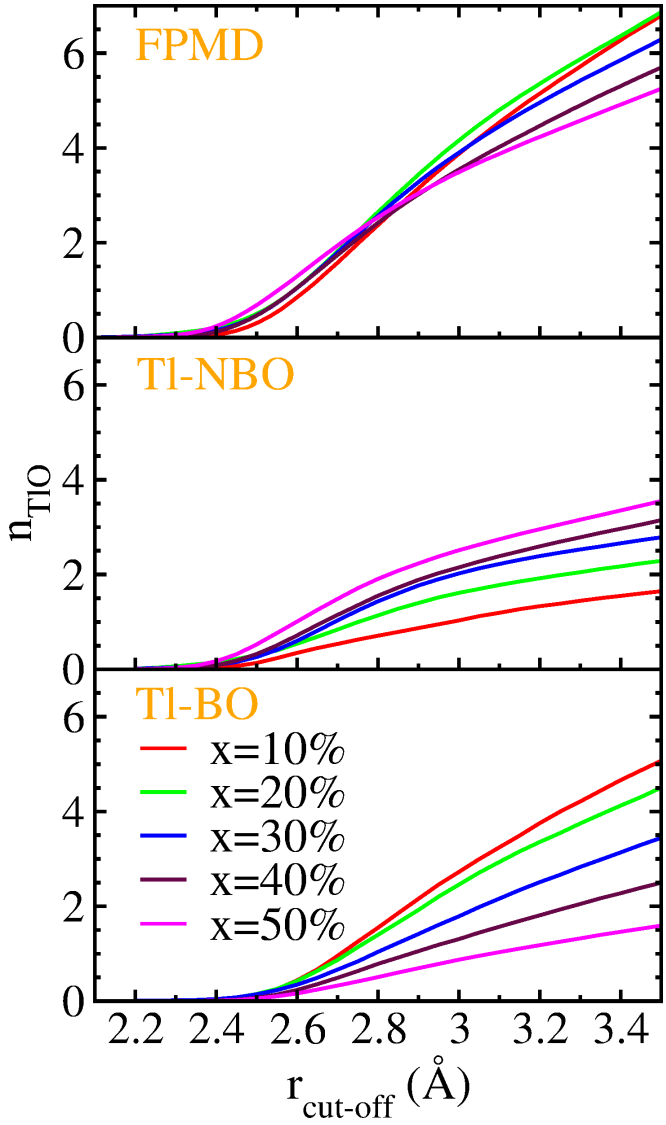

Figure 4.14: Running coordination of considered binary glasses. Top panel represents the coordination number $n_{Tl\text{-}O}$ as a function of distance obtained using integration of partial Tl-O PDF. Middle panel represents running $n_{Tl\text{-}NBO}$ with respect to non-bridging oxygen (NBO). Bottom panel shows running $n_{Tl\text{-}BO}$ with respect to bridging oxygen (BO).

$n_{Tl\text{-}O}$ coordination number with the physical picture of Tl motifs in different crystals based on crystal chemistry viewpoint. To begin with, the $Tl_2Te_3O_7$ system exhibits two Tl-based motifs, each of which has five folds. This results in an average coordination number of five, which is actually rather near to the measured $n_{Tl\text{-}O}$ value of 5.03. Additionally, we see that Tl1 has one BO (O2) and four NBO (O1, O1, O4, O5) bonds, whereas Tl2 has three NBO (O4, O4, O5) and two BO (O3, O6) bonds. As a result, we get an average of 1.5 and 3.5 for $n_{Tl\text{-}BO}$ and $n_{Tl\text{-}NBO}$, respectively which is quite similar to the computed value of 1.46 and 3.58 as shown in the table [4.3]. For $Tl_2Te_2O_5$ system, two Tl units with 5 and 6 folds are seen, resulting in an average $n_{Tl\text{-}O}$ coordination of 5.5, which is again found close to the value of 5.36 reported in the table

[4.3]. While Tl1 unit is linked with 2 NBO (O4, O5) and 3 BO (O2, O2, O3) in the $Tl_2Te_2O_5$ system, Tl2 unit connects with 3 NBO (O4, O5, O5) and 3 BO (O1, O1, O3). Both Tl contribute to the average $n_{Tl\text{-}BO}$ and $n_{Tl\text{-}NBO}$ values of 3 and 2.5, respectively in the experimental structure, which are fairly comparable to the value shown in the table [4.3]. As regard to Tl_2TeO_3 system, two Tl exhibiting 6 and 4 folds are identified, resulting in an average $n_{Tl\text{-}O}$ value of 5, which is reasonably close to the value of 4.67 in the table [4.3]. Furthermore, since Te contains all NBO oxygen, we anticipate that the average $n_{Tl\text{-}BO}$ and $n_{Tl\text{-}NBO}$ values will be 0 and 5, respectively. Once again, both values obtained are reasonably close to those shown in the table [4.3].

4.2.3 Atomic local environment

To gain access to the structural description of the network topology in $(TlO_{0.5})_x - (TeO_2)_{1-x}$ binary glasses we illustrate the l-fold fractions of TeO_x and TlO_x units present in various glassy systems.

Local environment decomposition of Te are shown in figure [4.15]. All the l-fold units contributing less than 2% are ignored. Other than 3-fold and 4-fold Te units we also encounter some over-coordinated 5-fold Te units. Generally, we observe that with the addition of modifier oxides, the concentration of TeO_3 units rises while the total concentration of 4-fold and 5-fold units decreases. This behavior can be explained on the basis of the structural depolymerization of TeO_2 glassy matrix by adding $TlO_{0.5}$ modifier, as it leads to the formation of NBOs (see figure [4.13]). Furthermore, considering Te-NBO has a shorter bond length than Te-BO (see figure [4.4]), therefore allowing fewer NBOs to satisfy atomic valency of central Te cation, and hence promoting more 3-fold Te local environment at higher modifier concentration (see figure [4.15]).

We now proceed to analyze the local environments around Te motifs by looking at the Q_m^n polyhedra where n and m represent number of Briding oxygen (BO) and total count of bonding oxygen attached. The Q_n^m values for each composition of glass are tabulated in table [4.4]. First, we can see that only at x = 50% of the $TlO_{0.5}$ concentration shows a considerable quantity of isolated TeO_3 (i.e., Q_3^0) units. This behavior reveals Tl's contribution to the full structural depolymerization of Te polyhedra by replacing Te-BO-Te bridges by Te-NBO-Tl bridges. Additionally, similar line of reasoning may also be applied to explain the declining trend of completely linked TeO_3 (Q_3^3) units along with the rising population of Q_3^1 units with the addition of modifier oxides. Moreover, because of the competing effects of rising Q_3^0 and Q_3^1 and decreasing Q_3^3 units. Q_3^2 units exhibit their peak at x = 30% modifier oxide concentration while remaining constant at roughly 12-14% for other concentrations. Furthermore, for four-fold Te atoms, similar analogy contingent upon structural depolymerization as in the case of TeO_3 units can be used to correlate the rise of Q_4^2 units to the decline of fully connected four-fold Q_4^4 units. In relation to the opposing effects of increasing and decreasing Q_4^2 and Q_4^4, respectively, Q_4^3 units exhibit an evolving pattern

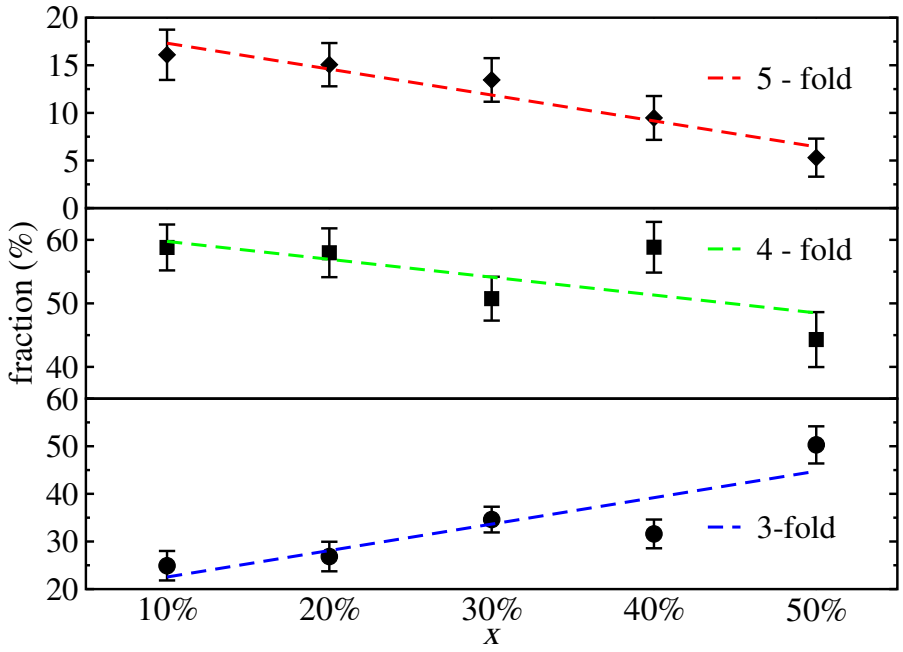

Figure 4.15: Percentage of l-fold coordinated Te atoms in all the considered composition of $(TlO_{0.5})_x - (TeO_2)_{1-x}$ binary glasses. Values less than 2% are ignored.

Q_m^n	x=10%	x=20%	x=30%	x=40%	x=50%
Q_3^0	-	-	-	-	8.22
Q_3^1	-	3.1	8.47	11.44	25.99
Q_3^2	11.24	12.21	18.06	15.62	14.58
Q_3^3	12.57	11.45	7.61	3.39	-
Q_4^2	-	2.45	2.9	8.19	10.61
Q_4^3	20.18	22.4	26.88	33.05	26.06
Q_4^4	37.43	33.06	20.86	17.06	6.17
Q_5^4	2.97	2.49	2.67	3.84	4.2
Q_5^5	13.11	12.5	10.71	5.38	-

Table 4.4: Q_m^n values (in percentage) evaluated for Te environments with $r_{cut\text{-}off}$ = 2.46 Å. Values less than 2% are ignored due to statistical error.

up to 40% of the modifier content before dropping. In the case of over-coordinated Te polyhedra, we notice the declining Q_5^5 population with addition of modifier oxide while Q_5^4 exhibits an almost insignificant proportion of roughly 3% and holds constant for all concentrations.

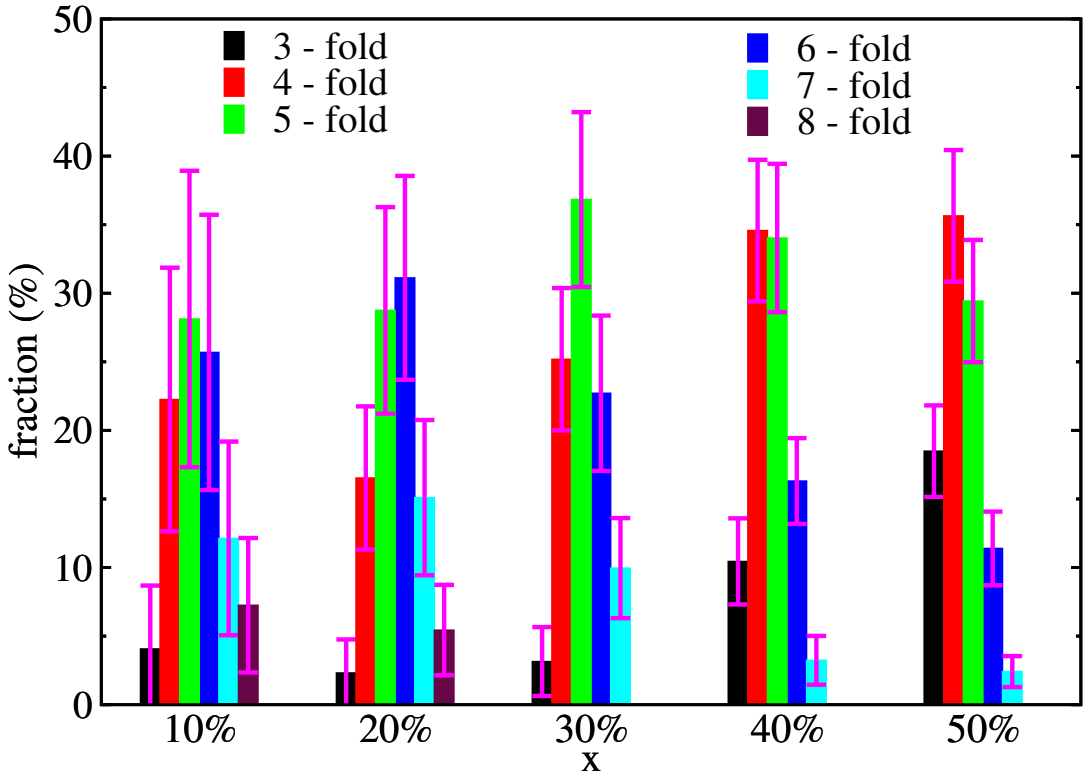

Figure 4.16: Percentage of l-fold coordinated Tl atoms in all the considered composition of $(TlO_{0.5})_x - (TeO_2)_{1-x}$ binary glasses. Further, values less than 2% are ignored.

To study the Tl local environment, we plot the l-fold fraction (%) for various concentrations using a cutoff radius = 3.26 Å (see figure [4.16]). Primarily, we see that these l-fold contributions can be divided into 3, 4, 5, 6, 7 and 8-fold Tl coordinations. We generally see that when the modifier concentration rises, 3 and 4-fold coordination increases. This behavior could be explained by the fact that when the concentration of the modifier grows, the population of Tl-BO bonds declines and that of Tl-NBO increases and since Tl-NBO features their peak position at shorter distances than Tl-BO (see figure [4.5]), this leads to lowering of average value overall of Tl-O bond lengths around central Tl atom. Moreover, from the distortion theorem of bond-valence sum rule it is clear that in order to satisfy the valence of a given atom, when one of its bonds reduces, another bond has to undergo a larger elongation. Therefore, we notice an increase in 3 and 4-fold coordination as concentration (x) increases. The fact that the higher l-folds, such 6, 7, are declining in fraction while the 5-fold hits its maximum at 30% and subsequently declines elsewhere lends credence to our explanation.

We have discussed the local environment evolution around cations, now we move towards discussing the various l-folds around O atoms. First, we see that when thallium-oxide concentration increases, the population of 1 and 2-fold O declines, however a notable increase in 3 and 4-fold O has been observed (see top panel of figure [4.17]). Additionally, we also depict the evolution of BO and NBO fractions for different concentrations (see bottom panel of figure [4.17]). Here we find that the population of BO oxygens forming environments such as O-(Te,Te), O-(Te,Te,Te), O-(Te,Te,Tl) and O-(Te,Te,Tl,Tl) declines on the verge of increase of NBO population encompassing O-(Te), O-(Te, Tl), O-(Te, Tl, Tl) and O-(Te-Tl-Tl-Tl) motifs. The straight forward explanation of the drop of BO species lies in the phenomenon of structural depolymerization and can be verified from the evolution of O-(Te,Te) and O-(Te,Te,Tl) population which dominates the BO population, and this ultimately gives rise of increase of NBO species. It is important to note that, NBO population only starts to grow significantly after $x = 20\%$ and this growth is mainly due to a rise in O-(Te,Tl), O-(Te,Tl,Tl) and O-(Te,Tl,Tl,Tl) populations. This suggests that Tl ion tend to associate within spatial proximity of NBO atom sites. This association can well be understood on the basis of highly negative partial charge present on NBO as compared to BO (see chapter [3] and as well as will be discussed in forthcoming analyses).

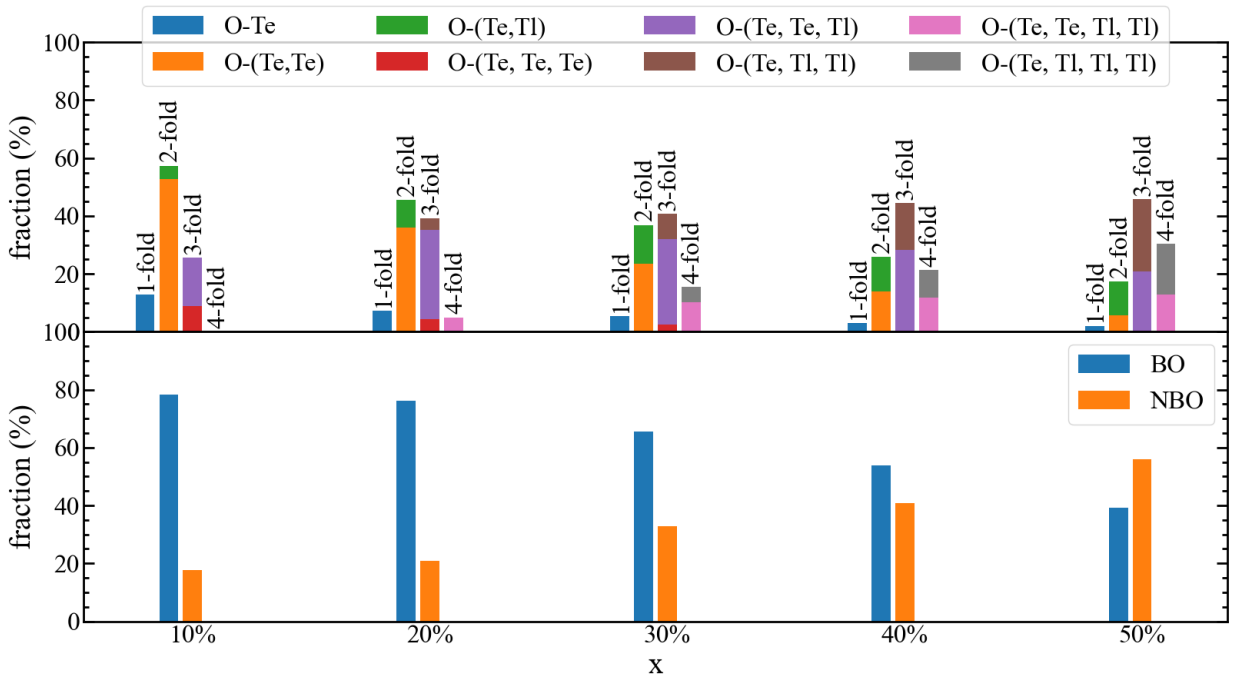

Figure 4.17: Top panel shows the decomposition of l-fold percentage for different neighbor contribution. Bottom panel displays the evolution of percentage of bridging and non-bridging oxygen for various concentrations.

4.2.4 Rings statistics

Rings statistics are mostly utilized to retrieve information complementary to those based on radial distribution functions and neutron or X-ray structural factors. In order to carry out rings analysis, we utilize the Rigorous Investigation of Networks Generated using Simulation (RINGS) software package to identify network connectivity profiles [121] between various atomic species using the King/Franzblau [122], [123] shortest paths criterion. The idea originated primarily to explore the connectivity of amorphous materials and enables scanning the network at a larger scale than the first or second coordination shells. We display the statistical averages of the distribution of rings sizes in figure [4.18].

We have used a cut-off radius $r_{cut\text{-}off}$ = 2.46 Å for defining the Te-O chemical bond and have not utilized the Wannier formalism with distance and angle constraints to define the chemical bonds as this is currently beyond the capability of RINGS code. In the case of Tl-O bonds, a cut-off radius $r_{cut\text{-}off}$ = 3.26 Å has been utilized based on the maximum bond length present in α-$Tl_2Te_2O_5$ crystalline system. The quantity reported in the figure [4.18], R(n), is the number of rings containing n atoms normalized to the total number of atoms. The calculation was carried out using a maximum search depth of 40 nodes, and the results were averaged over 100 configurations extracted from the trajectory at T = 300 K in order to get a good statistical description. In figure [4.18], the ring statistics R(n) for the five compositions in the $(TlO_{0.5})_x - (TeO_2)_{1-x}$ binary glassy systems is reported. From this figure, we inspect that the increase of thallium-oxide modifier concentration leads to a shift of R(n) distribution towards larger values of rings sizes (n) and hence, the average rings size increases. This evolution can be understood on the basis of structural depolymerization of the glassy network with the incorporation of thallium oxide modifier as it leads to replace -Te-O-Te- bridges by -Te=$O^- \cdots Tl^+$- linkages (see figure[4.11]) and hence opening smaller rings. In figure [4.19], we present snapshots highlighting the major rings size in various compositions in $(TlO_{0.5})_x - (TeO_2)_{1-x}$ binary glass. We observe that Te-O-Te chains alone make up the network and that Tl^+ ions have no role in polymerizing the ring. In fact, we here understand why the oxygen atom connecting tellurium and thallium atom is referred to as non-bridging oxygen (NBO) as no thallium atom is found to contribute to the formation of the possible rings observed in the glassy matrix (see figure [4.19a-d]). Additionally, figure [4.19e] shows that no significant ring-forming region for the x = 50% system was identified, leading to the bulk of Te-O-Te rings being completely depolymerized by Tl. All of our findings confirm the proposition [108]–[110] of depolymerization of the framework generated by tellurium structural units.

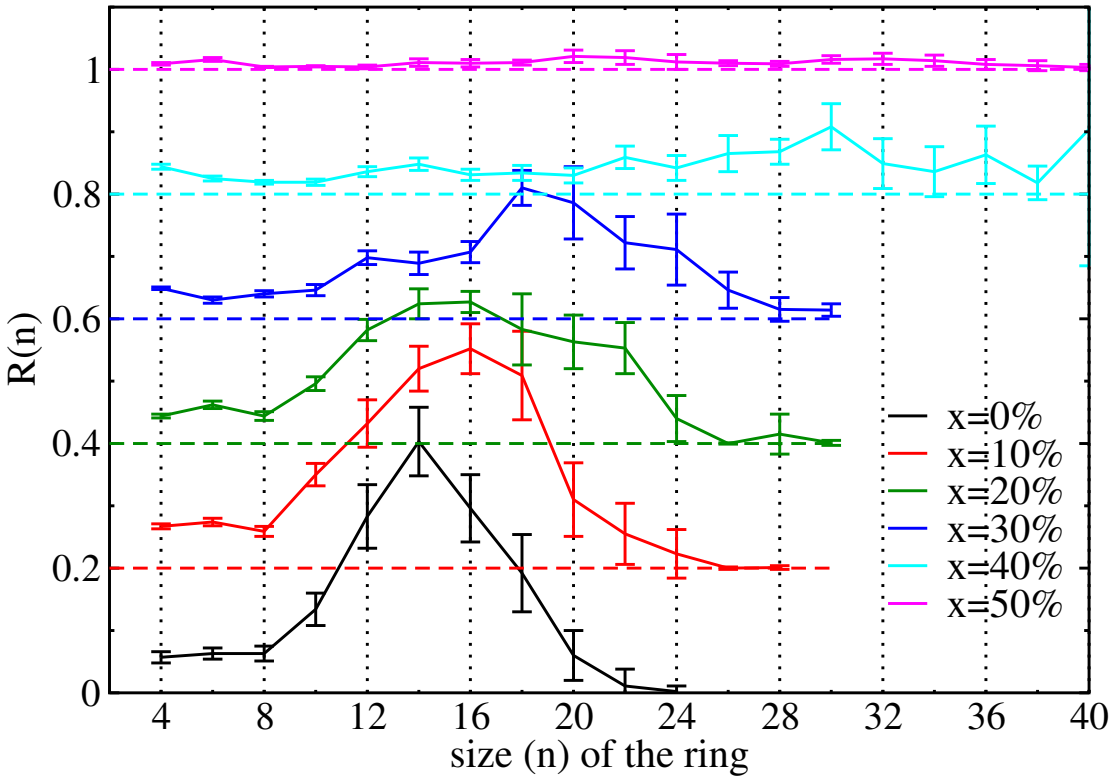

Figure 4.18: Rings size distribution profile for various compositions in various $(TlO_{0.5})_x - (TeO_2)_{1-x}$ binary glasses. For clarity, a vertical shift of 0.2 along with horizontal dashed line representing the zeros of various concentration curves is provided.

4.2.5 Bulk Modulus

The mechanical properties of a glass are significant in practical applications because they have an impact on its intrinsic durability. An atomistic connection between bonding and mechanical characteristics in glasses is necessary for understanding such phenomena. For the $(TlO_{0.5})_x - (TeO_2)_{1-x}$ binary glass models, figure [4.20] illustrates the evolution of the calculated bulk modulus using the stress-strain method. In practice, a small tensile and compressive strain of 0.4% is applied istropically along the simulation cell axis of each composition of $(TlO_{0.5})_x - (TeO_2)_{1-x}$ binary glass. Thereafter, we relax the atomic coordinates keeping the simulation cell volume constant to obtain energy versus volume curves, which can further be used to calculate the bulk modulus using Birch-Murnaghan equation of state [124], [125]. Our models predict, the bulk modulus of pure TeO_2 (480 atoms : Model 4, see chapter [3]) glass to be 22.12 ± 0.29 GPa which is smaller than the value obtained from the experimental value of 31.7 GPa [126]. Bulk modulus is predicted to decrease when a $TlO_{0.5}$ modifier oxide is incorporated into the glassy network as it lead to the formation of NBO and hence promoting depolymerization of -O-Te-O-Te-O- chains, despite a slight increase in the packing density of atoms due to the size of the heavier modifier element. As a result, knowing the relationship between concentration and mechanical strength will help us determine the optimal $(TlO_{0.5})_x - (TeO_2)_{1-x}$ binary glass

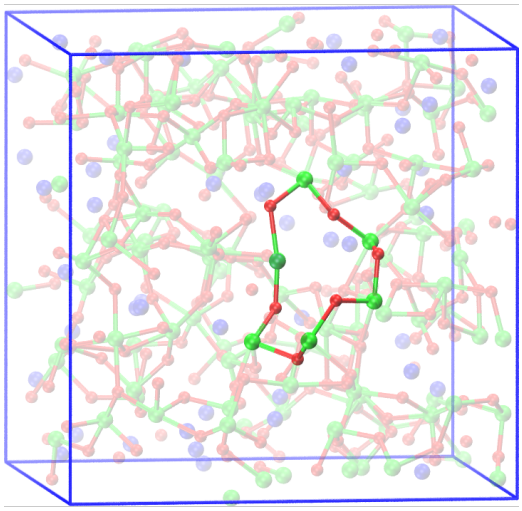

(a) Ring of size 12 in 30%-TlO_0.5-70%TeO_2.

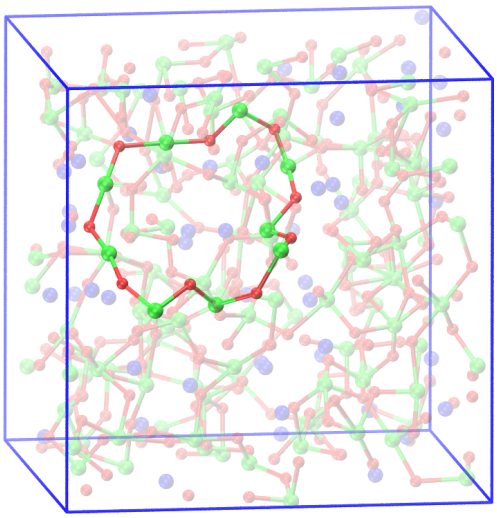

(b) Ring of size 18 in 30%-$TlO_{0.5}$-70%TeO_2.

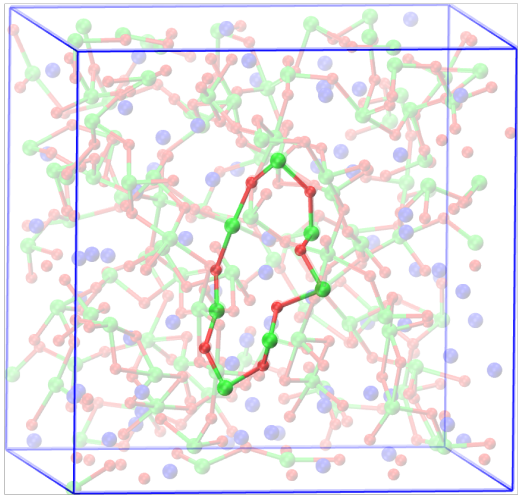

(c) Ring of size 14 in 40%-$TlO_{0.5}$-60%TeO_2.

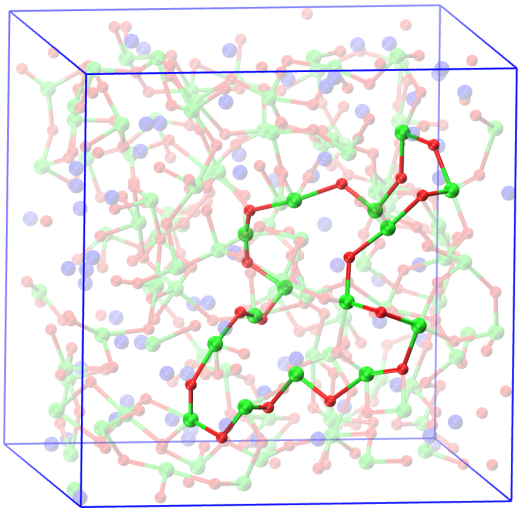

(d) Ring of size 30 in 40%-$TlO_{0.5}$-60%TeO_2

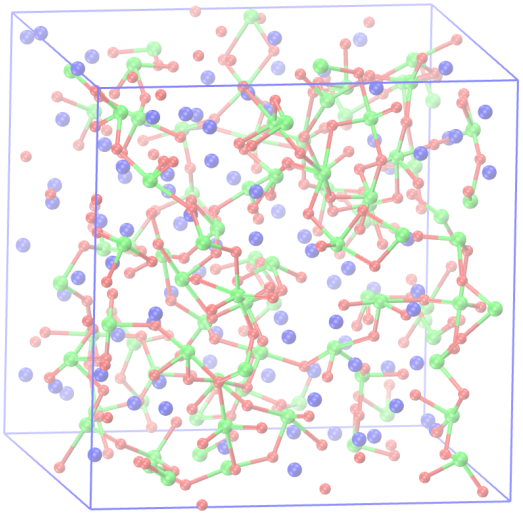

(e) No major rings in 50%-$TlO_{0.5}$-50%TeO_2.

Figure 4.19: Representation of rings in x=30% and 40% in $(TlO_{0.5})_x - (TeO_2)_{1-x}$ binary glass. Color code of atoms, red : oxygen, green : tellurium, blue : thallium.

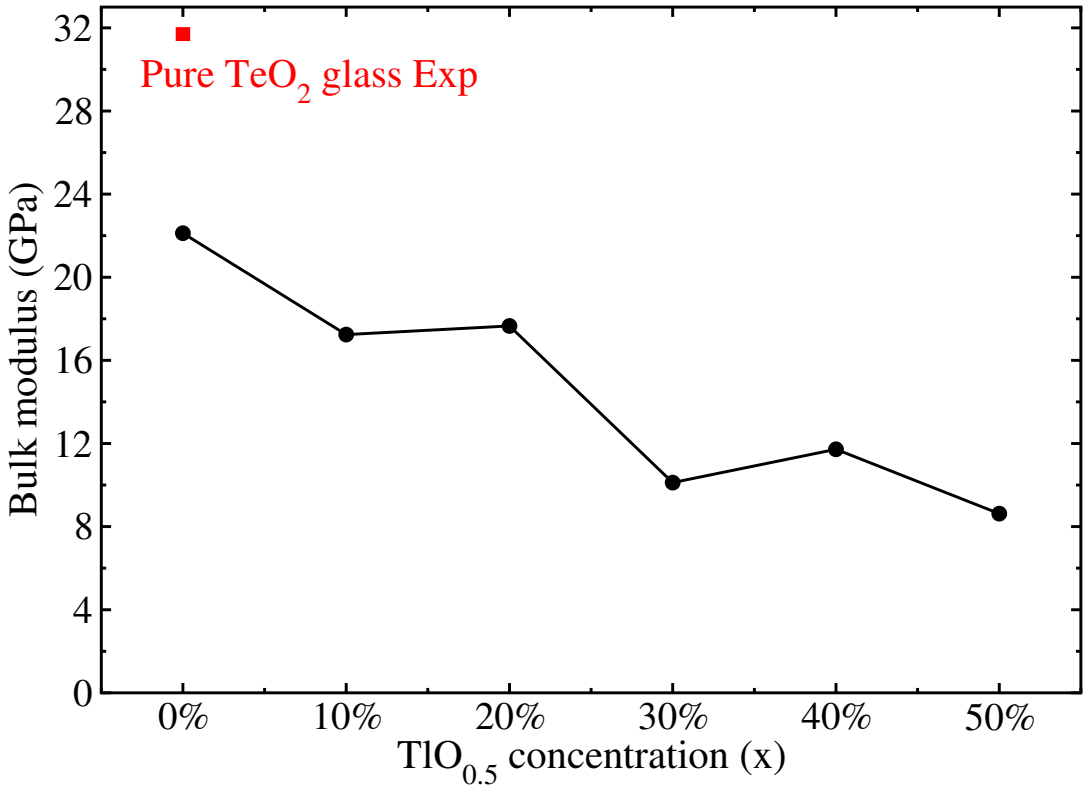

Figure 4.20: Evolution of the calculated bulk modulus for various compositions in $(TlO_{0.5})_x - (TeO_2)_{1-x}$ binary glasses.

composition. In figure [4.20], we illustrate the evolution of computed bulk modulus with respect to composition (x) in $(TlO_{0.5})_x - (TeO_2)_{1-x}$ binary glass. Indeed, integrating thallium into TeO_2 glass results in a decline in the values of bulk modulus, but what is even more significant is that increasing the modifier concentration above 20% results in a considerable decrease in the values of bulk modulus and hence a loss of its mechanical properties.

4.3 Relating structural and electronic properties

In the current section, we correlate the electronic properties with different local environments of Tl, Te and O ions. In practice, we make an attempt to understand how structural changes surrounding a given atom lead to different electronic properties.

4.3.1 Charge analysis

Analyzing how the charge density is assigned to the various types of atoms can yield additional information into the correlation of electronic and structural properties of the glasses. To do so, we compute the net atomic charge (NAC) on each atom by resorting to the density-derived

electrostatic and chemical (DDEC6) [72]–[75] partitioning method as utilized in the CHARGE-MOL package [76] (see chapter [2]). We report in table [4.5] the average NAC on Te atom and

Concentration	3-fold Te	4-fold Te	5-fold Te	Mean
x = 10%	1.568 ± 0.086	1.585 ± 0.081	1.609 ± 0.089	1.585 ± 0.085
x = 20%	1.500 ± 0.138	1.543 ± 0.077	1.584 ± 0.065	1.537 ± 0.101
x = 30%	1.471 ± 0.110	1.525 ± 0.080	1.561 ± 0.068	1.506 ± 0.110
x = 40%	1.447 ± 0.084	1.481 ± 0.077	1.536 ± 0.058	1.475 ± 0.082
x = 50%	1.408 ± 0.094	1.447 ± 0.076	1.506 ± 0.052	1.420 ± 0.132

Table 4.5: Evolution of Te NAC (e) charges for various l-folds and its mean value in $(TlO_{0.5})_x - (TeO_2)_{1-x}$ binary glasses at various compositions x.

its disassociation in various l-folds in $(TlO_{0.5})_x - (TeO_2)_{1-x}$ binary glasses. We notice that at constant modifier concentration, Te NAC grows linearly from 3 to 5-fold Te. This correlation between charges and Te l-fold may be described as fewer the number of oxygen atoms in Te coordination sphere, the lesser transfer of charge from Te to O will occur. Moreover, we also find that mean Te NAC decreases as a function of modifier concentration. This behavior is explained due to an increase of TeO_3 units with addition of thallium oxide (see section [4.2.3]) as Te in TeO_3 units carry less NAC than TeO_4 or TeO_5 units.

Further, in table [4.6], we illustrate for each glass composition the evolution of Tl charges in various l-folds. Similar to our previous analysis, we see that at constant thallium oxide concentration, Tl NAC increases with the coordination environment (l) and similar line of reasoning as in the case of Te can be utilized to understand this behavior. In addition, we also see that the mean Tl charge decreases as the concentration x increases. To understand this we follow the Tl l-fold trend observed in figure [4.16], where we have seen that with increasing x, 3 and 4-fold Tl fraction increases while 6 and 7-fold fraction decreases thus contribution of Tl NAC due to TlO_3 and TlO_4 units becomes more significant in the mean value of Tl NAC.

Concentration	3-fold Tl	4-fold Tl	5-fold Tl	6-fold Tl	7-fold Tl	Mean
x = 10%	0.675 ± 0.052	0.694 ± 0.051	0.695 ± 0.051	0.703 ± 0.049	0.714 ± 0.047	0.701 ± 0.052
x = 20%	0.647 ± 0.050	0.667 ± 0.065	0.674 ± 0.067	0.695 ± 0.067	0.710 ± 0.058	0.687 ± 0.067
x = 30%	0.628 ± 0.061	0.623 ± 0.064	0.662 ± 0.054	0.686 ± 0.047	0.703 ± 0.037	0.661 ± 0.061
x = 40%	0.590 ± 0.050	0.617 ± 0.055	0.647 ± 0.057	0.674 ± 0.056	0.694 ± 0.036	0.637 ± 0.061
x = 50%	0.562 ± 0.074	0.583 ± 0.068	0.615 ± 0.064	0.645 ± 0.065	0.688 ± 0.038	0.598 ± 0.074

Table 4.6: Evolution of Tl NAC (e) charges for various l-folds and its mean value in $(TlO_{0.5})_x - (TeO_2)_{1-x}$ binary glasses at various compositions x.

We further tabulate the O NAC in $(TlO_{0.5})_x - (TeO_2)_{1-x}$ binary glasses (see table [4.7]). In table [4.7], we have highlighted the NAC associated with NBO. We notice that, NBOs generally

feature higher NAC than BO atoms. This finding is significant since it is generally understood in the glass chemistry literature that the NBO has more negative charges than the BO because the NBO receives more charge transfer from the cation since the distances between Te-NBO and Tl-NBO are shorter than Te-BO and Tl-BO, respectively. This observation is in line with our previous results on pure TeO_2 glass (see chapter [3]).

l-fold	O Neighbor	x = 10%	x = 20%	x = 30%	x = 40%	x = 50%
1		-0.851 ± 0.038	-0.852 ± 0.038	-0.864 ± 0.038	-0.855 ± 0.037	-0.864 ± 0.051
	Te	-0.851 ± 0.038	-0.852 ± 0.038	-0.864 ± 0.038	-0.855 ± 0.037	-0.864 ± 0.051
	Tl	-	-	-	-	-
2		-0.801 ± 0.051	-0.806 ± 0.052	-0.822 ± 0.047	-0.824 ± 0.048	-0.818 ± 0.042
	Te,Te	-0.798 ± 0.050	-0.800 ± 0.053	-0.812 ± 0.050	-0.815 ± 0.053	-0.800 ± 0.044
	Te,Tl	-0.84 ± 0.039	-0.832 ± 0.038	-0.840 ± 0.036	-0.835 ± 0.038	-0.826 ± 0.038
	Tl,Tl	-	-	-	-	-
3		-0.803 ± 0.045	-0.800 ± 0.046	-0.800 ± 0.044	-0.808 ± 0.044	-0.806 ± 0.045
	Te,Te,Te	-0.817 ± 0.040	-0.812 ± 0.040	-0.812 ± 0.035	-0.813 ± 0.038	-0.800 ± 0.034
	Te,Te,Tl	-0.794 ± 0.045	-0.800 ± 0.047	-0.793 ± 0.045	-0.800 ± 0.048	-0.796 ± 0.047
	Te,Tl,Tl	-0.827 ± 0.046	-0.815 ± 0.038	-0.820 ± 0.036	-0.822 ± 0.035	-0.814 ± 0.040
	Tl,Tl,Tl	-	-	-	-	-
4		-0.821 ± 0.055	-0.805 ± 0.042	-0.797 ± 0.039	-0.809 ± 0.044	-0.809 ± 0.044
	Te,Te,Te,Te	-	-	-	-	-
	Te,Te,Te,Tl	-0.812 ± 0.042	-0.815 ± 0.034	-0.810 ± 0.037	-0.797 ± 0.037	-0.808 ± 0.049
	Te,Te,Tl,Tl	-0.824 ± 0.058	-0.801 ± 0.046	-0.795 ± 0.043	-0.794 ± 0.042	-0.794 ± 0.043
	Te,Tl,Tl,Tl	-	-0.810 ± 0.033	-0.798 ± 0.030	-0.828 ± 0.040	-0.818 ± 0.041
	Tl,Tl,Tl,Tl	-	-	-	-	-
Total		-0.809 ± 0.050	-0.807 ± 0.050	-0.811 ± 0.047	-0.814 ± 0.046	-0.811 ± 0.045

Table 4.7: Distribution of O NAC (e) and its dissociation into various cationic local environment contribution in $(TlO_{0.5})_x - (TeO_2)_{1-x}$ binary glasses at various compositions x. Rows highlighted in red color shows NBO contributions.

4.3.2 Electronic localization function

The classification of chemical bonding into ionic and covalent kinds facilitates the comprehension of the glass chemistry. The ideal covalent bond is clearly defined in bonds between identical elements, however this is only true when the surroundings of the two bonding entities are similar. Perfect ionic bonds with complete charge transfer don't exist. Therefore, the bonding interaction generally observed is intermediate to ionic and covalent bonds. Computing the electronic localization function (ELF) to analyze the degree of ionicity or covalency of bonding that are present in the glassy matrix is another interesting way to compare the electronic characteristics and the local environments.

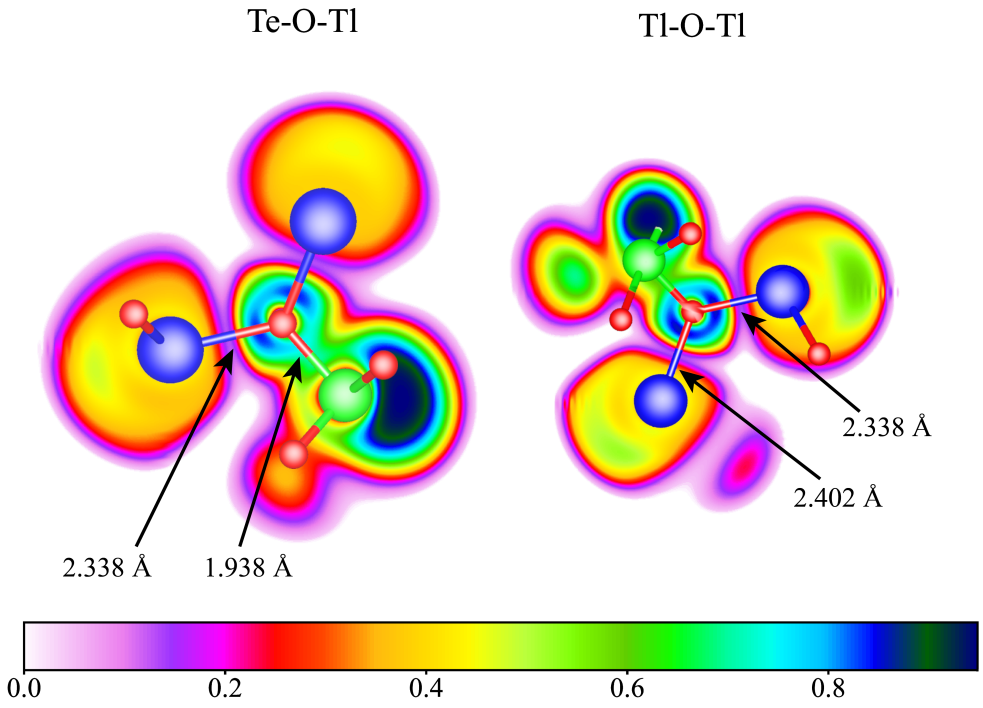

Figure 4.21: Electron localization function representation described for Tl-O-Tl (right) bridge and Te-O-Tl (left) bridge. Red, green and blue sphere shows oxygen, tellurium, and thallium atoms, respectively.

In particular, we have selected one structural motif from the glassy structure of x = 30% of $(TlO_{0.5})_x - (TeO_2)_{1-x}$ binary glass and passivated oxygen atoms with hydrogen atoms in order to maintain charge neutrality. Thereafter, we have relaxed the atomic positions of hydrogen atoms before calculating ELF. We chose the PBE0 hybrid functional to compute ELF since it has better performance for localizing the electron density than GGA functionals. Figure [4.21] shows the two-dimensional contour plots of the ELF in a plane spanned by Tl-O(NBO)-Tl and Te-O(NBO)-Tl bridge. One can see from this figure that the Te-O-Tl bridge has a strong ELF value of about 0.6 in the vicinity of Te and the bonding O, whereas the Tl and O linkage exhibits its minimum at less than 0.2, indicating the highly ionic nature of the Tl-O bond when compared to the more covalent Te-O bond. When it comes to the Tl-O-Tl bridge, we can see that both Tl-O linkages exhibit a fairly symmetric gradient in ELF values to the bond's center, with a minima smaller than 0.2 signifying a bond's identical ionic character.

It is noteworthy to highlight that Te and Tl cations contain $5s^2$ and $6s^2$ lone pair respectively, however, one can recognize from the figure [4.21] that the probability distribution of electron pair shows a strong electronic localization around Te atom (dark blue) in comparison with the highly diffused electronic localization for Tl lone pair (distorted circular yellow region). This observation complements the fact why the accuracy of the calculated total X-ray scattering PDF

in figure [4.1] increases with addition of modifier concentration. Tl's role in the amorphous network becomes more significant than Te as x increases in $(TlO_{0.5})_x - (TeO_2)_{1-x}$ binary glass. This is due to the diffusive nature of Tl's electronic localization (lone pair), since PBE functional is able to reproduce the experimental results for larger modifier concentrations. Conversely, at lower modifier concentrations, due to strong electronic pair localization of Te's lone pair, it becomes a key part in the glassy structure, making the use of hybrid functional theory necessary to mimic the experiments.

4.4 Conclusions

Using *ab-initio* calculations, a comparative study of several $(TlO_{0.5})_x - (TeO_2)_{1-x}$ binary glass compositions was conducted. In particular, we have studied the structural and electronic properties of the five binary thallium tellurite glasses. Overall fair agreement between the X-ray scattering PDF from experiments and modelling have allowed us to further investigate the structural matrix of the glass in depth. We see that $n_{Te\text{-}O}$ decreases when x increases, as adding modifier leads to a structural depolymerization of the network, replacing Te-O-Te bridges with weaker -Te-$O^- \cdots Tl^+$- bridges. Due to this, the concentration of NBO in the system increases as a function of the modifier concentration x. In addition, we also carry out rings analysis to identify the evolution of the frequency of maximum rings size in various concentrations of $(TlO_{0.5})_x - (TeO_2)_{1-x}$ binary glass. We found out that, the rings in the glassy matrix are formed by only -O-Te-O-Te- linkages where Tl does not contribute to the formation of rings. Moreover, adding thallium oxide leads to the opening of smaller rings and therefore shifting of the distribution of rings to higher ring sizes. This is a direct evidence of structural depolymerization of the glassy matrix due to the incorporation of Thallium. Additionally, we have also computed the bulk modulus for various compositions of $(TlO_{0.5})_x - (TeO_2)_{1-x}$ binary glass to assess the evolution of its mechanical properties. We found out that, adding modifier leads to lowering the bulk modulus, therefore making the glass to lose its mechanical properties. In particular, we see a significant drop in the values of bulk modulus for concentration x larger than 20%. Therefore, it is not advisable to incorporate thallium oxide ($TlO_{0.5}$) with concentration $x > 20\%$. Further, we have also investigated the electronic properties of the glass samples using *ab-initio* methods, paying special attention to the charge and ELF analysis. Charge analysis depicts that with the addition of modifier, charge transfer from Tl and Te to O decreases. In addition, we also found that NBOs carry more negative charge than BOs. Finally, the ELF analysis on O-centered structural fragment reveals that the Tl-O bonding has higher ionic character than Te-O bonds. In addition, we also found out that Tl has relatively diffused lone pair in comparison with Te. This research makes a step further in achieving a quantitative understanding of the properties of Tl-Te-O oxide glasses.

5

Structure of TiO_2-Tl_2O-TeO_2 ternary glasses

Summary

5.1 Generation and validation of the glassy models **156**
5.2 Structural analysis **158**
5.2.1 Partial distribution functions 160
5.2.2 Coordination number 164
5.2.3 Atomic local environment 169
5.2.4 Rings statistics 174
5.2.5 Bulk modulus 176
5.3 Conclusions **178**

Preliminary studies have shown that the addition of thallium oxide preserves the amplitude of the non-linear index, however we have seen that $TlO_{0.5}$ modifier oxide has no positive effect on improving the mechanical properties (see chapter [4]) and the thermal stability of the glass [9]. A separate study also showed that adding TiO_2 to TeO_2 increases the material's tolerance to heating and significantly increases its mechanical resistance [113], [127]–[129]. It was determined in practice that the O local environment around Ti and Te are comparable, and neither species can be viewed as a modifier with respect to the others. Dietzel's field strength criteria, which show that Ti belongs to the group of intermediate and has a field strength that is quite similar to Te (see table [1.2] in chapter [1]), might be used as further evidence to support this claim. Authors further purpose that Ti^{4+} prevents the formation of TeO_3 ortho-ions in the TiO_2-TeO_2 glassy system, leading to a well-polymerized fragments glassy matrix [127]. Additionally, the glassy network's high mechanical strength is provided by the comparatively stiff TiO_6 octahedrons connected by -Te-O-Ti- bridges in the structure [127]–[129]. Therefore, in subsequent investigations [130], researchers have advised adding titanium-oxide to the previously modified thallium-tellurite glasses in an effort to find the ideal chemical composition that offers a good compromise between mechanical and optical properties.

When several modifier ions are introduced to a glass, structural units of the network former may alter significantly its topology. Therefore, in this chapter, we make an attempt to study atomistic models of $(TiO_2)_x - (TlO_{0.5})_y - (TeO_2)_{1-x-y}$ glassy systems by resorting to *ab-initio* methods, as in the study of $(TlO_{0.5})_x - (TeO_2)_{1-x}$ binary glasses. To the best of our knowledge, there have been no theoretical or computational investigations on the structural properties of the $(TiO_2)_x - (TlO_{0.5})_y - (TeO_2)_{1-x-y}$ ternary glasses published in the literature. Understanding the role of Ti^{4+} ions in the $(TiO_2)_x - (TlO_{0.5})_y - (TeO_2)_{1-x-y}$ glassy matrix is the main goal of this chapter, with an emphasis on how Ti^{4+} influence the connectivity of the structural units in the material, which enhances its thermal and mechanical stability. Such knowledge is crucial since it will enable one to tailor at once the material's structural, mechanical and non-linear optical properties.

5.1 Generation and validation of the glassy models

We use *ab-initio* molecular dynamics based on DFT to study the structural models of $(TiO_2)_x - (TlO_{0.5})_y - (TeO_2)_{1-x-y}$ ternary glassy systems. MD simulations were carried out under periodic boundary conditions using quickstep module included in the CP2K code.

To obtain reasonable disordered initial configurations we have utilized the PACKMOL [112] package to randomly distribute the individual TiO_2, Tl_2O and TeO_2 molecules in the simulation cell at given mass densities and compositions of the glassy systems. Additionally, the simulation cell was chosen to be cubic in order to have equivalent separation distances between any atom and its periodic images in all the directions. Table [5.1], reports the simulation cell sizes, densities, and the number of atoms in each considered composition. Essentially, we aim to

Concentration (Abbreviation)	No. of Ti/Tl/Te/O atoms (Total)	Density [9] ρ(g.cm^{-3})	ρ_0 (Å^{-3})	Simulation cell length (Å)
x = 5%, y = 20% (Ti5-Tl20)	10/40/150/340 (540)	5.94	0.058	21.03
x = 5%, y = 30% (Ti5-Tl30)	10/60/130/310 (510)	6.21	0.056	20.93
x = 5%, y = 40% (Ti5-Tl40)	10/80/110/280 (480)	6.51	0.053	20.82
x = 10%, y = 10% (Ti10-Tl10)	16/16/128/296 (456)	5.60	0.061	19.52
x = 10%, y = 20% (Ti10-Tl20)	20/40/140/340 (540)	5.92	0.059	20.87
x = 10%, y = 30% (Ti10-Tl30)	20/60/120/310 (510)	6.20	0.057	20.78

Table 5.1: Description of $(TiO_2)_x - (TlO_{0.5})_y - (TeO_2)_{1-x-y}$ amorphous system with various molar concentrations in x and y. ρ and ρ_0 represents volumetric mass and number (simulation cell) densities [9]. For simplicity, we have abbreviated each system concentrations with the symbols shown in brackets of first column.

study six different glass forming compositions with varying titanium-oxide and thallium-oxide modifier concentrations of glass forming $(TiO_2)_x - (TlO_{0.5})_y - (TeO_2)_{1-x-y}$ ternary systems by quenching from the molten state at T = 2000 K. In fact, within our melt-quench protocol, we set the temperature to T = 2000 K well above the melting temperature of pure TeO_2 (T_m = 1006 K) glass and allow the system to evolve towards an energetically favorable state for a duration of $\sim$8 ps, assuring thereby a full decorrelation with regard to the initial random configuration as all the atoms diffuse over several inter-atomic bond lengths. Furthermore, before decreasing the temperature below T = 2000 K we have ensured that each of our models showed a liquid like self-diffusion coefficients for all atomic species involved. To obtain the room temperature glassy structure, the $(TiO_2)_x - (TlO_{0.5})_y - (TeO_2)_{1-x-y}$ glassy systems were gradually quenched as follows: (T = 1500 K, T = 1000 K, T = 600 K and T = 300 K, see figure [5.1]). The statistical averages of the last 10 ps of MD trajectories at T = 300 K are then used to compute the structural properties of the amorphous systems. A typical snapshot of the Ti10-Tl30 system configuration is shown in figure [5.2].

Figure [5.3], displays the computed time-averaged total G(r) compared to experimental data for the only available x = 10% and y = 30% system in $(TiO_2)_x - (TlO_{0.5})_y - (TeO_2)_{1-x-y}$ family. We notice that our model, slightly overestimates the position of the first peak in the Ti10-Tl30 system by $\sim$0.1 Å in comparison to experiments. The overestimation in our model towards larger distances was expected given that the GGA functional is known to overestimate bond-lengths.

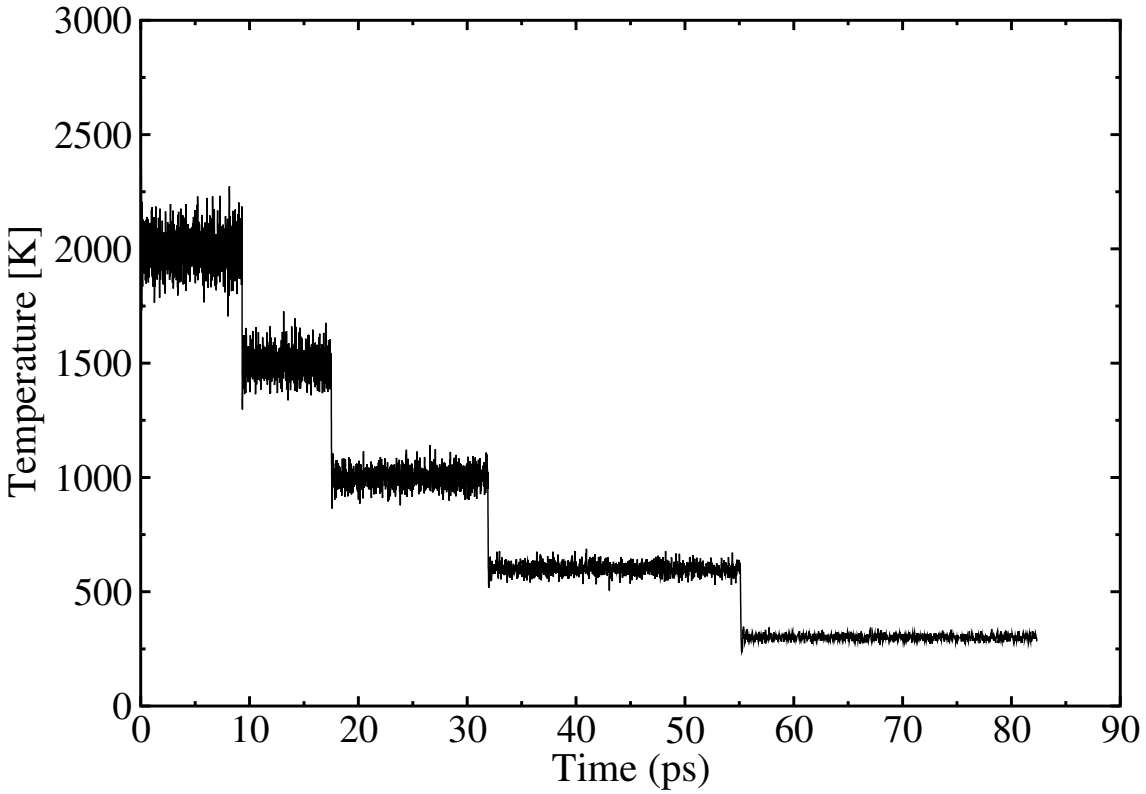

Figure 5.1: Typical thermal cycle protocol used for quenching various considered $(TiO_2)_x - (TlO_{0.5})_y - (TeO_2)_{1-x-y}$ ternary glasses (shown for Ti10-Tl10 glassy composition).

Moreover, we see from the figure [5.3] that the intensity of the peak reproduced by our model at 3.8 Å slightly overestimates the experimental one despite the good match of the peak position.

Further, due to lack of experimental data for the other systems, it was interesting to compare the computed G(r) for $(TiO_2)_x - (TlO_{0.5})_y - (TeO_2)_{1-x-y}$ ternary glass as with that corresponding to $(TlO_{0.5})_x - (TeO_2)_{1-x}$ binary glasses (see figure [5.4]) since the concentration of titanium-oxide introduced is small, and it is not expected to induce a major change in the G(r). We find that the obtained results for the ternary systems are in good agreement with their counterparts at constant thallium-oxide concentration in binary glasses. In fact, this comparison confirms the limited changes in the overall structural behavior of the $(TlO_{0.5})_x - (TeO_2)_{1-x}$ glassy matrix with the incorporation of a small content of TiO_2 modifying agent.

5.2 Structural analysis

In the following sections, we analyze the structural characteristics, including partial pair distribution function, bond-angle distribution, coordination number of each cation as a function

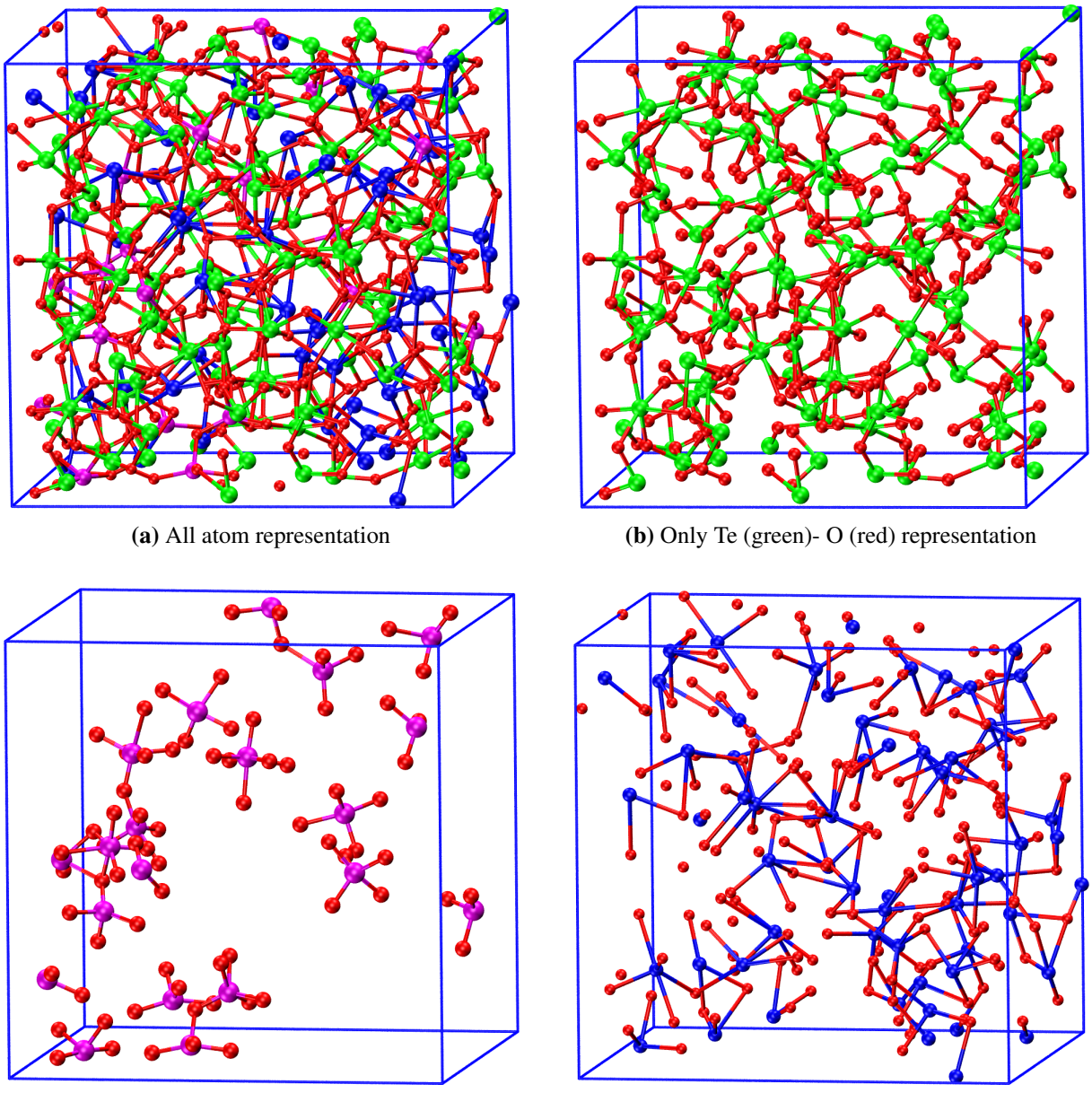

(a) All atom representation

(b) Only Te (green)- O (red) representation

(c) Only Ti (magenta)- O (red) representation

(d) Only Tl (blue)- O (red) representation

Figure 5.2: Snapshots of x = 10%, y = 30% of $(TiO_2)_x - (TlO_{0.5})_y - (TeO_2)_{1-x-y}$ glassy system.

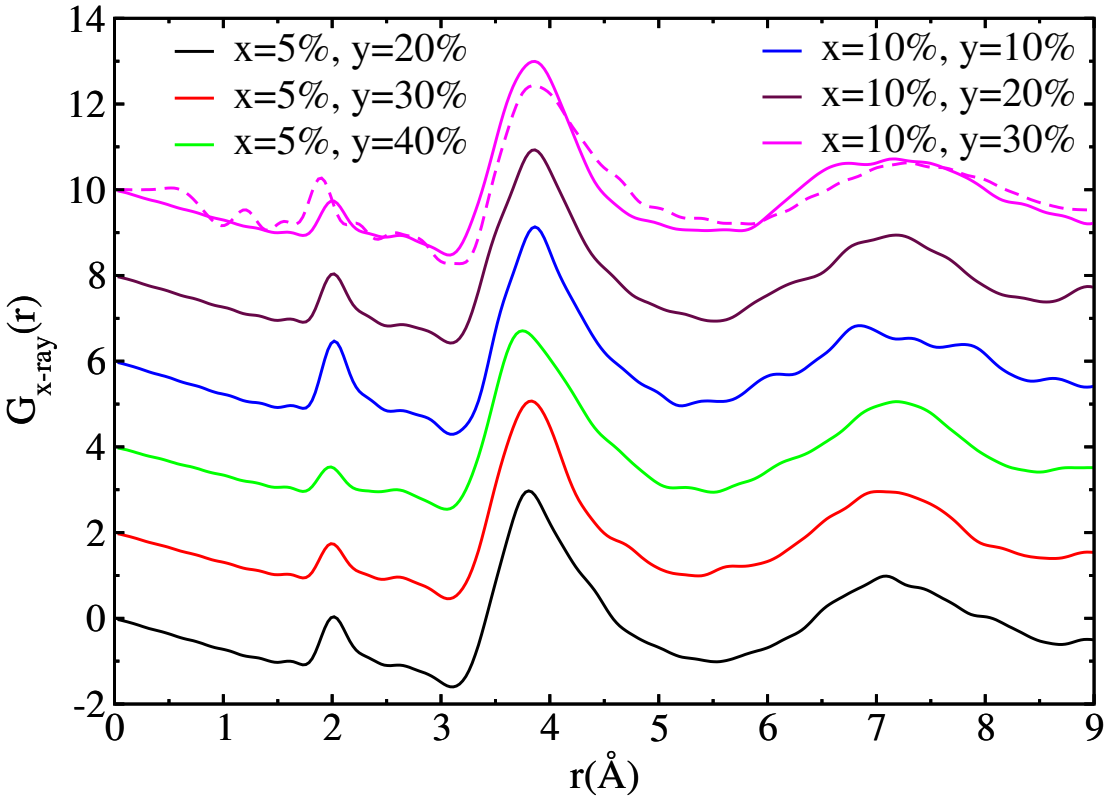

Figure 5.3: Description of total G(r) PDF for various compositions in $(TiO_2)_x-(TlO_{0.5})_y-(TeO_2)_{1-x-y}$ glassy system. Solid lines represent the computed G(r) while the dashed line shows experimental data [131]. For clarity, a vertical shift of 2 units is provided between various compositions.

of radial distance, atomic local environment, rings statistics and bulk modulus to get a deeper insight into the structure of the glass.

5.2.1 Partial distribution functions

We analyze the interatomic distances by plotting the partial PDF $g_{\alpha\beta}(r)$ and analyzing the location of the first peaks (see figure [5.5] and table [5.2]).

We begin by discussing $g_{\text{Te-O}}(r)$ partial PDF where we observe that at constant thallium-oxide concentration and increasing TiO_2 concentration there is no significant shift in the peak position of curve. However, we notice that increasing thallium-oxide while keeping the titanium-oxide concentration constant leads to a shift of the Te-O first peak towards shorter distances. This observation is in line with the trends obtained in our previous work dealing with $(TlO_{0.5})_x - (TeO_2)_{1-x}$ binary glasses (see chapter [4]). We found out that this behavior is due to a rise of non-bridging oxygens population in the system, which generally features shorter Te-NBO distances in comparison to Te-BO bond distances. Furthermore, the modest addition of TiO_2 modifier (5%, 10%) to the glassy network is the reason why there is visibly no shift in the peak

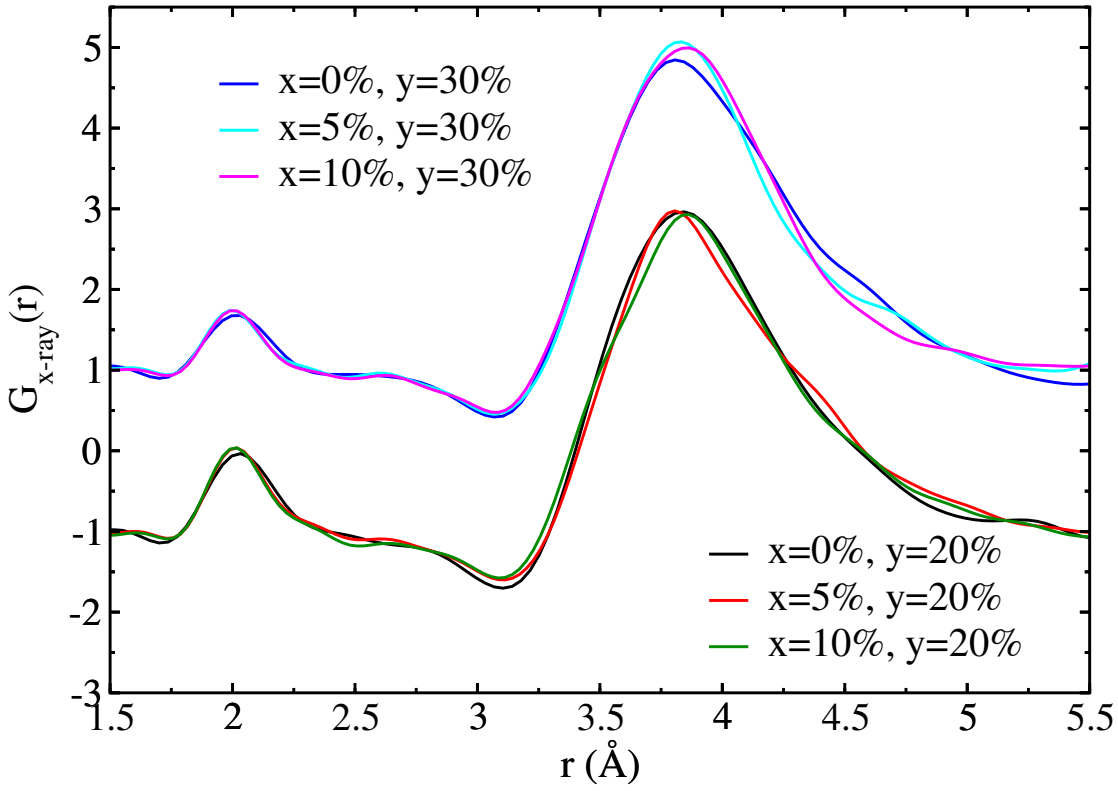

Figure 5.4: Comparison of computed X-ray diffraction total PDF G(r) between similar thallium-oxide composition in binary $(TlO_{0.5})_x - (TeO_2)_{1-x}$ and ternary $(TiO_2)_x - (TlO_{0.5})_y - (TeO_2)_{1-x-y}$ glassy system.

at constant thallium-oxide concentration. In addition, similar to our previous study, we find that increasing thallium-oxide modifier leads to rise in the first peak intensity of Te-O partial PDF, and it was understood that this rise is due to a decline of longer Te-O bonds making the curve appear relatively symmetric and intense.

Concentration (x, y)	$g_{O\text{-}O}(r)$	$g_{Te\text{-}O}(r)$	$g_{Tl\text{-}O}(r)$	$g_{Ti\text{-}O}(r)$	$g_{Te\text{-}Te}(r)$	$g_{Tl\text{-}Te}(r)$
x = 5%, y = 20%	2.90	1.98	2.78	1.92	3.73	3.88
x = 5%, y = 30%	2.89	1.97	2.68	1.88	3.74	3.83
x = 5%, y = 40%	2.90	1.96	2.66	1.90	3.64	3.78
x = 10%, y = 10%	2.86	2.00	2.77	1.86	3.85	3.93
x = 10%, y = 20%	2.88	1.99	2.82	1.87	3.79	3.91
x = 10%, y = 30%	2.87	1.98	2.69	1.89	3.66	3.89

Table 5.2: Location of first peak (in Å) for $g_{\alpha\text{-}\beta}(r)$ partial PDF in figure (5.5) for various concentrations in $(TiO_2)_x - (TlO_{0.5})_y - (TeO_2)_{1-x-y}$ glassy systems.

Now, we proceed to analyze trends observed in the $g_{Tl\text{-}O}(r)$ partial PDF. We notice that at constant thallium-oxide modifier concentrations and varying TiO_2 concentration, $g_{Tl\text{-}O}(r)$ features limited changes. Moreover, we do notice appreciable shift of the first peak towards smaller distances

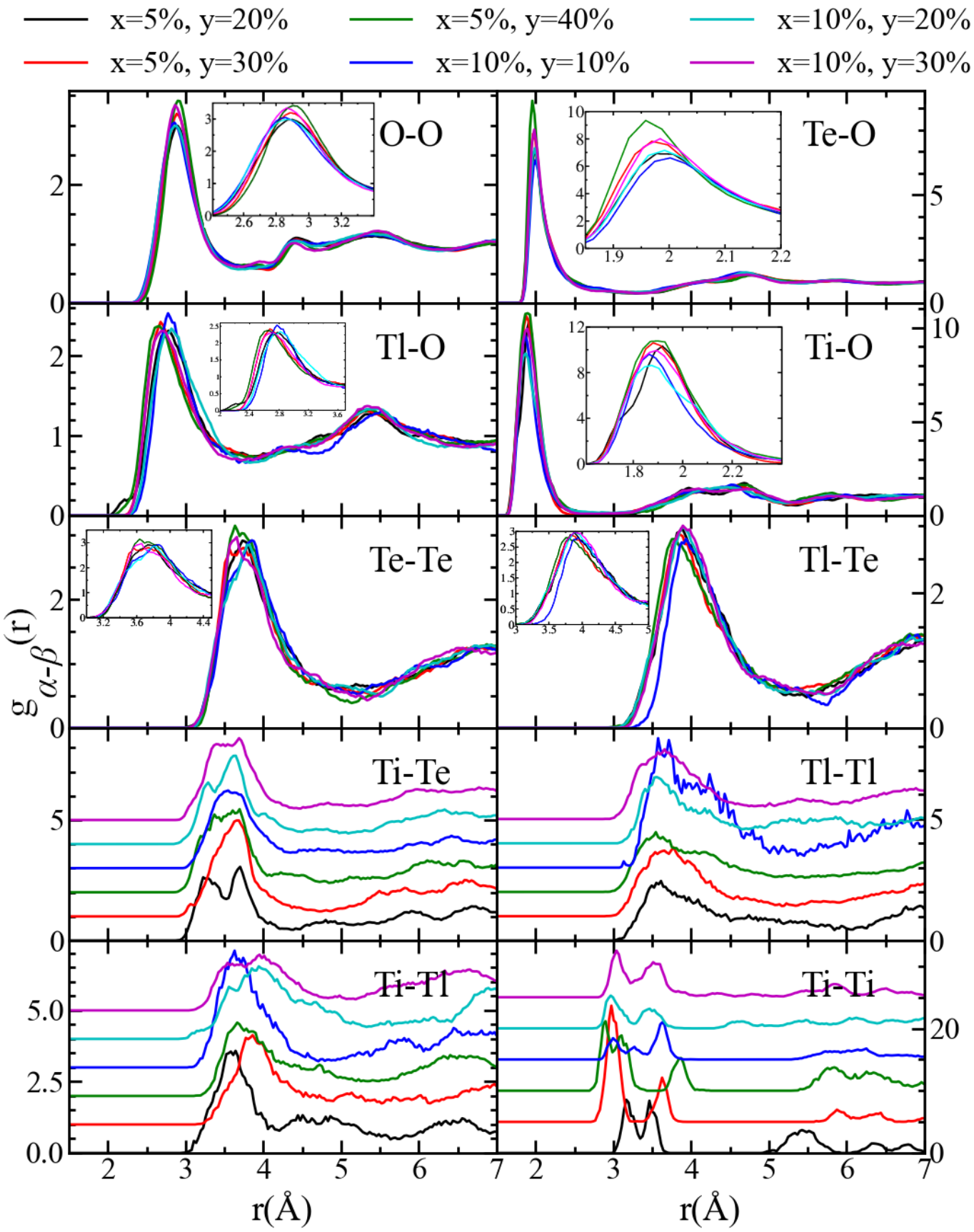

Figure 5.5: Partial pair distribution function $g_{\alpha\text{-}\beta}(r)$, for various possible pairs between atomic elements in $(TiO_2)_x - (TlO_{0.5})_y - (TeO_2)_{1-x-y}$ ternary glassy system.

with varying thallium-oxide while maintaining titanium-oxide concentration constant. This observation again reproduce our previous findings with binary $(TlO_{0.5})_x - (TeO_2)_{1-x}$ glasses, where we have assigned the cause of this effect to a rise of shorter Tl-NBO bond distances in contrast to longer Tl-BO distances.

In the case of $g_{\text{Ti-Ti}}(r)$ partial PDF, we find two peaks in the range 3 to 4 Å. This splitting can be associated with two phenomena. In particular, we have identified that some Ti atoms are situated close to each other, and hence connects to each other via edge or corner sharing yielding smaller Ti-Ti distances in the former case and vice versa as displayed in figure [5.6]. Moreover, due to small number of Ti atoms in the simulation cell, nearby clusters of Ti atoms may lead to large statistical fluctuation in $g_{\text{Ti-Ti}}(r)$ partial PDF curve.

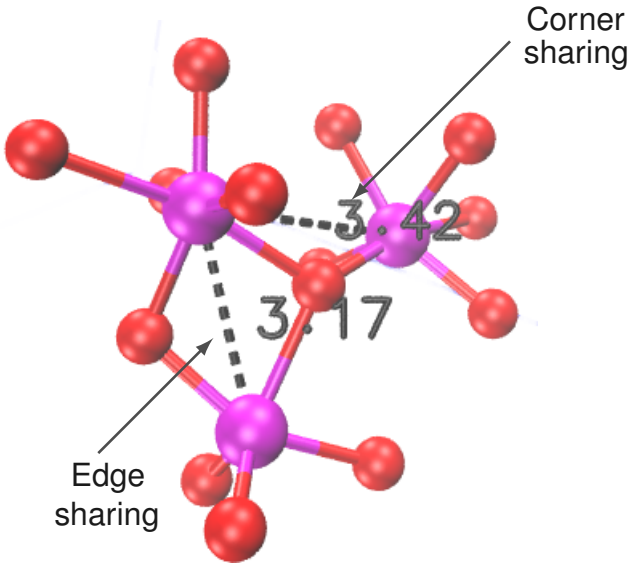

Figure 5.6: Edge and corner sharing representation of TiO_x polyhedra. Color code (red : oxygen, magenta : titanium)

We now proceed to discuss the trends observed in $g_{\text{O-O}}(r)$ partial PDF. From figure [5.5] and table [5.2], we observe that there is no significant change in the first peak location in $g_{\text{O-O}}(r)$ at constant TiO_2 concentration. However, we notice a tiny shift to smaller distances irrespective of thallium-oxide concentration, when changing TiO_2 modifier content from 5% to 10%. This shift can be explained on the basis of the topology of TiO_2 structural unit. In practice, by adding TiO_2 we are replacing Te ions with Ti ions, and based on our previous investigation with pure TeO_2 glass (see chapter [3]), we comprehend that Te^{4+} features a highly asymmetric polyhedra due to the presence of its lone pair in contrast to Ti^{4+}, therefore making O-O pair distance in TiO_x units smaller in average. Additionally, smaller O-O pair distance at higher TiO_2 modifier oxide can also be attributed to the smaller ionic radius of Ti^{4+} than Te^{4+}.

5.2.2 Coordination number

Te-O coordination number

According to our previous research with pure TeO_2 glass, binary $(TlO_{0.5})_x - (TeO_2)_{1-x}$ glass, and within the present chapter, we have seen that the partial PDF of $g_{Te\text{-}O}(r)$ fails to exhibit clear first minima $r_{cut\text{-}off}$, thus disallowing to define the upper limit of integration while calculating $n_{Te\text{-}O}$. Therefore, in spirit of defining the value of $r_{cut\text{-}off}$, we utilize the Maximally Localization

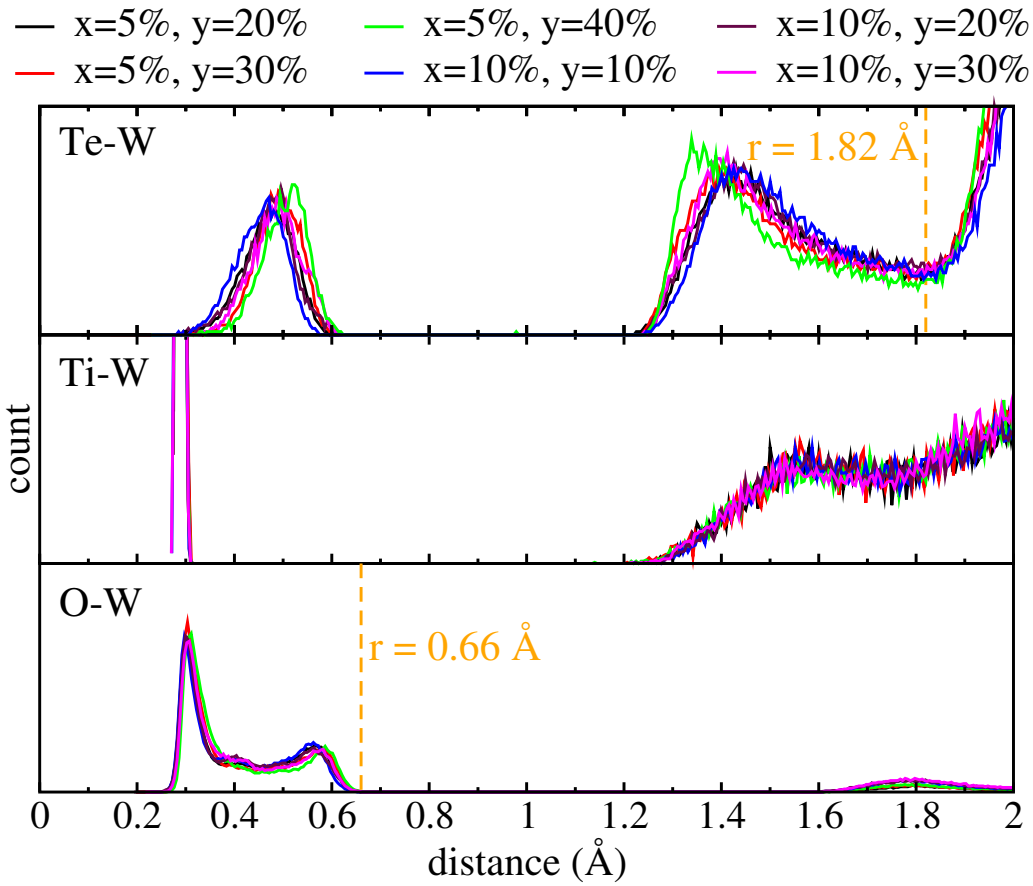

Figure 5.7: Histogram distribution of Te-W (top panel), Ti-W (middle panel) and O-W (bottom panel) pair distances $(TiO_2)_x - (TlO_{0.5})_y - (TeO_2)_{1-x-y}$.

Wannier Formalism (MLWF) to obtain Wannier functions centers (W). In figure [5.7], we have represented the distribution of histogram formed by Te-W, Ti-W and O-W pair distances. The first peak in the Te-W and O-W representations is due to the lone pair, while the second peak shows the contribution of the bonding W. The sum of the distances between the second minima of Te-W and O-W distribution gives a reasonable Te-O bond $r_{cut\text{-}off}$ = 2.48 Å. Despite this strategy of finding $r_{cut\text{-}off}$ being instructive, still $n_{Te\text{-}O}$ is highly dependent on choice of $r_{cut\text{-}off}$. Therefore, similar to our previous investigation (see chapters [3] and [4]), we adopt an alternate way of calculating the coordination number $n_{Te\text{-}O}$ by directly counting the number of neighbors around

Te and average them over the total count of Te atoms in the simulation cell. To do so, it is important to characterize W responsible for Te-O bonding and thus lying on or close to the line joining considered Te and O atoms. Therefore, we implement the distance constraint as follows:

$$|d(\text{Te,W}) + d(\text{O,W}) - d(\text{Te,O})| \leq 0.05 \text{ Å}, \tag{5.1}$$

Additionally, our earlier research shows that it is also mandatory to include angle constraint which only allows TeO to be qualified as a chemical bond if the angle between lone pair of Te and the oxygen atom is greater than 73° i.e.,

$$\Theta(\text{W}_{\text{Te}}^{\text{LP}} - \text{Te-O}) \geq 73°. \tag{5.2}$$

Thus, based on these two constraints we now plot the running coordination number $n_{\text{Te-O}}$ as a function of the radial distance r, see figure [5.8]. From the figure, we indeed see the efficiency

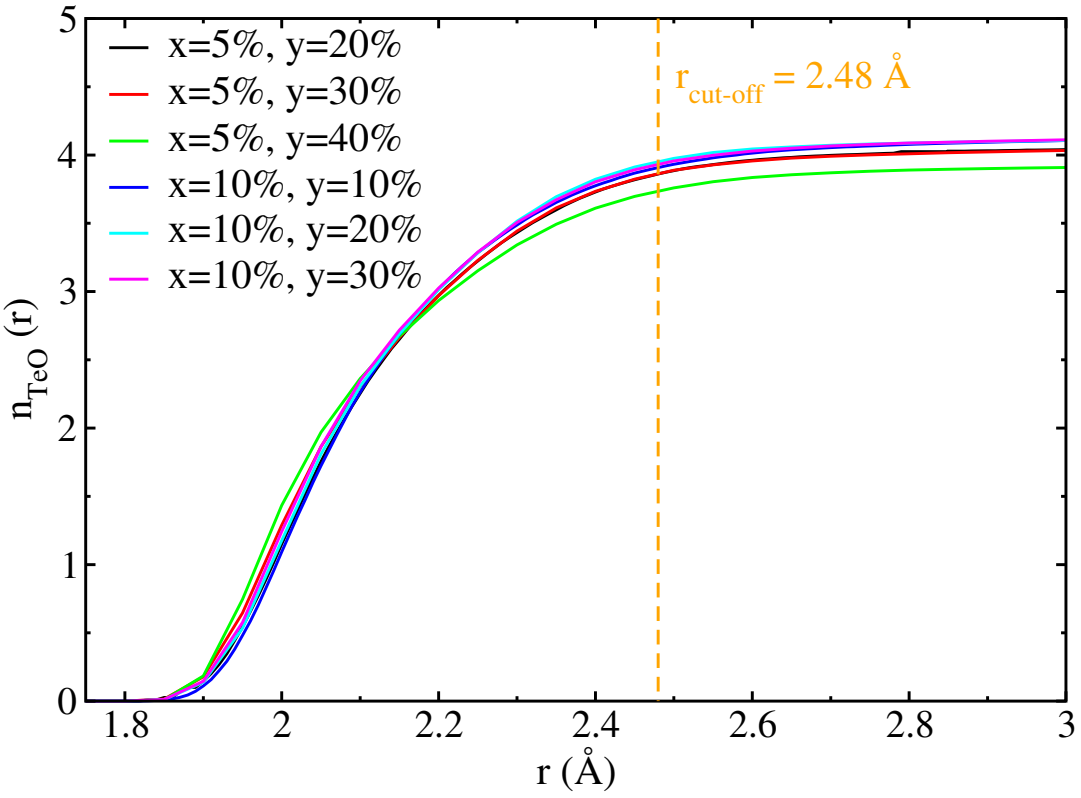

Figure 5.8: For all the compositions in the $(TiO_2)_x - (TlO_{0.5})_y - (TeO_2)_{1-x-y}$ ternary glasses taken into consideration, the running coordination number ($n_{\text{Te-O}}$) using MLWF formalism as a function of TeO pair distance.

of the protocol adopted in our strategy of computing $n_{\text{Te-O}}$. In practice, we find a very slowly evolving plateau region of $n_{\text{Te-O}}$ as a function of r. Based on the $r_{\text{cut-off}}$ = 2.48 Å, we report the $n_{\text{Te-O}}$ values of various composition of $(TiO_2)_x - (TlO_{0.5})_y - (TeO_2)_{1-x-y}$ ternary glasses in

table [5.3].

Compositions	$n_{Te\text{-}O}$ (at $r_{cut\text{-}off} = 2.48$ Å)
x = 5%, y = 20%	3.86 ± 0.03
x = 5%, y = 30%	3.87 ± 0.04
x = 5%, y = 40%	3.74 ± 0.05
x = 10%, y = 10%	3.91 ± 0.04
x = 10%, y = 20%	3.95 ± 0.03
x = 10%, y = 30%	3.93 ± 0.04

Table 5.3: Coordination number ($n_{Te\text{-}O}$) for all the considered modifier concentration in $(TiO_2)_x - (TlO_{0.5})_y - (TeO_2)_{1-x-y}$ ternary glass system.

First and foremost, we see from the table [5.3] that, in general, increasing thallium-oxide content at constant 5% of titanium oxide leads to a drop in the coordination of tellurium atoms, and this observation is in line with our previous investigation with binary $(TlO_{0.5})_x - (TeO_2)_{1-x}$ glass, where we have attributed the cause of this behavior to the rise of -Te-$O^- \cdots Tl^+$- bridges with increasing the concentration of modifier agent. Furthermore, it is interesting to note that increasing titanium-oxide modifier to 10% favors the coordination around Te to be equal to ~ 4 with a limited effect of thallium-oxide concentration at least up to a value of 30%. This behavior can be understood based on the evolution of the number density of the studied systems (see table [5.1]). We note that as we raise the TiO_2 modifier concentration from 5% to 10% at constant $TlO_{0.5}$ content, the number density (ρ_0) increases slightly, causing the system to induce more connections to form and resulting in a higher coordination value of $n_{Te\text{-}O}$.

Ti-O coordination number

We now proceed to discuss the coordination number of Ti, $n_{Ti\text{-}O}$, in $(TiO_2)_x - (TlO_{0.5})_y - (TeO_2)_{1-x-y}$ glasses. Figure [5.9] illustrates the running coordination number $n_{Ti\text{-}O}$, obtained using the integration of the partial PDF $g_{Ti\text{-}O}(r)$. We notice for r > 2.5 Å, $n_{Ti\text{-}O}$ starts to show a slowly evolving plateau region, hence, a cut-off distance of 2.5 Å can be considered to define the radius of first coordination shell around Ti [132]. Our calculations with the radius cut-off defined, shows that the atomic arrangement around Ti in the glassy matrix favors $n_{Ti\text{-}O}$ to be around 5.23 in average for all the compositions (see table [5.4]). Similar $n_{Ti\text{-}O}$ value has been observed experimentally in sputtered, sol-gel dip-coated layers and bulk powders as 5.4 ± 0.4, 4.5 ± 0.4 and 5.6 ± 0.4, respectively [133]. Moreover, $n_{Ti\text{-}O}$ value remains more or less constant with changing titanium-oxide concentration, which shows a limited change in the local structure of Ti for all the studied concentrations. The obtained values of $n_{Ti\text{-}O}$ are similar to the coordination number obtain experimentally using diffraction measurements, as 5.0(2) in the liquid [134] and 5.4 ± 0.4 (5.6 ± 0.4) in sputtered (bulk powder) amorphous-TiO_2 [133].

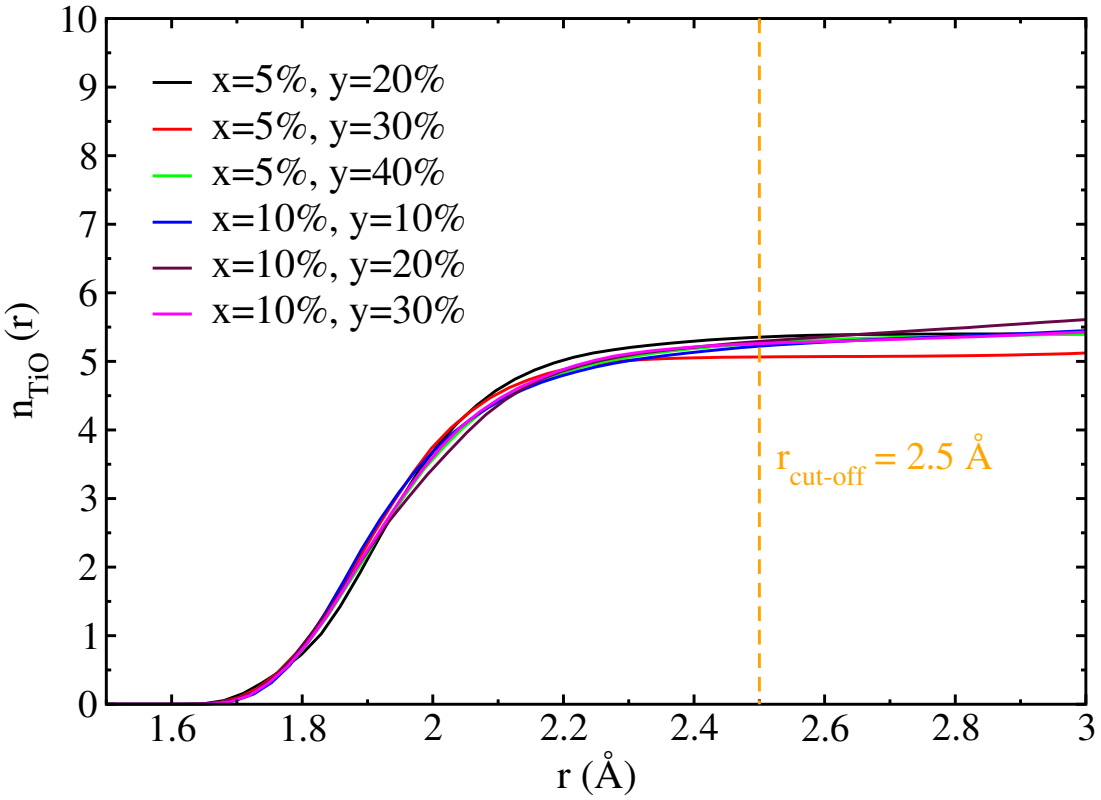

Figure 5.9: Running coordination ($n_{Ti\text{-}O}$) in $(TiO_2)_x - (TlO_{0.5})_y - (TeO_2)_{1-x-y}$ ternary glass. Vertical dashed line represents the considered radius of the first coordination shell around Ti.

Compositions	$n_{Ti\text{-}O}$ (at $r_{cut\text{-}off}$ = 2.5 Å)
x = 5%, y = 20%	5.35 ± 0.06
x = 5%, y = 30%	5.06 ± 0.05
x = 5%, y = 40%	5.26 ± 0.11
x = 10%, y = 10%	5.21 ± 0.07
x = 10%, y = 20%	5.28 ± 0.08
x - 10%, y = 30%	5.26 ± 0.06

Table 5.4: Coordination number ($n_{Ti\text{-}O}$) for all the considered modifier concentration in $(TiO_2)_x - (TlO_{0.5})_y - (TeO_2)_{1-x-y}$ ternary glass system.

Tl-O coordination number

We advance to investigate the Tl coordination number, $n_{Tl\text{-}O}$, where we resolve the oxygen into BO i.e. oxygen atom linked via Te-O-Te or Te-O-Ti bridge yielding $n_{Tl\text{-}BO}$, and NBO otherwise resulting in $n_{Tl\text{-}NBO}$ contributions, (see table [5.5]). In order to compute the coordination number of Tl, we adopt the fixed values of $r_{cut\text{-}off}$ = 3.26 Å chosen from the highest possible Tl-O bond length in α-$Tl_2Te_2O_5$ crystalline system similar to our prior analysis with $(TlO_{0.5})_x - (TeO_2)_{1-x}$ glasses (see chapter [4]). Overall, we see that $n_{Tl\text{-}O}$, increases as a function of increasing TiO_2

Concentration (x, y)	$n_{Tl\text{-}BO}$	$n_{Tl\text{-}NBO}$	$n_{Tl\text{-}O}$
x = 5%, y = 20%	3.69 ± 0.15	1.80 ± 0.12	5.50 ± 0.11
x = 5%, y = 30%	2.74 ± 0.11	2.20 ± 0.09	4.94 ± 0.10
x = 5%, y = 40%	2.00 ± 0.09	2.62 ± 0.09	4.62 ± 0.08
x = 10%, y = 10%	4.18 ± 0.20	1.45 ± 0.16	5.63 ± 0.18
x = 10%, y = 20%	3.93 ± 0.15	1.69 ± 0.11	5.62 ± 0.14
x = 10%, y = 30%	3.37 ± 0.12	1.73 ± 0.10	5.10 ± 0.09

Table 5.5: Estimation of coordination number ($n_{Tl\text{-}O}$ = $n_{Tl\text{-}BO}$ + $n_{Tl\text{-}NBO}$) evaluated at $r_{cut\text{-}off}$ = 3.26 Å for $(TiO_2)_x - (TlO_{0.5})_y - (TeO_2)_{1-x-y}$ ternary glass system.

content from 5% to 10% while keeping the $TlO_{0.5}$ amount constant. Similar to $n_{Te\text{-}O}$, we explain this on the basis of the evolution of number density of the systems (see table 5.1). Indeed, at constant $TlO_{0.5}$ and raising the TiO_2 concentration from 5% to 10%, the number density increases, which causes the system to promote additional linkages to form, therefore rising the coordination value $n_{Tl\text{-}O}$. Moreover, we witness that at constant TiO_2 content, increasing $TlO_{0.5}$ content leads to a decrease in the coordination value $n_{Tl\text{-}O}$. We utilize the similar line of explanation based on our previous study with $(TlO_{0.5})_x - (TeO_2)_{1-x}$ binary glasses, where we have seen that this tendency can be attributed to a rise of shorter Tl-NBO bonds with increasing $TlO_{0.5}$ modifier concentration (see figure [4.5]). As the distribution of Tl-NBO bonds rises and are centered at shorter distances than Tl-BO bonds with increasing thallium oxide, this results in Tl to make polyhedra with a smaller number of neighbors, hence reducing the value of $n_{Tl\text{-}O}$. Further, the trends observed in ($n_{Tl\text{-}BO}$) and ($n_{Tl\text{-}NBO}$) are also in line with our observation with $(TlO_{0.5})_x - (TeO_2)_{1-x}$ binary glasses when varying $TlO_{0.5}$ and at constant TiO_2 modifying agent concentrations. Similar to $n_{Tl\text{-}O}$, we notice $n_{Tl\text{-}BO}$ increases with increasing TiO_2 concentration and at constant $TlO_{0.5}$ modifier concentrations. In addition, this rise in $n_{Tl\text{-}BO}$ can also be attributed to a rise in the BO with increasing TiO_2, as TiO_2 is known to promote the polymerization of the network in $(TiO_2)_x - (TlO_{0.5})_y - (TeO_2)_{1-x-y}$ ternary glassy systems [9]. Once again similar to our previous analysis with $(TlO_{0.5})_x - (TeO_2)_{1-x}$ binary glasses, we see that $n_{Tl\text{-}NBO}$ increases with constant x and increasing y in $(TiO_2)_x - (TlO_{0.5})_y - (TeO_2)_{1-x-y}$ glasses. This behavior was explained on the basis of rise in Tl-NBO bonds (see figure [4.5]).

Interestingly we find that at constant $TlO_{0.5}$ and increasing TiO_2 content 5% to 10%, we notice a decline in $n_{Tl\text{-}NBO}$ and this can be associated with Ti's ability to promote BO.

5.2.3 Atomic local environment

In order to gain additional insights into the atomic local environments, we analyze in the forthcoming subsections, the evolution of structural motifs around each atom in relation with all the considered compositions of $(TiO_2)_x - (TlO_{0.5})_y - (TeO_2)_{1-x-y}$ ternary glasses.

Te local environment

In figure [5.10], we display the evolution of various local environments centered around Te atom for various compositions of $(TiO_2)_x - (TlO_{0.5})_y - (TeO_2)_{1-x-y}$ ternary glasses. We find that, at constant concentration of thallium-oxide i.e. at 20% and 30% molar concentrations, addition of TiO_2 leads to a rise of the fractions of 4 and 5-fold Te on the verge of decrease in the fraction of 3-fold Te. It is crucial to discuss the various Q^n_m polyhedral distributions surrounding

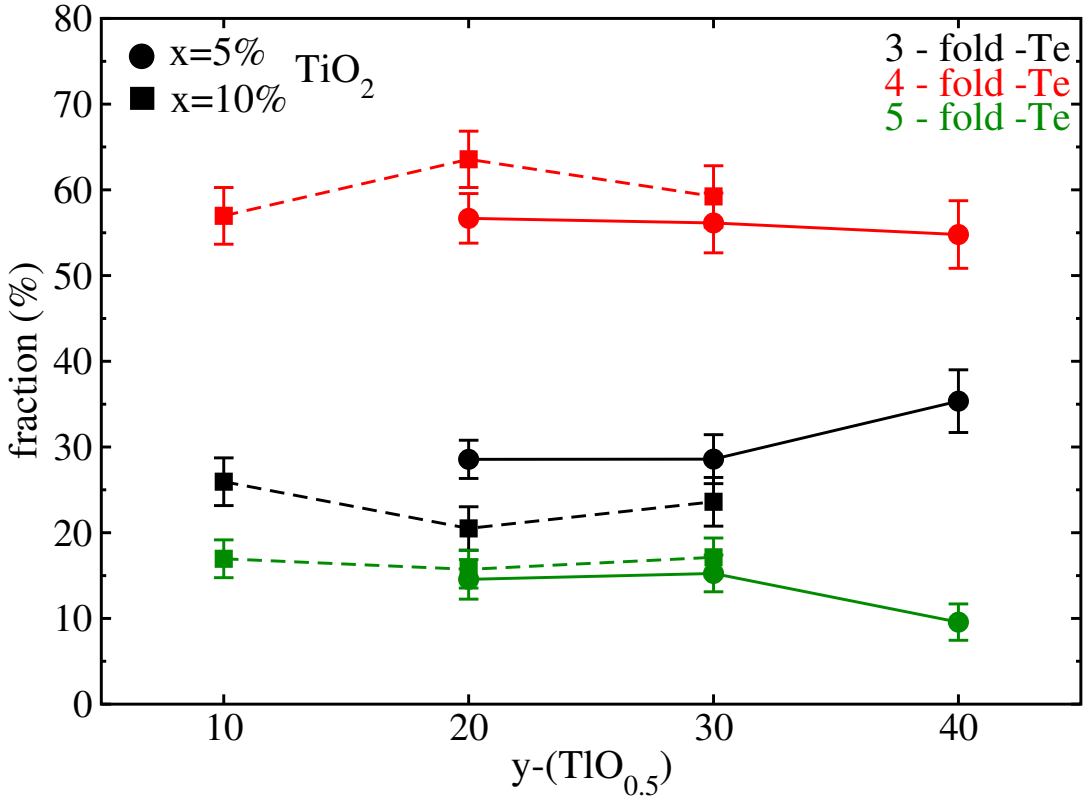

Figure 5.10: Coordination number distributions around Te atom in $(TiO_2)_x - (TlO_{0.5})_y - (TeO_2)_{1-x-y}$ ternary glass. Circles and square represent the 5% and 10% of TiO_2 modifier concentration.

Te atom in order to go further into the knowledge of the evolution of each l-fold since Te acts as a host material, it is largely responsible for establishing the glass matrix and its structural

framework. Table [5.6] reports the various fractions of Te Q^n_m units. From this table, we find that in general at constant TiO_2 content, fully connected Q^m_m units decreases due to structural depolymerization on the verge of increasing Q^n_m (n<m) units as we increase the thallium-oxide modifier concentration. However, it is interesting to note that, with increasing titanium-oxide while keeping the thallium-oxide content constant, fully connected Q^4_4 and Q^5_5 structural units are favored. This behavior is harmonious with our observation of increasing $n_{Te\text{-}O}$ value, with increasing TiO_2 concentration (see table [5.3]).

Q^n_m units	x = 5% y = 20%	x = 5% y = 30%	x = 5% y = 40%	x = 10% y = 10%	x = 10% y = 20%	x = 10% y = 30%
Q^1_3	3.21	3.59	10.33	-	-	2.58
Q^2_3	13.71	13.82	18.11	10.63	10.21	12.65
Q^3_3	11.63	11.05	6.71	14.26	9.16	8.3
Q^2_4	2.65	3.85	10.29	-	2.04	3.03
Q^3_4	20.69	28.02	28.19	14.99	20.32	22.94
Q^4_4	33.33	24.25	16.3	41.42	41.13	33.26
Q^4_5	2.53	4.49	4.83	-	-	3.32
Q^5_5	11.9	10.7	4.48	15.79	14.04	13.8

Table 5.6: Q^n_m values (in percentage) evaluated for Te environments with $r_{cut\text{-}off}$ = 2.48 Å and Wannier formalism constraints. Values less than 2% are ignored due to statistical error.

In addition, another interesting marker of Te environments analysis would be to compare O-Te-O bond-angle distribution obtained on all the models of $(TiO_2)_x - (TlO_{0.5})_y - (TeO_2)_{1-x-y}$ ternary glassy systems, as shown in figure [5.12]. All of these models depict a peak at 85-95° and a less pronounced peak at 160-170°. The broad distribution of peak at smaller angle we notice is due to angles formed between axial-equatorial and equatorial-equatorial oxygen atoms, while the peak at higher angle is due to the angle between axial-axial oxygen atom (see figure [5.11]).

In figure [5.12], we find that the curve corresponding to the highest thallium content model i.e. Ti5-Tl40 system is shifted towards higher angles and vice versa for Ti10-Tl10 system. Furthermore, the BAD for all the other compositions lie in between these two extremes of thallium-oxide concentrations. With the exception of 10% of $TlO_{0.5}$ modifier concentration, this behavior can be explained by the overall increase of 3-fold Te local environments (see figure [4.15]). In particular, increasing $TlO_{0.5}$ at constant TiO_2 concentration lead to transformation of 4 and 5-fold into 3-fold Te environments. Due to this, we notice shift of first peak in O-Te-O BAD towards higher angles. Furthermore, no significant change was observed in the peak position of BAD, with constant $TlO_{0.5}$ and increasing TiO_2 content.

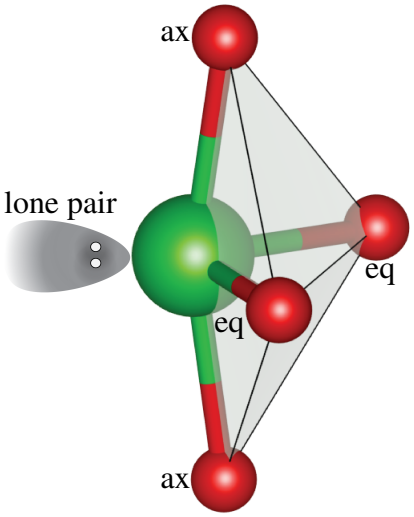

Figure 5.11: Structural unit representation of TeO_4 unit. Green sphere: Tellurium, Red sphere: Oxygen

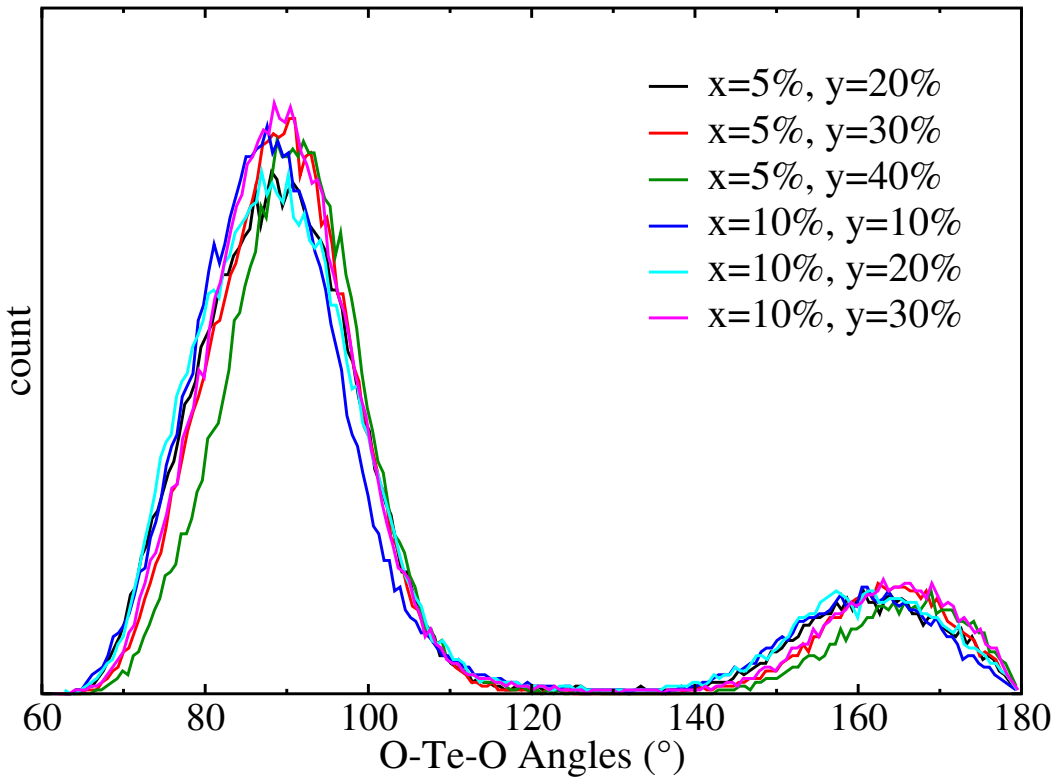

Figure 5.12: Bond-angles distribution of O-Te-O angles in $(TiO_2)_x - (TlO_{0.5})_y - (TeO_2)_{1-x-y}$ ternary glasses.

Ti local environment

From the table [5.4], we find that Ti^{4+} cation favors coordination number close to 5.2 for various composition in $(TiO_2)_x - (TlO_{0.5})_y - (TeO_2)_{1-x-y}$ ternary glasses. Further, we have observed the existence of 4-fold (tetrahedral $[TiO_4]^{4-}$), 5-fold (pentahedral $[TiO_5]^{5-}$, see figure [5.13 (a)]) and 6-fold (octahedral $[TiO_6]^{6-}$, see figure [5.13 (b)]) environments in ternary glasses. More details, about the structure of Ti environments can be obtained via O-Ti-O bond-angle

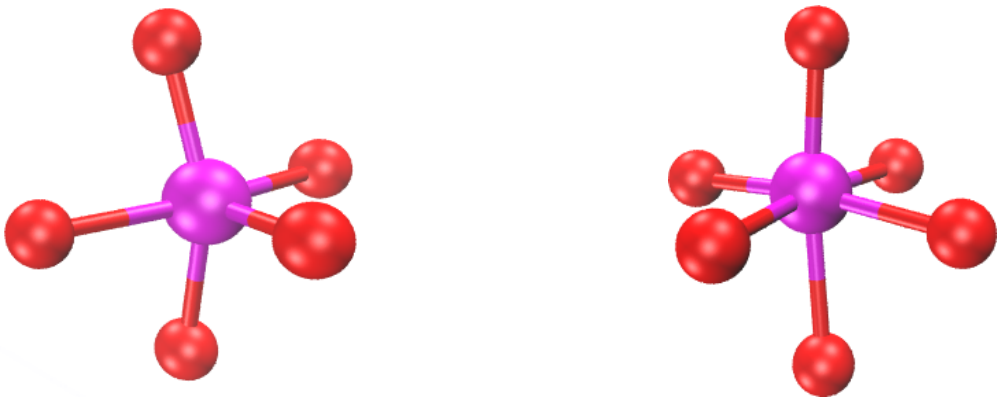

(a) Pentahedral TiO_5 unit **(b)** Octahedral TiO_6 unit

Figure 5.13: Polyhedra generated by TiO_x units in $(TlO_{0.5})_x - (TeO_2)_{1-x}$ binary and $(TiO_2)_x - (TlO_{0.5})_y - (TeO_2)_{1-x-y}$ ternary glass. Red sphere: Oxygen, Magenta sphere: Titanium

distribution as shown in figure [5.14]. In practice, we find two peaks centered around 90° (between the nearest oxygen, centered around Ti local environments) and 167° (oxygen pairs situated opposite to each other in Ti local environments) irrespective of the varying composition in $(TiO_2)_x - (TlO_{0.5})_y - (TeO_2)_{1-x-y}$ glass (see figure [5.13]). The TiO_x polyhedra depicted in figure [5.13] hints towards the distortion in the Ti structural motifs, and a better understanding of this distortion may be gained from O-Ti-O angle distributions. In particular, the sharp peak around 90° indicates the presence of octahedral like geometry and the other peak around 167° represents that the opposite pairs of oxygen atoms in TiO_x unit distort the polyhedra in one direction. In addition, the examination of the O-Ti-O angle distribution with coordination number resolved indicates that the 4 (< 13% fraction), 5, and 6 coordinated Ti atoms, are in distorted tetrahedral, trigonal bipyramidal, and octahedral environments respectively.

Tl local environment

In this subsection, we attempt to study the local environments around Tl atom. Our previous work with $(TlO_{0.5})_x - (TeO_2)_{1-x}$ binary glass have shown that Tl-O bond feature higher ionic character than Te-O bond, hence it is expected that Tl^+ features higher l-folds. Figure [5.15], depicts the evolution of various l-folds for different compositions in Tl $(TiO_2)_x - (TlO_{0.5})_y - (TeO_2)_{1-x-y}$ ternary glasses. Predominantly, we notice that 3 and 4-fold fractions increase in contrast to

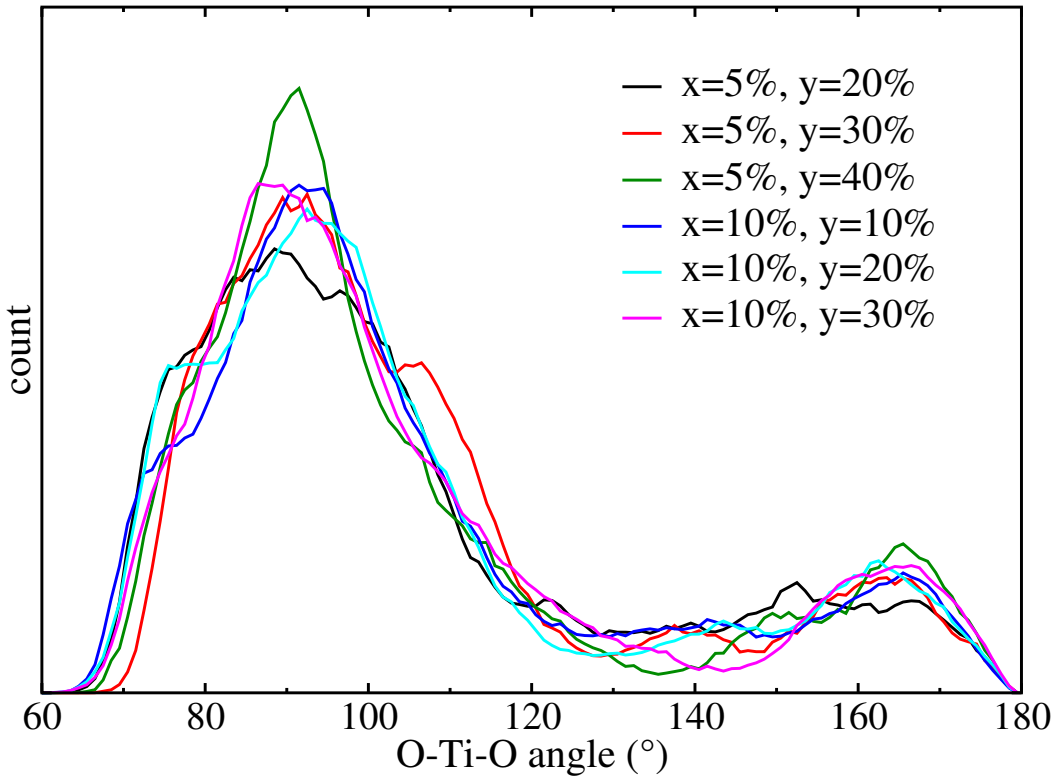

Figure 5.14: Angles O-Ti-O in $(TiO_2)_x - (TlO_{0.5})_y - (TeO_2)_{1-x-y}$

higher fold with increasing $TlO_{0.5}$ concentration. The evolution shows similar behavior as per our prior analysis with $(TlO_{0.5})_x - (TeO_2)_{1-x}$ binary glasses (see chapter [4]), where we assign the root cause of this to shifting of Tl-O partial PDF peaks towards shorter distances with decreasing thallium-oxide concentration. We have discussed in chapter [4], that Tl-NBO population increases as x increases in $(TlO_{0.5})_x - (TeO_2)_{1-x}$ binary glasses and since the distribution of Tl-NBO are centered toward shorter distances than Tl-BO distribution this makes it energetically not favorable to accommodate higher NBO atom. Hence, the higher than 5-fold motifs decrease leading to a rise in 3 and 4-folds. Moreover, with changing TiO_2 and constant $TlO_{0.5}$ concentration of 20% and 30%, generally 3, 4 and 5-fold shows declining trend on the verge of increasing l-folds higher than 5-fold.

O local environment

In the case of local environment analysis of O atoms shown in figure [5.16], we observe that for each TiO_2 concentration as $TlO_{0.5}$ increases, 1 and 2-fold O fractions decrease with a major decline in O-(Te, Te) environments while 3 and 4-fold environments show rising trend with predominantly rising of O-(Te, Tl, Tl) environments. Further, within radius cut-offs of 2.5 Å, we find that at constant $TlO_{0.5}$ and increasing TiO_2 from 5% to 10% illustrates increased O-(Te, Ti) linkages. This shows that within discussed radius as TiO_2 content is increased, -Te-O-Te-

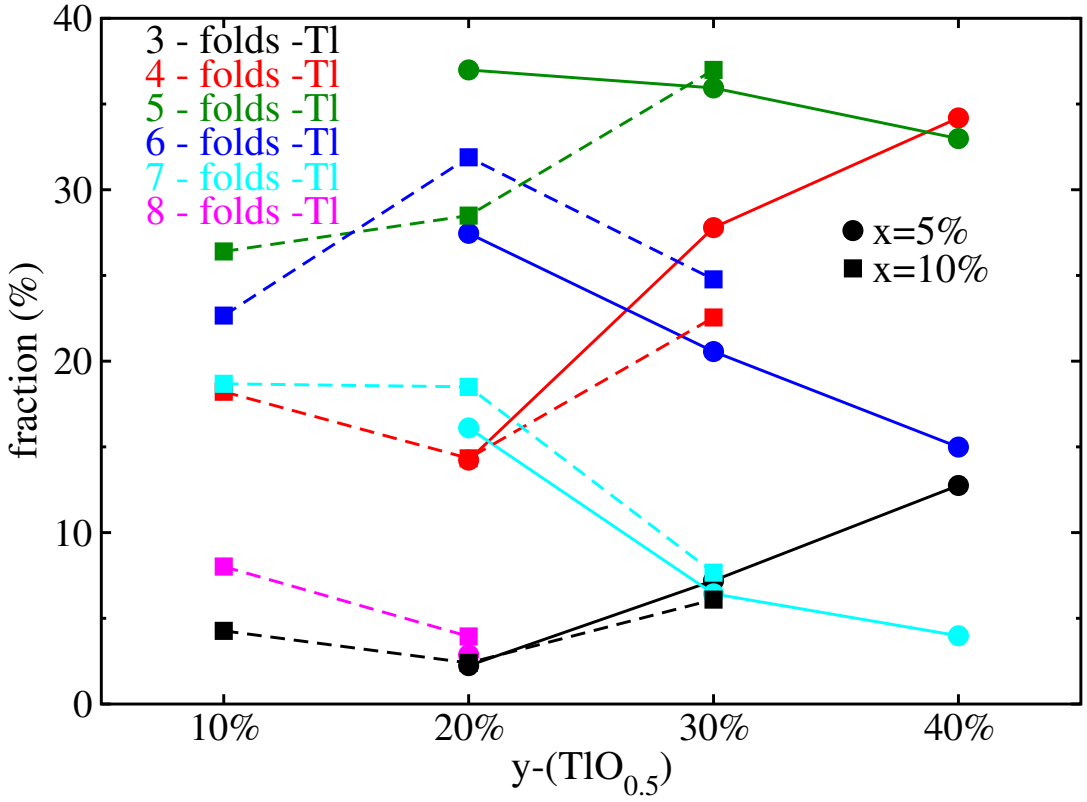

Figure 5.15: Description of l-folds around Tl^+ ion in various composition of $(TiO_2)_x - (TlO_{0.5})_y - (TeO_2)_{1-x-y}$ ternary glass. l-fold fractions less than 2% are not shown in the figure. Circular and square marks represent ternary glass at 5% and 10% TiO_2 modifier concentration respectively.

bridges are replaced by -Te-O-Ti- bridges. Therefore, Ti plays similar role in promoting the glassy network and in contrast to Tl does not promote NBO linkages (see figure [4.11]).

The bottom panel of figure [5.16] shows that adding $TlO_{0.5}$ leads to structural depolymerization and hence to a decline in the contribution of BO on the verge of rising NBO content at constant TiO_2 concentration. This finding is in line with our prior analysis with $(TlO_{0.5})_x - (TeO_2)_{1-x}$ binary glasses (see chapter [4]). However, it is interesting to note that at constant $TlO_{0.5}$ concentration, we see noticeably lower NBO count with rising TiO_2 concentration from 5% to 10%. For instance, Ti10-Tl20 (similarly, Ti10-Tl30) model displays smaller number of NBO than Ti5-Tl20 (similarly, Ti5-Tl30) model. This observation indicates that Ti^{4+} impede creation of NBO and hence promotes formation of linkages between structural units.

5.2.4 Rings statistics

In order to obtain a deeper understanding of the network topologies in $(TiO_2)_x - (TlO_{0.5})_y - (TeO_2)_{1-x-y}$ ternary glassy systems, we would like to focus our attention on connectivity profiles between various species using the King/Franzblau [122], [123] shortest paths criterion. To do so,

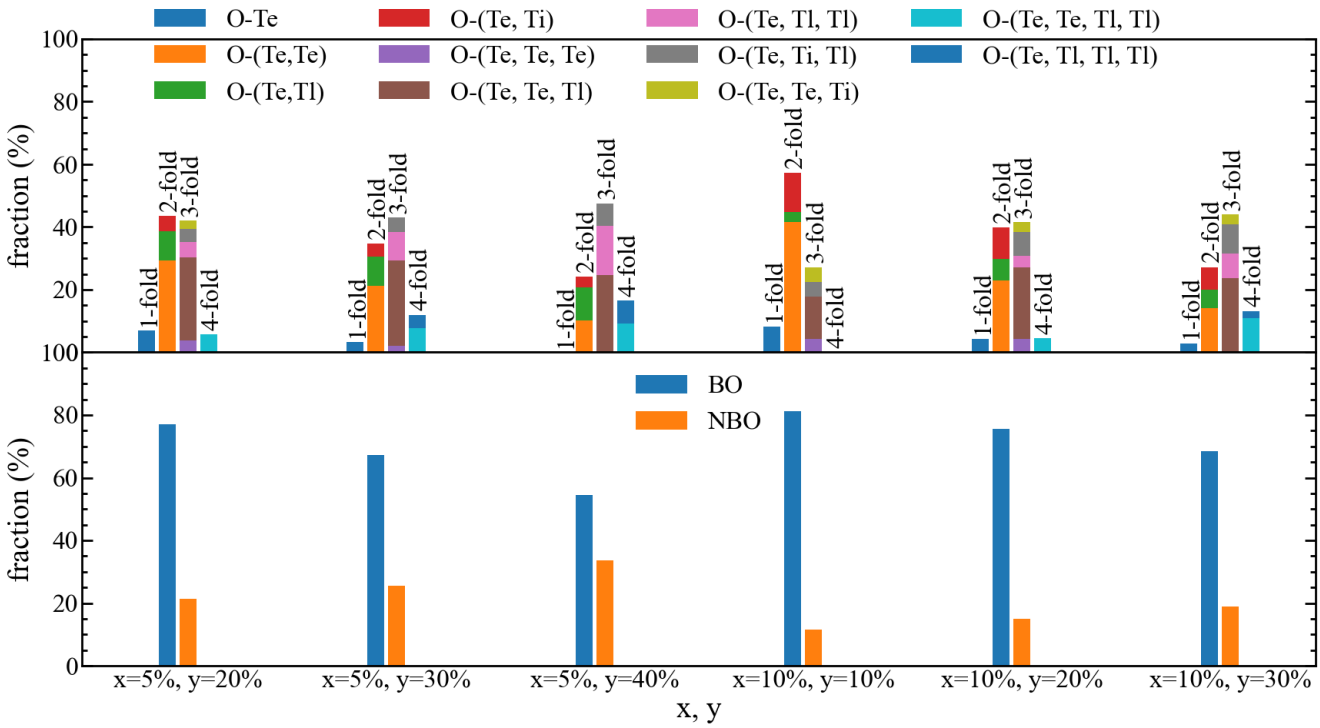

Figure 5.16: Description of l-folds around O for various compositions in $(TiO_2)_x - (TlO_{0.5})_y - (TeO_2)_{1-x-y}$ ternary glass. Top panel represents the percentage of categorization of various l-folds into different kinds of neighbor. Bottom panel displays the evolution of concentration of bridging oxygen (BO) and non-bridging oxygen (NBO) for various glass composition. Fractions less than 2% is not represented.

we use RINGS code [121], in which all the atoms are considered as initial points to begin the search for a given ring. We employ a direct search of Te or O atoms within the radius of $r_{cut\text{-}off}$ = 2.48 Å, without falling back to our Wannier formalism of categorizing the chemical bond. In addition, the cut-off for Tl-O and Ti-O bond distances are chosen to be $r_{cut\text{-}off}$ = 3.26 Å and $r_{cut\text{-}off}$ = 2.5 Å, respectively. We search for rings formed with maximum size of 40 atoms. Figure [5.17] illustrates rings statistics calculated on 100 snapshots from last 10 ps of MD trajectories at T = 300 K. Our calculations show that the peak of R(n) value for pure TeO_2 glass is centered around ring size n = 14 of the ring. Furthermore, based on our previous investigation, we find that adding $TlO_{0.5}$ modifier leads to structural depolymerization and hence breaking of the smaller –Te-O-Te-O– rings. In the figure, we see that the red and blue curves ($(TlO_{0.5})_x - (TeO_2)_{1-x}$ binary glass) are centered around higher values of n. However, it is interesting to notice that substituting $TlO_{0.5}$ with TiO_2 modifier in $(TlO_{0.5})_x - (TeO_2)_{1-x}$ binary glass while keeping the molar concentration of TeO_2 units constant, shifts the peak of the distribution (green and magenta) towards lower values of n, indicating that TiO_2 modifier helps in re-polymerizing the structure and thus making rings of smaller size. Further, we illustrate in figure [5.18] the major size rings forming units in $(TiO_2)_{0.1}$-$(TlO_{0.5})_{0.1}$-$(TeO_2)_{0.8}$ and $(TiO_2)_{0.1}$-$(TlO_{0.5})_{0.3}$-$(TeO_2)_{0.6}$

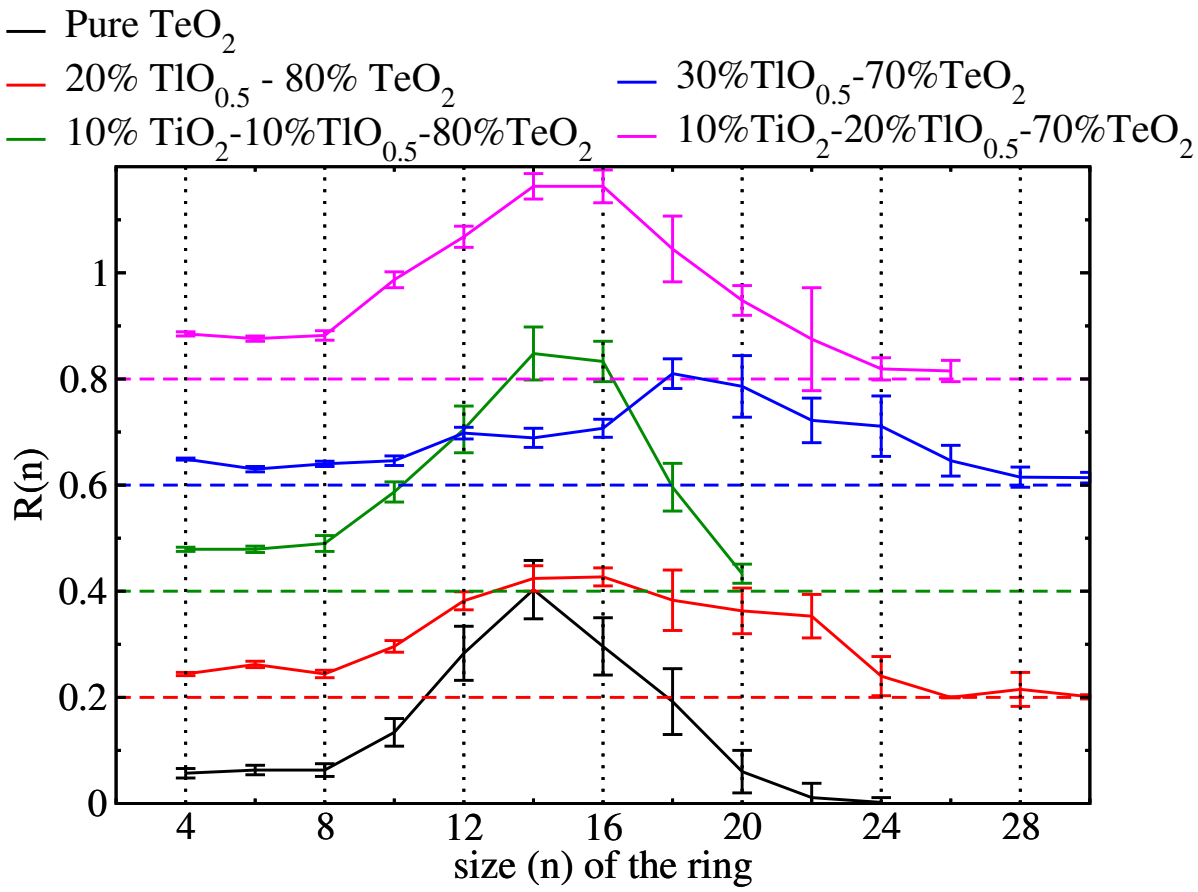

Figure 5.17: Connectivity profiles of various compositions in $(TiO_2)_x - (TlO_{0.5})_y - (TeO_2)_{1-x-y}$ ternary glass. Y-axis, represents, R(n), number of rings with size (n), and is normalized to total number of atoms in each model. Vertical bars represent the standard deviation in the obtained values. For clarity, a shift of 0.2 units between each composition along with dashed horizontal lines showing zeros for particular curve are provided.

ternary glasses. From the figure, we find that Ti^{4+} participates in forming the rings by just substituting -O-Te-O-Te-O- chains by -O-Te-O-Ti-O- units. This observation indicates that Ti^{4+} ions promote the polymerization of the glassy network unlike Tl^{+} ions which favors the structural depolymerization. Therefore, we hypothesize that, because Ti^{4+} helps in binding the network framework, it leads to increasing the mechanical strength of the material.

5.2.5 Bulk modulus

We now proceed further to assess titanium modifier impact on the mechanical strength of the glassy material. To do this, we analyze the bulk modulus using the same method as in our prior analysis with $(TlO_{0.5})_x - (TeO_2)_{1-x}$ binary glasses as described in chapter [4]. First and foremost, we see that at constant TiO_2 and increasing value of $TlO_{0.5}$, the value of bulk modulus decreases and this observation agrees what we have seen in the case of binary $(TlO_{0.5})_x - (TeO_2)_{1-x}$ glasses

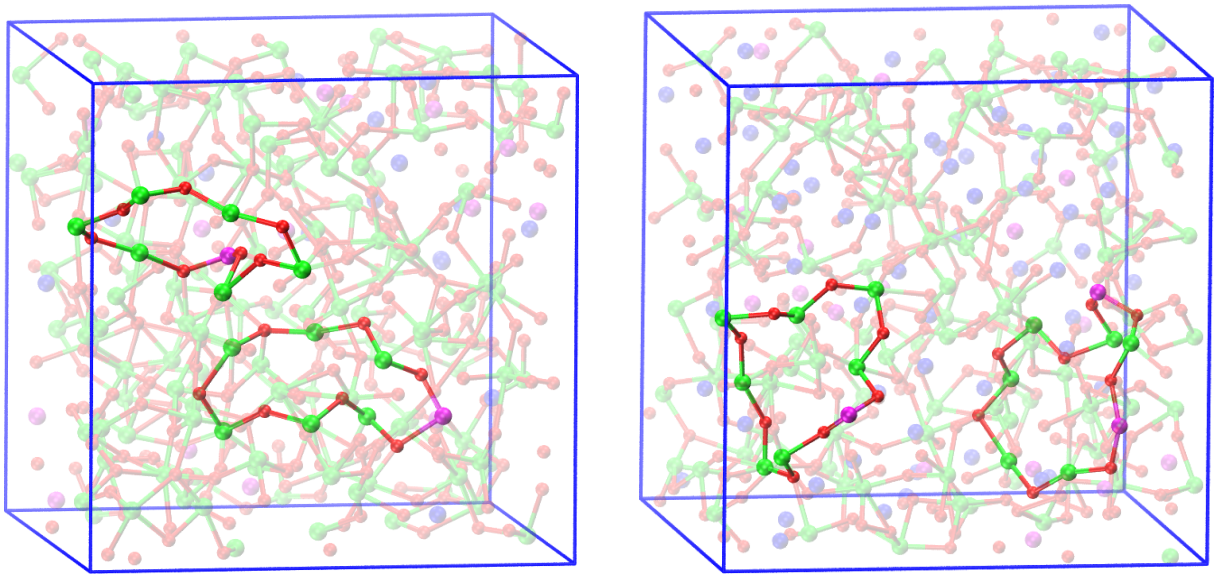

(a) Ring of size 12 in $(TiO_2)_{0.1}$-$(TlO_{0.5})_{0.1}$-$(TeO_2)_{0.8}$. **(b)** Ring of size 16 in $(TiO_2)_{0.1}$-$(TlO_{0.5})_{0.3}$-$(TeO_2)_{0.6}$.

Figure 5.18: Visualization of n-size rings in $(TiO_2)_x - (TlO_{0.5})_y - (TeO_2)_{1-x-y}$ ternary glass. Red sphere: Oxygen, Magenta sphere: Titanium, Green sphere: Tellurium, Blue sphere: Thallium

composition	Bulk modulus (GPa)
Pure TeO_2 glass	22.12
5%TiO_2-20%-$TlO_{0.5}$-75%TeO_2	16.43
5%TiO_2-30%-$TlO_{0.5}$-65%TeO_2	14.43
5%TiO_2-40%-$TlO_{0.5}$-55%TeO_2	12.56
20%-$TlO_{0.5}$-80%TeO_2	17.65
10%TiO_2-10%-$TlO_{0.5}$-80%TeO_2	19.87
30%-$TlO_{0.5}$-70%TeO_2	10.12
10%TiO_2-20%-$TlO_{0.5}$-70%TeO_2	17.96
10%TiO_2-30%-$TlO_{0.5}$-60%TeO_2	16.29

Table 5.7: Bulk modulus of various composition in $(TiO_2)_x - (TlO_{0.5})_y - (TeO_2)_{1-x-y}$ ternary glasses along with the comparison with similar composition of TeO_2 in binary $(TlO_{0.5})_x - (TeO_2)_{1-x}$ glass.

(see chapter [4]). Lower values of bulk modulus indicate the material has lower mechanical properties. In chapter [4], we have assigned the cause of the reduction of the bulk modulus values to the structural depolymerization of the glassy network by Tl ions. Moreover, we observe that at constant $TlO_{0.5}$, increasing TiO_2 leads to increase in the value of bulk modulus (especially in the case of y = 30% $TlO_{0.5}$). In practice, one can interpret increasing TiO_2 at constant $TlO_{0.5}$, as swapping TeO_2 units by TiO_2. And this swapping, highlights the role of Ti as compared to Te, in improving the mechanical strength of $(TiO_2)_x - (TlO_{0.5})_y - (TeO_2)_{1-x-y}$ ternary glasses. This indicates that titanium promotes the mechanical strength of the ternary glass and hence supporting the assertion put forward by authors in Ref [9]. Another interesting way of

understanding the evolution of bulk modulus of $(TiO_2)_x - (TlO_{0.5})_y - (TeO_2)_{1-x-y}$ ternary glasses is to compare its value with binary $(TlO_{0.5})_x - (TeO_2)_{1-x}$ glasses at constant TeO_2 concentrations. We see that, at 70% and 80% of TeO_2, when we substitute fraction of $TlO_{0.5}$ with TiO_2 units, this leads to an amplification of bulk modulus values. In contrast to Tl^+, Ti^{4+} seems to make stronger bonding with oxygen atoms due to higher field strength.

5.3 Conclusions

Using *ab-initio* molecular dynamics we have studied the structures of $(TiO_2)_x - (TlO_{0.5})_y - (TeO_2)_{1-x-y}$ ternary glasses for 6 different compositions. We have utilized the PDF to understand how the short-range order evolves as a function of varying thallium oxide and titanium oxide contents. Further, we see that in contrast to $TlO_{0.5}$, increasing TiO_2 modifier concentration promotes the coordination number $n_{Te\text{-}O}$. This increased value of $n_{Te\text{-}O}$ shows that adding TiO_2 promotes better network connectivity in $(TiO_2)_x - (TlO_{0.5})_y - (TeO_2)_{1-x-y}$ ternary glasses. Further, we have studied how the local environments around each species vary as a function of compositional dependence of the modifier. We find that, at constant $TlO_{0.5}$ concentration, adding TiO_2 leads to decrease in 3-fold Te while the 4 and 5-fold Te motifs increase. Moreover, in the case of O local environments we have seen that incorporating TiO_2 at constant concentration of $TlO_{0.5}$ displays a rise in BO. As evidenced by rings analysis, our work highlights that Ti^{4+} acts as substituent of Te^{4+} cation and promotes the polymerization of the glassy network. In this chapter, we also put forward that the mechanical resistance of the ternary glass will be higher than $(TlO_{0.5})_x - (TeO_2)_{1-x}$ binary glasses due to the formation of smaller rings containing Ti^{4+} ions. The findings of this work can be viewed as an important step forward in the search around the TeO_2-based glassy systems with optimum chemical composition of $TlO_{0.5}$ and TiO_2 modifier oxides.

6

Vibrational and optical properties of TeO_2-based glasses

Summary

6.1 Methodology **180**
6.2 Raman spectra **182**
6.2.1 Pure TeO_2 glass 182
6.2.2 Modified TeO_2 glasses 189
6.3 Non-linear optical properties **193**
6.4 Conclusions **201**

We present a computational scheme combining periodic DFT and finite difference method that enables the calculation of accurate Raman spectra and non-linear optical properties on large models of oxide glasses and compared it to the experimental results. Despite the progress in achieving a fine understanding of the structure of TeO_2 based glasses (see chapters [1], [3], [4], [5]), the study of their vibrational and non-linear optical properties remains scarce. The main stumbling block in computing spectroscopic and optical properties is the huge computational effort required when dealing with amorphous systems within a periodic DFT calculation. On the one hand, the proper description of these glasses requires an atomistic model containing several hundreds of atoms. On the other hand, the existent methodologies are either suitable for small size systems or only work well in the case of crystalline materials [135]–[140]. As such, a method able to compute accurate Raman and NLO properties on large periodic amorphous models at a reasonable computational cost would enable access to important quantities required to properly correlate the macroscopic properties of the material to its microscopic structure setting the scenes thereby to a better design roots of functional oxide materials. We provide a computational scheme in the next section that allows one to simulate Raman spectra with a reasonable computational expense for periodic systems containing several hundreds of atoms by relying on the efficiency of the CP2K code for DFT calculations and a finite difference method. Furthermore, we also present a computational scheme that enables the calculations of the third order nonlinear susceptibility of the glass. Hence, our modelling scheme paves the way towards systematic computational studies of non-linear optical and vibrational properties of oxide glasses.

6.1 Methodology

In close collaboration with Dr. Evgenii M. Roginskii[1], we have developed a technique for computing Raman spectra that is based on the finite difference approach and makes use of CP2K to perform Density Functional Perturbation Theory (DFPT) calculations. In this scheme, one starts with optimizing the geometry of the studied system in order to achieve a relaxed structure at the minimum of the electronic energy. To do so, DFT calculations are carried out within the GGA formalism to DFT as implemented in CP2K software package. The PBE functional was used in all the calculations. The GPW method [88] was used to form wavefunctions basis set with cut-off energy equal to E_g = 1000 Ry for plane wave part and using triple-zeta valence basis for local combination of molecular orbitals part. GTH pseudopotentials are used to describe core-valence interactions. As the system vibrations are directly related to the curvature of the potential energy surface, a very high numerical accuracy is required to get accurate frequencies. The self-consistent calculations were performed with an electronic convergence criterion of 10^{-8} Ha. Geometry optimization is performed by relaxing both cell parameters and atomic positions at fixed angles for a given atomistic configuration. During the relaxation, atomic displacements and

[1]Ioffe Institute, Polytekhnicheskaya 26, 194021 St. Petersburg, Russia

lattice parameters were varied until forces on atoms become below 10^{-5} Ha/Bohr and pressure below 10^{-2} GPa. Subsequently, phonon calculations are performed to extract the vibration frequencies and the normal modes. We here resort to the PHONOPY software package [141] to compute the dynamical matrix using finite difference method where the diagonalization of the mass unweighted force constant matrix in units Ha/Bohr provides a direct access to Phonon frequencies and normal modes (see method 2 in workflow of figure [6.1]). Alternatively, the vibrational analysis can also be performed using CP2K code instead of resorting to PHONOPY software package (see method 1 in workflow of figure [6.1]) in order to obtain Phonon frequencies and normal modes. See Appendix [A.7] for a stepwise implementation of the below workflow.

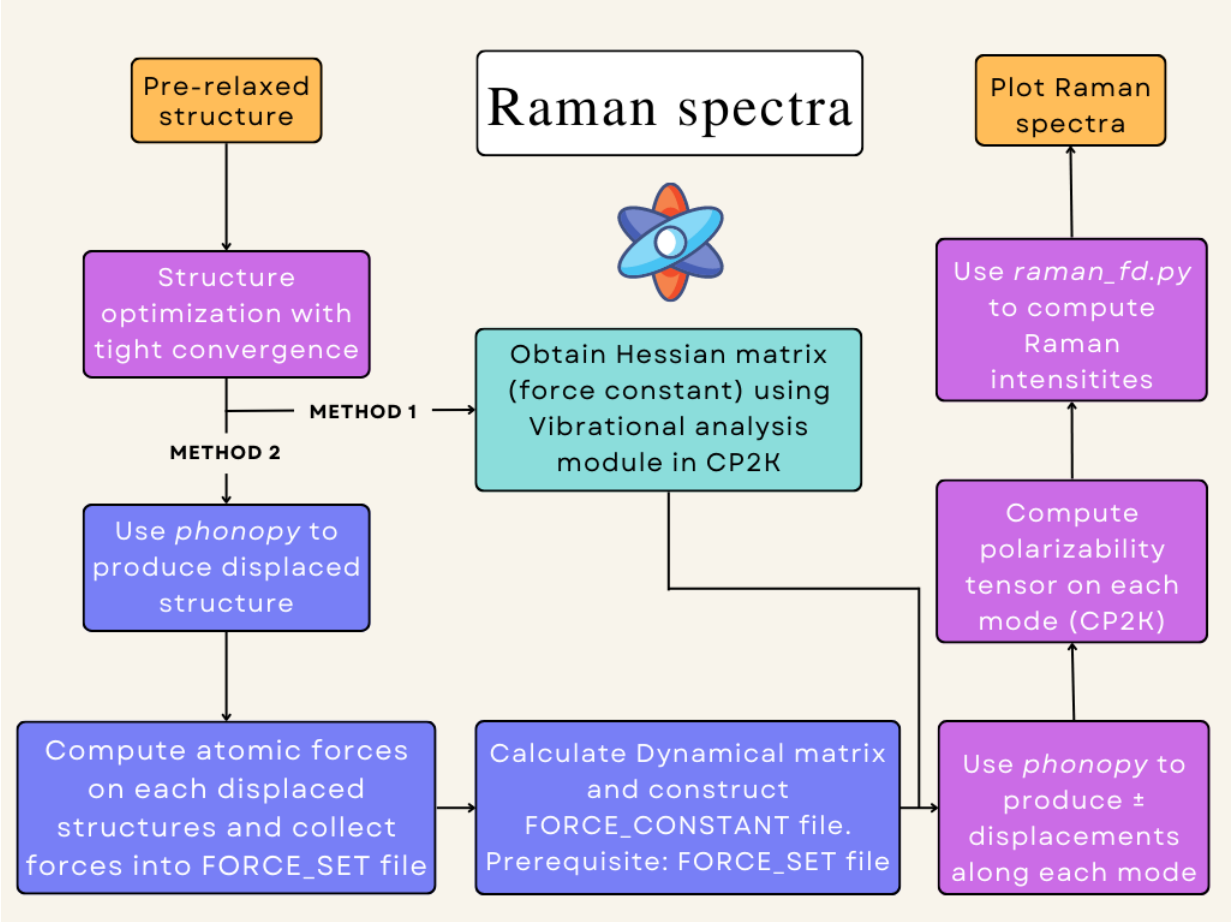

Figure 6.1: Computational workflow used for computing Raman spectra.

In addition, the DFPT approach has been used to compute the polarizability tensor and then using finite difference method Raman tensor has been calculated as defined in chapter [2] equation [2.92]. This method is based on generation of structures with atomic displacements along each normal mode in positive and negative directions, followed by calculations of the susceptibility tensor χ_{ij} for each distorted structure using linear response approach as implemented in CP2K

[142]. Finally, the values of Raman tensor components for each vibrational mode are obtained as derivatives of the susceptibility with respect to normal vectors obtained by finite difference methods (see equation [2.92] in chapter [2]).

6.2 Raman spectra

6.2.1 Pure TeO_2 glass

We calculated Raman spectra (see section [2.6.2.2] in chapter [2]) on glassy TeO_2 and glassy SiO_2 as an average of 10 spectra computed on 10 amorphous configurations sampled from the T = 300 K trajectory of the glass for each system. Amorphous SiO_2 model generation details are described in the Appendix [A.3]. The obtained results are presented in figure [6.2] and compared with experimental results.

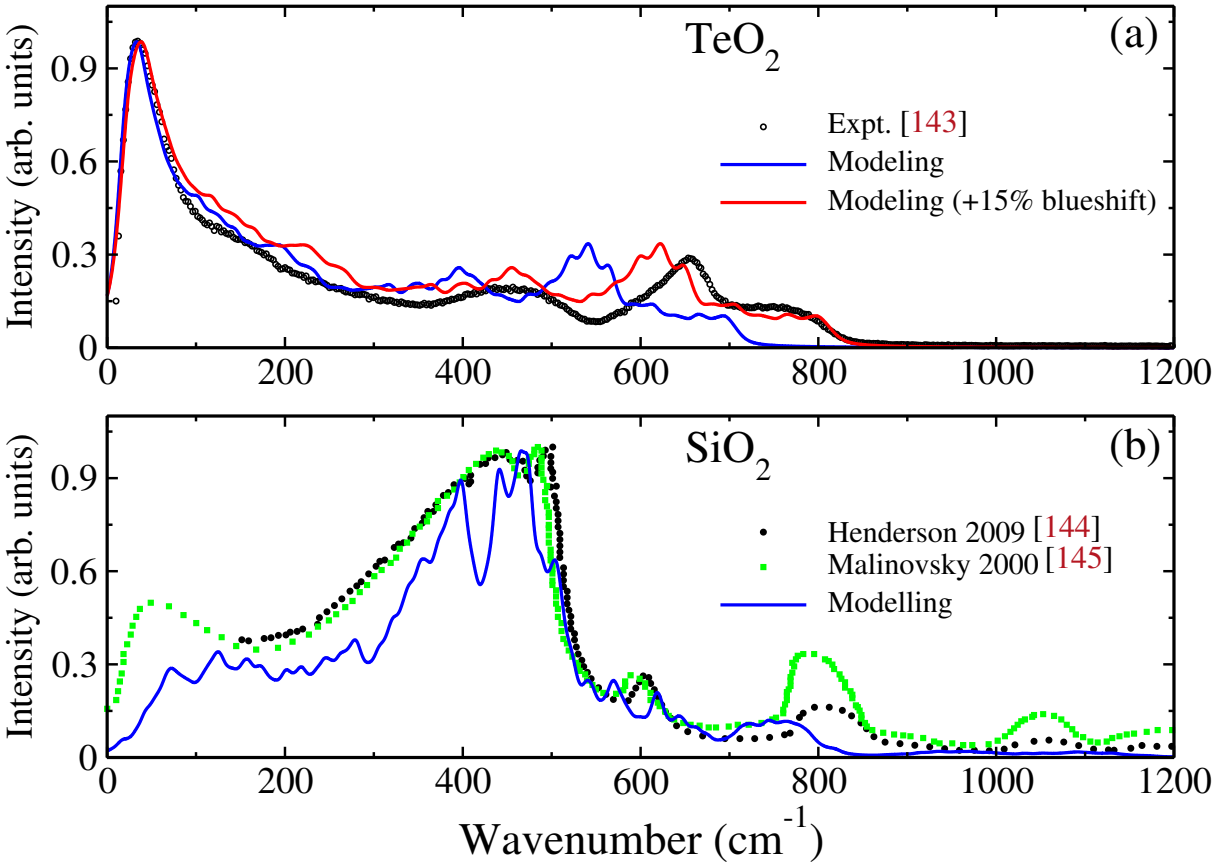

Figure 6.2: Calculated Raman spectra on glassy TeO_2 (a) and glassy SiO_2 (b) compared to experimental results from Refs. [143],[144] and [145], respectively. A 15% blue shift was applied to the Raman shift in the case of TeO_2. The Raman intensity is normalized to the maximum peak intensity.

By inspecting the experimental Raman spectra of TeO_2 one can identify several ranges with

particular signatures that have been correlated in the literature to particular vibrational modes. In the low wavenumbers region, one can associate the main peak centered around 30 cm^{-1} to the Boson peak [146], while the shoulder around 140 cm^{-1} can be attributed to the intra-chain vibrations of Te-Te bonds [147]. In the central wavenumbers range a broad peak coincides with the typical signatures of symmetric stretching vibrations in nearly symmetric (425 cm^{-1}) and symmetric (500 cm^{-1}) stretching vibrations in Te-O-Te bridges [22], [23]. As for the asymmetric stretching vibrations in nearly symmetric and asymmetric Te-O-Te bridges, they lead to typical signatures around 605 cm^{-1} and 660 cm^{-1}, respectively [22], [23]. Finally, the frequency band in the high wavenumber region can be attributed to the asymmetric stretching vibrations in asymmetric Te-O-Te bridges (710 cm^{-1}) and asymmetric stretching of essentially covalent TeO bonds (770 cm^{-1}) [22], [23].

By looking at the calculated Raman spectrum one can distinguish all the observed features in the experimental spectra. Nevertheless, for wavenumbers higher than 300 cm^{-1} all the bands positions are under-estimated by about 15%. This discrepancy is due to the small overestimation of the Te-O bond length in our models by about 0.04 Å [148] (see chapter [3]). This is a well-known issue related to the GGA functional family of exchange and correlation functionals that slightly overestimate the lattice parameters and inter-atomic bond lengths [30], [49]. In addition, the large asymmetry around O atoms might impact the obtained frequencies. Therefore, applying a 15% blueshift leads to modeled spectra with an unprecedented good agreement with the measured one over the whole range of frequencies (see figure [6.2]).

Similarly, the calculated Raman spectrum of glassy SiO_2 shows a well reproduction of the experimental one. In this case, we note a very limited blueshift thanks to the very well defined structure of SiO_2. Compared to the TeO_2, the Raman spectrum of glassy SiO_2 features a small peak at around 50 cm^{-1} that corresponds to the Boson peak. Given that the origins of the Boson peak in amorphous TeO_2 remain largely unknown, a comparative study of the Raman spectra between the TeO_2 and SiO_2 turns out to be instructive. The Raman intensity calculated from equation [2.90] (see chapter [2]) contains two main contributions, the squared Raman tensor components and the pre-factor $\mathcal{G} = (1 + n_m(\omega))/\omega$ which contains a dumping inverse frequency term $1/\omega$ multiplied by the Bose-Einstein distribution function n_m. In order to disentangle the contributions of the various terms in equation [2.90] (see chapter [2]) to the total Raman intensity, we show in figure [6.3] the calculated temperature dependent Raman spectra of TeO_2 and SiO_2. The temperature dependence of the spectra is triggered by the temperature dependence of the Bose-Einstein distribution function n_m.

It is noteworthy that the simulated Raman spectra at zero temperature reveals no Boson peak feature for both oxides. At zero temperature Bose-Einstein term is negated and the pre-factor $\mathcal{G}$ is acting simply as a dumping function $(1/\omega)$ for the squared Raman tensor components (see

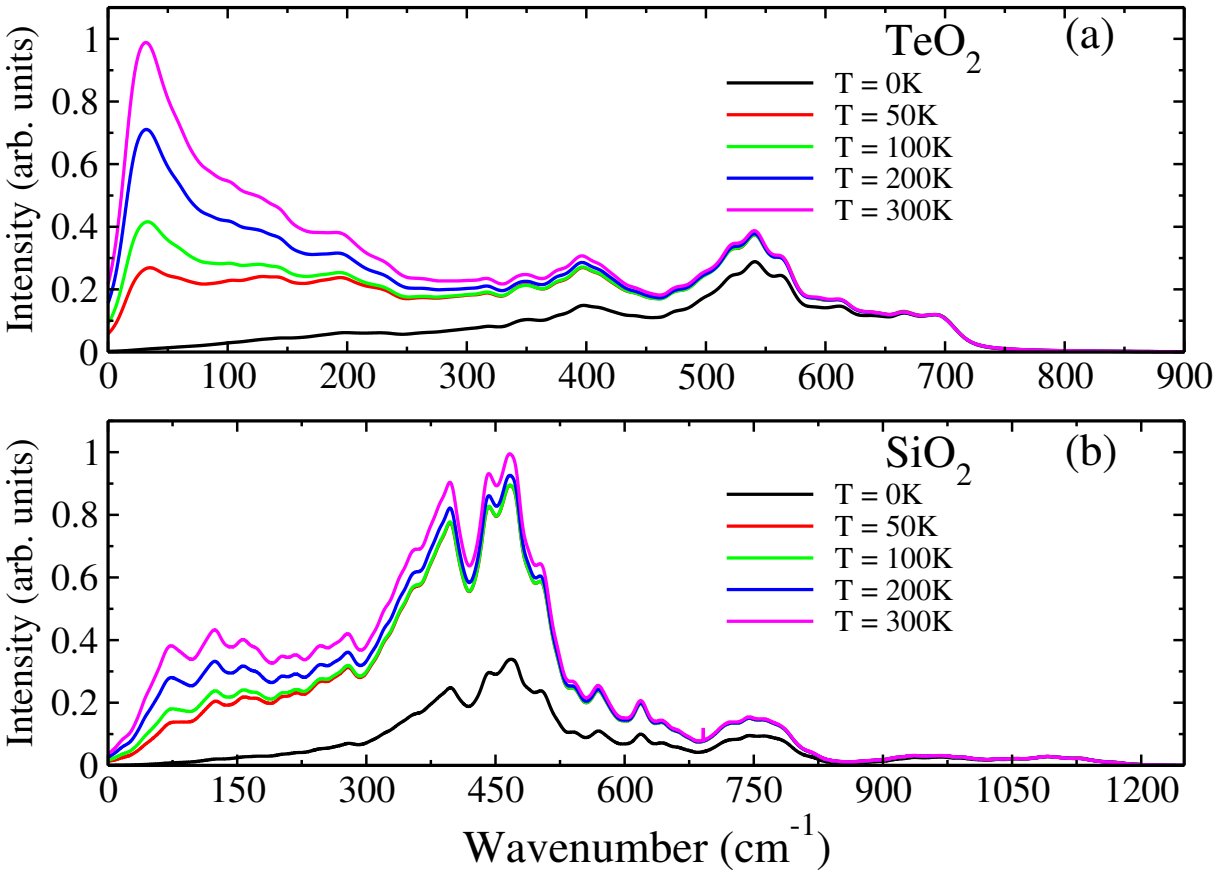

Figure 6.3: Simulated Raman spectra of glassy TeO_2 (a) and glassy SiO_2 (b) at different temperatures. The spectra are normalized to the highest frequency band, where the effect of pre-factor is minimal.

chapter [2], equation [2.90]). Interestingly, we observe that the "natural" Raman activity (i.e. squared Raman tensor components) is very small in the low frequency range (indeed the highest intensity band in range [0-50] cm^{-1} is related to the highest intensity band in the whole spectra as 1:100). As temperature increases, the impact of the Bose-Einstein distribution function become more clear and one can find a significant response in Raman spectra in the low frequency range. At T = 100 K, one can clearly see that the Bose-Einstein distribution overpower the dumping function in the low frequency range which leads to an "amplification" of the Raman spectra in the low frequency range. Therefore, the pre-factor $\mathcal{G}$ takes a key role in the low frequency range Raman spectra. In general, at finite temperature it acts as an amplifier for the low frequency range, and the strength of this amplification depends on a competition between the two terms in the pre-factor $\mathcal{G}$ according to the temperature and the frequency of the considered Raman band.

As soon the nature of low frequency Raman spectra amplification is established, it is worth to compare the spectra of TeO_2 and SiO_2. At zero temperature, Raman spectra of TeO_2 shows a monotonically growth of the intensity starting rapidly from zero frequency. Actually, the lowest Raman band occurs at 17 cm^{-1}. In the case of SiO_2, the spectra show a zero intensity

at very low frequencies and starts to grow weakly only at approximately 50 cm^{-1} (the lowest frequency Raman band is found at 32 cm^{-1}). At finite temperature, the band at low frequencies is clearly observed in the case of TeO_2. Nevertheless, in the case of SiO_2 glass even at T = 300 K this band is not that strong as in the Raman spectra of TeO_2. This can be explained by a frequency dependence of the pre-factor $\mathcal{G}$. This dependence follows a simple rule: the lower the frequency of the band the higher the amplification of the Raman spectra is. As mentioned above, the smallest phonon frequency of TeO_2 is found at 17 cm^{-1}, while the lowest frequency phonon in the case of silica glass is found at 32 cm^{-1} . This difference in ca. 15 cm^{-1} leads to a significant difference in the intensity of the Boson peak.

The advantage of the method presented in this chapter is that it allows to make a deep analysis of the Raman bands as it gives access to the normal modes (atomic displacements of vibrational modes) of the Raman active vibrations. Due to the amorphous nature of the system where no crystallographic symmetry exists, a very big number of normal modes is always obtained. In order to limit the analysis to the most important modes we here focus on those having a Raman activity of at least 9% of the maximum calculated Raman intensity. In addition, the atomic displacements responsible for a given Raman active modes are considered in the analysis only if displaced by at least 0.005 Å (see figure [6.4a]).

By analyzing the structural fragments involved in vibrations related to the Boson peak, one infers that these modes are the result of a collective vibrations of structural units (TeO_4, TeO_3, TeO_5) as a whole (see figure [6.4b], snapshot A). This result is consolidated by investigating the overall weight of the chemical species (Te, O) in a given Raman active mode, which is calculated as a sum of displacements made by atoms of a given chemical species with respect to the sum of displacements of all atoms in a given vibrational mode. In figure [6.5] the weight for each chemical species is plotted as a function of the Raman frequency. It is noteworthy that the weight of O atoms will always be at least twice as much than the one of Te atoms since the amount of O atoms is twice as much than Te atoms in TeO_2 glass. This factor two is exactly satisfied at the low frequency range where the impact of Te and O atoms is nearly the same (taking factor of 2 into account). In opposite, in the high frequency range the weight of oxygen atoms becomes dominant indicating the key role of O vibrations in this range of frequencies. Overall, we find that in the low frequency range, vibrational modes are attributed to displacements of the structural units (TeO_3/TeO_4/TeO_5) as a whole, while the opposite occur in the middle and high frequency range where the general displacements are due to oxygen atoms displacements with respect to Te atoms, which remain nearly fixed in their respective equilibrium positions (see figure [6.4b], snapshots (C, D and E)). This assumption provides an explanation of the origin of the weak "natural" Raman activity observed for the low frequency vibrational modes. In fact, the vibrations of the whole structural units lead to a weak change of the polarizability of the whole system and therefore to a small Raman response, which in turn is proportional to the derivative of

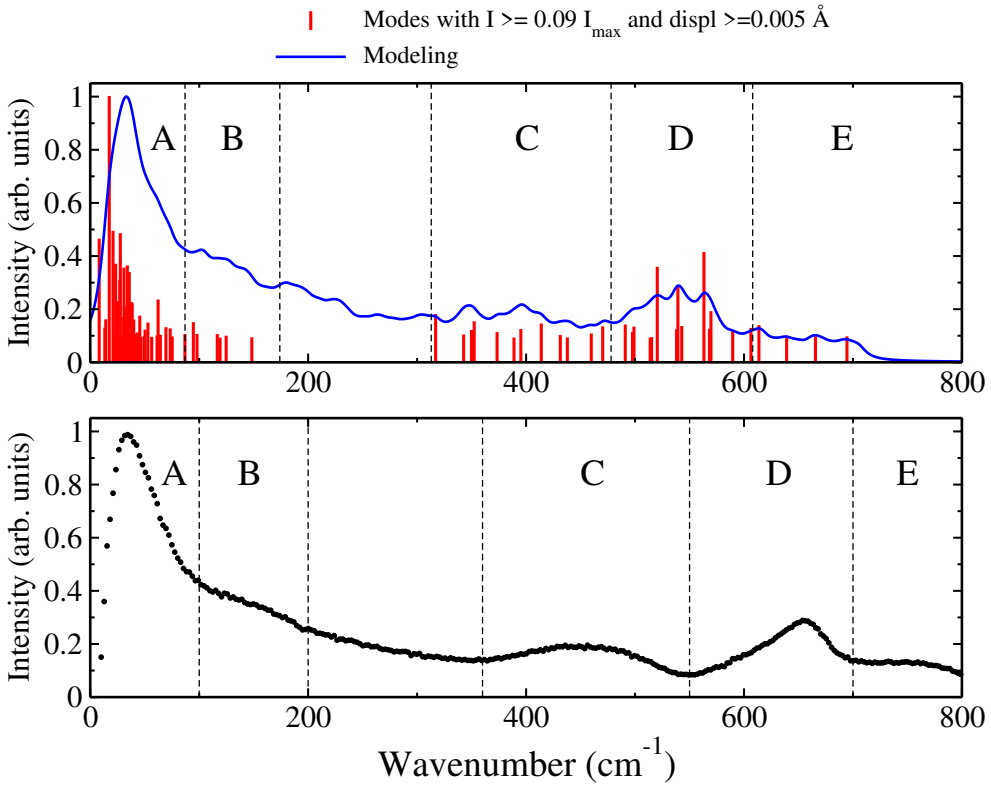

(a) Calculated Raman spectra on glassy TeO_2 with modes contributing more 9% of maximum Raman intensity and atomic displacement more than 0.005 Å (top).

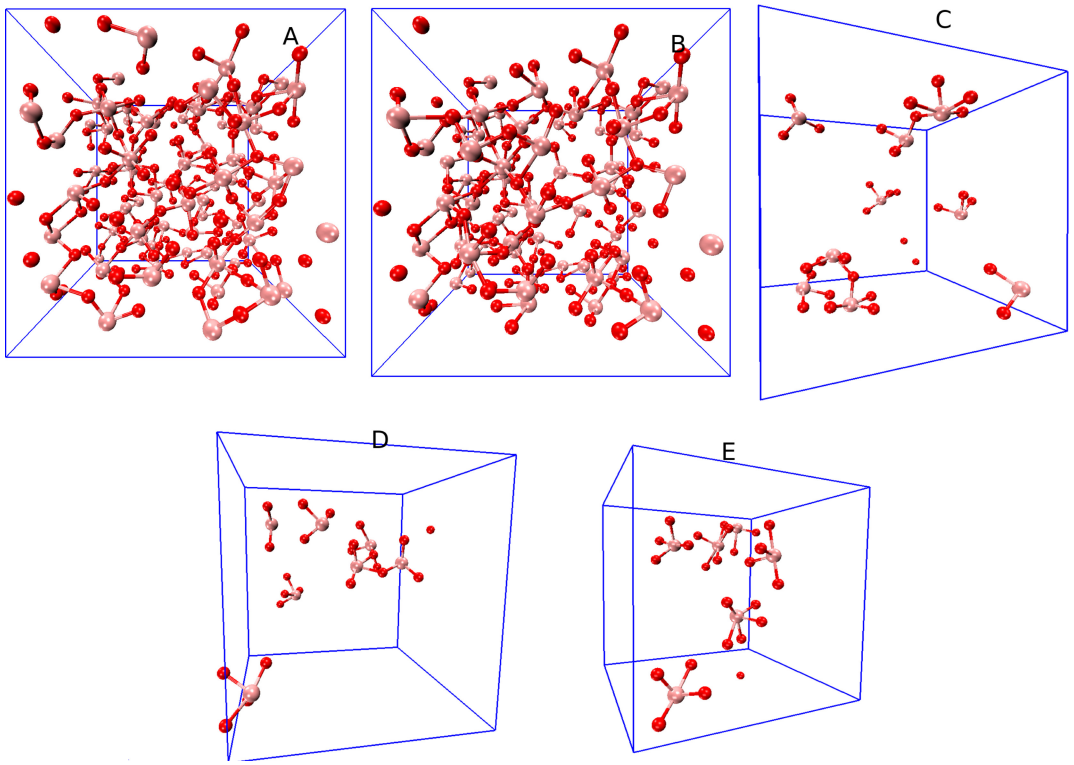

(b) Structural motifs involved in various regions (A, B, C, D and E) of vibrational modes. Moreover, Te atoms in C, D and E representations are shown for clarity although being displaced much less than 0.005 Å.

Figure 6.4: Calculated (a) Raman spectra and (b) the structural motifs involved in the vibrational modes.

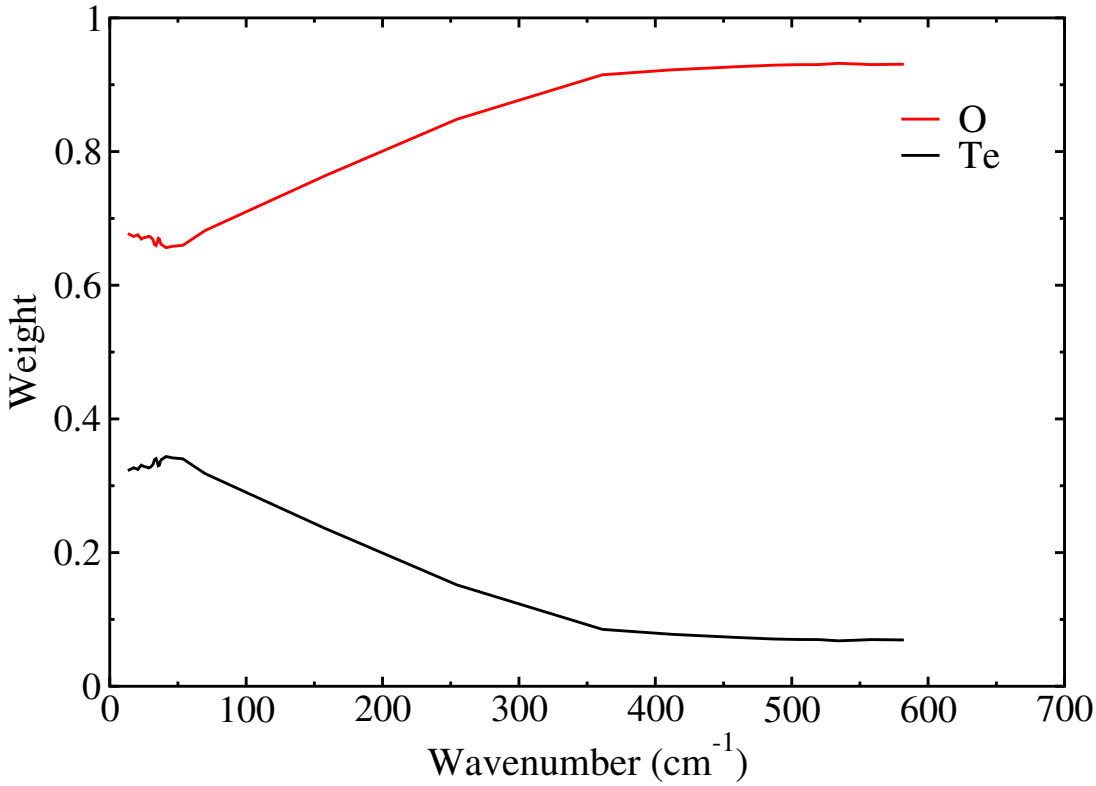

Figure 6.5: Frequency dependence of displacement weights of Te and O atoms in Raman active vibrational modes.

the polarizability with respect to atomic displacements. However, the dominant Te-O vibrations in the middle and high frequency ranges, including bending, vibration and stretching, leads to a significant impact on the polarizability changes, and consequently to a high Raman activity.

Finally, the origins of the strong Boson peak in TeO_2, explained earlier by the low frequency vibrational states, compared to SiO_2 can be also attributed to the physical properties of both systems. In particular, assuming that the low frequency states are related to displacements of the whole structural units, one can put forward a correlation between their low frequency and the mass of the structural units involved in these vibrational states. In a simple harmonic approximation, the frequency is proportional to the inverse square root of the mass $\omega = \sqrt{k/m}$. Assuming the value of k to be more or less constant for TeO_2 and SiO_2, and having in mind that the mass of the structural unit TeO_4 is almost twice as much than the one of SiO_4, one can easily establish that the ratio of Boson peak frequency for TeO_4 and SiO_4 systems is equal to $\sqrt{2}$. The experimental frequency of Boson peak of TeO_2 is 35 cm^{-1} taking the ratio $\sqrt{2}$ into account one obtains a frequency shift up to 49.5 cm^{-1} for SiO_2 amorphous silica, which is very close to experimental data plotted in figure [6.2b]. This correlation is of a particular interest since it is only related to the mass of the structural units involved in the vibrational

modes. Therefore, it is possible to predict the position and the strength of the Boson peak in Raman spectra in other amorphous materials.

The Boson peak observed in Raman spectra of amorphous TeO_2 (see figure [6.2]) is significantly stronger than the one in SiO_2. This can be explained by the high concentration of phonon states in the low-frequency range. In figure [6.6] the vibrational density of phonon states (VDOS) is plotted. The strong low frequency band in VDOS of TeO_2, compared to the much weaker band in VDOS of SiO_2, rise rapidly and reach a maximum at frequency $\sim$50 cm^{-1}. In opposite, the low frequency band in VDOS of SiO_2 is very broad and have a maximum at $\sim$130 cm^{-1}. It is noteworthy that prefactor $\mathcal{G}$ acts as a dumping factor at higher frequencies and this is, additional to lower density of states in VDOS of SiO_2, the reason which explains why the Boson peak in Raman spectra of SiO_2 is weaker than the one of TeO_2. This finding shows that the intensity and frequency of Boson peak could be qualitatively estimated by analysis of VDOS.

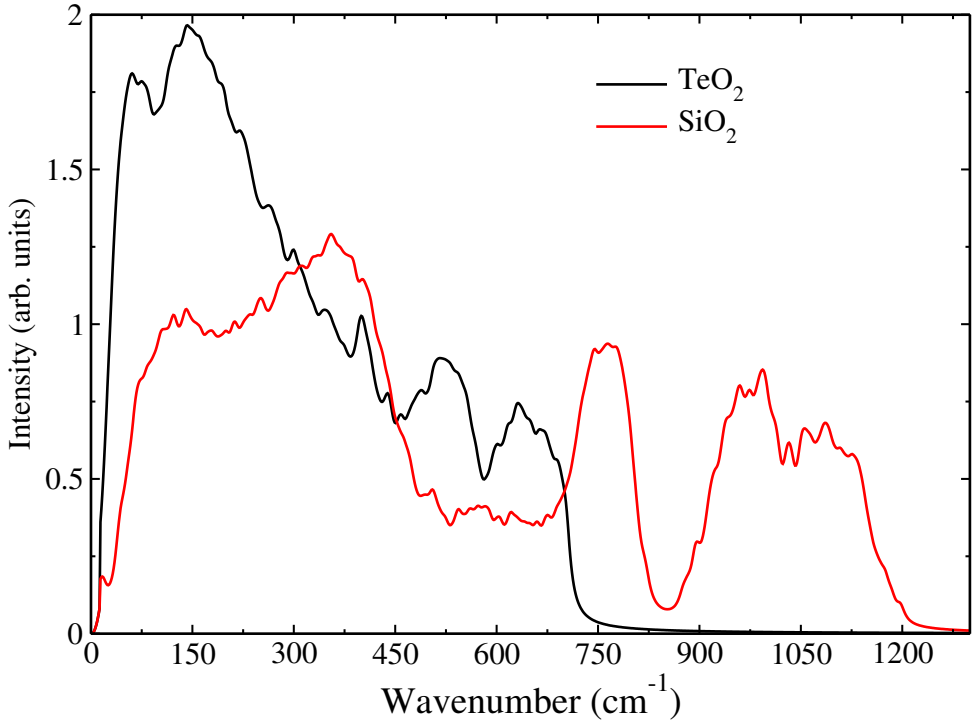

Figure 6.6: Calculated phonon density of states of amorphous TeO_2 and SiO_2.

Such approach could be extended to the analysis of the VDOS of crystalline oxides which can be used to achieve a qualitative analysis of the Boson peak nature where the dispersion of acoustic branches, which are related to sound velocity, are a key feature to predict the strength of the Boson peak. An amorphous system can be considered as a crystal system with breaking of periodic boundary conditions which leads to many times Brillouin zone folding, and consequently the whole Brillouin zone degenerate to Γ-point. Therefore, as a first approximation one can

consider the phonon density of states integrated over the whole Brillouin zone in the crystal as a phonon density of states in glass. In figure [6.7] the phonon band structure and phonon density of states are plotted for paratellurite α-TeO_2 crystal. One can distinguish a sharp and strong peak in TeO_2 VDOS at a frequency of $\sim$55 cm^{-1} which is close to the Boson peak frequency. This band mostly consists of acoustic branches, which have a small dispersion due to low sound velocity. In opposite, in case of α-SiO_2, VDOS is weak and broad in low-frequency range having a maximum at $\sim$75 cm^{-1}. The sound of speed in α-SiO_2 is high, and the band consist of a mixture of acoustical and optical phonon branches. Such a mixture triggers the formation of a broad band from 0 up to 500 cm^{-1} with local maxima. The results of crystalline systems VDOS analysis are in line with the one made on amorphous one. Therefore, it can be used for qualitative analysis of the Boson peak nature where the dispersion of acoustic branches, which is related to the sound velocity, is a key feature to predict the strength of the Boson peak.

6.2.2 Modified TeO_2 glasses

We now proceed to discuss the Raman spectra of $(TlO_{0.5})_x - (TeO_2)_{1-x}$ binary glasses. In particular, figure [6.8] depicts the evolution of Raman spectra for various compositions of the binary glass. In figure [6.8a], we compare the simulated Raman spectra with its experimental counterpart. We have provided a blueshift of 15% to the wavenumber for the Raman spectra of each composition in $(TlO_{0.5})_x - (TeO_2)_{1-x}$ binary glasses to account for the overestimation of Te-O bond lengths by GGA-PBE functional. We find that our model is able to reproduce all the major peaks present in the experimental data and their evolution as a function of the composition. As per our prior discussion with pure TeO_2 glass, the peak in the middle frequency range of 400-500 cm^{-1}, is due to symmetric stretching of Te-O-Te bridges and thus indicate the extent to which TeO_x structural units are polymerized. Further, in the figure [6.8a], we find that, addition of thallium-oxide modifier leads to decline in the intensity of the peak in this particular region and this can be correlated to the reduction of Te-O-Te bridges which promotes the structural depolymerization of the glass. As a consequence, this depolymerization effect is more pronounced in the case of 50% modified oxide leading to the formation of Tl_2TeO_3 ortho-tellurite phases [108]. This finding is consistent with our structural analysis of the $(TlO_{0.5})_x - (TeO_2)_{1-x}$ binary glasses (see chapter 4). As for the broad peak contribution, higher than 600 cm^{-1} wavenumber, it can be attributed to the asymmetric stretching of Te=O$\cdots$Te bridge (O$\cdots$Te denotes longer and weaker bond) or Te=O terminal bonds in association with Raman spectra of pure TeO_2 glass. In particular, we notice declining intensity of the shoulder peak at 660 cm^{-1} with increasing the modifier concentration, which can be explained by replacement of highly asymmetric Te=O$\cdots$Te bridge (dominated in pure TeO_2 glass) by Te=O(NBO)-Tl linkages. In fact, for the case of 50% of thallium-oxide we find a peak at 725 cm^{-1}, which is due to the formation of isolated $[TeO_3]^{2-}$ ortho-ions separated by Tl cation (Te=O(NBO)-Tl) where each Te-O (NBO) bond pulsate to contribute to this peak [110].

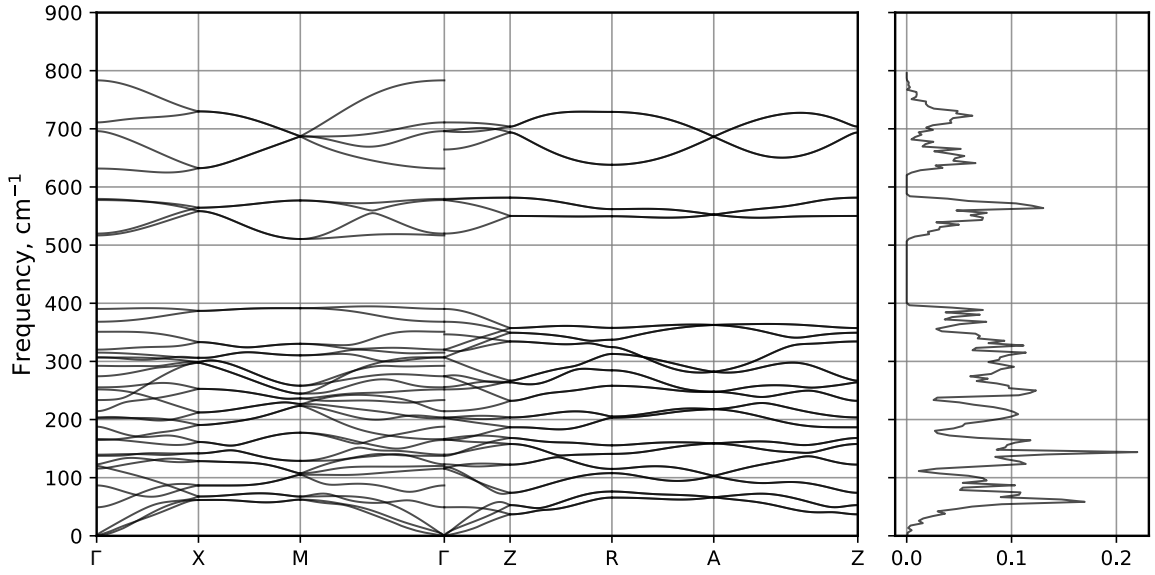

(a) Paratellurite α-TeO_2

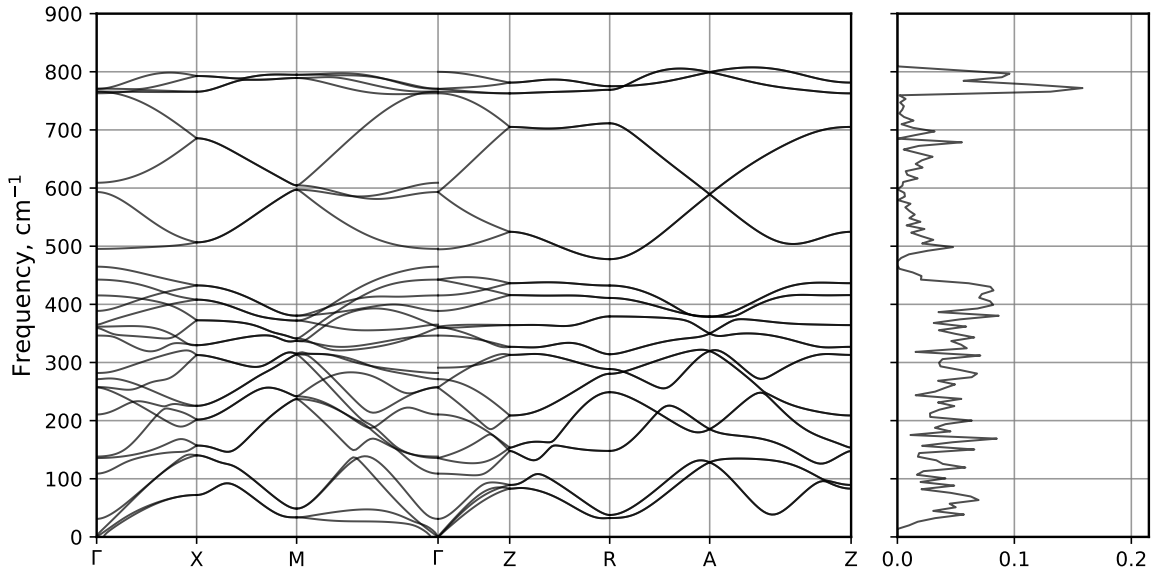

(b) Crystobalite SiO_2

Figure 6.7: Phonon dispersion and phonon density of states of (a) paratellurite α-TeO_2 and (b) crystobalite α-SiO_2 (bottom).

Next, for all compositions, figure [6.8b] depicts the Raman spectra over the whole range of wavenumbers contributing to the spectra. We see that the highest peak position centered around 30 cm^{-1} wavenumber can be associated to Boson peak contribution.

Furthermore, we have also simulated the Raman spectra of different glasses forming compositions of $(TiO_2)_x - (TlO_{0.5})_y - (TeO_2)_{1-x-y}$ ternary system (see figure [6.9]). Due to the significant computation resources required, we only took into account one snapshot for each composition at T = 300 K as listed in table [5.1] (see chapter [5]) for computing the Raman spectra. Figure [6.9a], shows simulated ternary glass Raman spectra along with its comparison with experimental data. Additionally, we have assigned the wavenumbers a 15% blueshift, similar to the cases of pure TeO_2 and binary $(TlO_{0.5})_x - (TeO_2)_{1-x}$ glasses. Providing such a shift result in a very good agreement of simulated Raman with experimental data, demonstrating the effectiveness of our methodology adopted to compute Raman spectra. We note that our model for $(TiO_2)_{0.1} - (TlO_{0.5})_{0.1} - (TeO_2)_{0.8}$ glass with similar DFT setup and 15% blueshift in wavenumber shows a limitation in reproducing the correct positions of the peak around 450 and 660 cm^{-1}. This disparity can be explained by the small number of configurations used to generate the Raman spectra, and it can be minimized by analyzing more configurations and averaging them.

First and foremost, we note that the general behavior of the Raman spectra curve especially the peak position and the intensity around 460 and 660 cm^{-1} did not significantly change by replacing TeO_2 with TiO_2 at constant $TlO_{0.5}$ units. This suggests that Ti behaves similarly to Te and maintains the polymerization of the glassy framework. In practice, titanium-oxide substitute the -O-Te-O$\cdots$Te-O- linkages by stronger -O-Te-O-Ti-O-Te-O- bridges, where both Te-O and Ti-O features very close bond lengths. This observation is in line with our rings statistics analysis in chapter 5, where we have seen that Ti^{4+} promotes the formation of small rings. Additionally, it is known that Ti-O bonds have larger force constants than Te-O bonds [149], hence enhancing the mechanical strength of the glassy structure. Further, analyzing $(TiO_2)_x - (TlO_{0.5})_y - (TeO_2)_{1-x-y}$ ternary systems at constant TiO_2 and varying $TlO_{0.5}$ shows similar evolution as that of binary $(TlO_{0.5})_x - (TeO_2)_{1-x}$ glasses (see figure [6.8b]). In particular increasing of $TlO_{0.5}$ component at fixed TiO_2 concentration in the ternary glasses, we notice several trends:

1. The intensity corresponding to the vibration of symmetric Te-O-Te bridges ($\sim$ 450 cm^{-1}) gradually decreases (structural depolymerization).
2. The intensity corresponding to the vibration of asymmetric stretching of Te=O$\cdots$Te ($\sim$ 660 cm^{-1}) decreases.
3. The intensity corresponding to the vibration of Te=O bond in Te=O$\cdots$Tl bridges increases ($\sim$ 720 cm^{-1}).

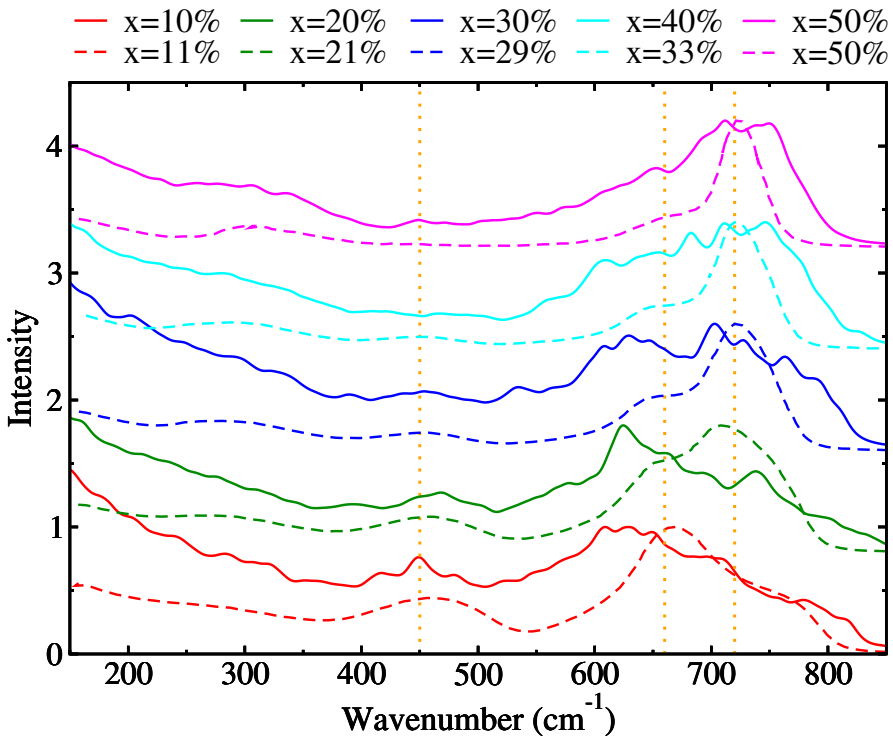

(a) Comparison of computed (solid lines) 15% blueshifted Raman spectra of $(TlO_{0.5})_x - (TeO_2)_{1-x}$ binary glassy system with experimental data (dashed lines) [9]. Vertical dotted lines are shown for visualizing horizontal shift relative to each curve.

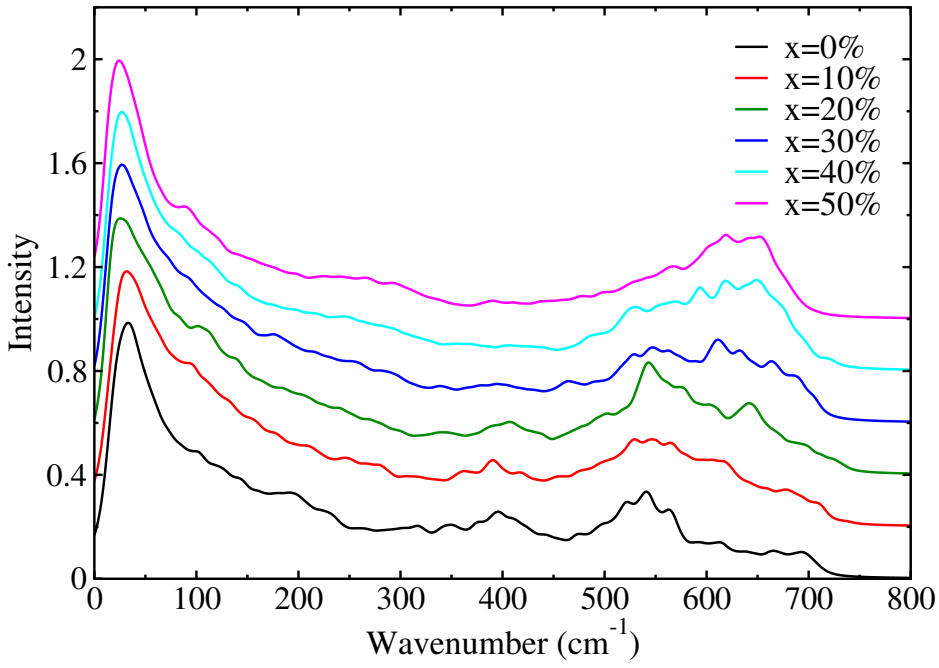

(b) Computed Raman spectra of $(TlO_{0.5})_x - (TeO_2)_{1-x}$ binary glass over whole range of wavenumbers.

Figure 6.8: Computed Raman spectra of $(TlO_{0.5})_x - (TeO_2)_{1-x}$ binary glassy system. A vertical shift has been provided in the intensity of each composition for clarity.

Moreover, increasing TiO_2 modifier oxide from 5% to 10% in $(TiO_2)_x-(TlO_{0.5})_y-(TeO_2)_{1-x-y}$ ternary glass at constant $TlO_{0.5}$ concentration shows that peak ($\sim$ 450 cm^{-1}) becomes slightly more pronounced, which indicates that Ti^{4+} in Te-O-Ti bridges has better capability in polymerizing the glassy network than Te^{4+} in Te-O-Te bridges. This pronounced effect allows one to deduce that no structural depolymerization of the glassy network occurs as the peak ($\sim$ 660 cm^{-1}) shows a limited change. These observations depict that, incorporation of Ti^{4+} does not lead to formation of NBO unlike Tl^{+}. Rings analysis in chapter [5], also shows the similar results.

We also display in figure [6.9b] the simulated Raman over whole contributing range of wavenumber compared to experimental reference. Similar, to the case of pure TeO_2 and binary $(TlO_{0.5})_x-(TeO_2)_{1-x}$ glasses, we encounter the highest peak close to 30 cm^{-1} wavenumber due to Boson peak.

6.3 Non-linear optical properties

We now focus on the nonlinear linear optical property (NLO) of glassy TeO_2 and in particular in the calculations of the third order nonlinear susceptibility and its comparison to experimental results [150]. NLO properties were calculated using 10 snapshots extracted from the MD trajectory of TeO_2 at T = 300 K in order to have a good statistical sampling of the calculated non-linear properties. Similar approach is also applied in the case of glassy SiO_2.

We further perform convergence tests to investigate the validity of our approach for system size dependence. To do so, we rely on the achieved periodic 270 atoms, 480 atoms and $2 \times 2 \times 2$ supercell constructed from 270 atoms TeO_2 and SiO_2 systems. This corresponds to three systems with 270, 480 and 2160 atoms, respectively. The generated supercell was fully relaxed before computing the polarizability tensor. We note that although supercell model was not produced by full equilibration of the supercell at finite temperature, it is expected to give a reasonable estimation of the polarizability tensor as this later have showed a little dependence on the statistical fluctuations of the glassy structure. In the case of amorphous systems the mean values of $\chi^{(1)}$, diagonal $\chi_d^{(3)}$ and non-diagonal $\chi_{nd}^{(3)}$ components are obtained as arithmetical mean of tensor elements of $\chi^{(1)}$ and $\chi^{(3)}$, respectively while the mean value of nonlinear third order susceptibility is obtained as follows:

$$\langle\chi^{(3)}\rangle = \frac{1}{5}\left(\chi^{(3)}_{xxxx} + \chi^{(3)}_{yyyy} + \chi^{(3)}_{zzzz} + 2\chi^{(3)}_{xxyy} + 2\chi^{(3)}_{xxzz} + 2\chi^{(3)}_{yyzz}\right) \tag{6.1}$$

The results of these calculations for amorphous TeO_2 and SiO_2 are presented in table [6.1] compared to experimental data [150]–[152]. Despite a slight overestimation, our calculations

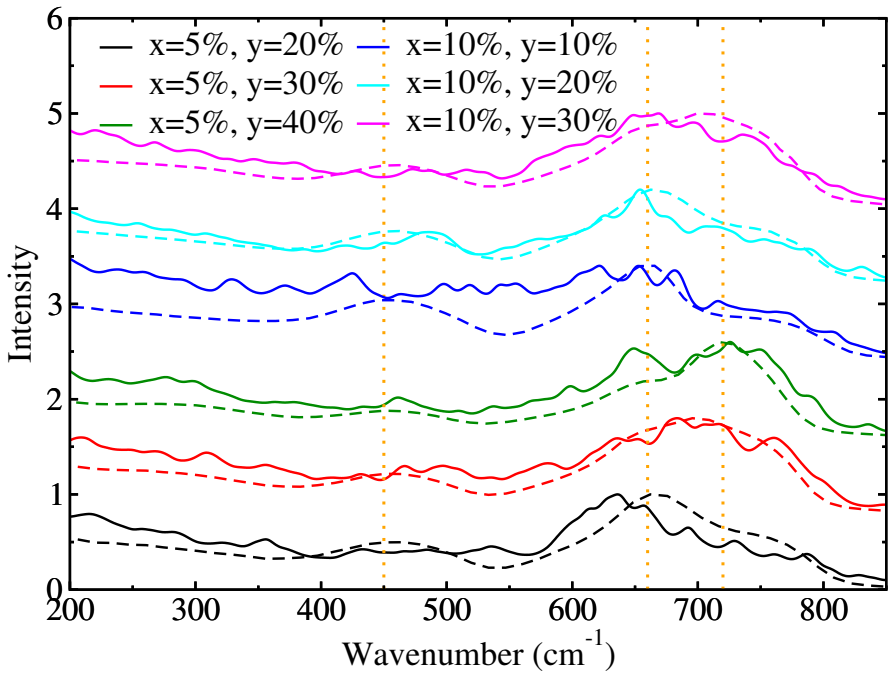

(a) Comparison of computed (solid lines) 15% blueshifted Raman spectra of ternary $(TiO_2)_x - (TlO_{0.5})_y - (TeO_2)_{1-x-y}$ glassy system with experimental data (dashed lines) [9].

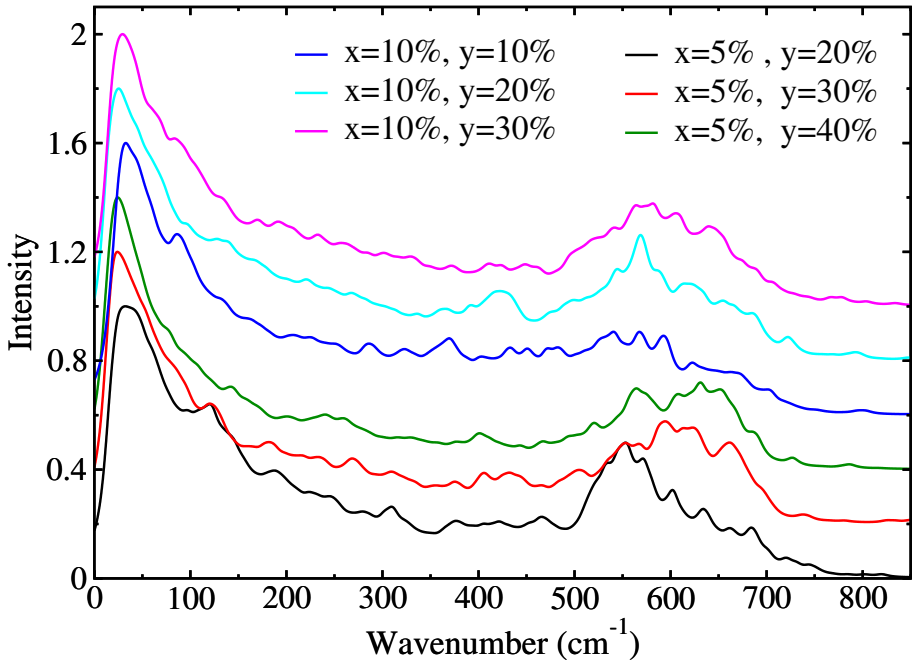

(b) Computed Raman spectra of $(TiO_2)_x - (TlO_{0.5})_y - (TeO_2)_{1-x-y}$ ternary glassy system over whole range of wavenumbers.

Figure 6.9: Computed Raman spectra of $(TiO_2)_x - (TlO_{0.5})_y - (TeO_2)_{1-x-y}$ ternary glassy system. A vertical shift has been provided in the intensity of each composition for clarity.

Table 6.1: Linear susceptibility $\chi^{(1)}$ and third order non-linear susceptibility $\chi^{(3)}$ in 10^{-22} m^2/V^2 calculated for glassy TeO_2 and glassy SiO_2. Experimental reference values from Ref. [150]–[152] are given in parentheses for α-TeO_2 (paratellurite).

Property	SiO_2			TeO_2		
Number of atoms	270	456	2160	270	480	2160
n_0	1.49	1.5 (1.458)[151]	1.51	2.25	2.34 (2.22) [152]	2.34
$\chi_d^{(3)}$	1.02	1.22	1.69	38.01	56.05 (95.1) [150]	84.58
$\chi_{nd}^{(3)}$	0.41	0.48	0.6	17.31	24.26 (42.0) [150]	33.29
$\chi_d^{(3)}/\chi_{nd}^3$	2.49	2.54	2.82	2.20	2.31 (2.26) [150]	2.54
$\langle\chi^{(3)}\rangle$	1.10	1.31 (2.095) [150]	1.73	41.49	62.67 (102.8) [150]	90.69

yield values of refractive index n_0 for TeO_2 and SiO_2 in good agreement with experiments (see table [6.1]), obtained from $\chi^{(1)}$ as:

$$n_0 = \sqrt{1 + \chi^{(1)}} \tag{6.2}$$

Coming to $\chi^{(3)}$, we find that for all the system sizes, the absolute values calculated on our glassy TeO_2 models are slightly underestimated in comparison to their experimental counterpart in α-TeO_2 paratellurite. However, we find that they are of the same order of magnitude as in α-TeO_2 (see table [6.1]). Hence, one can infer that the NLO response of the material only weakly depend on the structural disorder. This result can be explained by the origins of the high NLO properties of TeO_2 that were associated to the hyperpolarizability of the Te atom due to its electronic lone pair and to the asymmetric Te-O-Te bridges. Both features are maintained in the glassy phase and could explain the maintain of the strong NLO properties of glassy TeO_2 as predicted from our study. Furthermore, it is noteworthy that experimental data obtained for crystalline paratellurite are only obtained for components in the (a, b) plane, therefore, additional data for $\chi^{(3)}$ tensor elements may result in the experimental mean value of $\chi^{(3)}$ in the crystal to be concordant with our results.

Experimentally, the non-linear susceptibility of a given material is usually measured with respect to another reference material. In the case of paratellurite single crystal, the measurements were performed with respect to a fused silica reference glass plate [150]. Thus, in figure [6.10], we display the convergence of $\langle\chi^{(3)}\rangle$ ratio between TeO_2 and SiO_2 glasses for various system sizes. We see that when the simulation size is extended from 480 atoms to 2160 atoms, the $\langle\chi^{(3)}\rangle$ ratio changes by less than 10%. Furthermore, dealing with a system with 2160 atoms, which is 4.5 times bigger than a system of 480 atoms, is not computationally viable, as this extension in simulation size leads to little change in the ratio of $\langle\chi^{(3)}\rangle$ between TeO_2 and SiO_2 glasses. In addition, performing *ab-initio* MD simulation with 2160 system to obtain fully equilibrated trajectory is currently beyond the capability of CP2K code within reasonable time. Therefore, we

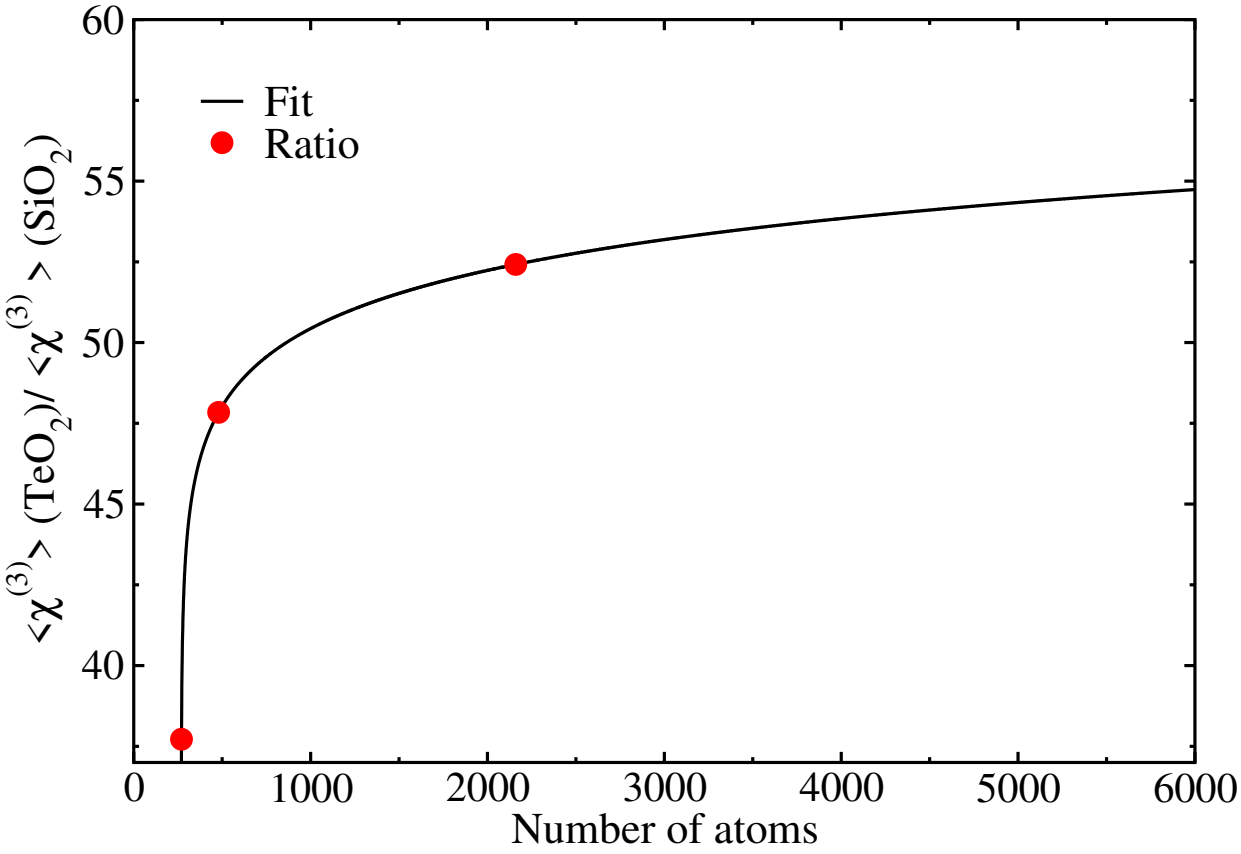

Figure 6.10: Ratio of non-linear susceptibility planar average $\langle\chi^{(3)}\rangle$ of pure TeO_2 and SiO_2 dependence on system size. Convergence of the fit is performed by log function $(a \times \ln(x-b)+c)$.

resort to the 480 atoms size model for further analysis in an attempt to understand the evolution of the nonlinear properties of the TeO_2 and SiO_2 glasses.

Moreover, by focusing on the ratio of the $\langle\chi^{(3)}\rangle$ obtained from TeO_2 and SiO_2 at 480 atoms model sizes, we grant a legitimacy to our methodology to provide results directly comparable with their experimental counterpart. Table [6.2] further shows the calculated ratio of diagonal and non-diagonal components $\chi^{(3)}$ on TeO_2 versus amorphous SiO_2 in comparison to experimental results for α-TeO_2 paratellurite from Ref. [150]. We find that the calculated ratio between the diagonal and non-diagonal $\chi^{(3)}$ components in the glass reproduces very well the one measured experimentally for α-TeO_2 paratellurite (see table [6.2]). These results, once again demonstrates that the disorder does not significantly alter the non-linear optical response of the material.

Next, we proceed to analyze the evolution of non-linear optical properties with incorporation of modifier oxides in the glassy matrix. Various component of $\chi^{(3)}$ and refractive index of binary $(TlO_{0.5})_x-(TeO_2)_{1-x}$ and $(TiO_2)_x-(TeO_2)_{1\text{-}x}$ and ternary $(TiO_2)_x-(TlO_{0.5})_y-(TeO_2)_{1-x-y}$ glass have been reported in the table [6.3], [6.4]. Amorphous $(TiO_2)_x-(TeO_2)_{1\text{-}x}$ glassy

Ratio	Calculations			Experimental
Number of atoms	270	480	2160	Paratellurite [150]
$\chi_d^{(3)}(TeO_2)/\chi_d^{(3)}(SiO_2)$	37.26	45.94	50.05	45.4
$\chi_{nd}^{(3)}(TeO_2)/\chi_d^{(3)}(SiO_2)$	16.97	19.88	19.7	20.04
$\langle\chi^{(3)}\rangle(TeO_2)/\langle\chi^{(3)}\rangle(SiO_2)$	37.72	47.84	52.42	49.1

Table 6.2: Diagonal $\chi_d^{(3)}$, non-diagonal $\chi_{nd}^{(3)}$, and average $\langle\chi^{(3)}\rangle$ ratios calculated for glassy TeO_2 with respect to glassy SiO_2. Experimental reference values for α-TeO_2 (paratellurite) from Ref. [150]

model generation details are shown in the Appendix [A.2]. From table [6.3], we find that the calculated values of $\chi_d^{(3)}$ in $(TlO_{0.5})_x - (TeO_2)_{1-x}$ binary glasses are in good agreement with the experimentally obtained values. However, it is important to highlight that the absolute values of $\langle\chi^{(3)}\rangle$ depends on the choice of the experimental setup, therefore we can only observe the trend of evolving $\langle\chi^{(3)}\rangle$ with the modifier concentration. Our calculations suggest that $\langle\chi^{(3)}\rangle$ values remain almost constant with respect to $TlO_{0.5}$ modifier, similar to the experimentally observed values (see chapter [1]). For $(TiO_2)_x - (TeO_2)_{1\text{-}x}$ binary glasses, we observe that $\langle\chi^{(3)}\rangle$ values slightly decrease with respect to addition of modifier similar to experiments [85]. In fact, replacing TeO_2 units with TiO_2 units in the glassy matrix leads to decrease in $\langle\chi^{(3)}\rangle$ values because the absence of electronic lone pair on Ti atom reduces the hyperpolarizabilities of the material which arises from a cumulative contribution of electronic lone pair in the proximity of Te atoms. All the trends observed in binary $(TlO_{0.5})_x - (TeO_2)_{1-x}$ and $(TiO_2)_x - (TeO_2)_{1\text{-}x}$ glasses remains true in the case of ternary $(TiO_2)_x - (TlO_{0.5})_y - (TeO_2)_{1-x-y}$ glasses.

From figure [6.11], we find that for either glasses, substituting TeO_2 units with modifying agents leads to a decrease in the refractive index (n_0). Similar to our prior analysis with pure TeO_2, we compare the various $\langle\chi^{(3)}\rangle$ values of various modified glasses with respect to pure SiO_2 systems (see table [6.5]). We notice that the ratio of $\chi_d^{(3)}$ and $\chi_{nd}^{(3)}$ computed on studied modified tellurite glasses to $\chi_d^{(3)}$ of silicate glasses remains close around 45.4 and 20.04, respectively as witnessed in the case of paratellurite TeO_2 crystal [150]. In addition, the ratio of $\langle\chi^{(3)}\rangle$(A)/$\langle\chi^{(3)}\rangle$ (SiO_2) where A represents modified tellurite glass, was measured to be in very good agreement with the values obtain for paratellurite TeO_2 crystal [150] (see table [6.4]). As discussed with the case of $(TiO_2)_x - (TeO_2)_{1\text{-}x}$ binary glasses in previous paragraph, where we have seen that increasing concentration $x > 5\%$ leads to decline in $\langle\chi^{(3)}\rangle$ properties, similar results were also seen for the ratio of obtained $\langle\chi^{(3)}\rangle$ to that of silicate glass (see table [6.4] and figure [6.11]). As a result, we avoid adding high concentration of TiO_2 modifier into the system, and resort to adding both modifier $TlO_{0.5}$ and TiO_2 in order to maintain the non-linear optical properties while also maintaining the mechanical properties of the material [130]. In fact, we see that with 5% of TiO_2 in $(TiO_2)_x - (TlO_{0.5})_y - (TeO_2)_{1-x-y}$ ternary glass shows similar $\langle\chi^{(3)}\rangle$(A)/$\langle\chi^{(3)}\rangle$

Table 6.3: Refractive index, first and third order non-linear susceptibility calculated for pure TeO_2, binary $(TlO_{0.5})_x - (TeO_2)_{1-x}$ and SiO_2 glassy system. We also provide the diagonal χ^3_d (10^{-22} m^2/V^2) and non-diagonal χ^3_{nd} (10^{-22} m^2/V^2) averages of the χ^3 (10^{-22} m^2/V^2) matrix, in addition $\langle\chi^{(3)}\rangle$. Experimental results for paratellurite are given in small parenthesis.

Property	SiO_2				$(TlO_{0.5})_x - (TeO_2)_{1-x}$				
					x = 10%	x = 20%	x = 30%	x = 40%	x = 50%
Number of atoms	270	408	432	456	456	432	408	432	40
E_g (eV)	4.78	3.28	3.77	3.39	1.97 ± 0.04	1.35 ± 0.05	1.43 ± 0.09	1.99 ± 0.06	1.38 ± 0.07
n_0	1.49	1.50	1.50	1.50 (1.458) [18]	2.29	2.24	2.21	2.17	2.14
χ^1 (a.u)	1.22	1.25	1.26	1.25	4.25 ± 0.02	4.02 ± 0.01	3.88 ± 0.02	3.71 ± 0.04	3.58 ± 0.05
$\chi^{(3)}_d$	1.02	1.19	1.23	1.22	54.38	54.26	55.68	52.45	55.52
$\chi^{(3)}_{nd}$	0.41	0.46	0.47	0.48	23.59	23.51	24.38	22.44	24.14
$\chi^{(3)}_d/\chi^3_{nd}$	2.45	2.59	2.62	2.54	2.30	2.31	2.28	2.34	2.3
$\langle\chi^{(3)}\rangle$	1.1	1.27	1.30	1.30 (2.095) [150]	60.90	60.78 (48.2 ,x=25%) [46]	62.81	58.36 (47.6) [46]	62.22

Table 6.4: Refractive index, first and third order non-linear susceptibility calculated for binary $(TiO_2)_x - -(TeO_2)_{1-x}$ and ternary $(TiO_2)_x - (TlO_{0.5})_y - (TeO_2)_{1-x-y}$ glassy system. We also provide the diagonal χ^3_d (10^{-22} m^2/V^2) and non-diagonal χ^3_{nd} (10^{-22} m^2/V^2) averages of the χ^3 (10^{-22} m^2/V^2) matrix, in addition to $\langle\chi^{(3)}\rangle$. Experimental results for paratellurite are given in small parenthesis.

Property	$(TiO_2)_x - -(TeO_2)_{1-x}$			$(TiO_2)_x - (TlO_{0.5})_y - (TeO_2)_{1-x-y}$					
	x = 5%	x = 10%	x = 15%	x = 5%, y = 20%	x = 5%, y = 30%	x = 5%, y = 40%	x = 10%, y = 10%	x = 10%, y = 20%	x = 10%, y = 30%
Number of atoms	480 atoms	480 atoms	480 atoms	540 atoms	510 atoms	480 atoms	456 atoms	540 atoms	510 atoms
E_g (eV)	2.02 ± 0.03	1.80 ± 0.05	2.05 ± 0.04	1.60 ± 0.01	1.95 ± 0.02	1.38 ± 0.02	1.98 ± 0.05	2.08 ± 0.02	1.94 ± 0.05
n_0	2.34	2.35	2.33	2.25	2.21 (2.12) [9]	2.18	2.27	2.22	2.21
χ^1 (a.u)	4.46	4.51	4.43	4.08	3.87	3.77	4.13	3.95	3.88
$\chi^{(3)}_d$	54.33	52.32	49.46	55.91	49.73	53.56	45.02	46.53	48.68
$\chi^{(3)}_{nd}$	23.75	22.34	20.81	24.13	21.36	23.33	19.19	20.08	20.46
$\chi^{(3)}_d/\chi^3_{nd}$	2.29	2.34	2.38	2.32	2.33	2.30	2.35	2.32	2.38
$\langle\chi^{(3)}\rangle$	61.22	58.20 (42.2) [46]	54.61 (39.6) [46]	62.48	55.49	60.10	50.16	52.05	53.74

Compositions	$\chi_d^{(3)}$(A)/$\chi_d^{(3)}$(B)	$\chi_{nd}^{(3)}$(A)/$\chi_d^{(3)}$(B)	$\langle\chi^{(3)}\rangle$(A)/$\langle\chi^{(3)}\rangle$(B)
A = $(TlO_{0.5})_{0.0} - (TeO_2)_{1.0}$, B = SiO_2 (456)	45.94 (45.4) [150]	19.88 (20.04) [150]	47.84 (49.1) [150]
A = $(TlO_{0.5})_{0.1} - (TeO_2)_{0.9}$, B = SiO_2 (456)	44.57	19.34	46.84
A = $(TlO_{0.5})_{0.2} - (TeO_2)_{0.8}$, B = SiO_2 (432)	44.11	19.11	46.75
A = $(TlO_{0.5})_{0.3} - (TeO_2)_{0.7}$, B = SiO_2 (408)	46.79	20.49	49.46
A = $(TlO_{0.5})_{0.4} - (TeO_2)_{0.6}$, B = SiO_2 (432)	42.64	18.24	44.90
A = $(TlO_{0.5})_{0.5} - (TeO_2)_{0.5}$, B = SiO_2 (408)	46.65	20.29	49.00
A =$(TiO_2)_{0.05} - (TeO_2)_{0.95}$, B = SiO_2 (456)	44.53	19.47	47.09
A =$(TiO_2)_{0.1} - (TeO_2)_{0.90}$, B = SiO_2 (456)	42.88	18.31	44.77
A =$(TiO_2)_{0.15} - (TeO_2)_{0.85}$, B = SiO_2 (456)	40.54	17.06	42.00
A =$(TiO_2)_{0.05} - (TlO_{0.5})_{0.2} - (TeO_2)_{0.75}$,B = SiO_2 (456)	45.83	19.78	48.06
A =$(TiO_2)_{0.05} - (TlO_{0.5})_{0.3} - (TeO_2)_{0.65}$,B = SiO_2 (456)	40.76	17.51	42.68
A =$(TiO_2)_{0.05} - (TlO_{0.5})_{0.4} - (TeO_2)_{0.55}$,B = SiO_2 (456)	43.90	19.12	46.23
A =$(TiO_2)_{0.1} - (TlO_{0.5})_{0.1} - (TeO_2)_{0.8}$, B = SiO_2 (456)	36.90	15.73	38.54
A =$(TiO_2)_{0.1} - (TlO_{0.5})_{0.2} - (TeO_2)_{0.7}$, B = SiO_2 (456)	38.14	16.46	40.04
A =$(TiO_2)_{0.1} - (TlO_{0.5})_{0.3} - (TeO_2)_{0.6}$, B = SiO_2 (456)	39.90	16.77	41.34

Table 6.5: Diagonal χ_d^3, non-diagonal χ_{nd}^3, and $\langle\chi^{(3)}\rangle$ ratios calculated for pure TeO_2, binary $(TlO_{0.5})_x - (TeO_2)_{1-x}$ and $(TiO_2)_x - (TeO_2)_{1\text{-}x}$ and ternary $(TiO_2)_x - (TlO_{0.5})_y - (TeO_2)_{1-x-y}$ glasses with respect to glassy SiO_2. Experimental reference values from Ref. [150] are given parenthesis.

(SiO_2) values (≈ 50) to that of binary $(TlO_{0.5})_x - (TeO_2)_{1-x}$ glass. However, increasing TiO_2 concentration to 10%, shows smaller $\langle\chi^{(3)}\rangle$(A)/$\langle\chi^{(3)}\rangle$ (SiO_2) value close to 40.

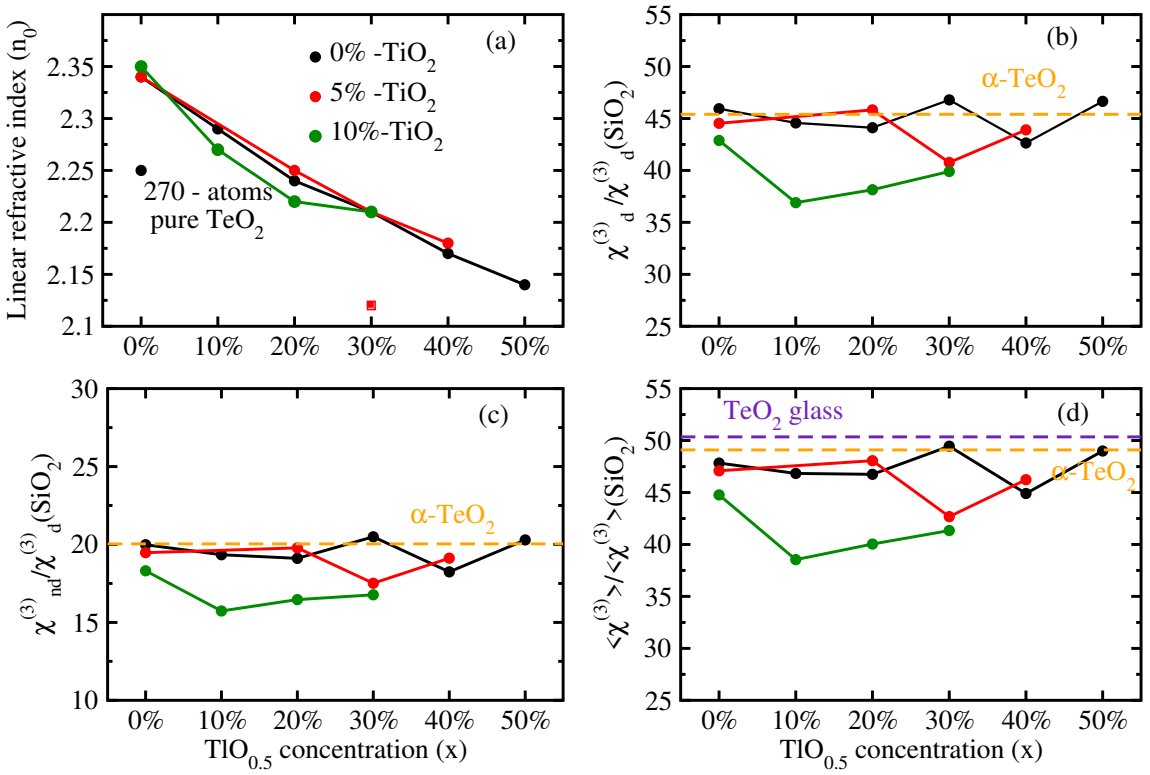

Figure 6.11: Description of evolution of various linear and non-linear properties in $(TlO_{0.5})_x - (TeO_2)_{1-x}$ and $(TiO_2)_x - (TeO_2)_{1\text{-}x}$ ($y = 0$) and ternary $(TiO_2)_x - (TlO_{0.5})_y - (TeO_2)_{1-x-y}$ glasses. Orange color horizontal dashed lines displays the value obtained experimentally for paratellurite [150]. Violet color dashed line shows the ratio of $\chi^{(3)}$ in TeO_2 to SiO_2 glass as observed by Kim et al. [18].

6.4 Conclusions

In summary, by combining density functional theory and finite difference method we develop an efficient scheme able to achieve Raman spectra on amorphous oxide models with a high level of agreement with experiments and this is for models containing several hundreds of atoms. Such an achievement is made possible thanks to the efficient scalability of the CP2K code that grants a quite reasonable and time efficient computational cost. Next, we focus on the origins of the strong Boson peak observed in glassy TeO_2 in close comparison to the less pronounced Boson peak reported in glassy SiO_2. At the mathematical level, the Boson peak appears to be as an amplification of the low frequency range of the Raman spectra. This amplification depends on a competition between a damping inverse frequency term and the Bose-Einstein distribution at a given temperature and for a given active Raman mode. Interestingly, we find that TeO_2 is subject to strong amplification than SiO_2 as it features at T = 0 K lower frequencies down to 17 cm^{-1}, while the SiO_2 spectra shows a null intensity up to 32 cm^{-1}. By inspecting the normal modes contributing to the Boson peak we find that they involve collective vibrations of the whole glass which in turn induce a weak change in the polarizability of the system and therefore a small Raman response. Based on this result, and given the harmonic approximation, we find that the position of the Boson peak for a given system can evolve proportionally to the mass ratio of the main structural units of this system with respect to another reference glassy system. As such, assuming that the frequency weakly depends on the spring constant k, the Boson peak frequency is expected to be shifted as follows $\omega^{\mathrm{Boson}}_{\mathrm{TeO_2}}/\Omega^{\mathrm{Boson}}_{\mathrm{SiO_2}} \approx \sqrt{m_{\mathrm{SiO_4}}/m_{\mathrm{TeO_4}}}$. We extend our analysis by studying the phonons density of states and find a qualitative indicator that can be correlated to the appearance of the Boson peak. Additionally, we also investigate the simulated Raman spectra of modified TeO_2 glasses with $TlO_{0.5}$ and TiO_2 modifier. We find that our models are able to reproduce all the major experimental peaks, however we do not discuss here the decomposition of various structural units contributing to different modes in Raman spectra and the evolution of Boson peak as we did in the case of pure TeO_2 glass. Finally, we focus on third order hyperpolarizability of the pure and modified TeO_2 glassy systems. Our scheme yields values of refractive index and third-order non-linear susceptibility in a very good agreement with experimental results. We find that adding 5% of TiO_2 and less than 30% of $TlO_{0.5}$ to TeO_2 glass maintains the high non-linear and mechanical properties of the glass. Overall, we demonstrate that our computational scheme enables one to compute accurate Raman spectra and hyperpolarizability of large glassy systems paving the way towards a systematic computational study of non-linear optical and vibrational properties in oxide glasses.

7

General conclusions

TeO_2 based glasses show promising results for their application in many devices due to their high NLO properties. To understand the origins of these properties, we made an attempt to link the microscopic properties of the glassy network to the macroscopic physio-chemical properties by modelling their structure at the atomic level. This research work utilizes the most comprehensive atomic scale methodology and the high-performance supercomputers currently available to offer a thorough understanding of TeO_2 based materials. We utilized *ab-initio* molecular dynamics to create several TeO_2 glassy and melt models. Further, by modifying the TeO_2 glass with modifier oxide in our study, we are able to better understand the behavior of binary $(TlO_{0.5})_x - (TeO_2)_{1-x}$ and ternary $(TiO_2)_x - (TlO_{0.5})_y - (TeO_2)_{1-x-y}$ glasses in relation to their macroscopic properties. The following are the main conclusions of this thesis:

Structure of glassy and molten TeO_2

We have carried out first-principles molecular dynamics by resorting to a variety of DFT based schemes. The produced models allowed us to assess the effects of the choice of the DFT XC functional, model size effects, quenching rate and variable density effects on the final structure of TeO_2 glass. We demonstrate that only molecular dynamics carried out at the hybrid exchange and correlation functional level of theory, with the PBE0 functional, combined with a variable density melt-quench approach, allows one to achieve an atomistic model of TeO_2 that reproduces the structural features measured experimentally.

Next, we resort to the Wannier function formalism and provide a cut-off independent definition of the chemical bonds based on the positions of the Wannier centers and the geometry of the Te local environment. Based on this approach, we demonstrate that Te features a coordination number of 3.96 in the glass and 3.65 in the melt, in good agreement with recent experimental results. The study of the atomic local environments reveals that Te is mainly found in 4-fold units with a non-negligible fractions of 3- and 5-fold units, while O typically occurs in 2-fold units with a substantial fraction of non-bridging and 3-fold O atoms. The fraction of non-bridging O increases with the temperature which explains the observed reduction of the Te coordination numbers. Furthermore, we focus on the short-range disorder around Te and O and show that the melt exhibits an overall broader distribution of asymmetry around both species. In the case of Te, we infer that the increase of the temperature leads to an increase of the TeO_4 units asymmetry that transform it into a highly asymmetric TeO_3 units. As the asymmetry of two-fold O increases we observe that the short bond undergoes a slow contraction while the long bond elongates more rapidly which provides a plausible hypothesis of the transformation of Te-O-Te bridges into terminal Te=O groups due to the increase of the short-range disorder around O atom.

The study of the net atomic charge shows that Te features a slightly lower charge in the melt while O features a slightly larger charge. Interestingly, we find that 5-fold Te and 1-fold O

show more important change in NAC compared to other Te and O structural units, respectively. Moreover, our results highlight the correlation between the 2-fold O NAC and the Te-O-Te bridge asymmetry, where the O NAC tend to larger negative values when the asymmetry increases. The study of the ELF of a symmetric and an asymmetric Te-O-Te bridge shows that in the first case, Te-O bonds are iono-covalent with a substantial charge localization along the bond and a higher ELF values at the vicinity of O, while in the second case, the short bond shows a charge localization similar to that observed in symmetric bridge whereas the long bond shows a low charge localization along the Te-O connection which indicates an ionic character on this bond.

Our study provides a benchmark of the performances of hybrid functional molecular dynamics applied to oxide materials. In summary, the picture stemming out of our work describes TeO_2 as a network made of a variety of TeO_n units featuring a substantial short-range disorder. This disorder translates into bond asymmetry and increases as a function of the temperature. As a consequence, the coordination number of Te reduces from ~ 4 in the glass to 3.65 in the melt. In addition, the increasing disorder around two fold-O atoms leads to the elongation of one Te-O bond and subsequently to the increase of the O negative charge, which tends towards that observed for non-bridging O atoms. Hence, both structural and electronic properties analyses provide concordant evidence on the occurrence of Te=O groups in TeO_2.

Structure of Tl_2O-TeO_2 binary glasses

In binary $(TlO_{0.5})_x - (TeO_2)_{1-x}$ glasses, introducing thallium-oxide modifier leads to a decrease in the Te coordination number $n_{Te\text{-}O}$. This reduction is due to the structural depolymerization of glassy network by replacing Te-O-Te bridges with weaker Te-$O^- \cdots Tl^+$ bridges. Further, due to the decline in Te-O-Te bridges, we notice the rise of NBO population in the $(TlO_{0.5})_x - (TeO_2)_{1-x}$ system. This rise leads to the increase of $n_{Tl\text{-}NBO}$ (and decrease of $n_{Tl\text{-}BO}$) with increasing modifier concentration. The local environment analysis around Te indicates that 3-fold Te increases while 4 and 5-fold Te decreases with increasing $TlO_{0.5}$ concentration. In the case of Tl local environment, it was seen that 3 and 4-fold Tl evolves as x increases from 10% to 50% whereas higher folds show declining trends except 5-fold which shows its maximum at 30%. The idea of depolymerization of network is further explained by the rings analysis, where we have seen that Tl^+ ions does not contribute to the rings formation and hence its incorporation opens the smaller rings formed by Te-O-Te bridges. Additionally, we calculate the bulk modulus for each glassy composition because the opening of the smaller rings signals that the mechanical strength of the glass may be decreasing after incorporating thallium-oxide modifier. We found that increasing $TlO_{0.5}$ content and TeO_2 glass leads to a decline in the value of bulk modulus, hence their mechanical properties reduce as well. In particular, we have seen that for $x > 20\%$ in binary $(TlO_{0.5})_x - (TeO_2)_{1-x}$ glass leads to sudden fall in bulk modulus values. Therefore, it is always recommended adding $TlO_{0.5}$ modifier up to 20% molar concentration.

Next, we correlate the various structural motifs to the electronic properties. To do so, we do charge analysis and compute electronic localization function. We find that with addition of thallium-oxide modifier charge transfer from Tl and Te cations to O anion decreases. Additionally, we also found that non-bridging oxygen carry higher negative charge than bridging oxygen. Finally, the ELF analysis of the O-centered structural fragment containing Tl-O and Te-O bond demonstrates that the Tl-O bonds has higher ionic character than Te-O bonds. We also find that, in contrast to Te, Tl possesses a significantly diffused lone pair.

Structure of TiO_2-Tl_2O-TeO_2 ternary glasses

We find that addition of titanium-oxide in $(\mathrm{TiO_2})_x - (\mathrm{TlO_{0.5}})_y - (\mathrm{TeO_2})_{1-x-y}$ ternary glasses at constant $TlO_{0.5}$ concentration, increase the coordination numbers $n_{Te\text{-}O}$ and $n_{Tl\text{-}O}$. This increase in coordination numbers owing to inclusion of TiO_2 modifier suggests that Ti^{4+} stimulates the formation of more network connections in the ternary $(\mathrm{TiO_2})_x - (\mathrm{TlO_{0.5}})_y - (\mathrm{TeO_2})_{1-x-y}$ glasses. Further, as observed with the case of $(\mathrm{TlO_{0.5}})_x - (\mathrm{TeO_2})_{1-x}$ binary glasses, we have noticed that increasing $TlO_{0.5}$ concentration at constant TiO_2 content, leads to decline in the value of $n_{Te\text{-}O}$ due to structural depolymerization of the $(\mathrm{TiO_2})_x - (\mathrm{TlO_{0.5}})_y - (\mathrm{TeO_2})_{1-x-y}$ glassy network.

The central point of our results in the analysis of $(\mathrm{TiO_2})_x - (\mathrm{TlO_{0.5}})_y - (\mathrm{TeO_2})_{1-x-y}$ ternary glasses is that the incorporation of TiO_2 into binary $(\mathrm{TlO_{0.5}})_x - (\mathrm{TeO_2})_{1-x}$ glasses as modifier provides tellurite glasses with high mechanical properties. This claim is verified by calculating bulk modulus, where we have seen that adding TiO_2 modifier oxide stimulates the effect of repolymerization of tellurite glassy network. Further, we also notice that in our rings analysis unlike Tl^+ ion, Ti^{4+} does participate in the formation of rings. Additionally, we found that replacing TeO_2 with TiO_2 leads to reduction in the fraction of non-bridging oxygens. All these findings, give credence to our explanation of high mechanical and thermal stability in $(\mathrm{TiO_2})_x - (\mathrm{TlO_{0.5}})_y - (\mathrm{TeO_2})_{1-x-y}$ ternary glasses.

Vibrational and optical properties of TeO_2-based glasses

We focus on glassy TeO_2 where we assign the observed strong Boson peak to an amplification of the low frequency range of the Raman spectra. This amplification depends on a competition between a damping inverse frequency term and the Bose-Einstein distribution at a given temperature and for a given active Raman mode. Interestingly, we find that this amplification is more pronounced for systems that show very low frequencies at T = 0 K. Furthermore, by inspecting the normal modes contributing to the Boson peak we find that they are collective vibrations of the whole glass which results in a weak change in the polarizability of the system and leads consequently to a smaller Raman response for lighter systems. Our analysis is further supported

by the phonons density of states. In addition, we also compare the simulated Raman spectra of pure TeO_2 and SiO_2 glasses to better understand the evolution of Raman spectra. Further, we also focus on the simulated Raman spectra of various compositions in binary $(TlO_{0.5})_x - (TeO_2)_{1-x}$ and ternary $(TiO_2)_x - (TlO_{0.5})_y - (TeO_2)_{1-x-y}$ glasses. We found that the obtained Raman spectra of binary $(TlO_{0.5})_x - (TeO_2)_{1-x}$ glasses show declining peak intensity around 400-500 cm^{-1} (attributed to -Te-O-Te- bridges), indicating structural depolymerization of the glasses with increasing modifier concentration x. Furthermore, in ternary $(TiO_2)_x - (TlO_{0.5})_y - (TeO_2)_{1-x-y}$ glasses it was found that at constant thallium-oxide concentration increasing TiO_2 content leads to a slight increase in the peak around 400-500 cm^{-1} which implies two characteristics: first incorporation of TiO_2 shows the promotion of structural polymerization in contrast to $TlO_{0.5}$, and second, O environments in Te-O-Te in Te-O-Ti bridges remains more or less identical. In addition, at constant TiO_2 and increasing $TlO_{0.5}$ modifier oxide shows similar structural depolymerization as noticed in the case of binary $(TlO_{0.5})_x - (TeO_2)_{1-x}$ glasses.

Finally, we provide calculated refractive index and third-order non-linear susceptibility for pure TeO_2, binary $(TlO_{0.5})_x - (TeO_2)_{1-x}$ and ternary $(TiO_2)_x - (TlO_{0.5})_y - (TeO_2)_{1-x-y}$ glasses. We found that the high $\chi^{(3)}$ value of the pure TeO_2 remains maintained with increasing $TlO_{0.5}$ concentration x in binary $(TlO_{0.5})_x - (TeO_2)_{1-x}$ glasses. In the case of ternary $(TiO_2)_x - (TlO_{0.5})_y - (TeO_2)_{1-x-y}$ glasses it was observed that increasing TiO_2 concentration more than 5% illustrates the significant decline in the absolute values of $\chi^{(3)}$ compared to the pure TeO_2 glass. Furthermore, the diagonal $\chi_d^{(3)}$ and non-diagonal $\chi_{nd}^{(3)}$ ratio of modified tellurite glasses with respect to diagonal $\chi_d^{(3)}$ of silicate glasses show values close to one observed experimentally for α-TeO_2 crystal. In addition, our calculations show that the $\langle\chi^{(3)}\rangle$ values of tellurite glasses are almost 50 times than silicate glasses except 10% TiO_2 in ternary $(TiO_2)_x - (TlO_{0.5})_y - (TeO_2)_{1-x-y}$ glasses. Hence, our modeling scheme paves the way toward systematic computational studies of non-linear optical and vibrational properties of oxide glasses.

Final remarks

We understand that the origin of high NLO properties in pure TeO_2 glass is due to $5s^2$ electronic lone pair of Te and Te-O-Te linkages. Further, adding modifier oxide in TeO_2 glass leads to decline in the NLO properties. However, incorporation of polarizable ion Tl^+ (specifically, thallium-oxide) into TeO_2 glass has shown the NLO properties of TeO_2 glasses to be maintained. This comes from the fact that Tl^+ cation has more diffused electronic lone pair localization than Te^{4+} cation thus, it easily orients and contributes to promote the overall hyperpolarizability of the material under external field. Moreover, it was found that adding thallium-oxide reduces the mechanical strength of the TeO_2 glass. Therefore, it is necessary to add another ion Ti^{4+} (specifically, titanium-oxide) into binary $(TlO_{0.5})_x - (TeO_2)_{1-x}$ glass which promotes the mechanical strength while still maintaining the NLO properties of TeO_2 glasses. Therefore,

a small amount of TiO_2 (i.e. 5%) (so that, we do not lose much available Te^{4+} lone pair and Te-O-Te bridges) is enough to promote the mechanical and the thermal properties of binary $(TlO_{0.5})_x - (TeO_2)_{1-x}$ glasses while still maintaining its NLO properties.

Perspectives

In this thesis, we have simulated TeO_2-based glasses. The obtained results and data lay the path for numerous additional investigations. In future works, the obtained DFT MD trajectories can be used as a training database to develop Machine learning potentials capable to simulate systems with several hundred thousand atoms. This would allow in-depth understanding of the extended properties such as voids, rings or chains formation in the glassy network. This would further enable to understand the process of micro segregation and phase separation in tellurite glasses. Additionally, the statistics of the Raman spectra can be enhanced by computing Raman spectra on larger numbers of configurations of modified tellurite glasses to understand the evolution of the position of the Boson peak as a function of the system composition. Moreover, the contribution of various structural motifs in different compositions of binary and ternary glasses that leads to evolution in Raman spectra can further be understood by analyzing the atomistic nature of the normal modes.

A

Annexes

Summary

A.1 Classical molecular dynamics simulation of glasses **209**
A.1.1 Tl_2O-TeO_2 system 209
A.1.1.1 Introduction 209
A.1.1.2 Methodology 209
A.1.1.3 Results and discussion 213
A.1.1.4 Conclusions 219
A.1.2 TiO_2-Tl_2O-TeO_2 system. 221
A.2 *Ab-initio* simulation of TiO_2-TeO_2 glassy system **223**
A.3 *Ab-initio* simulation of SiO_2 glassy system **226**
A.4 Workflow of computing NLO properties **228**
A.5 Workflow of computing Raman spectra **237**
A.6 CP2K input file **238**
A.7 Structural analysis code : *amorphy* **242**

A.1 Classical molecular dynamics simulation of glasses

A.1.1 Tl_2O-TeO_2 system

A.1.1.1 Introduction

Modelling can help one to disentangle the role of thallium oxide in structural and optical properties of Tl_2O-TeO_2 binary glasses. Atomistic models can be obtained through first-principles molecular dynamics based on a quantum mechanical description of the particles interaction. Nevertheless, such a technique is computationally expensive. Alternatively, classical molecular dynamics based on empirical interatomic potentials (IAPs) offer the possibility of modelling large glassy systems over long periods of time at a very reasonable computational cost and keeping a good accuracy.

Modelling Tl_2O-TeO_2 glasses requires the development of an IAP that accounts for elemental interactions in this system. To date, only one classical IAP exists for $Te^{4+}-O^{2-}$ interaction. This potential has been developed by Gulenko *et al.* [31] and further improved by Torzuoli *et al.* [153]. In these studies, the authors adopted a fully ionic description (i.e. electronic charges equal to oxidation number) of the system with a Buckingham core-shell potential formulation that leads to very good results on reproducing lattice parameters of various TeO_2 crystalline phases within 2% of mean absolute error. In addition, their potential was used to model glassy TeO_2 leading to structural properties in fair agreement with experimental measurements.

In the present work, we focus on developing a classical IAP for $Tl^{+}-O^{2-}$ interaction in order to model amorphous $(TlO_{0.5})_x - (TeO_2)_{1-x}$ compounds (for convenience, we use hereafter $TlO_{0.5}$ notation instead of Tl_2O). Our potential is tested against various Tl(I) containing oxides and proved to be transferable. Furthermore, we produce amorphous models of various $(TlO_{0.5})_x - (TeO_2)_{1-x}$ glasses featuring a good agreement with experimental measurements.

A.1.1.2 Methodology

Theory

In this work, we adopt the Buckingham formulation of the classical IAP [154] in conjunction with an electrostatic interaction model that turned successful on modelling a variety of materials [31],[155]. In practice, the potential energy U_{ij} of a given system is written as follows:

$$U_{ij} = A_{ij}e^{-r/\rho_{ij}} - C_{ij}r^{-6} + \frac{q_i q_j}{4\pi\epsilon_0}\frac{1}{r}, \tag{A.1}$$

where A_{ij}, ρ_{ij} and C_{ij} are the Buckingham potential parameters and q_i is the charge (=oxidation number) of ion i. The first term in equation [A.1] describes the electronic repulsion at the short range due to the overlap of closed electron shells. The middle term in equation [A.1] represents the attractive London dispersion contribution. Finally, the last term contributing to U_{ij} is the coulombic interaction. Due to the long range nature of this term, it requires a special treatment during its calculation which is handled through the Ewald summation technique [156]. Classical description of ions that carry an electronic LP, such as Te^{4+} and Tl^{+}, requires a careful account of their ionic polarizabilities. We resort to the Dick and Overhauser's shell model [32] that allows for an analytical description of the ionic polarisibility. In this technique, a mass-less shell is attached to the massive core of the ion. The core and the shell of the same ion are coloumbically screened, but coupled through a harmonic spring of force constant K_h and possibly an anharmonic force constant K_{ah}. This scheme induces a polarization on the considered ion as its associated shell is displaced. The potential energy contribution of this core-shell model, E_{cs} is given by:

$$E_{cs} = \frac{1}{2!}K_h r_{cs}^2 + \frac{1}{4!}K_{ah} r_{cs}^4, \tag{A.2}$$

where r_{cs} is the distance between ionic core and its associated shell. This model allows one to derive environment based polarizabilities, α, which are expressed as:

$$\alpha = \frac{q_{sh}^2}{K_h}, \tag{A.3}$$

where q_{sh} is the charge assigned to the shell of the ion.

Coupling the Buckingham interaction potential with the core-shell model allows one to develop classical IAPs by relying on a proper account of the ionic polarizibility of the system, as implemented in the General Utility Lattice Program (GULP) [157] software.

Deriving interatomic potential for $Tl^{+}-O^{2-}$

In order to produce and study the amorphous structure of thallium tellurite glasses, IAPs accounting for Te, Tl, and O interactions are required. In previous works, Gulenko *et al.* [31] and Torzuoli *et al.* [153] have proposed a Buckingham potential model for Te^{4+} and O^{2-} that allows a good description of TeO_2-based crystals and pure TeO_2 glass. In this work, we intend to extend this model to be able to describe Te−Tl−O compounds. In practice, energy parameters (see equation [A.1]) accounting for the $Tl^{+}-O^{2-}$ and $Tl^{+}-Tl^{+}$ interactions need

to be fitted on the basis of experimental data.

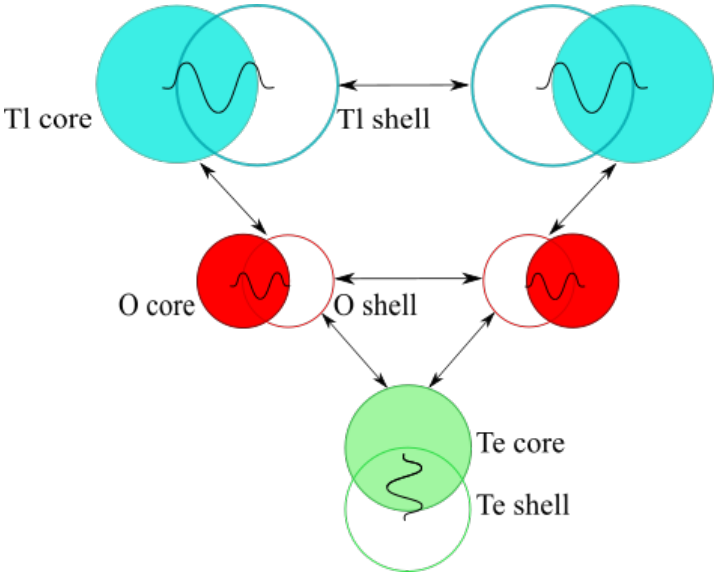

Figure A.1: Schematic representation of interactions between shells and/or cores in Te−Tl−O systems used in our work.

We note that core-shell interactions used by Gulenko *et al* [31] are somehow unconventional. In particular, instead of a direct Te shell and O shell interaction, the authors allowed Te core to interact directly with O shell. Following the same legacy, in this work we allow O shell to interact with Tl core instead of Tl shell, as illustrated in figure [A.1].

In order to optimize the potential parameters, we consider three Te−Tl−O crystal structures, namely α-$Tl_2Te_2O_5$ [158], $Tl_2Te_3O_7$ [159] and Tl_2TeO_3 [160] (see crystal structure projections along c axis in figure [A.2]) simultaneously to fit the $Tl^{+}-O^{2-}$ and $Tl^{+}-Tl^{+}$ interaction model. In particular, we consider experimental lattice parameters and atomic positions as observables to be reproduced by the Buckingham interaction model.

The convergence of a fit is evaluated by computing the final sum of squares between these experimental observables and their calculated counterpart obtained through the IAP model. The sum of squares, F, is defined as follows:

$$F = \sum_{\text{observables}} w * (f_{calc} - f_{obs})^2, \tag{A.4}$$

where f_{calc} and f_{obs} are the calculated and observed quantities and w is a weighting factor. F is minimized with respect to the variable potential parameters using the Newton-Raphson method. In addition, in the case where more than one set of parameters led to F convergence, the one that

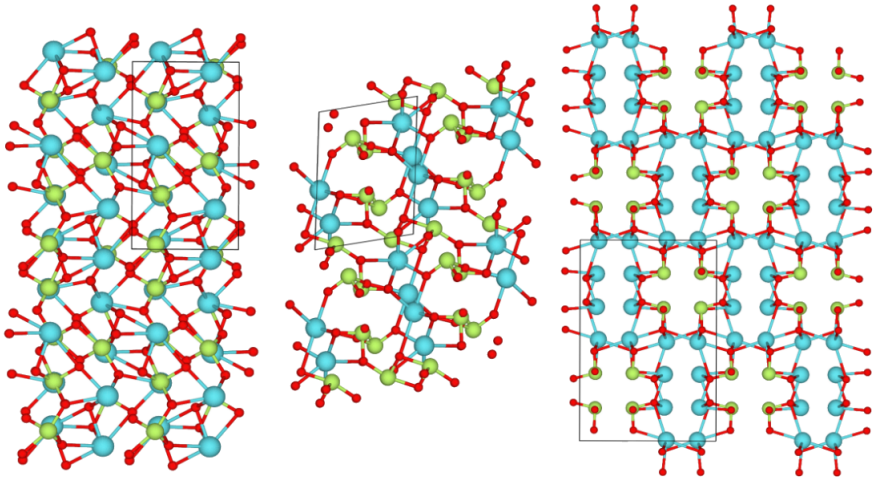

(a). α-$Tl_2Te_2O_5$ (b). $Tl_2Te_3O_7$ (c). Tl_2TeO_3

Figure A.2: Three crystalline thallium tellurite crystal structures used in the fit of IAP. (a) α-$Tl_2Te_2O_5$: space group - $P2_1/n$, (b) $Tl_2Te_3O_7$: space group - P_1, (c) Tl_2TeO_3 : space group - Pban. Color code: oxygen (red), tellurium (green) and thallium (cyan).

leads to the least deviation from the experimental lattice parameters is selected.

In our strategy, we start by adding a $Tl^{+}-O^{2-}$ energy term to the $Te^{4+}-O^{2-}$ Buckingham potential from Ref. [113]. The initial parameters of this potential energy term were initialized to $Tl^{3+}-O^{2-}$ parameters available in Woodley library of potentials for GULP [161]. Then, we fix ρ_{ij}, C_{ij}, q_{sh}, K_h and K_{ah} and vary A_{ij} from 100 eV to 5000 eV. The value of A_{ij} yielding the best fit has then been kept fixed and other parameters were subsequently varied. Following the flowchart presented in figure [A.3], ρ_{ij} is varied in the interval 0.1 to 0.6 Å, K_h from 10 to 200 eV.$Å^{-2}$, q_{sh} from 0.2 to 0.6 e, C_{ij} from 0 to 50 eV.$Å^{-6}$ and lastly, K_{ah} from 0 to 200 eV.$Å^{-4}$.

After this loop of fitting is finished, the obtained $Tl^{+}-O^{2-}$ interaction parameters are then fixed and a new interaction term is added to account for the $Tl^{+}-Tl^{+}$ interaction. We found that adding such an interaction term is required in order to prevent the systems from undergoing important geometrical deformation. The initial ρ_{ij} and C_{ij} values are fixed to those obtained in the case of $Tl^{+}-O^{2-}$ interaction and A_{ij} is varied to minimise the final sum of squares. As in the case of $Tl^{+}-O^{2-}$ interaction, a complete loop on the potential parameters is performed following the fit flowchart (see figure [A.3]) until convergence is achieved.

After these two loops of optimization we obtained a reasonable parametrization of the $Tl^{+}-O^{2-}$ and $Tl^{+}-Tl^{+}$ potentials. In order to achieve a full convergence of the Buckingham interatomic potential for Te−Tl−O compounds and ensure its stability, we repeatedly carried out

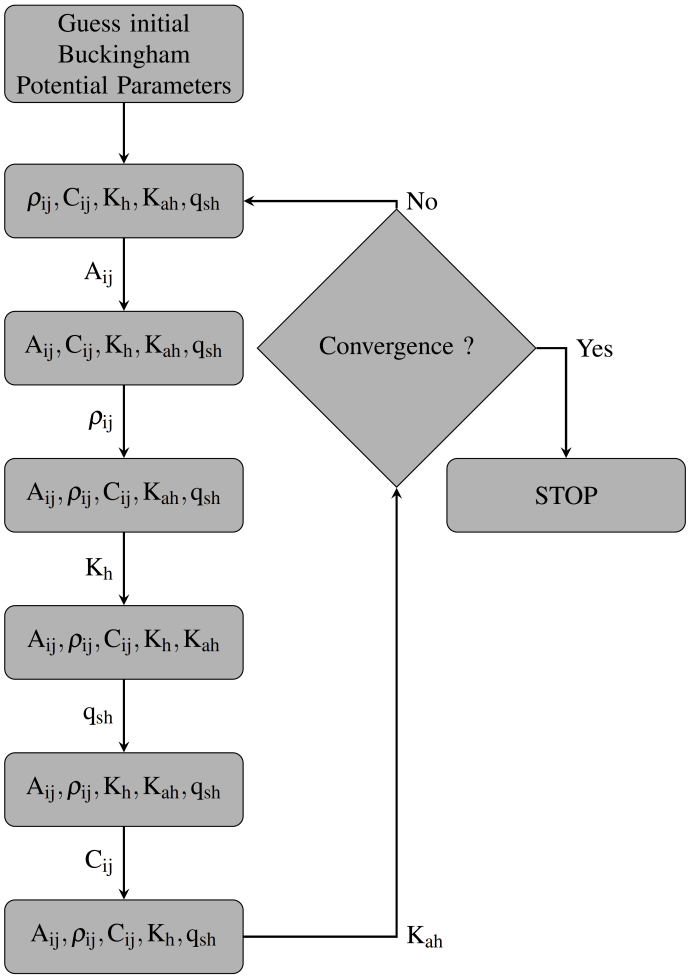

Figure A.3: Illustration of the fitting flowchart used to develop the Te−Tl−O IAP. Parameters fixed during the fit are shown in rectangular boxes, while the variable parameter is displayed along the arrows.

the potential parameters fitting until their values reach convergence and do not change significantly when refitted. The final Buckingham potential parameters for Te−Tl−O compounds are listed in table [A.1].

A.1.1.3 Results and discussion

Validation of the interatomic potential

The quality of an IAP is inherently related to its capability of describing various chemical environments. As such, we test the transferrability of the obtained IAP by considering several thallium (I) oxide based crystalline compounds. The considered crystals were extracted from the Open Quantum Materials Database [162], [163] and listed in table [A.2]. Other than the IAPs derived in this work, the potential parameters for atomic interaction in compounds mentioned in

Buckingham Potential

	A (eV)	ρ (Å)	C (eV.Å^{-6})
	Torzuoli *et al.* [153]		
Te_c^{4+}-O_{sh}^{2-}	1631.810731	0.346336	0.020139
O_{sh}^{2-}-O_{sh}^{2-}	47902.536233	0.175930	33.029759
	This Work		
Tl_c^{+}-O_{sh}^{2-}	826.731161	0.341763	17.097819
Tl_{sh}^{+}-Tl_{sh}^{+}	924.000025	0.392193	9.906808

Shell Model

	K_h (eV.Å^{-2})	K_{ah} (eV.Å^{-4})	q_{sh}(e)
	Torzuoli *et al.* [153]		
Te^{4+}	30.827429	90.0	-1.975415
O^{2-}	61.600546	0.00	-3.122581
	This Work		
Tl^{+}	111.754795	81.0	-2.852493

Table A.1: Obtained Buckingham IAP parameters for thallium core-oxygen shell and thallium shell-thallium shell interaction along with the charges and spring constants. Data for Te_c^{4+}-O_{sh}^{2-} and O_{sh}^{2-}-O_{sh}^{2-} interactions have been taken from Torzuoli *et al.* [153] work.

table [A.2] were taken from "Database of Published Interatomic Potential Parameters - UCL" [164]. The sources of all the considered potentials are cited in table [A.2]. For each compound, a variable cell geometry optimization is achieved through the BFGS algorithm [165]–[168]. Final results are presented in table [A.2].

The obtained mean absolute errors (MAE) on the lattice parameters of various Tl (I) based compounds show a very good accuracy with values less than 6% (see table [A.2]). Such a good result proves the versatility of our potential in accounting for different Tl(I) environments ranging from TlO_3 to TlO_9 units. Nevertheless, one remarks that simple Tl_2O shows relatively high MAE that reflects the large elongation of the cell along the c direction. This result is most likely ascribed to the layered arrangement of crystalline Tl_2O compound that would require a higher level of theory to be properly described [175].

For this reason, and after few tests, we ruled out pure Tl_2O from the potential fitting procedure and only considered crystalline phases of α-$Tl_2Te_2O_5$, $Tl_2Te_3O_7$ and Tl_2TeO_3. For these

ICSD No.	Tl^+ based compound	Tl^+ environment	a (%)	b (%)	c (%)	MAE (%)
50457	$TlCuPO_4$ [169], [170]	TlO_3	-8.56	0.97	-1.93	3.82
33579	$TlGaO_2$ [171]	TlO_9	6.62	6.62	-0.46	4.57
202028	Na_3TlO_2 [172]	TlO_3	4.93	1.92	-7.92	4.92
98627	$Tl_2Ni_4P_4O_{15}$ [170], [173]	TlO_3/TlO_5	0.04	0.81	0.82	0.56
74811	$TlZnPO_4$ [170], [174]	TlO_4/TlO_5	-2.63	1.26	12.70	5.53
98625	$TlNi_4P_3O_{12}$ [170], [173]	TlO_6	0.63	-4.92	0.73	2.09
98626	$Tl_4NiP_6O_{24}$ [170], [173]	$TlO_4/TlO_6/TlO_7$	0.40	2.04	1.93	1.46
77699	Tl_2O	TlO_3	8.89	2.78	18.83	10.17
86782	α-$Tl_2Te_2O_5$ [153]	TlO_4	2.56	-4.95	2.11	3.21
200965	Tl_2TeO_3 [153]	TlO_4	0.15	-5.69	8.76	4.87
150779	$Tl_2Te_3O_7$ [153]	TlO_3/TlO_4	-0.68	-0.30	1.15	0.71

Table A.2: Percentage change in reproducing lattice parameters (a, b, c) compared with experiments and the mean absolute error (MAE) of investigated crystalline Tl (I) based oxides has been shown. A cut-off bond length of 3 Å is used in describing different Tl (I) environments (for the case of $TlGaO_2$, cut-off of 3.3Å is used).

three compounds, a good accuracy in predicting experimental lattice parameters is obtained. Furthermore, we present in table [A.3] the experimental and calculated Tl^+-O^{2-} bond distances in the α-$Tl_2Te_2O_5$, $Tl_2Te_3O_7$ and Tl_2TeO_3 crystalline systems and find that they are well reproduced compared to experiments with an average error of 4.7%.

Compound	Tl^+-O^{2-} (Å) (Experiment)	Tl^+-O^{2-} (Å) (Calculated)
α-$Tl_2Te_2O_5$ [158]	Tl(1)-O: 2.580/2.584/2.646/2.840 Tl(2)-O: 2.681/2.775/2.799/2.813	Tl(1)-O: 2.513/2.377/2.722/2.844 Tl(2)-O: 2.564/2.600/3.164/2.509
$Tl_2Te_3O_7$ [159]	Tl(1)-O: 2.471/2.588/2.700/2.828 Tl(2)-O: 2.488/2.652/2.736/2.942	Tl(1)-O: 2.465/2.561/2.560/2.663 Tl(2)-O: 2.400/2.585/2.722/2.895
Tl_2TeO_3 [160]	Tl(1)-O: 2.548/2.746/2.810 Tl(2)-O: 2.508/2.636/2.663/2.870	Tl(1)-O: 2.728/2.577/2.679 Tl(2)-O: 2.538/2.651/2.368/3.086

Table A.3: Tl^+-O^{2-} bond distances for three different $Tl-Te-O$ crystalline structures based on experimental data and calculations from our IAP.

Classical molecular dynamics (MD) study of thallium tellurite glasses

We further validate our potential in the case of thallium tellurite glasses and show its capability in producing good description of their glassy states. In practice, we generate random initial configurations for $(TlO_{0.5})_x-(TeO_2)_{1-x}$ with concentrations x = 0.1, 0.2, 0.3, 0.4, and 0.5, using Packmol software [112]. The detailed simulation cell information can be found in table [A.4].

We carried out MD simulations as implemented in the DL_POLY software package [176] using our IAP presented in table [A.1]. An integration time step of 1.0 fs is used to integrate the Newton's equations of motion. Starting from the random configurations, each configuration underwent a thermal cycle featuring 50ps at 2000K, 70ps at 1500K, 70ps at 1000K, 70ps at 600K and lastly maintained for 70ps at 300K (see figure [A.4](a)). These runs are performed at fixed density in the NVT (constant number of particles, volume and temperature) ensemble. We ensured that at high temperature all the configurations exhibited a considerable diffusion and completely lost memory of the initial state. As maintaining the system at the experimental density might lead to spurious effects due to the residual pressure in the cell, we extend the MD at 300 K in the NPT (constant number of particles, pressure and temperature) ensemble during a period of about 100ps. During this run we allow the cell volume to vary isotropically.

We note that polarisiblity effects are included in our simulation through core-shell IAP model. In particular, we resort to the DL_POLY Relaxed Shell Model (RSM) [177] implementation in which shells are massless and their motion follows the motion of the cores under the constraint of keeping vanishing forces acting on the shells.

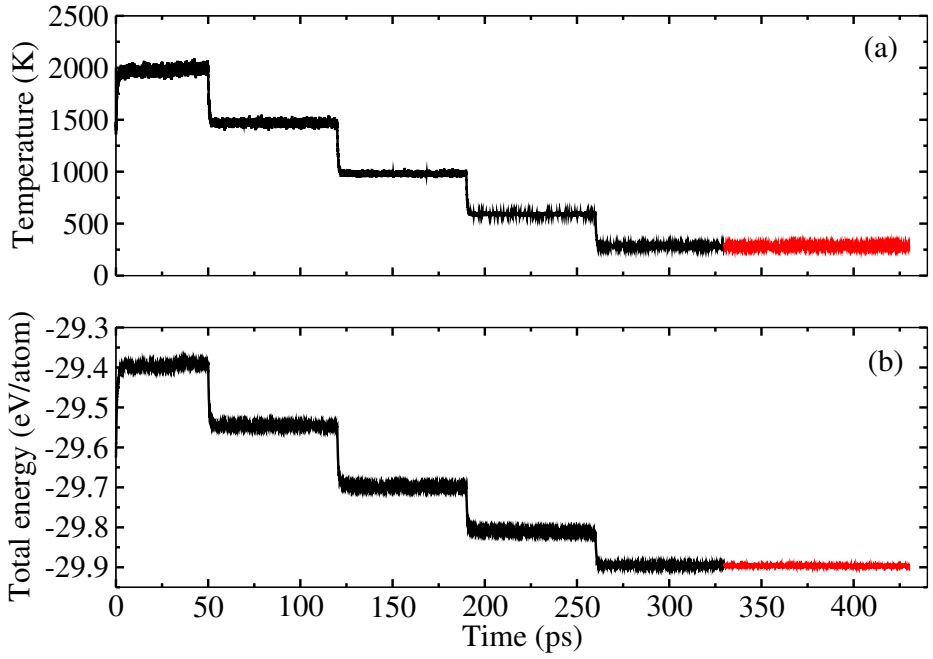

Figure A.4: (a) Temperature and (b) Total Energy variation as function of Time for x=0.4 in $(TlO_{0.5})_x - (TeO_2)_{1-x}$; Black and Red lines represent NVT and NPT ensembles respectively.

The stability of our IAP is assessed during the MD run by looking at the total energy of the

system. Figure [A.4](b) shows the time-evolution of the total energy for $(TlO_{0.5})_x - (TeO_2)_{1-x}$ with $x = 0.4$. At high temperatures, it is particularly difficult to account for core-shell models as shells move away from the cores due to their high kinetic energy resulting in simulation crash [31]. It is noteworthy that in our work the energy is conserved even for temperature as high as 2000 K and during extended time-scales, reflecting the numerical accuracy of our IAP potential. This remains true as well for the NPT run where the cell size is allowed to vary. In this case, the stability of the potential is further proved by the very good stability of the dynamical variable, such as the lattice constant and the pressure for $x = 0.4$, as shown in figure [A.5].

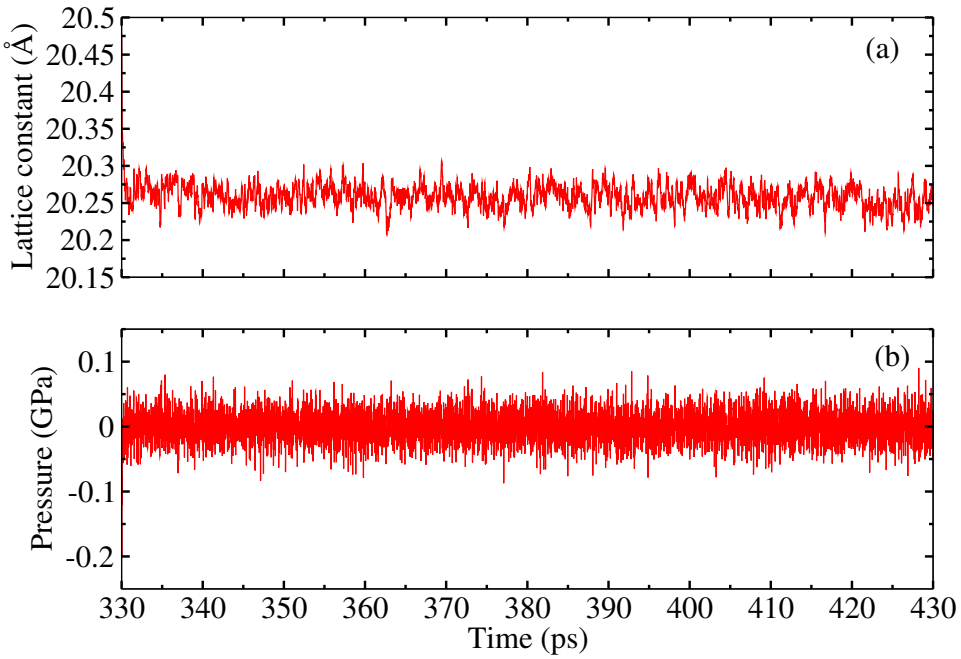

Figure A.5: (a) Lattice constant of the smallest cell vector and (b) Pressure variation as a function of Time during NPT ensemble run.

We find that the pressure is very well conserved within a standard deviation of 0.016 GPa. The same behavior is observed for the evolution of the lattice constant, where we find a standard deviation of 0.023 Å. For all the studied $(TlO_{0.5})_x - (TeO_2)_{1-x}$ models, we report the final equilibrium densities obtained by averaging the cell volume over the last 20ps during the NPT run. These values are also compared to experimental results from Ref. [113]. We find that our models successfully reproduce the experimental densities within an error of 3.02%, see table [A.4]. After checking the numerical stability and convergence of our IAP, we now confront the obtained atomic-scale models to experiments. In particular, we concentrate on measurable structural properties, the pair distribution function (PDF), and the static structure factor, in order to quantify the effectiveness of our IAP. The reduced X-ray PDFs $G(r)$ calculated using RINGS code [121]

Con. (x)	No. of Tl/Te/O (Total)	Expt. ρ ($g.cm^{-3}$) [113]	Calc. ρ ($g.cm^{-3}$)	Lattice Constant (Å)	$\Delta\rho$ (%)
0.1	64/576/1184 (1824)	5.85	5.80	39.25/39.25/19.62	0.85
0.2	128/512/1088 (1728)	6.12	6.06	39.08/39.08/19.54	0.98
0.3	192/448/992 (1632)	6.40	6.30	38.98/38.98/19.49	1.56
0.4	288/432/1008 (1728)	6.68	6.50	40.51/40.51/20.25	2.69
0.5	360/360/900 (1620)	6.95	6.74	40.41/40.41/20.21	3.02

Table A.4: Description of $(TlO_{0.5})_x - (TeO_2)_{1-x}$ amorphous system with various concentrations (x). Percentage change in density ($\Delta\rho$) between experimental (Expt.) density and after NPT run i.e. final calculated (Calc.) density. All configurations feature tetragonal simulation cell.

are presented in figure [A.6] and compared to their experimental counterpart from Ref. [113].

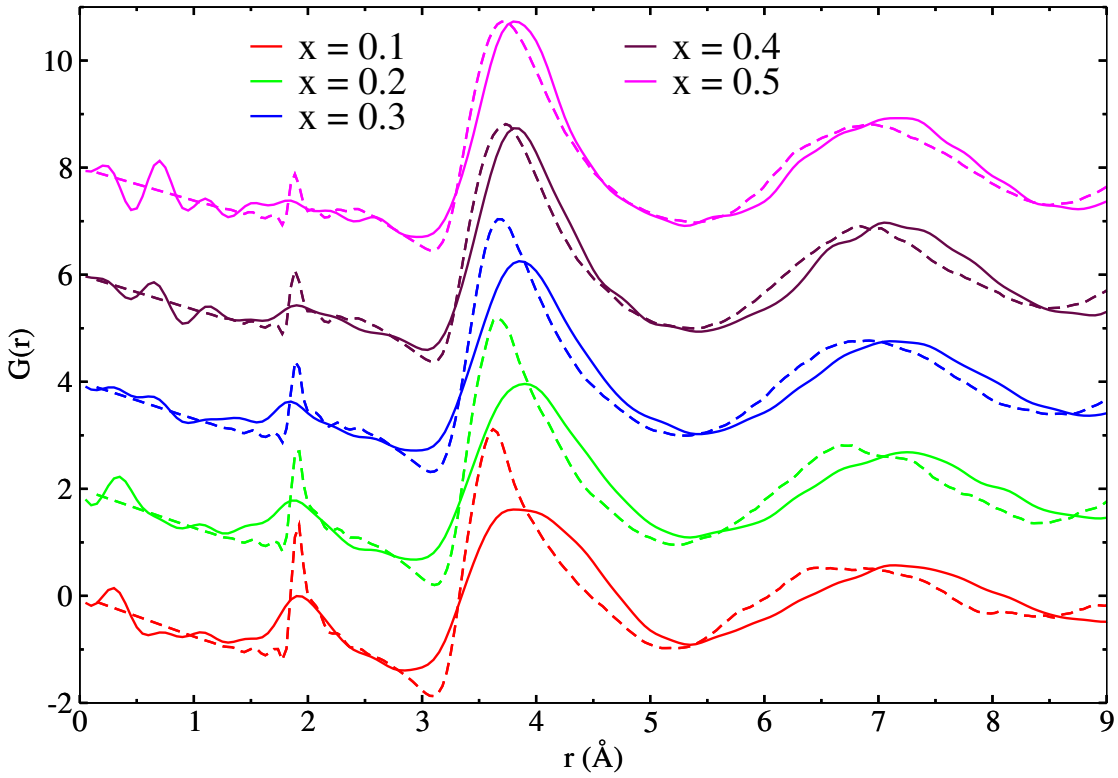

Figure A.6: Comparison of G(r) between experiments and classical MD for $(TlO_{0.5})_x - (TeO_2)_{1-x}$ amorphous system with various concentrations (x). Solid lines: experimental; dashed lines: classical MD (analysed over the last 20ps of NPT run). A shift of 2 units is given to various concentrations for better analysis of the graph.

Overall, our models reproduce with a good accuracy the experimental pair distribution functions. In particular, the positions of the peaks located at 1.9 Å, 3.8 Å and 7.1 Å are in very good agreement with the experimental measurements. Furthermore, we find that the intensities of the peaks corresponding to Te−O distances ($\approx$ 1.9 Å) and Tl−O distances ($\approx$ 2.4 Å) follow closely the trends observed experimentally. Specifically, our model reproduces the experimentally

observed reduction of the intensity of the peak at ≈ 1.9 Å with increasing concentration of $TlO_{0.5}$ in TeO_2-based glass. In addition, the accuracy in reproducing the broad peak centered around 3.8 Å, which corresponds to Te−Te, Te−Tl and Tl−Tl distances, increases with higher concentration of $TlO_{0.5}$ modifier oxide. For r > 5 Å, we remark that, while the PDFs obtained from our models reproduce well the intensity of the broad peak in this region, they underestimate its position by about 0.5 Å. In addition, a better description of this peak might require a more sophisticated description of the Van der Waals interactions in the system. Nevertheless, we note that the integral of the peaks which directly correlate with the number of neighbors is very similar from theory and experiments.
The static structure factor S(q) is obtained from Fourier transforming the G(r) as follows:

$$\mathrm{S}(q) = 1 + \int_0^{r_{\max}} \mathrm{G}(r)\frac{\sin(qr)}{q}\mathrm{d}r \tag{A.5}$$

where q and r_{max} are the scattering vector and upper limit of integration in real space, respectively. A comparison of experimental [113] and calculated S(q) is presented in figure [A.7]. The first diffraction peak (FDP) centered around 2 $Å^{-1}$ is fairly reproduced by our models in comparison to their experimental counterparts. It is also worth mentioning that similar to experiments our IAP records the increase of the amplitude of the FDP as a function of the concentration x of $(TlO_{0.5})_x - (TeO_2)_{1-x}$. Furthermore, similar to the behavior observed for the G(r), the computed FDP tends to show a better reproduction of the experimental S(q) as the concentration of $TlO_{0.5}$ in the glass increases. Finally, we remark that for q vectors larger than 3 $Å^{-1}$ our models fairly reproduce the experimental pattern.

A.1.1.4 Conclusions

In summary, we obtained the Buckingham IAP parameters of Tl^+-O^{2-} and Tl^+-Tl^+ interaction through fitting experimental observables of α-$Tl_2Te_2O_5$, $Tl_2Te_3O_7$ and Tl_2TeO_3 crystalline compounds. The obtained potential has been tested on several other thallium (I) oxide based crystalline compounds and shows good accuracy in reproducing their atomic environments and lattice parameters with less than 6% of error. Furthermore, our potential is used to produce various $(TlO_{0.5})_x - (TeO_2)_{1-x}$ amorphous models (0.1≤x≤0.5) with less than 4% error on their final densities compared to reference experimental data. The obtained models feature good real and reciprocal space properties, in comparison to their experimental counterparts. The main peak positions and intensities of the $G(r)$ and S(q) are well reproduced, thus our IAP is able to reproduce the general features of the structures of $(TlO_{0.5})_x - (TeO_2)_{1-x}$ glasses.

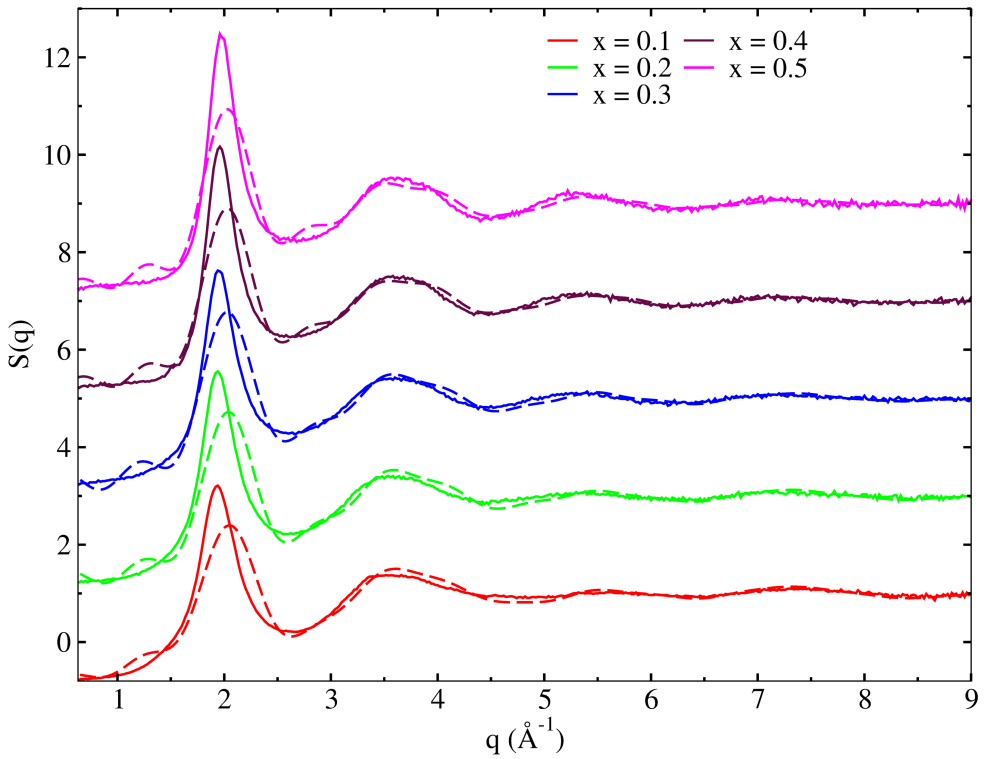

Figure A.7: Comparison of $\mathrm{S(q)}$ X-ray diffraction between experiments and classical MD for $(\mathrm{TlO}_{0.5})_x - (\mathrm{TeO}_2)_{1-x}$ amorphous system with various concentrations (x). Solid lines: experimental; dashed lines: classical MD (analyzed over the last 20 ps of NPT run). A shift of 2 units is given to various concentrations for better analysis of the graph.

A.1.2 TiO_2-Tl_2O-TeO_2 system.

Classical MD has been used to heat the various compositions in $(TiO_2)_x-(TlO_{0.5})_y-(TeO_2)_{1-x-y}$ ternary glasses (see chapter [5], table [5.1]). Similar MD setup as utilized for binary $(TlO_{0.5})_x-(TeO_2)_{1-x}$ glasses has been adopted for performing the MD simulation of ternary glasses (see Appendix [A.1.1]). Buckingham inter-atomic potential parameters for performing MD simulation are listed in table [A.5].

Furthermore, we have also quenched the system at room temperature and checked the performance of the interatomic potential by comparing the calculated total X-ray G(r) and its comparison with available experimental counterpart (see figure [A.8]). We find that for x = 10% and y = 30% in $(TiO_2)_x-(TlO_{0.5})_y-(TeO_2)_{1-x-y}$ ternary glass, our MD model is able to reproduce all the peaks in the PDF (see figure [A.8]).

Buckingham Potential

	A (eV)	ρ (Å)	C (eV.Å^{-6})
Te_c^{4+}-O_{sh}^{2-}	1631.810731	0.346336	0.020139 [153]
O_{sh}^{2-}-O_{sh}^{2-}	47902.536233	0.175930	33.029759 [153]
Tl_c^{+}-O_{sh}^{2-}	826.731161	0.341763	17.097819
Tl_{sh}^{+}-Tl_{sh}^{+}	924.000025	0.392193	9.906808
Ti_{sh}^{4+}-O_{sh}^{2-}	5111.7	0.2625	0.0 [178]

Shell Model

	K_h (eV.Å^{-2})	K_{ah} (eV.Å^{-4})	q_{sh}(e)
Te^{4+}	30.827429	90.0	-1.975415 [153]
O^{2-}	61.600546	0.00	-3.122581 [153]
Tl^{+}	111.754795	81.0	-2.852493
Ti^{4+}	314.00	0.0	-0.1 [178]

Table A.5: Buckingham IAP parameters for various core-shell interaction along with the charges and spring constants in $(TiO_2)_x-(TlO_{0.5})_y-(TeO_2)_{1-x-y}$ ternary glasses.

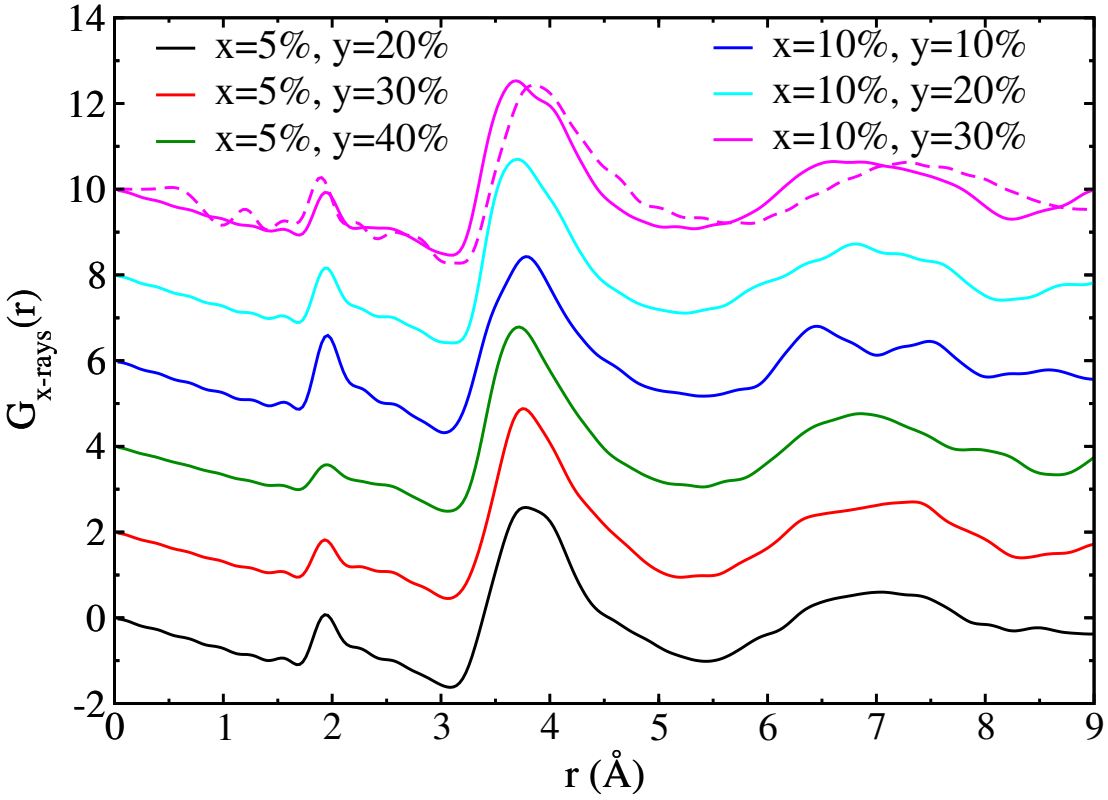

Figure A.8: Description of total G(r) PDF for various compositions in $(TiO_2)_x-(TlO_{0.5})_y-(TeO_2)_{1-x-y}$ glassy system. Solid lines represent the computed G(r) from classical MD simulations while the dashed line shows experimental data [131]. For clarity, a vertical shift of 2 units is provided between various compositions.

A.2 *Ab-initio* simulation of TiO_2-TeO_2 glassy system

We utilized *ab-initio* MD simulation using GGA-PBE functional to produce three structural models of $(TiO_2)_x - (TeO_2)_{1-x}$ binary glasses with compositions ranging from x = 5% to 15%. The densities, lattice parameters, and total number of atoms in the simulated cell at various concentrations are listed in table [A.6]. The MD simulation for each model was started by heating

Concentration (x)	No. of Ti/Te/O (Total)	ρ (g.cm^{-3}) [113]	Lattice Constant (Å)
x = 5%	8/152/320 (480)	5.62	19.45
x = 10%	16/144/320 (480)	5.48	19.45
x = 15%	24/136/320 (480)	5.37	19.41

Table A.6: Description of $(TiO_2)_x - (TeO_2)_{1-x}$ amorphous systems with various concentrations (x) in a cubic simulation cell.

the system at T = 300 K for 4 ps, then at T = 600 K for 4 ps. Subsequently, we have maintained each system at T = 1000 K for 30 ps close to melting temperature of pure TeO_2 glass to obtain good equilibration. In order to obliterate the initial thermal history we have further heated all the systems to T = 2000 K for 1 ps. Following that, we quenched/cooled each composition to T = 1500 K for 3 ps, T = 1000 K for 7 ps, T = 600 K for 25 ps and T = 300 K for 25 ps (see figure [A.9]). Later, we have validated our model with experimental data [113] by computing

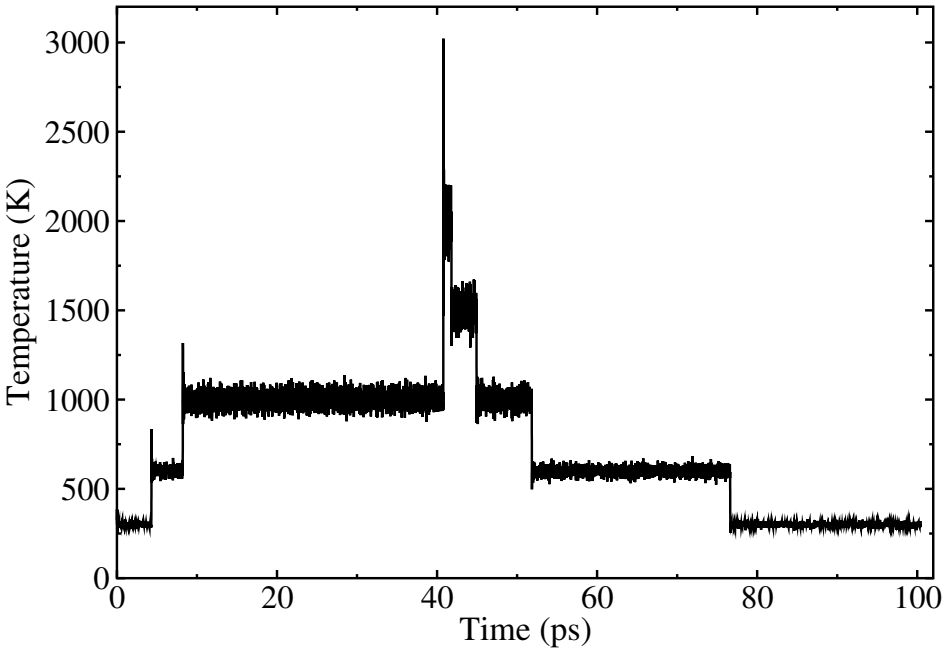

Figure A.9: Thermal cycle for x = 5% in $(TiO_2)_x - (TeO_2)_{1-x}$ binary glass.

total X-ray scattering PDF G(r) (see figure [A.10]). We find that our model overestimates the

first peak position in comparison to experimental data [113]. This discrepancy can be attributed to the adapted DFT model with GGA XC functional which is known to overestimate bond-lengths. Furthermore, we also observe that our model fails to reproduce the double peak around 3.8 Å which can be attributed to Te-Te or possibly Te-Ti distances that are not linked with oxygen atoms in between (see chapter [3]). Further, we also attempt to understand the partial

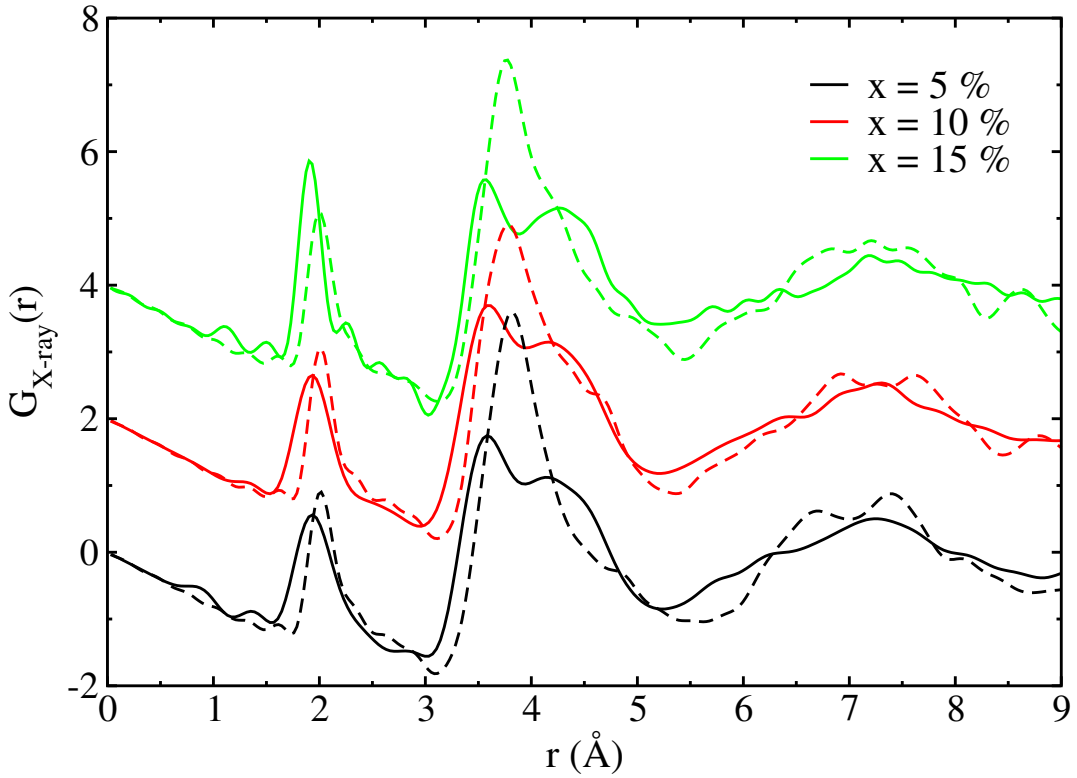

Figure A.10: Comparison of total X-ray scattering PDF G(r) between experiments (solid lines) [113] and *ab-initio* MD simulation (dashed lines) for $(TiO_2)_x - (TeO_2)_{1-x}$ binary glassy system with various concentrations (x). A shift of 2 units in the y-axis is given to various concentrations for better clarity of the graph.

contribution of each pair of atomic species to the total G(r) (see figure [A.11]). We find that the Te-O and O-O distributions remain almost unchanged with increasing x from 5% to 15% in $(TiO_2)_x - (TeO_2)_{1-x}$ binary glassy systems. Further, no clear trends can be observed from other pairs in partial PDFs due to very small contribution of titanium.

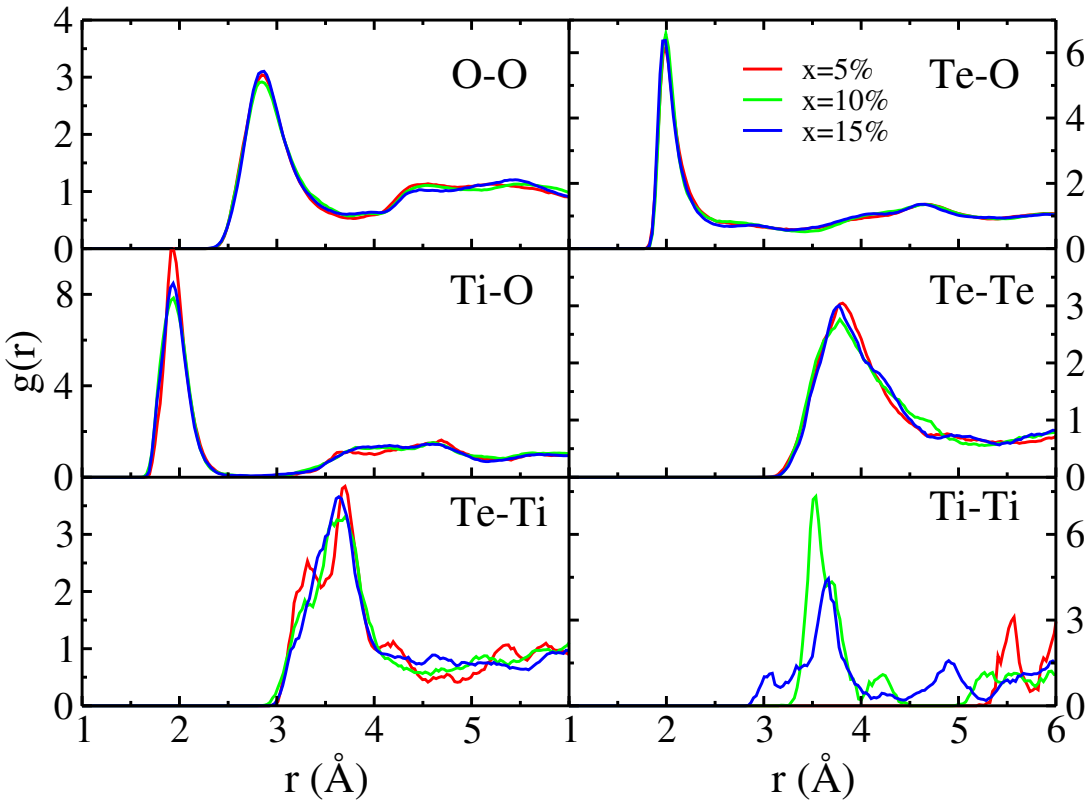

Figure A.11: The partial pair correlation functions $g_{O\text{-}O}(r)$, $g_{Te\text{-}O}(r)$, $g_{Ti\text{-}O}(r)$, $g_{Te\text{-}Te}(r)$, $g_{Te\text{-}Ti}(r)$ and $g_{Ti\text{-}Ti}(r)$ for various concentration of modifier in binary $(TiO_2)_x - (TeO_2)_{1-x}$ glass. The curves are shifted vertically for clarity.

A.3 *Ab-initio* simulation of SiO_2 glassy system

We have performed *ab-initio* MD to obtained four structural models of SiO_2 glass with varying simulation sizes. In particular, we have simulated system with 270, 408, 432 and 456 atom sizes at constant density of 2.2 g.cm^{-3}. The starting *ab-initio* model for each composition was initialized with performing a classical MD run at T = 2000 K for 1000 ps using BKS type potential with potential parameters taken from Ref. [179]. Further, all the models have been quenched to room temperature following the thermal cycle shown in figure [A.12] under NVT conditions. The primary motivation of this simulation is to obtain reference values for computing Raman spectra, and non-linear optical properties of TeO_2-based glasses with respect to SiO_2 glasses. To begin, with we analyze the partial PDF generated by each model (see figure [A.13]).

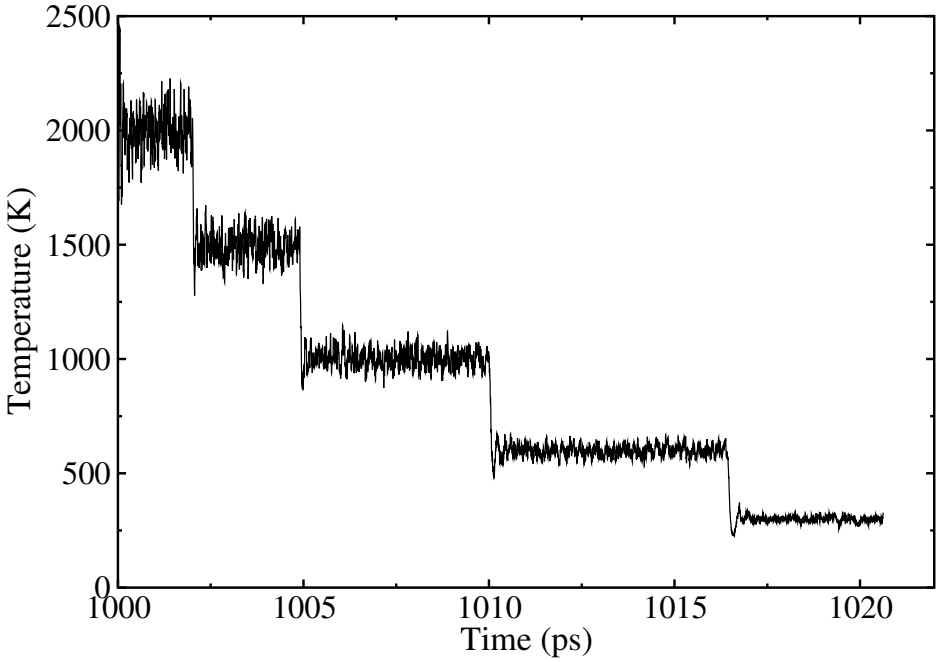

Figure A.12: Thermal cycle for 432 atom size SiO_2 glass.

From the figure, it can be seen that the structural order for whole range of r in the comparison of total X-ray g(r) overall remains the same which shows that, the simulation size has a limited effect on the overall statistical behavior. Moreover, to assess further influence of simulation size on the short-range order of structural motifs we plot the BAD for O-Si-O angles (see figure [A.14]). We notice that the peak position for each simulation size remain the same. Thus, based on the structural analysis, we conclude that all the considered models generates similar structural reorientation of the structural motifs and hence give nearly identical statistical results.

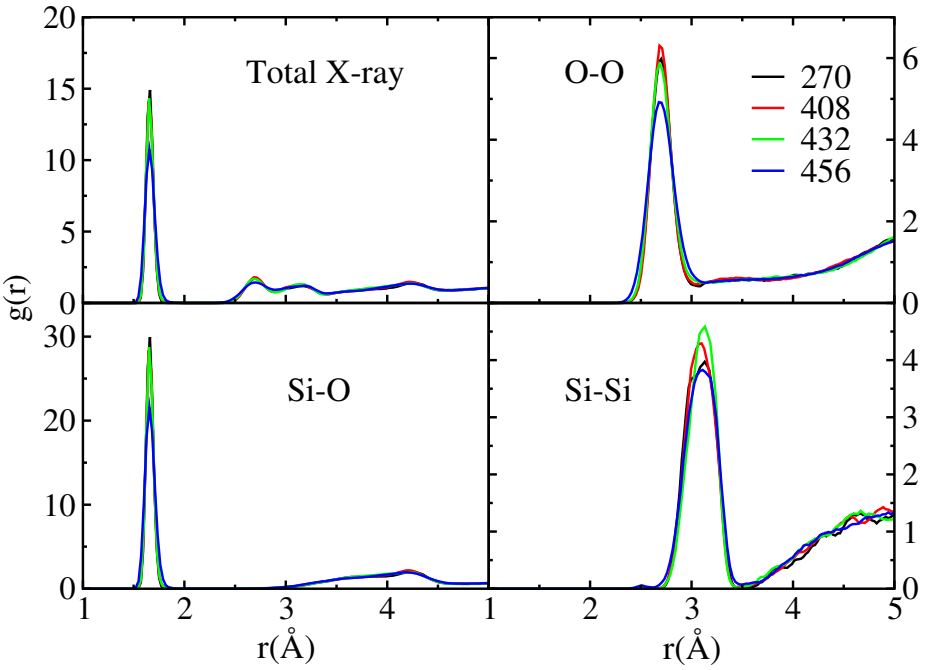

Figure A.13: Comparison of total X-ray and partial O-O, Si-O, Si-Si g(r) PDFs for various simulation sizes.

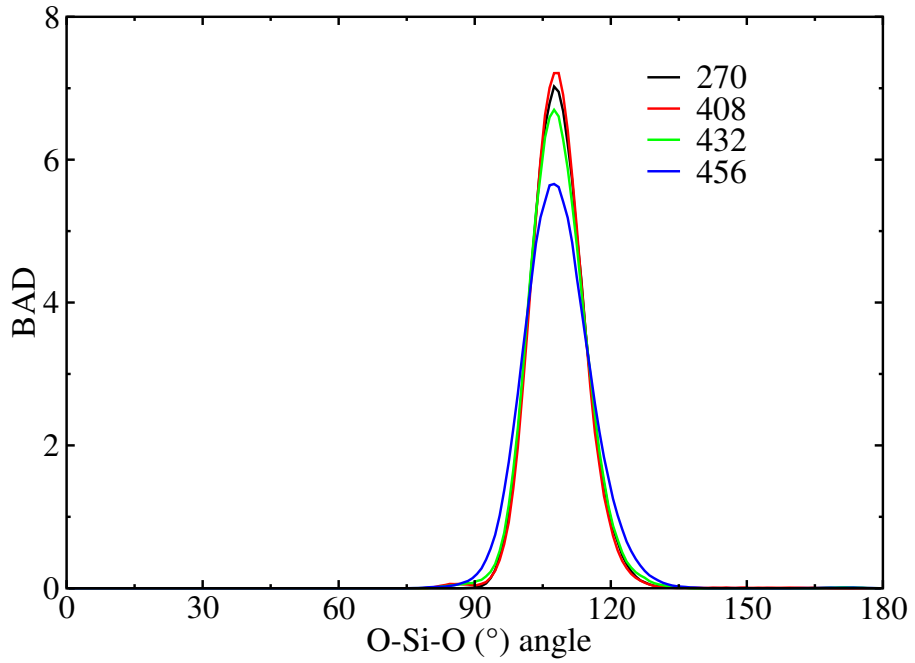

Figure A.14: O-Si-O bond-angle distribution for various simulation sizes.

A.4 Workflow of computing NLO properties

$\chi^{(1)}$ and $\chi^{(3)}$ can be obtained by fitting equations [2.81] the polarizability dependence on electric field using a second order polynomial expansion. To do that one has to calculate the polarizability tensor α_{ij} as a function of applied electric field using Linear response theory as implemented in the CP2K package. In practice, electric field [142], [180] is applied with intensities ranging from 0 to $E_{max} = \frac{E_g}{e \times max(a,b,c)}$ (E_g refers the calculated band gap, e is the electronic charge, and $max(a,b,c)$ corresponds to the largest lattice constants along x, y or z directions) with a step of 0.00008 a.u. to find the dependence of the polarizability as a function of the electric field. For each applied electric field we consider three directions of electric field: (1,0,0), (0,1,0) and (0,0,1). Therefore, for a number of polarizability components, equation [2.81] can be expanded as follows:

$$\alpha_{xx} = \frac{\partial \mu_x}{\partial E_x} - \beta_{xxx} E_x - \frac{1}{2}\gamma_{xxxx} E_x^2 \qquad E = (E_x, 0, 0)$$
$$\alpha_{xx} = \frac{\partial \mu_x}{\partial E_x} - \beta_{xxy} E_y - \frac{1}{2}\gamma_{xxyy} E_y^2 \qquad E = (0, E_y, 0)$$
$$\alpha_{xx} = \frac{\partial \mu_x}{\partial E_x} - \beta_{xxz} E_z - \frac{1}{2}\gamma_{xxzz} E_z^2 \qquad E = (0, 0, E_z)$$

Similar equations can be written for α_{yy} and α_{zz}. Using these equations, a second order

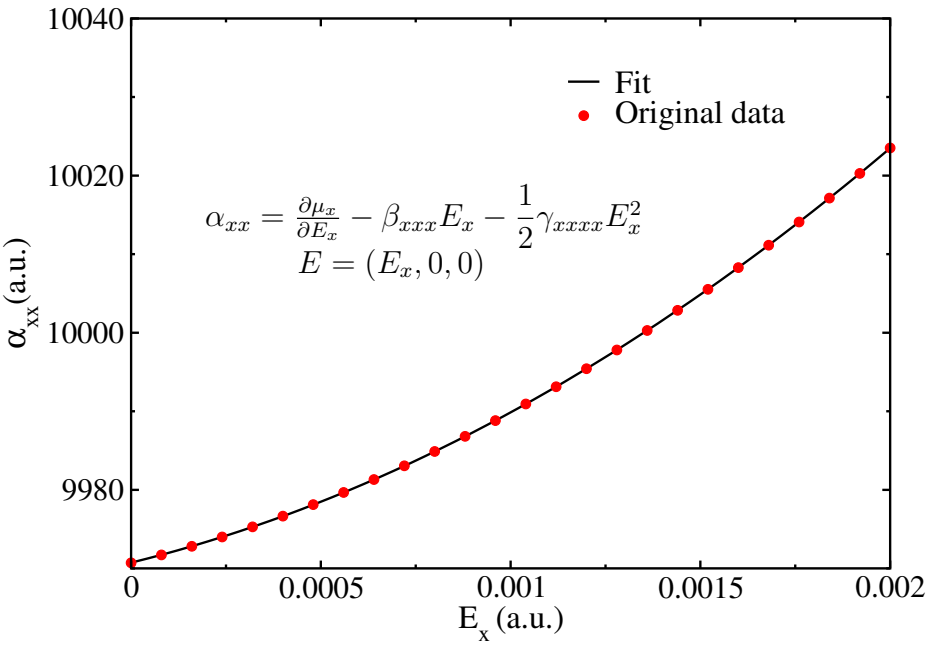

Figure A.15: Second order polynomial fit of α_{xx} with respect to E_x to obtain parameters $\frac{\partial \mu_x}{\partial E_x}$, β_{xxx} and γ_{xxxx}.

polynomial expansion can be used to fit each of the polarizability components as a function of the

electric field and extract the values of hyperpolarizabilities (see figure [A.15]). Bash and Python scripts for achieving various polarizability and hyperpolarizability tensor are mentioned below:

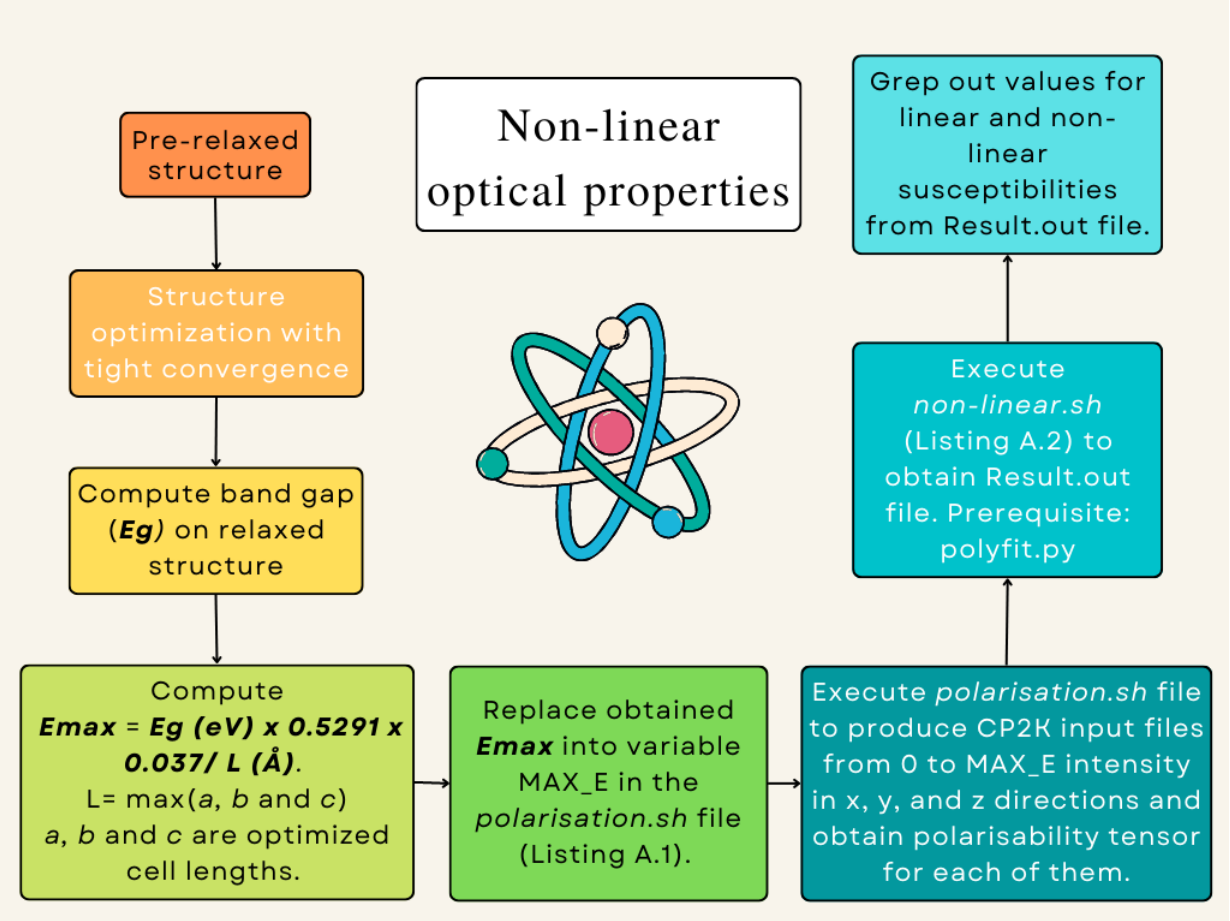

Figure A.16: Computational workflow used for computing linear and non-linear optical properties. Bash and python scripts are mentioned below.

Listing A.1: polarisation.sh

```
#!/bin/bash
LANG=en_US
# Creating folders of different intensties

MAX_E=0.0025
STEP_E=0.0001

for intensity in $(seq 0 $STEP $MAX_E); do
    mkdir Intensity_$intensity
    cd Intensity_$intensity

    # Creating folder for different directions
    for direction in X Y Z; do
        mkdir $direction
        cd $direction
```

```
16
17            cp ../../input.inp .
18            cp ../../config.xyz .
19
20            Intensity=$(grep INTENSITY input.inp)
21            sed -i -e "s/$Intensity/     INTENSITY    $intensity/g" input.inp
22
23            Polarisation=$(grep POLARISATION input.inp)
24            Direction_X="1 0 0"
25            Direction_Y="0 1 0"
26            Direction_Z="0 0 1"
27            direction_row=$(eval echo "\$Direction_$direction")
28            sed -i -e "s/$Polarisation/     POLARISATION    $direction_row/g" input.inp
29
30
31            if [[ ! -f TeO2-raman-1.data ]]; then
32                sbatch script.sh
33                echo "No Raman data file found submitting job"
34                sleep 0.5
35            else
36                echo "Found Raman data file in Intensity_$intensity in $direction folder."
37            fi
38
39            cd ..
40        done
41        cd ..
42    done
```

Listing A.2: non-linear.sh

```
1  #!/bin/bash
2
3  grep xx Intensity_*/X/*raman* | sed -n 'p;n' > x-Ex.dat
4  sed -i -e 's@Intensity_@@g' x-Ex.dat
5  sed -i -e 's@/X/SiO2-raman-1_0.data:@@g' x-Ex.dat
6  sed -i -e 's@xx,yy,zz@@g' x-Ex.dat
7  sort -nk 1 -o x-Ex.dat x-Ex.dat
8
9  grep yy Intensity_*/Y/*raman* | sed -n 'p;n' > y-Ey.dat
10 sed -i -e 's@Intensity_@@g' y-Ey.dat
11 sed -i -e 's@/Y/SiO2-raman-1_0.data:@@g' y-Ey.dat
12 sed -i -e 's@xx,yy,zz@@g' y-Ey.dat
13 sort -nk 1 -o y-Ey.dat y-Ey.dat
14
15 grep zz Intensity_*/Z/*raman* | sed -n 'p;n' > z-Ez.dat
16 sed -i -e 's@Intensity_@@g' z-Ez.dat
17 sed -i -e 's@/Z/SiO2-raman-1_0.data:@@g' z-Ez.dat
18 sed -i -e 's@xx,yy,zz@@g' z-Ez.dat
19 sort -nk 1 -o z-Ez.dat z-Ez.dat
20
21
22 Alpha_diagnoal_array=()
23
24
25 LatX=`grep ABC input.inp | awk '{print $2}'`
```

```
LatY=`grep ABC input.inp | awk '{print $2}'`
LatZ=`grep ABC input.inp | awk '{print $4}'`


volume_SI=$(echo "$LatX * $LatY * $LatZ" | bc -l)


# Converting to AU units
LatX_AU=$(echo "scale=6; $LatX/0.529177249" | bc -l)
LatY_AU=$(echo "scale=6; $LatY/0.529177249" | bc -l)
LatZ_AU=$(echo "scale=6; $LatZ/0.529177249" | bc -l)

volume_AU=$(echo "$LatX_AU * $LatY_AU * $LatZ_AU" | bc -l)


# Checking for the presence for Result.out file
if [[ -f "Result.out" ]]; then
    rm Result.out
fi

echo '#########################################################################' >> Result.out
echo '                                                                         ' >> Result.out
echo '-------------------------------------------------------------------------' >> Result.out
echo '                        Simulation Cell Properties                       ' >> Result.out
echo '-------------------------------------------------------------------------' >> Result.out
echo ' ' >> Result.out
echo 'NOTE :  This works for orthorhombic cells only '                           >> Result.out
echo ' ' >> Result.out
echo '----------------------|--------------------|-------------------------' >> Result.out
echo '   Lattice Parameter   |     Angstorm       |      Atomic Units       ' >> Result.out
echo '----------------------|--------------------|-------------------------' >> Result.out
echo '           X          |      ' $LatX  '    |       ' $LatX_AU          >> Result.out
echo '           Y          |      ' $LatY  '    |       ' $LatY_AU          >> Result.out
echo '           Z          |      ' $LatZ  '    |       ' $LatZ_AU          >> Result.out
echo '-------------------------------------------------------------------------' >> Result.out
echo ' ' >> Result.out
echo 'Volume of simulation cell = ' $volume_SI ' (Ang^3)'                       >> Result.out
echo 'Volume of simulation cell = ' $volume_AU ' (AU^3) '                       >> Result.out



echo '-------------------------------------------------------------------------' >> Result.out
echo '                                                                         ' >> Result.out
echo '                                                                         ' >> Result.out

# For obtaining alpha values
count=1
for file in x-Ex.dat y-Ey.dat z-Ez.dat; do
    python3 polyfit.py -i $file -o output -c $count
    Alpha=$(grep Alpha output | awk '{print $3}')
    Alpha_diagonal_array+=($Alpha)
    rm output
    count=$((count + 1))
done

```

```
81
82  echo '#########################################################################' >> Result.out
83  echo '                                                                         ' >> Result.out
84  echo '-------------------------------------------------------------------------' >> Result.out
85  echo '                      Linear Polarizabilities (Alpha)                    ' >> Result.out
86  echo '-------------------------------------------------------------------------' >> Result.out
87  echo ' ' >> Result.out
88
89  # Writing values to the file
90  echo '       Alpha_xx        |        Alpha_yy         |       Alpha_zz    ' >> Result.out
91  echo '-----------------------|-------------------------|-------------------' >> Result.out
92  sum=0
93  for value in "${Alpha_diagonal_array[@]}"; do
94      echo -n $value " | ">> Result.out
95      sum=$(echo "$sum + $value" | bc -l)
96  done
97
98  echo ' ' >> Result.out
99  echo ' ' >> Result.out
100 MeanAlpha=$(echo "$sum/3" | bc -l)
101 echo '(1/3) Trace of Polarizability alpha matrix =' $MeanAlpha '(A.U.)'      >> Result.out
102 echo '                                                                      '>> Result.out
103 echo '                                                                     ' >> Result.out
104
105 echo '#########################################################################' >> Result.out
106 echo '                                                                         ' >> Result.out
107 echo '-------------------------------------------------------------------------' >> Result.out
108 echo '                        Calculating linear properties                    ' >> Result.out
109 echo '-------------------------------------------------------------------------' >> Result.out
110 echo ' ' >> Result.out
111
112 CHI_1=$(echo "4*3.141592654 * $MeanAlpha / $volume_AU" | bc -l)
113 echo 'Linear suscceptibility X(1) = ' $CHI_1 '(A.U.)'                         >> Result.out
114 n=$(echo "sqrt(1+$CHI_1)" | bc -l)
115 echo 'Linear refractive index (n) = ' $n                                      >> Result.out
116
117 echo '                                                                    '  >> Result.out
118 echo '                                                                    '  >> Result.out
119
120 echo '#########################################################################' >> Result.out
121 echo '                                                                         ' >> Result.out
122 echo '-------------------------------------------------------------------------' >> Result.out
123 echo '                      Calculating non-linear properties                  ' >> Result.out
124 echo '-------------------------------------------------------------------------' >> Result.out
125 echo '                                                                       ' >> Result.out
126
127
128 python3 polyfit.py -i x-Ex.dat -o output -c 1
129 Gamma_XXXX=$(grep Gamma output | awk '{print $3}')
130 CHI_3_XXXX=$(echo "scale=8; 2*3.141592654* $Gamma_XXXX / ( 3 * $volume_AU)" | bc -l)
131 CHI_3_XXXX_SI=$(echo "scale=4; $CHI_3_XXXX / 5.14220632^2 " | bc -l)
132 rm output
133
134
135 python3 polyfit.py -i y-Ey.dat -o output -c 1
```

```
Gamma_XXYY=$(grep Gamma output | awk '{print $3}')
CHI_3_XXYY=$(echo "scale=8; 2*3.141592654* $Gamma_XXYY / ( 3 * $volume_AU)" | bc -l)
CHI_3_XXYY_SI=$(echo "scale=4; $CHI_3_XXYY / 5.14220632^2 " | bc -l)
rm output


python3 polyfit.py -i z-Ez.dat -o output -c 1
Gamma_XXZZ=$(grep Gamma output | awk '{print $3}')
CHI_3_XXZZ=$(echo "scale=8; 2*3.141592654* $Gamma_XXZZ / ( 3 * $volume_AU)" | bc -l)
CHI_3_XXZZ_SI=$(echo "scale=4; $CHI_3_XXZZ / 5.14220632^2 " | bc -l)
rm output


python3 polyfit.py -i x-Ex.dat -o output -c 2
Gamma_YYXX=$(grep Gamma output | awk '{print $3}')
CHI_3_YYXX=$(echo "scale=8; 2*3.141592654* $Gamma_YYXX / ( 3 * $volume_AU)" | bc -l)
CHI_3_YYXX_SI=$(echo "scale=4; $CHI_3_YYXX / 5.14220632^2 " | bc -l)
rm output


python3 polyfit.py -i y-Ey.dat -o output -c 2
Gamma_YYYY=$(grep Gamma output | awk '{print $3}')
CHI_3_YYYY=$(echo "scale=8; 2*3.141592654* $Gamma_YYYY / ( 3 * $volume_AU)" | bc -l)
CHI_3_YYYY_SI=$(echo "scale=4; $CHI_3_YYYY / 5.14220632^2 " | bc -l)
rm output


python3 polyfit.py -i z-Ez.dat -o output -c 2
Gamma_YYZZ=$(grep Gamma output | awk '{print $3}')
CHI_3_YYZZ=$(echo "scale=8; 2*3.141592654* $Gamma_YYZZ / ( 3 * $volume_AU)" | bc -l)
CHI_3_YYZZ_SI=$(echo "scale=4; $CHI_3_YYZZ / 5.14220632^2 " | bc -l)
rm output



python3 polyfit.py -i x-Ex.dat -o output -c 3
Gamma_ZZXX=$(grep Gamma output | awk '{print $3}')
CHI_3_ZZXX=$(echo "scale=8; 2*3.141592654* $Gamma_ZZXX / ( 3 * $volume_AU)" | bc -l)
CHI_3_ZZXX_SI=$(echo "scale=4; $CHI_3_ZZXX / 5.14220632^2 " | bc -l)
rm output



python3 polyfit.py -i y-Ey.dat -o output -c 3
Gamma_ZZYY=$(grep Gamma output | awk '{print $3}')
CHI_3_ZZYY=$(echo "scale=8; 2*3.141592654* $Gamma_ZZYY / ( 3 * $volume_AU)" | bc -l)
CHI_3_ZZYY_SI=$(echo "scale=4; $CHI_3_ZZYY / 5.14220632^2 " | bc -l)
rm output



python3 polyfit.py -i z-Ez.dat -o output -c 3
Gamma_ZZZZ=$(grep Gamma output | awk '{print $3}')
CHI_3_ZZZZ=$(echo "scale=8; 2*3.141592654* $Gamma_ZZZZ / ( 3 * $volume_AU)" | bc -l)
CHI_3_ZZZZ_SI=$(echo "scale=4; $CHI_3_ZZZZ / 5.14220632^2 " | bc -l)
```

```
rm output



echo '                  2nd Order Hyper-Polarizability                    ' >> Result.out
echo '                                                                    ' >> Result.out
echo '--------------------------------------------------------------------' >> Result.out
echo ' CHI_3 Component | SI Units (X10^-22 m2/V2) |     Atomic Units      ' >> Result.out
echo '-----------------|--------------------------|-----------------------' >> Result.out
echo '      XXXX       |    ' $CHI_3_XXXX_SI '    |    ' $CHI_3_XXXX        >> Result.out
echo '      XXYY       |    ' $CHI_3_XXYY_SI '    |    ' $CHI_3_XXYY        >> Result.out
echo '      XXZZ       |    ' $CHI_3_XXZZ_SI '    |    ' $CHI_3_XXZZ        >> Result.out
echo '      YYXX       |    ' $CHI_3_YYXX_SI '    |    ' $CHI_3_YYXX        >> Result.out
echo '      YYYY       |    ' $CHI_3_YYYY_SI '    |    ' $CHI_3_YYYY        >> Result.out
echo '      YYZZ       |    ' $CHI_3_YYZZ_SI '    |    ' $CHI_3_YYZZ        >> Result.out
echo '      ZZXX       |    ' $CHI_3_ZZXX_SI '    |    ' $CHI_3_ZZXX        >> Result.out
echo '      ZZYY       |    ' $CHI_3_ZZYY_SI '    |    ' $CHI_3_ZZYY        >> Result.out
echo '      ZZZZ       |    ' $CHI_3_ZZZZ_SI '    |    ' $CHI_3_ZZZZ        >> Result.out
echo '--------------------------------------------------------------------' >> Result.out



echo '--------------------------------------------------------------------' >> Result.out
echo '                              END OF FILE                           ' >> Result.out
echo '--------------------------------------------------------------------' >> Result.out
```

Listing A.3: polyfit.py

```
import numpy as np
import sys
import argparse


class CurveFit():

    def __init__(self, inputData, outputData, columnNumber):
        self.inputData = inputData
        self.outputData = outputData
        self.columnNumber = columnNumber
        self.fetchInput()


    def fetchInput(self):
        X = []
        Y = []

        for values in self.inputData[:]:
            X.append(float(values.split()[0]))
            Y.append(float(values.split()[self.columnNumber]))

        self.x = np.array(X)
        self.y = np.array(Y)


    def writeOutput(self):
```

```
        with open(self.outputData, 'w') as fileOpen:
            fileOpen.write(f' Gamma = {2*self.coefficient[0]} \n Beta =
            {self.coefficient[1]} \n Alpha = {self.coefficient[2]} \n')


    def funcFit(self):
        self.coefficient = np.polyfit(self.x, self.y, 2)
        print(f' Gamma = {2*self.coefficient[0]} \n Beta =
        {self.coefficient[1]} \n Alpha = {self.coefficient[2]} \n')
        return self.coefficient

    def plotData(self, Plotting=False):
        fig = plt.figure()
        ax = fig.add_subplot(111)

        plt.scatter(self.x, self.y, label='Input Data')
        plt.title('Plot Data')

        if Plotting:
            Y_fit = []
            for values in self.x:
                z = self.coefficient[0]*values**2 +
                    self.coefficient[1]*values +
                    self.coefficient[2]
                Y_fit.append(float(z))
            self.z = np.array(Y_fit)
            plt.plot(self.x, self.z, label='Fit')
            plt.text(0.5, 0.5 ,f' Gamma= {2*self.coefficient[0]} \n Beta =
               {self.coefficient[1]} \n Alpha = {self.coefficient[2]}',
               horizontalalignment='center', verticalalignment='center',
               transform = ax.transAxes, fontsize = 10)
            plt.title('Non-linear fitting')
        plt.legend()
        plt.xlabel('x')
        plt.ylabel(f'y {self.columnNumber}')
        plt.show()


def main():

    parser = argparse.ArgumentParser(description='This code fits
                                    the polynomial to the data points.')

    parser.add_argument('-i', '--input', type=str, action='store' ,
                        dest='inputData', help='Input data file name',
                        required=True)
    parser.add_argument('-o', '--output', type=str, action='store',
                        dest='outputData', default='Output.dat',
                        help='Output data file name')
    parser.add_argument('-p', '--plot',  action='store_true',
                        dest='outputPlot', help='Plot the data')
    parser.add_argument('-n', '--nofit', action='store_true',
                        dest='nofit', help='No fitting of data')
    parser.add_argument('-c', '--col', type=int, action='store',
                        dest="column", default=1, help="Column number")
```

```
83
84      args = parser.parse_args()
85
86      try:
87          with open(args.inputData, 'r') as fileOpen:
88              inputData = fileOpen.readlines()
89      except FileNotFoundError as FNFE:
90          print(f'File not found : {FNFE}')
91          sys.exit(1)
92
93
94      Evaluation = CurveFit(inputData, args.outputData, args.column)
95
96
97      if args.nofit and args.outputPlot:
98          Evaluation.plotData()
99      elif not args.nofit and args.outputPlot:
100         Evaluation.funcFit()
101         Evaluation.plotData(args.outputPlot)
102         Evaluation.writeOutput()
103     elif not args.nofit and not args.outputPlot:
104         Evaluation.funcFit()
105         Evaluation.writeOutput()
106     else:
107         print('No fit and  no plot options are provided so no work to do.')
108
109
110 if __name__ == '__main__':
111     main()
112     sys.exit(0)
```

A.5 Workflow of computing Raman spectra

Codes used to achieve calculation of Raman spectra are available at Ref. [181].

Listing A.4: Steps for computing Raman spectra

```
1  ./read_hessian -H TeO2-Hessian-1.hess -i input.inp
2  python3 raman_fd.py -i input.inp --readfc --soft cp2k -p displ
3  python3 raman_fd.py --readfc -i input.inp -p calc -o raman_PBE_glass_480.dat --soft cp2k
4  python3 arc_spectra.py -o raman_cp2k_TeO2Tl2O.hdf -g glass_TeO2_PBE -l
5                          "raman_PBE_glass_480.dat" -c "func:PBE;glass;NVT;270"
6  python3 list_hd5_content.py -i raman_cp2k_TeO2.hdf
7  python3 plot_spectra.py
```

Listing A.4 description

Line 1: Fortran excecutable file to obtain force constant from Hessian file obatined from CP2K.

Line 2: Python script to produce displacement for finite difference method.

Line 3: Python script to collect polarizability tensor for each displacement and fit Lorentzian.

Line 4: Python script to store data in hdf file.

Line 6: Python script to view items in hdf file.

Line 7: Python script to plot Raman spectra.

A.6 CP2K input file

CP2K is a Fortran95 program to perform atomistic and molecular simulations. Input file required to do *ab-initio* calculations are shown in the listing [A.6].

Listing A.5: Implementation of CP2K input file

```
&GLOBAL
  PROJECT TeO2
  PRINT_LEVEL LOW
  RUN_TYPE ENERGY
  WALLTIME 60:50:00
&END GLOBAL

#&EXT_RESTART
#  RESTART_FILE_NAME TeO2-1.restart
#&END EXT_RESTART

&FORCE_EVAL
  METHOD QS
  STRESS_TENSOR ANALYTICAL
  &DFT
      BASIS_SET_FILE_NAME Basis_set_folder/GTH_BASIS_SETS.dat
      BASIS_SET_FILE_NAME Basis_set_folder/BASIS_MOLOPT_UCL.dat
      BASIS_SET_FILE_NAME Basis_set_folder/BASIS_ADMM_MOLOPT.dat
      BASIS_SET_FILE_NAME Basis_set_folder/BASIS_ADMM.dat
      POTENTIAL_FILE_NAME Potential_folder/GTH_POTENTIALS.dat
    WFN_RESTART_FILE_NAME ../TeO2-RESTART.wfn
    &MGRID
      CUTOFF 1000
      REL_CUTOFF 60
    &END MGRID
    &QS
      EPS_DEFAULT 1.0E-13
      EPS_PGF_ORB 1.0E-31
      WF_INTERPOLATION PS
      EXTRAPOLATION_ORDER 3
      METHOD GPW
    &END QS
    &SCF
      &DIAGONALIZATION OFF
      &END DIAGONALIZATION
      &MIXING
        ALPHA 0.3
        METHOD BROYDEN_MIXING
        NBROYDEN 8
      &END MIXING
      !CHOLESKY INVERSE
      SCF_GUESS RESTART

      EPS_SCF 1.0E-6
      &OT ON
        MINIMIZER CG
        LINESEARCH 3PNT
```

```
      PRECONDITIONER FULL_SINGLE_INVERSE
      ENERGY_GAP 0.01
    &END OT
    MAX_SCF 30
    &OUTER_SCF
      MAX_SCF 30
      EPS_SCF 1.0E-6
    &END OUTER_SCF
  &END SCF

  &AUXILIARY_DENSITY_MATRIX_METHOD
     METHOD BASIS_PROJECTION
     ADMM_PURIFICATION_METHOD MO_DIAG
  &END AUXILIARY_DENSITY_MATRIX_METHOD

  &XC
    &XC_FUNCTIONAL
     &PBE
       SCALE_X 0.75
       SCALE_C 1.0
     &END PBE
    &END XC_FUNCTIONAL
    &HF
      FRACTION 0.25
      &SCREENING
        EPS_SCHWARZ 1.0E-6
        SCREEN_ON_INITIAL_P TRUE
      &END
      &INTERACTION_POTENTIAL
        POTENTIAL_TYPE TRUNCATED
        CUTOFF_RADIUS 9.0
        T_C_G_DATA ../t_c_g.dat
      &END
    &END HF
  &END XC
  &LOCALIZE
    METHOD JACOBI
    EPS_LOCALIZATION 1.0E-6
    &PRINT
      !&WANNIER_CUBES
      !&END
      ! Output the centers of all Wannier functions as xyz-file
      &WANNIER_CENTERS
          IONS+CENTERS .TRUE.
      &END
      &WANNIER_SPREADS ON
      &END

      &WANNIER_STATES
      &END WANNIER_STATES

    &END
  &END
  &PRINT
    &E_DENSITY_CUBE
```

```
            STRIDE 1
            #       TOTAL_DENSITY .TRUE.
          &END E_DENSITY_CUBE
        &END PRINT
      &END DFT

      &SUBSYS
        &CELL
          ABC 19.52325657542347  19.52325657542347  19.52325657542347
          ALPHA_BETA_GAMMA 90.0000 90.0000 90.0000
          PERIODIC XYZ
        &END CELL
        &TOPOLOGY
          COORDINATE XYZ
          COORD_FILE_NAME config.xyz
        &END TOPOLOGY

        &PRINT
          &ATOMIC_COORDINATES ON
          &END
        &END

        &KIND Ti
          BASIS_SET     TZVP-MOLOPT-SR-GTH
          POTENTIAL     GTH-PBE-q12
          BASIS_SET AUX_FIT cFIT13
        &END KIND
        &KIND Tl
          BASIS_SET     TZVP-MOLOPT-SR-GTH
          POTENTIAL     GTH-PBE-q13
          BASIS_SET AUX_FIT cFIT9
        &END KIND
        &KIND Te
          BASIS_SET     TZVP-MOLOPT-SR-GTH
          POTENTIAL     GTH-PBE-q6
          BASIS_SET AUX_FIT cFIT6
        &END KIND
        &KIND O
          BASIS_SET TZVP-GTH-q6
          POTENTIAL GTH-PBE-q6
          BASIS_SET AUX_FIT cFIT3
        &END

      &END SUBSYS
      &PRINT
         &STRESS_TENSOR  ON
           FILENAME __STD_OUT__
         &END STRESS_TENSOR
       &END PRINT
    &END FORCE_EVAL

    &MOTION

     #   &GEO_OPT
     #     OPTIMIZER BFGS
```

```
    #      MAX_ITER 1000
    #    &END GEO_OPT

     &MD
      ENSEMBLE NVT  ! sampling the canonical ensemble, accurate properties might need NVE
      TEMPERATURE [K] 300
      TIMESTEP [fs] 1.00
      STEPS 50000
       &THERMOSTAT
         REGION MASSIVE
         TYPE NOSE
         &NOSE
           TIMECON  20
         &END NOSE
       &END THERMOSTAT
     &END MD
    &PRINT
      &TRAJECTORY
        &EACH
          MD 1
        &END EACH
      &END TRAJECTORY
      &VELOCITIES OFF
      &END VELOCITIES
      &FORCES OFF
      &END FORCES
      &RESTART_HISTORY
        &EACH
          MD 100
        &END EACH
      &END RESTART_HISTORY
      &RESTART
        BACKUP_COPIES 2
        &EACH
          MD 1
        &END EACH
      &END RESTART
    &END PRINT
  &END MOTION
```

A.7 Structural analysis code : *amorphy*

During my PhD tenure, me in collaboration with my supervisor Dr. Assil Bouzid, we have written a code named "*amorphy*". The purpose of this code base is to perform structural analysis for amorphous system. The coordination number, local environment, charge analysis etc. reported in this work have been computed using "*amorphy*" code.

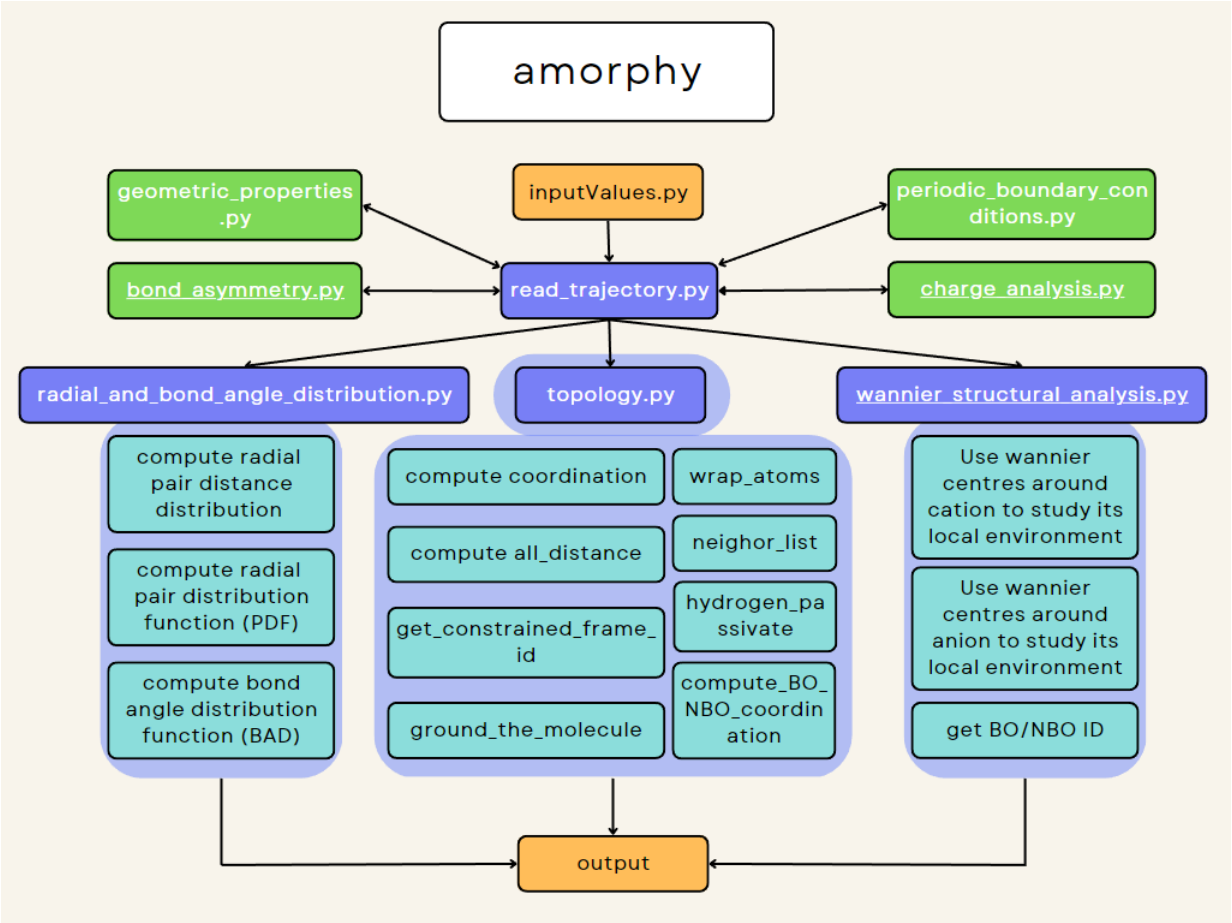

Figure A.17: Codes utilized for structural analysis of amorphous system

The github link to "*amorphy*" : `https://github.com/rvraghvender/amorphy`

Description of *amorphy* code

- **inputValues.py:** Implements the function for computing desired properties and takes the input parameters such as cut-offs, atomic symbols etc.
- **read_trajectory.py:** This module read/load the MD trajectory (xyz format).
- **bond_asymmetry.py:** This module computes the asymmetry in bond-length around given atom.

- **geometric_properties.py:** This module performs the geometrical analysis such as identifying the shape of simulation cell (orthorhombic/ non-orthorhombic), rotate the molecule etc.
- **periodic_boundary_conditions.py:** This module helps in implementing the periodic boundary conditions in orthorhombic or non-orthorhombic systems.
- **charge_analysis.py:** This module provides an interface to the charges obtained from DDEC6 or Bader analysis.
- **radial_and_bond_angle_distribution.py:** This module calculates the following:
  - Radial pair distance distribution: In this submodule, distance distribution between two atomic species is calculated.
  - Radial distribution function: In this submodule, partial PDF is calculated between two atomic species.
  - Bond-angle distribution function (BAD): In this submodule, bond-angle distribution of angle between atoms β to α and γ is calculated.
- **topology.py:** This module performs the following operations:
  - Compute coordination: In this submodule, the coordination number for given atom under cut-off value is calculated.
  - Wrap atoms: This submodule, wraps the atoms placed outside the simulation cell into the box using periodic boundary conditions.
  - Compute all distances: This submodule, prints all the possible distance between two atomic species for each frame.
  - Neighbor list: This submodule, returns a list of atomic ID around given atom.
  - Get constrained frame ID: This submodule, returns the frame ID in which two atoms come closer than the cut-off values defined.
  - Hydrogen passivate: This submodule, attaches hydrogen atom to the terminal oxygen atoms in a molecular fragment.
  - Ground the molecule: Given atomic ID of three atoms, this submodule, translates and rotates the whole molecular fragment in such a way that the given IDs are placed on the z = 0 plane.
  - Compute BO/NBO coordination: This submodule, computes the coordination number of cation with respect to bridging oxygen and non-bridging oxygen separately.
- **wannier_structural_analysis.py:** This module performs the following operations:
  - Use wannier centers around cation to study its local environment: Here considering cation as a host atom, the local environments such coordination number resolved percentage, average charge, bond asymmetry etc. around cation are obtained under the applied Wannier center constraints.

- Use wannier centers around anion to study its local environment: Here considering anion as a host atom, the local environments such as coordination number resolved percentage, average charge, bond asymmetry etc. around anion are obtained under the applied Wannier center constraints.
- Get BO/NBO ID: In this submodule, the atomic ID of bridging and non-bridging oxygen are returned.

B

Bibliography

Summary

References **246**
List of Works **260**

References

[1] H. Takebe, S. Pujino, and K. Morinaga, "Refractive-Index Dispersion of Tellurite Glasses in the Region from 0.40 to 1.71 μm," *Journal of the American Ceramic Society*, vol. 77, no. 9, pp. 2455–2457, 1994.

[2] A. K. YAKHKIND, "Tellurite glasses," *Journal of the American Ceramic Society*, vol. 49, no. 12, pp. 670–675, 1966.

[3] W. Vogel, Ed., *Glass Chemistry*, en. Berlin, Heidelberg: Springer, 1994. (visited on 08/19/2022).

[4] S. Tanabe, K. Hirao, and N. Soga, "Upconversion fluorescences of TeO_2-and Ga_2O_3-based oxide glasses containing Er^{3+}," *Journal of non-crystalline solids*, vol. 122, no. 1, pp. 79–82, 1990.

[5] H. Nasu, O. Matsushita, K. Kamiya, H. Kobayashi, and K. Kubodera, "Third harmonic generation from Li_2O-TiO_2-TeO_2 glasses," *Journal of non-crystalline solids*, vol. 124, no. 2-3, pp. 275–277, 1990.

[6] K. Kimura, "Optical recording materials based on TeO_x films," *Japanese Journal of Applied Physics*, vol. 28, no. 5R, p. 810, 1989.

[7] M. Weber, "Science and technology of laser glass," *Journal of Non-Crystalline Solids*, vol. 123, no. 1-3, pp. 208–222, 1990.

[8] E. M. Vogel, M. Weber, and D. Krol, "Nonlinear optical phenomena in glass," *Physics and chemistry of glasses*, vol. 32, no. 6, pp. 231–254, 1991.

[9] M. Udovic, P. Thomas, A. Mirgorodsky, *et al.*, "Formation domain and characterization of new glasses within the Tl_2O-TiO_2-TeO_2 system," *Materials Research Bulletin*, vol. 44, no. 2, pp. 248–253, 2009.

[10] F. He, M. Jotz, H. Wegener, M. Hahn, N. Da, and J. Zimmer, "17-3: towards flexible glass: ultra-thin glass with tight dimensional tolerance and high strength achieved by ion exchange," *SID Symposium Digest of Technical Papers*, vol. 48, no. 1, pp. 218–221, 2017.

[11] M. D. Demetriou, M. E. Launey, G. Garrett, *et al.*, "A damage-tolerant glass," *Nature Materials*, vol. 10, no. 2, pp. 123–128, Feb. 2011.

[12] A. K. Varshneya, *Fundamentals of Inorganic Glasses, The Science of Microfabrication*. Elsevier Science Publishing Co Inc, Dec. 1993.

[13] V. M. Goldschmidt, "Die gesetze der krystallochemie," *Naturwissenschaften*, vol. 14, no. 21, pp. 477–485, 1926.

[14] W. H. Zachariasen, "The atomic arrangement in glass," *Journal of the American Chemical Society*, vol. 54, no. 10, pp. 3841–3851, 1932.

[15] A. K. Varshneya and J. C. Mauro, "Chapter 3 - glass formation principles," in *Fundamentals of Inorganic Glasses (Third Edition)*, A. K. Varshneya and J. C. Mauro, Eds., Third Edition, Elsevier, 2019, pp. 37–69.

[16] A. Dietzel, *Sprechsaal*, vol. 75, p. 9, 1942.

[17] E. R. Barney, A. C. Hannon, D. Holland, *et al.*, "Terminal oxygens in amorphous TeO_2," *The Journal of Physical Chemistry Letters*, vol. 4, no. 14, pp. 2312–2316, 2013.

[18] S.-H. Kim, T. Yoko, and S. Sakka, "Linear and nonlinear optical properties of TeO_2 glass," *Journal of the American Ceramic Society*, vol. 76, no. 10, pp. 2486–2490, 1993.

[19] P. Sarjeant and R. Roy, "New glassy and polymorphic oxide phases using rapid quenching techniques," *Journal of the American Ceramic Society*, vol. 50, no. 10, pp. 500–503, 1967.

[20] J. E. STANWORTH, "Tellurite glasses," *Nature*, vol. 169, no. 4301, pp. 581–582, Apr. 1952.

[21] S. Blanchandin, P. Marchet, P. Thomas, J. Champarnaud-Mesjard, B. Frit, and A. Chagraoui, "New investigations within the TeO_2-WO_3 system: phase equilibrium diagram and glass crystallization," *Journal of materials science*, vol. 34, no. 17, pp. 4285–4292, 1999.

[22] J. Champarnaud-Mesjard, S. Blanchandin, P. Thomas, A. Mirgorodsky, T. Merle-Mejean, and B. Frit, "Crystal structure, Raman spectrum and lattice dynamics of a new metastable form of tellurium dioxide: γ-TeO_2," *Journal of physics and chemistry of solids*, vol. 61, no. 9, pp. 1499–1507, 2000.

[23] A. Mirgorodsky, T. Merle-Méjean, J.-C. Champarnaud, P. Thomas, and B. Frit, "Dynamics and structure of TeO2 polymorphs: model treatment of paratellurite and tellurite; Raman scattering evidence for new γ-and δ-phases," *Journal of physics and chemistry of solids*, vol. 61, no. 4, pp. 501–509, 2000.

[24] S. Blanchandin, P. Thomas, P. Marchet, J. C. Champarnaud-Mesjard, and B. Frit, "Equilibrium and non-equilibrium phase diagram within the TeO_2-rich part of the TeO_2-Nb_2O_5 system," *Journal of Materials Chemistry*, vol. 9, no. 8, pp. 1785–1788, 1999.

[25] P. A. Thomas, "The crystal structure and absolute optical chirality of paratellurite, α-TeO_2," *Journal of Physics C: Solid State Physics*, vol. 21, no. 25, pp. 4611–4627, 1988.

[26] V. H. Beyer, "Verfeinerung der kristallstruktur von tellurit, dem rhombischen teo_2," vol. 124, pp. 228–237, 1967.

[27] D. M. Martin, "TeO_2 - based film glasses for photonic applications: structural and optical properties"," Ph.D. dissertation, Laser Processings Group Universidad Investigaciones Cientcas Instituto de Optica Complutense de Madrid, 2009.

[28] J. Champarnaud-Mesjard, S. Blanchandin, P. Thomas, A. Mirgorodsky, T. Merle-Méjean, and B. Frit, "Crystal structure, Raman spectrum and lattice dynamics of a new metastable form of tellurium dioxide: γ-TeO_2," *Journal of Physics and Chemistry of Solids*, vol. 61, no. 9, pp. 1499–1507, 2000.

[29] Gulenko, Anastasia, "Etude structurale du verre de TeO_2 et de la variété désordonnée TeO_2-δ par dynamique moléculaire.," Ph.D. dissertation, Universite de Limoges, 2014.

[30] F. Pietrucci, S. Caravati, and M. Bernasconi, "TeO_2 glass properties from first principles," *Physical Review B*, vol. 78, no. 6, p. 064 203, 2008.

[31] A. Gulenko, O. Masson, A. Berghout, D. Hamani, and P. Thomas, "Atomistic simulations of TeO_2 -based glasses: interatomic potentials and molecular dynamics," en, *Phys. Chem. Chem. Phys.*, vol. 16, no. 27, pp. 14 150–14 160, 2014. (visited on 02/13/2021).

[32] B. G. Dick and A. W. Overhauser, "Theory of the Dielectric Constants of Alkali Halide Crystals," *Phys. Rev.*, vol. 112, pp. 90–103, 1 Oct. 1958.

[33] M. N. Garaga, U. Werner-Zwanziger, J. Zwanziger, *et al.*, "Short-range structure of TeO_2 glass," *The Journal of Physical Chemistry C*, vol. 121, no. 50, pp. 28 117–28 124, 2017.

[34] P. Gupta and A. Cooper, "Topologically disordered networks of rigid polytopes," *Journal of Non-Crystalline Solids*, vol. 123, no. 1-3, pp. 14–21, 1990.

[35] R. A. Narayanan and J. W. Zwanziger, "The glass forming ability of tellurites: a rigid polytope approach," *Journal of non-crystalline solids*, vol. 316, no. 2-3, pp. 273–280, 2003.

[36] R.Aravinda Narayanan and Josef W. Zwanziger, "The glass forming ability of tellurites: a rigid polytope approach," *Journal of Non-Crystalline Solids*, vol. 316, no. 2, pp. 273–280, 2003.

[37] M. A. Marple, M. Jesuit, I. Hung, Z. Gan, S. Feller, and S. Sen, "Structure of TeO_2 glass: Results from 2D 125Te NMR spectroscopy," *Journal of Non-Crystalline Solids*, vol. 513, pp. 183–190, 2019.

[38] O. Alderman, C. J. Benmore, S. Feller, *et al.*, "Short-range disorder in TeO_2 melt and glass," *The Journal of Physical Chemistry Letters*, vol. 11, no. 2, pp. 427–431, 2019.

[39] H. Niida, T. Uchino, J. Jin, S.-H. Kim, T. Fukunaga, and T. Yoko, "Structure of alkali tellurite glasses from neutron diffraction and molecular orbital calculations," *The Journal of Chemical Physics*, vol. 114, no. 1, pp. 459–467, 2001.

[40] J. C. McLaughlin, S. L. Tagg, and J. W. Zwanziger, "The structure of alkali tellurite glasses," *The Journal of Physical Chemistry B*, vol. 105, no. 1, pp. 67–75, 2001.

[41] C. R. Becker, S. L. Tagg, J. C. Huffman, and J. W. Zwanziger, "Crystal Structures of Potassium Tetratellurite, $K_2Te_4O_9$, and Potassium Ditellurite, $K_2Te_2O_5$, and Structural Trends in Solid Alkali Tellurites," *Inorganic Chemistry*, vol. 36, no. 24, pp. 5559–5564, 1997.

[42] R. L. Thomas, "Synthesis and characterization of tellurium oxide glasses for photonic applications," Ph.D. dissertation, International School of Photonics, Cochin University of Science and Technology, Apr. 2013.

[43] B. Buchalter and G. R. Meredith, "Third-order optical susceptibility of glasses determined by third harmonic generation," *Applied Optics*, vol. 21, no. 17, pp. 3221–3224, 1982.

[44] D. Milam, "Review and assessment of measured values of the nonlinear refractive-index coefficient of fused silica," *Applied optics*, vol. 37, no. 3, pp. 546–550, 1998.

[45] O. Noguera and S. Suehara, "High nonlinear optical properties in TeO_2-based materials: Localized hyperpolarisability approach," *Ferroelectrics*, vol. 347, no. 1, pp. 162–167, 2007.

[46] M. Dutreilh-Colas, P. Thomas, J. Champarnaud-Mesjard, and E. Fargin, "New TeO_2 based glasses for nonlinear optical applications: study of the Tl_2O-TeO_2-Bi_2O_3, Tl_2O-TeO_2-PbO and Tl_2O-TeO_2-Ga_2O_3 systems," *Physics and Chemistry of Glasses*, vol. 44, no. 5, pp. 349–352, 2003.

[47] B. Jeansannetas, S. Blanchandin, P. Thomas, *et al.*, "Glass structure and optical nonlinearities in thallium (i) tellurium (iv) oxide glasses," *Journal of Solid State Chemistry*, vol. 146, no. 2, pp. 329–335, 1999.

[48] T. Uchino and T. Yoko, "Ab initio cluster model calculations on the vibrational frequencies of TeO_2 glass," *Journal of non-crystalline solids*, vol. 204, no. 3, pp. 243–252, 1996.

[49] M. Ceriotti, F. Pietrucci, and M. Bernasconi, "Ab initio study of the vibrational properties of crystalline TeO_2: The α, β, and γ phases," *Phys. Rev. B*, vol. 73, p. 104 304, 10 2006.

[50] O. Noguera, T. Merle-Mejean, A. Mirgorodsky, P. Thomas, and J.-C. Champarnaud-Mesjard, "Dynamics and crystal chemistry of tellurites. II. Composition- and temperature-dependence of the Raman spectra of $x(Tl_2O)+(1-x)TeO_2$ glasses: Evidence for a phase

separation?" *Journal of Physics and Chemistry of Solids - J PHYS CHEM SOLIDS*, vol. 65, pp. 981–993, May 2004.

[51] P. Hohenberg and W. Kohn, "Inhomogeneous electron gas," *Physical review*, vol. 136, no. 3B, B864, 1964.

[52] P.-F. ç. Loos, "Generalized local-density approximation and one-dimensional finite uniform electron gases," *Phys. Rev. A*, vol. 89, p. 052 523, 5 May 2014.

[53] J. M. Seminario, M. C. Concha, and P. Politzer, "Calculation of molecular geometries and energies by a local density functional approach," *International Journal of Quantum Chemistry*, vol. 40, no. S25, pp. 249–259, 1991.

[54] J. K. Labanowski and J. W. Andzelm, *Density functional methods in chemistry*. Springer Science & Business Media, 2012.

[55] R. O. Jones and O. Gunnarsson, "The density functional formalism, its applications and prospects," *Rev. Mod. Phys.*, vol. 61, pp. 689–746, 3 Jul. 1989.

[56] J. P. Perdew, J. A. Chevary, S. H. Vosko, *et al.*, "Atoms, molecules, solids, and surfaces: applications of the generalized gradient approximation for exchange and correlation," *Physical review B*, vol. 46, no. 11, p. 6671, 1992.

[57] A. Becke, "Completely numerical calculations on diatomic molecules in the local-density approximation," *Physical Review A*, vol. 33, no. 4, p. 2786, 1986.

[58] A. D. Becke, "Density functional theories in quantum chemistry," in *The Challenge of d and f Electrons*, ch. 12, pp. 165–179.

[59] J. P. Perdew, "Accurate density functional for the energy: real-space cutoff of the gradient expansion for the exchange hole," *Physical Review Letters*, vol. 55, no. 16, p. 1665, 1985.

[60] J. P. Perdew and Y. Wang, "Accurate and simple analytic representation of the electron-gas correlation energy," *Physical review B*, vol. 45, no. 23, p. 13 244, 1992.

[61] J. P. Perdew, K. Burke, and Y. Wang, "Generalized gradient approximation for the exchange-correlation hole of a many-electron system," *Physical review B*, vol. 54, no. 23, p. 16 533, 1996.

[62] J. P. Perdew, K. Burke, and M. Ernzerhof, "Generalized gradient approximation made simple," *Physical review letters*, vol. 77, no. 18, p. 3865, 1996.

[63] A. D. Becke, "Density-functional exchange-energy approximation with correct asymptotic behavior," *Physical review A*, vol. 38, no. 6, p. 3098, 1988.

[64] C. Lee, W. Yang, and R. G. Parr, "Development of the colle-salvetti correlation-energy formula into a functional of the electron density," *Physical review B*, vol. 37, no. 2, p. 785, 1988.

[65] A. Janotti and C. G. Van de Walle, "LDA+U and hybrid functional calculations for defects in ZnO, SnO_2, and TiO_2," *physica status solidi (b)*, vol. 248, no. 4, pp. 799–804, 2011.

[66] R. Car and M. Parrinello, "Unified approach for molecular dynamics and density-functional theory," *Physical review letters*, vol. 55, no. 22, p. 2471, 1985.

[67] S. Nosé, "A unified formulation of the constant temperature molecular dynamics methods," *J. Chem. Phys.*, vol. 81, no. 1, pp. 511–519, 1984.

[68] S. Nosé, *Mol. Phys.*, vol. 52, pp. 255–268, 1984.

[69] W. G. Hoover, *Phys. Rev. A.*, vol. 31, pp. 1695–1697, 3 1985.

[70] V. Rühle, "Berendsen and nose-hoover thermostats," 2007.

[71] P. L. Silvestrelli, N. Marzari, D. Vanderbilt, and M. Parrinello, "Maximally-localized wannier functions for disordered systems: application to amorphous silicon," *Solid State Communications*, vol. 107, no. 1, pp. 7–11, 1998.

[72] T. A. Manz and N. G. Limas, "Introducing ddec6 atomic population analysis: part 1. charge partitioning theory and methodology," *RSC Adv.*, vol. 6, pp. 47 771–47 801, 53 2016.

[73] N. G. Limas and T. A. Manz, "Introducing ddec6 atomic population analysis: part 2. computed results for a wide range of periodic and nonperiodic materials," *RSC Adv.*, vol. 6, pp. 45 727–45 747, 51 2016.

[74] T. A. Manz, "Introducing ddec6 atomic population analysis: part 3. comprehensive method to compute bond orders," *RSC Adv.*, vol. 7, pp. 45 552–45 581, 72 2017.

[75] N. G. Limas and T. A. Manz, "Introducing ddec6 atomic population analysis: part 4. efficient parallel computation of net atomic charges, atomic spin moments, bond orders, and more," *RSC Adv.*, vol. 8, pp. 2678–2707, 5 2018.

[76] Chargemol, *Program computing ddec atomic charges*, https://sourceforge.net/projects/ddec/, Accessed: 2022-01-10, 2017.

[77] J. VandeVondele, M. Krack, F. Mohamed, M. Parrinello, T. Chassaing, and J. Hutter, "Quickstep: fast and accurate density functional calculations using a mixed gaussian and plane waves approach," *Comput. Phys. Commun.*, vol. 167, no. 2, pp. 103–128, 2005.

[78] C. Hartwigsen, S. Gœdecker, and J. Hutter, "Relativistic separable dual-space gaussian pseudopotentials from h to rn," *Physical Review B*, vol. 58, no. 7, p. 3641, 1998.

[79] S. Goedecker, M. Teter, and J. Hutter, "Separable dual-space gaussian pseudopotentials," *Phys. Rev. B*, vol. 54, no. 3, p. 1703, 1996.

[80] J. VandeVondele and J. Hutter, "An efficient orbital transformation method for electronic structure calculations," *The Journal of chemical physics*, vol. 118, no. 10, pp. 4365–4369, 2003.

[81] I. Bethune, "Improving the scalability of cp2k on multi-core systems," Tech. Rep., 2010.

[82] M. Born and R. Huang, *Dynamical Theory of Crystal lattices*. Oxford University Press, 1954.

[83] K. Miwa, "Prediction of raman spectra with ultrasoft pseudopotentials," *Physical Review B*, vol. 84, no. 9, p. 094 304, 2011.

[84] D. A. Long, *The Raman effect: A unified treatment of the theory of Raman scattering by molecules*. WILEY, May 31, 2002, 624 pp.

[85] M. Dutreilh-Colas, P. Thomas, J.-C. Champarnaud-Mesjard, and E. Fargin, "New TeO_2 based glasses for nonlinear optical applications: study of the Tl_2O-TeO_2-Bi_2O_3, Tl_2O-TeO_2-PbO and Tl_2O-TeO_2-Ga_2O_3 systems," *Physics and chemistry of glasses*, vol. 44, no. 5, pp. 349–352, 2003.

[86] S. Suehara, P. Thomas, A. Mirgorodsky, *et al.*, "Localized hyperpolarizability approach to the origin of nonlinear optical properties in teo_2-based materials," *Physical Review B*, vol. 70, no. 20, p. 205 121, 2004.

[87] A. Mirgorodsky, M. Soulis, P. Thomas, T. Merle-Méjean, and M. Smirnov, "Ab initio study of the nonlinear optical susceptibility of teo_2-based glasses," *Physical Review B*, vol. 73, no. 13, p. 134 206, 2006.

[88] J. VandeVondele and J. Hutter, "Gaussian basis sets for accurate calculations on molecular systems in gas and condensed phases," *J. Chem. Phys.*, vol. 127, no. 11, p. 114 105, 2007.

[89] J. P. Perdew, K. Burke, and M. Ernzerhof, *Phys. Rev. Lett*, vol. 77, no. 18, pp. 3865–3868, 1996, *erratum* Phys. Rev. Lett. **78**, 1396 (1997).

[90] A. D. Becke, "Density-functional exchange-energy approximation with correct asymptotic behavior," *Phys. Rev. A*, vol. 38, no. 6, p. 3098, 1988.

[91] C. Lee, W. Yang, and R. G. Parr, "Development of the Colle-Salvetti correlation-energy formula into a functional of the electron density," *Phys. Rev. B*, vol. 37, no. 2, p. 785, 1988.

[92] C. Adamo and V. Barone, "Toward reliable density functional methods without adjustable parameters: the pbe0 model," *J. Chem. Phys.*, vol. 110, no. 13, pp. 6158–6170, 1999.

[93] J. P. Perdew, M. Ernzerhof, and K. Burke, "Rationale for mixing exact exchange with density functional approximations," *J. Chem. Phys.*, vol. 105, no. 22, pp. 9982–9985, 1996.

[94] N. Troullier and J. L. Martins, "Efficient pseudopotentials for plane-wave calculations. II. operators for fast iterative diagonalization," *Phys. Rev. B*, vol. 43, no. 11, p. 8861, 1991.

[95] J. Hutter, M. Parrinello, D. Marx, *et al.*, "Computer code cpmd," *IBM Zurich Research Laboratory and MPI für Festkörperforschung*, vol. 2001, 1995.

[96] R. Car and M. Parrinello, "Unified approach for molecular dynamics and density-functional theory," *Phys. Rev. Lett.*, vol. 55, no. 22, p. 2471, 1985.

[97] T. D. Kühne, M. Krack, F. R. Mohamed, and M. Parrinello, "Efficient and accurate car-parrinello-like approach to born-oppenheimer molecular dynamics," *Phys. Rev. Lett.*, vol. 98, no. 6, p. 066 401, 2007.

[98] A. Bouzid, C. Massobrio, M. Boero, G. Ori, K. Sykina, and E. Furet, "Role of the van der waals interactions and impact of the exchange-correlation functional in determining the structure of glassy gete 4," *Phys. Rev. B*, vol. 92, no. 13, p. 134 208, 2015.

[99] M. Ceriotti, F. Pietrucci, and M. Bernasconi, "Ab initio study of the vibrational properties of crystalline TeO_2: The α, β, and γ phases," *Phys. Rev. B*, vol. 73, no. 10, p. 104 304, 2006.

[100] P. Naresh, "Influence of TeO_2 on the UV, electrical and structural studies of Li_2O-ZnO-B_2O_3 glasses," *Journal of Molecular Structure*, vol. 1213, p. 128 184, 2020.

[101] G. W. Brady, "Structure of Tellurium Oxide Glass," *The Journal of Chemical Physics*, vol. 27, no. 1, pp. 300–303, 1957.

[102] Garaga, Mounesha N. and Werner-Zwanziger, U. and Zwanziger, J. W. and DeCeanne, A. and Hauke, B. and Bozer, K. and Feller, S., "Short-Range Structure of TeO_2 Glass," *The Journal of Physical Chemistry C*, vol. 121, no. 50, pp. 28 117–28 124, 2017.

[103] L. S. El-Deen, M. A. Salhi, and M. M. Elkholy, "IR and UV spectral studies for rare earths-doped tellurite glasses," *Journal of Alloys and Compounds*, vol. 465, no. 1, pp. 333–339, 2008.

[104] N. Elkhoshkhany, R. Essam, and E. S. Yousef, "Influence of La_2O_3 on the structural, optical and thermal properties of TeO_2-ZnO-Li_2O-Nb_2O_5 glass," *Journal of Non-Crystalline Solids*, vol. 536, p. 119 994, 2020.

[105] K. M. Kaky, G. Lakshminarayana, S. Baki, I. Kityk, Y. Taufiq-Yap, and M. Mahdi, "Structural, thermal and optical absorption features of heavy metal oxides doped tellurite rich glasses," *Results in Physics*, vol. 7, pp. 166–174, 2017.

[106] N. Tagiara, D. Palles, E. Simandiras, V. Psycharis, A. Kyritsis, and E. Kamitsos, "Synthesis, thermal and structural properties of pure TeO_2 glass and zinc-tellurite glasses," *Journal of Non-Crystalline Solids*, vol. 457, pp. 116–125, 2017.

[107] R. A. H. El-Mallawany, *Tellurite Glasses Handbook : Physical Properties and Data, Second Edition*, en. CRC Press, Apr. 2016. (visited on 04/28/2021).

[108] M. Soulis, A. Mirgorodsky, T. Merle-Méjean, O. Masson, P. Thomas, and M. Udovic, "The role of modifier's cation valence in structural properties of TeO_2-based glasses," *Journal of Non-Crystalline Solids*, vol. 354, no. 2, pp. 143–149, 2008, Physics of Non-Crystalline Solids 11.

[109] B. Jeansannetas, S. Blanchandin, P. Thomas, *et al.*, "Glass Structure and Optical Nonlinearities in Thallium(I) Tellurium(IV) Oxide Glasses," en, *Journal of Solid State Chemistry*, vol. 146, no. 2, pp. 329–335, Sep. 1999.

[110] T. Sekiya, N. Mochida, A. Ohtsuka, and M. Tonokawa, "Raman spectra of $MO_{1/2}$-TeO_2 (M = Li, Na, K, Rb, Cs and Tl) glasses," en, *Journal of Non-Crystalline Solids*, vol. 144, pp. 128–144, Jan. 1992.

[111] O. Noguera, T. Merle-Méjean, A. Mirgorodsky, P. Thomas, and J.-C. Champarnaud-Mesjard, "Dynamics and crystal chemistry of tellurites. II. Composition- and temperature-dependence of the Raman spectra of x(Tl_2O)+(1-x)TeO_2 glasses: evidence for a phase separation?" *Journal of Physics and Chemistry of Solids*, vol. 65, no. 5, pp. 981–993, 2004.

[112] L. Martínez, R. Andrade, E. G. Birgin, and J. M. Martínez, "PACKMOL: A package for building initial configurations for molecular dynamics simulations," *Journal of Computational Chemistry*, vol. 30, no. 13, pp. 2157–2164, 2009.

[113] Torzuoli, Lyna, "Etude de la structure des verres des systèmes TeO_2-M_xO_y (M = Ti, TI) par diffusion totale des rayons X et dynamique moléculaire," Ph.D. dissertation, Universite de Limoges, 2020.

[114] H. Nesbitt, G. Henderson, G. Bancroft, and R. Ho, "Experimental evidence for na coordination to bridging oxygen in na-silicate glasses: implications for spectroscopic studies and for the modified random network model," *Journal of Non-Crystalline Solids*, vol. 409, pp. 139–148, 2015.

[115] J. Du and A. Cormack, "The medium range structure of sodium silicate glasses: a molecular dynamics simulation," *Journal of Non-Crystalline Solids*, vol. 349, pp. 66–79, 2004, Glass Science for High Technology. 16th University Conference on Glass Science.

[116] A. Cormack, J. Du, and T. Zeitler, "Sodium ion migration mechanisms in silicate glasses probed by molecular dynamics simulations," *Journal of Non-Crystalline Solids*, vol. 323, no. 1, pp. 147–154, 2003, Natural Glasses 4: Glasses in Geosciences, Environmental Sciences and Archeometry.

[117] R. N. Mead and G. Mountjoy, "A molecular dynamics study of the atomic structure of $(CaO)_x$-$(SiO_2)_{1-x}$ glasses," *The Journal of Physical Chemistry B*, vol. 110, no. 29, pp. 14 273–14 278, 2006.

[118] A. Tilocca and N. H. de Leeuw, "Structural and electronic properties of modified sodium and soda-lime silicate glasses by car–parrinello molecular dynamics," *Journal of Materials Chemistry*, vol. 16, no. 20, pp. 1950–1955, 2006.

[119] F. Kargl, A. Meyer, M. Koza, and H. Schober, "Formation of channels for fast-ion diffusion in alkali silicate melts: a quasielastic neutron scattering study," *Physical Review B*, vol. 74, no. 1, p. 014 304, 2006.

[120] J. Machacek, O. Gedeon, and M. Liska, "The md study of mixed alkali effect in alkali silicate glasses," *Physics and Chemistry of Glasses-European Journal of Glass Science and Technology Part B*, vol. 51, no. 1, pp. 65–68, 2010.

[121] S. L. Roux and P. Jund, "Ring statistics analysis of topological networks: New approach and application to amorphous GeS_2 and SiO_2 systems," *Computational Materials Science*, vol. 49, no. 1, pp. 70–83, 2010.

[122] S. V. King, "Ring configurations in a random network model of vitreous silica," *Nature*, vol. 213, no. 5081, pp. 1112–1113, 1967.

[123] D. Franzblau, "Computation of ring statistics for network models of solids," *Physical Review B*, vol. 44, no. 10, p. 4925, 1991.

[124] F. Birch, "Finite elastic strain of cubic crystals," *Phys. Rev.*, vol. 71, pp. 809–824, 11 Jun. 1947.

[125] F. D. Murnaghan, "The compressibility of media under extreme pressures," *Proceedings of the National Academy of Sciences*, vol. 30, no. 9, pp. 244–247, 1944.

[126] E. Lambson, G. Saunders, B. Bridge, and R. El-Mallawany, "The elastic behaviour of TeO_2 glass under uniaxial and hydrostatic pressure," *Journal of non-crystalline solids*, vol. 69, no. 1, pp. 117–133, 1984.

[127] J. Sabadel, P. Armand, D. Cachau-Herreillat, *et al.*, "Structural and nonlinear optical characterizations of tellurium oxide-based glasses: TeO_2-BaO-TiO_2," *Journal of Solid State Chemistry*, vol. 132, no. 2, pp. 411–419, 1997.

[128] M. Udovic, P. Thomas, A. Mirgorodsky, *et al.*, "Thermal characteristics, Raman spectra and structural properties of new tellurite glasses within the Bi_2O_3-TiO_2-TeO_2 system," *Journal of Solid State Chemistry*, vol. 179, no. 10, pp. 3252–3259, 2006.

[129] J.-C. Sabadel, P. Armand, P.-E. Lippens, D. Cachau-Herreillat, and E. Philippot, "Mössbauer and xanes of teo_2-bao-tio_2 glasses," *Journal of non-crystalline solids*, vol. 244, no. 2-3, pp. 143–150, 1999.

[130] M. Udovic, P. Thomas, A. Mirgorodsky, *et al.*, "Formation domain and characterization of new glasses within the Tl_2O-TiO_2-TeO_2 system," en, *Materials Research Bulletin*, vol. 44, no. 2, pp. 248–253, Feb. 2009. (visited on 03/31/2021).

[131] *Total X-ray diffraction pair distribution function G(r) for x = 10% and y = 30% ternary $(TiO_2)_x - (TlO_{0.5})_y - (TeO_2)_{1-x-y}$ glass*, Internal data from IRCER laboratory, Axe: 3.

[132] V. Van Hoang, "Structural properties of simulated liquid and amorphous TiO_2," *physica status solidi (b)*, vol. 244, no. 4, pp. 1280–1287, 2007.

[133] V. Petkov, G. Holzhüter, U. Tröge, T. Gerber, and B. Himmel, "Atomic-scale structure of amorphous TiO2 by electron, X-ray diffraction and reverse Monte Carlo simulations," *Journal of non-crystalline solids*, vol. 231, no. 1-2, pp. 17–30, 1998.

[134] O. Alderman, L. Skinner, C. Benmore, A. Tamalonis, and J. Weber, "Structure of molten titanium dioxide," *Physical Review B*, vol. 90, no. 9, p. 094 204, 2014.

[135] P. Partovi-Azar, T. D. Kühne, and P. Kaghazchi, "Evidence for the existence of Li_2S_2 clusters in lithium–sulfur batteries: ab initio Raman spectroscopy simulation," *Physical Chemistry Chemical Physics*, vol. 17, no. 34, pp. 22 009–22 014, 2015.

[136] S. Luber, M. Iannuzzi, and J. Hutter, "Raman spectra from *ab-initio* molecular dynamics and its application to liquid S-methyloxirane," *The Journal of Chemical Physics*, vol. 141, no. 9, p. 094 503, 2014.

[137] P. Partovi-Azar and T. D. Kühne, "Efficient "on-the-fly" calculation of raman spectra from ab-initio molecular dynamics: application to hydrophobic/hydrophilic solutes in bulk water," *Journal of Computational Chemistry*, vol. 36, no. 29, pp. 2188–2192, 2015.

[138] A. Calzolari and M. B. Nardelli, "Dielectric properties and raman spectra of zno from a first principles finite-differences/finite-fields approach," *Scientific reports*, vol. 3, no. 1, pp. 1–6, 2013.

[139] Q. Liang, S. Dwaraknath, and K. A. Persson, "High-throughput computation and evaluation of raman spectra," *Scientific data*, vol. 6, no. 1, pp. 1–7, 2019.

[140] M. Lazzeri and F. Mauri, "First-Principles Calculation of Vibrational Raman Spectra in Large Systems: Signature of Small Rings in Crystalline SiO_2," *Physical Review Letters*, vol. 90, no. 3, p. 036 401, 2003.

[141] A. Togo and I. Tanaka, "First principles phonon calculations in materials science," *Scripta Materialia*, vol. 108, pp. 1–5, 2015.

[142] I. Souza, J. Íniguez, and D. Vanderbilt, "First-principles approach to insulators in finite electric fields," *Physical review letters*, vol. 89, no. 11, p. 117 602, 2002.

[143] M. R. Zaki, D. Hamani, M. Dutreilh-Colas, J.-R. Duclère, O. Masson, and P. Thomas, "Synthesis, thermal, structural and linear optical properties of new glasses within the TeO_2-TiO_2-WO_3 system," *Journal of Non-Crystalline Solids*, vol. 484, pp. 139–148, 2018.

[144] G. S. Henderson, D. R. Neuville, B. Cochain, and L. Cormier, "The structure of GeO_2-SiO_2 glasses and melts: A Raman spectroscopy study," *Journal of Non-Crystalline Solids*, vol. 355, no. 8, pp. 468–474, 2009.

[145] V. Malinovsky, V. Novikov, N. Surovtsev, and A. Shebanin, "Investigation of amorphous states of sio 2 by raman scattering spectroscopy," *Physics of the solid state*, vol. 42, pp. 65–71, 2000.

[146] A. Sokolov, A. Kisliuk, M. Soltwisch, and D. Quitmann, "Medium-range order in glasses: comparison of raman and diffraction measurements," *Physical Review Letters*, vol. 69, no. 10, p. 1540, 1992.

[147] T. Vasileiadis and S. N. Yannopoulos, "Photo-induced oxidation and amorphization of trigonal tellurium: a means to engineer hybrid nanostructures and explore glass structure under spatial confinement," *Journal of Applied Physics*, vol. 116, no. 10, p. 103 510, 2014.

[148] R. Raghvender, A. Bouzid, S. Cadars, D. Hamani, P. Thomas, and O. Masson, "Structure of amorphous TeO_2 revisited: A hybrid functional ab initio molecular dynamics study," *Phys. Rev. B*, vol. 106, p. 174 201, 17 Nov. 2022.

[149] M. Soulis, T. Merle-Méjean, A. Mirgorodsky, *et al.*, "Local molecular orbitals and hyper-susceptibility of TeO_2 glass," *J. Non-Cryst. Solids*, vol. 354, no. 2, pp. 199–202, 2008, Physics of Non-Crystalline Solids 11.

[150] J.-R. Duclère, T. Hayakawa, E. Roginskii, *et al.*, "Third order nonlinear optical properties of a paratellurite single crystal," *Journal of Applied Physics*, vol. 123, no. 18, p. 183 105, 2018.

[151] I. H. Malitson, "Interspecimen comparison of the refractive index of fused silica," *Josa*, vol. 55, no. 10, pp. 1205–1209, 1965.

[152] N. Uchida, "Optical properties of single-crystal paratellurite (TeO_2)," *Physical Review B*, vol. 4, no. 10, p. 3736, 1971.

[153] L. Torzuoli, A. Bouzid, P. Thomas, and O. Masson, "An enhanced core–shell interatomic potential for Te–O based oxides," *Materials Research Express*, vol. 7, no. 1, p. 015 202, Jan. 2020.

[154] B. W. H. van Beest, G. J. Kramer, and R. A. van Santen, "Force fields for silicas and aluminophosphates based on ab-initio calculations," *Phys. Rev. Lett.*, vol. 64, pp. 1955–1958, 16 Apr. 1990.

[155] X.-Y. Qu, X.-F. Gou, and T.-G. Wang, "A highly accurate interatomic potential for $LaMnO_3$ perovskites with temperature-dependence of structure and thermal properties," *Computational Materials Science*, vol. 193, p. 110 406, 2021.

[156] P. P. Ewald, "Die Berechnung optischer und elektrostatischer Gitterpotentiale," *Annalen der Physik*, vol. 369, no. 3, pp. 253–287, 1921.

[157] J. D. Gale and A. L. Rohl, "The General Utility Lattice Program (GULP)," *Molecular Simulation*, vol. 29, no. 5, pp. 291–341, 2003.

[158] B. Jeansannetas, P. Thomas, J. Champarnaud-Mesjard, and B. Frit, "Crystal structure of α-$Tl_2Te_2O_5$," *Materials Research Bulletin*, vol. 33, no. 11, pp. 1709–1716, 1998.

[159] B. Jeansannetas and P. Thomas and J.C. Champarnaud-Mesjard and B. Frit, "Crystal structure of $Tl_2Te_3O_7$," *Materials Research Bulletin*, vol. 32, no. 1, pp. 51–58, 1997.

[160] B. Frit, D. Mercurio, P. Thomas, and J.-C. Champarnaud-Mesjard, "Refinement of the crystal structure of dithallium(I) trioxotellurate(IV), TI_2TeO_3," *Zeitschrift für Kristallographie - New Crystal Structures*, vol. 214, no. 4, pp. 439–440, 1999.

[161] S. M. Woodley, P. D. Battle, J. D. Gale, and C. Richard A. Catlow, "The prediction of inorganic crystal structures using a genetic algorithm and energy minimisation," *Phys. Chem. Chem. Phys.*, vol. 1, pp. 2535–2542, 10 1999.

[162] J. E. Saal, S. Kirklin, M. Aykol, B. Meredig, and C. Wolverton, "Materials Design and Discovery with High-Throughput Density Functional Theory: The Open Quantum Materials Database (OQMD)," en, *JOM*, vol. 65, no. 11, pp. 1501–1509, Nov. 2013. (visited on 03/29/2021).

[163] S. Kirklin, J. E. Saal, B. Meredig, *et al.*, "The Open Quantum Materials Database (OQMD): assessing the accuracy of DFT formation energies," en, *npj Computational Materials*, vol. 1, no. 1, pp. 1–15, Dec. 2015, Number: 1 Publisher: Nature Publishing Group. (visited on 03/29/2021).

[164] *Database of published interatomic potential parameters*, https://www.ucl.ac.uk/klmc/Potentials/, Accessed: 2020-11-30.

[165] C. G. Broyden, "The Convergence of a Class of Double-rank Minimization Algorithms 1. General Considerations," *IMA Journal of Applied Mathematics*, vol. 6, no. 1, pp. 76–90, Mar. 1970.

[166] R. Fletcher, "A new approach to variable metric algorithms," *The Computer Journal*, vol. 13, no. 3, pp. 317–322, Jan. 1970.

[167] D. Goldfarb, "A family of variable-metric methods derived by variational means," en, *Mathematics of Computation*, vol. 24, no. 109, pp. 23–26, 1970. (visited on 03/29/2021).

[168] D. F. Shanno, "Conditioning of quasi-Newton methods for function minimization," en, *Mathematics of Computation*, vol. 24, no. 111, pp. 647–656, 1970. (visited on 03/29/2021).

[169] M. S. Islam and L. J. Winch, "Defect chemistry and oxygen diffusion in the $HgBa_2Ca_2Cu_3O_{8+\delta}$ superconductor: A computer simulation study," *Phys. Rev. B*, vol. 52, pp. 10 510–10 515, 14 Oct. 1995.

[170] J. D. Gale and N. J. Henson, "Derivation of interatomic potentials for microporous aluminophosphates from the structure and properties of berlinite," *J. Chem. Soc., Faraday Trans.*, vol. 90, pp. 3175–3179, 20 1994.

[171] T. S. Bush, J. D. Gale, C. R. A. Catlow, and P. D. Battle, "Self-consistent interatomic potentials for the simulation of binary and ternary oxides," *J. Mater. Chem.*, vol. 4, pp. 831–837, 6 1994.

[172] R. A. Jackson and C. R. A. Catlow, "Computer simulation studies of zeolite structure," *Molecular Simulation*, vol. 1, no. 4, pp. 207–224, 1988.

[173] G. V. Lewis and C. R. A. Catlow, "Potential models for ionic oxides," *Journal of Physics C: Solid State Physics*, vol. 18, no. 6, p. 1149, Feb. 1985.

[174] D. Jason Binks and R. W. Grimes, "The non-stoichiometry of zinc and chromium excess zinc chromite," *Solid State Communications*, vol. 89, no. 11, pp. 921–924, 1994.

[175] P. Nicolini and T. Polcar, "A comparison of empirical potentials for sliding simulations of MoS_2," *Computational Materials Science*, vol. 115, pp. 158–169, 2016.

[176] I. T. Todorov, W. Smith, K. Trachenko, and M. T. Dove, "DL_POLY_3: new dimensions in molecular dynamics simulations via massive parallelism," *J. Mater. Chem.*, vol. 16, no. 20, pp. 1911–1918, 2006, Publisher: The Royal Society of Chemistry.

[177] P. J. D. Lindan and M. J. Gillan, "Shell-model molecular dynamics simulation of superionic conduction in CaF_2," *Journal of Physics: Condensed Matter*, vol. 5, no. 8, pp. 1019–1030, Feb. 1993.

[178] C. L. Olson, J. Nelson, and M. S. Islam, "Defect chemistry, surface structures, and lithium insertion in anatase TiO_2," *The Journal of Physical Chemistry B*, vol. 110, no. 20, pp. 9995–10 001, 2006.

[179] A. Carré, L. Berthier, J. Horbach, S. Ispas, and W. Kob, "Amorphous silica modeled with truncated and screened coulomb interactions: a molecular dynamics simulation study," *The Journal of Chemical Physics*, vol. 127, no. 11, p. 114 512, Sep. 2007.

[180] P. Umari and A. Pasquarello, "Ab initio molecular dynamics in a finite homogeneous electric field," *Physical Review Letters*, vol. 89, no. 15, p. 157 602, 2002.

[181] *Codes for computing raman spectra are available at*, https://github.com/ladyteam/ramanpy, Accessed: 2022-11-30.

List of works

Publications

- R. Raghvender, A. Bouzid, D. Hamani, P. Thomas, and O. Masson, "A Buckingham interatomic potential for thallium oxide (Tl_2O): Application to the case of thallium tellurite glasses," *Computational Materials Science*, vol. 201, p. 110 891, 2022.
- R. Raghvender, A. Bouzid, S. Cadars, D. Hamani, P. Thomas, and O. Masson, "Structure of amorphous TeO_2 revisited: A hybrid functional *ab-initio* molecular dynamics study," *Phys. Rev. B*, vol. 106, p. 174 201, 17 Nov. 2022.
- E. M. Roginskii, R. Raghvender, O. Noguera, P. Thomas, O. Masson, and A. Bouzid, "Ab-initio study of Raman spectra of amorphous oxides: Insights into the Boson peak nature in glassy TeO_2," *Physica Status Solidi - Rapid Research Letters*, 2022, submitted.

Conferences

- Raghvender Raghvender, Assil Bouzid, David Hamani, Philippe Thomas, and Olivier Masson, "Atomic-scale modeling of tellurium oxide glass: network topology and third-order non-linear properties," *Society of glass technology, Canterbury (UK)*, Jul. 2022, Oral presentation.
- Raghvender Raghvender, Assil Bouzid, Philippe Thomas, David Hamani and Olivier Masson, "Buckingham interatomic potential for thallium oxide (Tl^{+}-O^{2-}); application to the case of thallium tellurite glasses," *European materials research society*, Sep. 2021, Online poster presentation.

ETUDE AB-INITIO DE LA STRUCTURE DES VERRES A BASE D'OXYDE DE TELLURIUM: un pas en avant dans l'etablissement de la relation structure-proprietes

Résumé : Les verres de TeO_2 présentent des propriétés optiques non linéaires de troisième ordre 50 fois supérieures à celles des verres de silicate classiques, ce qui en fait des candidats prometteurs pour les mécanismes de conversion de fréquence, les commutateurs optiques et d'autres applications. L'existence d'une paire libre de type $5s^2$ sur l'atome de Te dans le réseau vitreux est à l'origine de ces propriétés exceptionnelles. Bien que plusieurs études aient examiné la structure du verre TeO_2, l'ordre à court et moyen termes dans ce matériau restent un sujet de débat. En particulier, l'effet de l'ajout d'un oxyde modificateur dans le système vitreux TeO_2 a montré un fort effet sur ses propriétés optiques, mécaniques et chimiques. Cependant, une étude complète sur l'évolution de la structure à l'échelle atomique dans ces verres en corrélation avec les propriétés du matériau fait toujours défaut. Dans cette thèse, nous recourons aux techniques de dynamique moléculaire des premiers principes pour produire des modèles quantitatifs amorphes de TeO_2 pur, de Tl_2O-TeO_2 binaire et de TiO_2-Tl_2O-TeO_2 ternaire présentant un bon accord avec les mesures expérimentales. Ces modèles sont ensuite utilisés pour étudier la topologie du réseau des systèmes à base de TeO_2 en fonction de la concentration d'oxyde modificateur, avec une attention particulière à l'ordre à courte portée corrélé aux propriétés électroniques du matériau. En outre, nous étudions les propriétés vibrationnelles et optiques non linéaires des verres à base de TeO_2 afin d'améliorer notre compréhension de la relation structure-propriétés.

Mots clés : Verres à base de TeO_2, Propriétés d'optique non linéaires, nombre de coordination Te, verre binaire Tl_2O-TeO_2, verre ternaire TiO_2-Tl_2O-TeO_2, Spectroscopie vibrationnelle, *Ab-initio* dynamique moléculaire

AB-INITIO STUDY OF THE STRUCTURE OF TELLURIUM-OXIDE BASED GLASSES: a step forward in establishing the structure-properties relationships

Abstract: TeO_2 glasses exhibit third order non-linear optical properties 50 times higher than conventional silicate glasses, making them promising candidates for frequency conversion mechanism, optical switches and other applications. The existence of $5s^2$ lone pair on Te atom in the glassy network is at the origin of these outstanding properties. Despite the fact that several studies have investigated the structure of TeO_2 glass, the short and medium range orders in this material remain a matter of debate. In particular, the effect of adding a modifier oxide into the glassy TeO_2 system has show a strong effect on its optical, mechanical and chemical properties. Yet, a comprehensive study on the atomic scale structure evolution in these glasses and its correlation to the material properties is still lacking. In this thesis, we resort to first-principles molecular dynamics techniques to produce quantitative pure TeO_2, binary Tl_2O-TeO_2 and ternary TiO_2-Tl_2O-TeO_2 amorphous models featuring a good agreement with the experimental measurements. These models are then used to study the network topology of TeO_2-based systems as a function of the modifier concentration with a particular focus on the short-range order correlated to the electronic properties of the material. Furthermore, we study the vibrational and non-linear optical properties of TeO_2 -based glasses in order to improve our understanding of the structure-properties relationships.

Keywords: TeO_2-based glasses, Non-linear optical properties, Te coordination number, Tl_2O-TeO_2 binary glass, TiO_2-Tl_2O-TeO_2 ternary glass, Vibrational spectroscopy, *Ab-initio* molecular dynamics

Université de Limoges, CNRS, IRCER, UMR 7315, 87000 Limoges, France